UNIVERSIDADE DE SANTIAGO DE COMPOSTELA

FACULTADE DE FÍSICA

Departamento de Física de Partículas

LabCAF

RESEARCH AND DEVELOPMENTS ON TIMING RPC'S. APPLICATION TO THE ESTRELA DETECTOR OF THE HADES EXPERIMENT AT GSI

Diego González Díaz

Santiago de Compostela, February 2006

D. Juan Antonio Garzón Heydt

Profesor titular da área de Física Atómica Molecular e Nuclear

e

D. Paulo Jorge Ribeiro da Fonte

Profesor-coordinador do Instituto Superior de Engenhería de Coimbra (ISEC)

Investigador no Laboratorio de Investigação e Física Experimental de Partículas (LIP)

CERTIFICAN

que a tese titulada:

Research and developments on timing RPC's. Application to the ESTRELA detector of the HADES experiment at GSI.

foi realizada por D. Diego González Díaz
no **Departamento de Física de Partículas**
da **Universidade de Santiago de Compostela**
baixo a súa dirección, e constitúe a tese
que presenta para acadar o título de Doutor.

Santiago de Compostela, Febreiro do 2006

(defendida en Marzo do 2006)

(**revisada en Setembro do 2006**)

Asinado:

Juan Antonio Garzón Heydt Paulo Jorge Ribeiro da Fonte

Agradecementos

O camiño cara a tese é largo e non está exento de incertezas e frustracións; é tamén unha época na que, de maneira forzosa, profundizamos nas nosas capacidades e as levamos a limites que non sospeitabamos. O mundo da investigación que se me mostrou durante a elaboración do presente traballo posúe múltiples caras: baste mencionar a alarmante proximidade do *éxito* e do *fracaso* que nos obriga a relativizar sobre estas e outras cuestións fundamentais, ou a imperiosa necesidade de distinguir entre o plano *profesional* e o *personal*: desgraciadamente, a miña idea romántica da ciencia difícilmente casa co feito de que o investigador é, ante todo, un ser humano. Por encima das diferencias persoais, a existencia dun grupo de traballo aberto e con capacidade de crítica, no que as persoas poden expresar as súas opinións ó mesmo nivel e dunha maneira honesta, paréceme esencial de cara ó éxito común.

Un último pensamento: a grande especialización da ciencia actual obríganos a traballar en cuestións extremadamente técnicas que teñen, a cotío, unha enorme influencia sobre avances posteriores na nosa comprensión do mundo; sen embargo, son frecuentemente estes últimos traballos os que alcanzan renome e importancia. Compaxinar o disfrute desta especialización, chegando a perceber o papel último que ela xoga no avance global da ciencia e da sociedade debe ser, penso eu, o motor que impulse a investigación moderna.

Primeiramente, debo expresar o meu agradecemento cara ó catedrático E. Zas e, en especial, cara ó profesor R. Vázquez. Con eles tiven a oportunidade de estudiar un problema de enorme actualidade no campo das astropartículas: a caracterización dos fluxos de neutrinos procedentes da interacción de protóns con enerxías acima do corte GZK con fotóns do fondo universal de microondas, tema central do meu traballo de investigación tutelado (TIT). É sabido por todos os meus coñecidos ata que punto estes dous primeiros anos marcaron o meu carácter e a miña forma de entender a ciencia. Gardo gratos recordos desta primeira época, en particular das discusións (disertacións) cos meus compañeiros de despacho, Lorenzo, Ángel e Kike.

Nembargantes, o texto actual, que constitúe a miña tese de doutoramento, non sería posible sen o apoio ilusionado e incondicional do profesor J. A. Garzón (Hans), que me incorporou ó proxecto ESTRELA (*Electrically Shielded Timing RPCs Ensemble for Low Angles*) no experimento HADES no GSI, Alemaña. Foi gracias a él que puiden coñecer a P. Fonte, nos laboratorios LIP en Coimbra, Portugal. Non teño palabras para describir as virtudes de Paulo, baste decir que é unha persoa cun grande sentido da responsabilidade tanto no ámbito cientfico coma no personal. Creo ser consciente da sorte que tiven ó poder traballar con él. A lista de agradecementos profesionais non estaría completa sen A. Mangiarotti; a súa profunda e crítica maneira de ollar cara a vida e cara a ciencia, impregna esta tese desde a primeira palabra até a última. *Muito obrigado* Paulo e Alessio.

I must acknowledge a lot of other people with whom I had the oportunity to work along the years: to V. Ponce and N. Arista and the intense discussions on the fluorescence yield in Bariloche: to all the Coimbra staff, specially to A. Blanco and L. Lopes, to me an example of scientific integrity and friendship; to the GSI/HADES staff, in special to W. Koenig and P. Salabura, who showed me how to deal with an experiment of the size of HADES and still keeping a charming personality; thanks to my friend H. Alvarez-Pol from whom I learnt the importance of the **details** *and to M. Sánchez who always finds time to discuss about HADES; thanks to W. Riegler and C. Lippmann, our common discussions have being certainly enlightening and possibly paved the road to forthcoming works; I am endebted to M. Abbrescia who left a strong footprint in the last chapter of the thesis, and finally to F. Gómez for introducing me to the world of* **uncertainty** *propagation, for his availability and honestity.*

Máis, alén da traxectoria profesional, sinto que teño unha débeda igual de importante cos meus: con Silviña, que me viu nacer; con Rober, que de algunha maneira sempre está presente; gracias a Pablo pola súa amizade e amor polo axedrez; ao 'Tiempos Modernos' e todas as súas versións anteriores; a Dan, Ángel, Chis, Torri, Rubén, Paxtor, Lu, Isa, Eva, Enma e Mónica por tantos e tantos momentos; a Lucía pola súa compañía e paciencia; gracias a Julkin, por ser un tipo cojonudo, a pesar de ser o meu irmán; gracias a María, por ser a miña irmá; gracias a Carlos e Marga (a parella imposible) pola súa amizade; a Nacho '*Xotehplico*' por ter sempre algo que explicarme; a Jaime, por abrirme o camiño; a Bea, a secretaria do departamento, sen a cal esta tese non sería posible; ós camareiros da cafetería de Física, Pachín, pola súa presencia, a Isa e, especialmente, a Iván por demostrar que un mundo mellor é posible; ós meus compañeiros de despacho José Camino, Lorenzo, Ángel, Kike e Teresa por tantas discusións interminables sobre calquera tema imaxinable, e, recentemente, a Inés, Víctor e Gonzalo, herdeiros desta longa tradición dos despachos 003 e 005; especialmente gracias a Manu, por ser así e selo ata o fin, e a Tona, por soportalo; moitas gracias Noe, por ter sempre un momento para escoitarme; gracias ó resto de estudiantes, a M. Zappata sen o cal ESTRELA sería imposible, a Martín, Alex, Carme, Miguel, Eva, David e en especial a Pablo e Dani, por aturarme, *thanks to my friends at GSI, specially to Gosia, Kasia, Svicek, Stashu, Alex, Alberto, Gonzalo and Isaac, thanks to Gilo and his pizza fromaggio that allowed me (and still allows) to survive in Wixhausen, to Bella Italia and to all the HADES PhD students... (being a PhD student in HADES is not easy, I know)*; gardo unha débeda moi especial con Chiqui, que resistiu case ata o final, pola sua serenidade e apoio nos momentos máis duros; por último gracias ós meus pais e ós pais dos meus pais, que me apoiaron cegamente mesmo sen ter unha idea precisa do que fago en realidade. É a eles a quen o meu esforzo e traballo van fundamentalmente adicados, *gracias*.

Contents

List of Tables

Notation

In order to facilitate the reading, the magnitudes and constants more frequently used in the following are compiled here, together with their abbreviated notation and typical units.

letter	magnitude	typical units
A	mass number	-
A	influenced area per avalanche	mm^2
A_g	area of the glass plate	cm^2
$\mathcal{A}$	Acceptance (also activity)	- (mC)
a	q-V constant	pC/kV
α	Townsend coefficient	mm^{-1}
α^*	effective Townsend coefficient	mm^{-1}
B	magnetic field	T
b	prompt to total charge ratio	-
b	impact parameter	fm
β	velocity normalized to c	-
C	capacitance	pC/kV
c	speed of light	cm/ns
D	diffusion coefficient	mm^2/ns
D	cell length	cm
$\mathcal{D}$	lepton detection probability	-
d	thickness of the resistive plate	mm
δ	probability of electron extraction at the cathode	-
E	electric field	kV/cm
E	total energy	MeV
E_{kin}	kinetic energy	MeV
E_w	weighting field	cm^{-1}
e	electron charge	pC
ϵ	energy of a particle from the swarm	eV
ϵ_o	vacuum dielectric constant	F m^{-1}
ϵ_r	relative dielectric constant	-
ε	detector efficiency	-
η	attachment coefficient	mm^{-1}
η	density	g/cm^3
Φ, ϕ	rate	Hz/cm^2
ϕ_{lab}	azimuthal angle in 'lab'	-

letter	magnitude	typical units
g	gap size	mm
γ	relativistic factor	-
I	primary intensity	Hz, ions/s
I	mean excitation energy	eV
i, I	electric current	nA
k	Boltzmann constant	eV/K
K, K_{σ}	intrinsic time resolution	-
K_{T}	intrinsic time at maximum	-
K	rate capability	Hz/cm^2
κ	relative rate capability	-
κ	compressibility of nuclear matter	MeV
ξ	projected angle in the plane YZ	-
L	separation distance	cm
$\mathcal{L}$	ideal electron detection probability	-
λ	ionization mean free path	mm
M	mass	MeV/c^2
m	avalanche gain	-
$m_t e$	charge threshold	-
m_e	electron mass	MeV/c^2
μ_i	ion mobility	$V^{-1}\ m^2/s$
N	number of gaps	-
N_A	Avogadro number	-
N_o	number of primary clusters	-
n	average occupancy	-
n_o	average number of primary clusters	-
n'_o	average number of effective primary clusters	-
P	pressure	bar
p	momentum	MeV/c
q, q_{total}	total charge	pC
q_p, q_{prompt}	prompt induced charge	pC
$q_{induced}$	total induced charge in the gap	pC
R	resistance	Ω
ρ	resistivity	Ω cm
S	avalanche growth coefficient	ns^{-1}
σ_{T}	time resolution	ps
T	kinetic energy	MeV
T	temperature	K
t	time	s
t_{eq}	stabilization time	s
t_o	time at maximum	ns
τ_g, τ	relaxation time (also intrinsic time)	s (-)
θ_{lab}	polar angle	-

letter	magnitude	typical units
V^*	reduced voltage	kV
V_{th}	threshold voltage for Space-Charge regime	kV
v_e	electron drift velocity	cm/ns
v_{prop}	propagation velocity of signal	cm/ns
w	cell width	cm
X_{lab}	x coordinate in 'lab'	cm
x	x coordinate in local tRPC system	cm
X_o	radiation length	cm
Y_{lab}	y coordinate in 'lab'	cm
y	y coordinate in local tRPC system	cm
Z	impedance	Ω
Z	charge of the atoms of the media	-
Z_{lab}	z coordinate in 'lab'	cm
z	z coordinate in local tRPC system	cm
z	charge of the primary particle	-

Chapter 1

Motivation

The development of RPCs in 1981 gave a chance to operate gaseous detectors under parallel geometries at very high electric fields, providing a very fast and narrow time response and, what is more important, avoiding the detector breakdown. Due to the uniform electric field, the avalanche multiplication starts immediately after the first electron-ion pair is produced at *any* position within the gas gap. This represents a fundamental difference when compared to the cylindrical geometries used in proportional detectors, where the free charges must drift up to the multiplication region. As a consequence, the fluctuations in the time measured with an RPC are linked to the avalanche fluctuations during the processes of primary ionization and multiplication of electrons in the gas: they ultimately regulate the fluctuations in the size of the signal induced in the read-out electronics, resulting in different crossing times at the threshold of the comparator, and yielding its characteristic time resolution. On the other hand, the variations on the position of the first interaction cause a high independence of the released charge from the collected one (contrary to the case of proportional detectors), resulting in a poor estimate of the energy lost by the primary particle.

Possibly it was the realization of the importance of the tolerances in narrow gaps that allowed, in year 2000, to improve the RPC time resolutions up to the level of 50 ps, being competitive with present 'state of the art' fast scintillators and providing, as a benefit, a reduced price per channel and magnetic field compatibility. Such technology has been named *timing RPCs* or simply tRPCs.

There are several works that demonstrate that operation of RPCs, in any of their more usual configurations, takes place under a very strong Space-Charge effect, resulting from an avalanche self-field of the order of the applied electric field. There is a classical argument for wide gaps due to Raether, that links Space-Charge with the apparition of streamers. Notably, RPCs can be operated in a region of fields where Space-Charge is strong but streamers are absent. The presence of the last would result in, at least, a worsening of the rate capabilities, limiting the maximum reachable voltage in many applications and therefore resulting in an overall worsening of the performances.

As in the case of the RPCs developed in the 80's, yielding time resolutions at the level of 1 ns, the recent introduction of timing RPCs in 2000, with time resolutions at the level of 100 ps, has opened the possibility of application in nuclear and particle physics.

This thesis represents a small part of a project that is aimed at covering the region at the lower polar angles of the HADES spectrometer placed at GSI in Darmstadt, Germany. Such tRPC wall represents an upgrade of the current spectrometer, that will allow to explore heavy ion collisions of Au+Au up to 1.5 GeV/A, increasing our understanding of the properties of hadronic matter at densities more than twice larger than in ordinary conditions.

The tRPC wall project, internally called ESTRELA (Electrically Shielded Timing RPCs Ensemble for Low Angles) is based on recent encouraging developments of similar concepts, but incorporates the features that make HADES to be an unique environment. Among its more demanding requirements, the following must be mentioned: the tRPC wall must provide: a) a high multi-hit capability and b) working rates up to almost 1 kHz/cm^2 with c) an homogeneous time distribution at the level of 100 ps. The experiment is devoted to probe dense media through the measurement of lepton pairs coming from light pseudo-vector mesons; the low branching ratio of the process (10^{-5}-10^{-4}) requires also a very high detection efficiency and geometric acceptance, to provide reasonable statistics. The design presented in chapter 5 has been devised to meet those requirements.

Successful tests of a concept based on electrically shielded cells took place in spring 2003 and a detailed analysis is presented in chapter 6, together with the main 'pros' and 'cons' of the approach. Recent results (November 2005) on a new tRPC prototype are out of the scope of the present work but can be found elsewhere [1].

In view of the recent interest in reaching higher and higher primary rates, chapter 8 is devoted to the study of a technology that allows for an extension of the rate capability in one order of magnitude, based still on ordinary float-glass, but moderately warmed. Also a more general description of rate effects on this kind of detectors, beyond a simple DC model, is proposed in chapter 9, and used to describe the data from chapter 6. Aiming at a quantitative comparison, a way for obtaining experimentally the parameter of the swarm $S = \alpha^* v_e$ is accomplished in chapter 7 for a number of different gas admixtures.

Chapter 2

Processes in ionization gas detectors

2.1 Electromagnetic interactions with matter

Of the four known fundamental interactions, the electromagnetic one is the basic principle of almost all the detector systems that are nowadays used in experiments of nuclear and particle physics. Among the main reasons, the following can be mentioned: a) it is well understood, b) most of the particles of interest have electromagnetic charge, and therefore they interact electromagnetically[1], c) the electromagnetic interaction probability is large even for very thin media.

Despite this, both the energy and charge released in a detector via electromagnetic interactions are usually undetectable. The amplification of the few released charges to sizable signals becomes a technical problem, whose solution results in different detector families. Moreover, not always detection takes place through the ionization of the media, being also possible to make use of excitation and de-excitation processes (scintillators), Cherenkov emission (RICH[2]), transition radiation (TRD[3]) or all of them (electromagnetic calorimeter). From those who resort to ionization, the most widely used detector geometries are: a) the very fast parallel geometries as PPACs[4] and RPCs[5], b) the cylindrical/proportional ones popularized for tracking in *Wire Chambers*. Other detectors that are worth to mention and that also make use of the ionization are the GEMs (Gas Electron Multipliers), TPCs (Time Projection Chambers) or solid state detectors popularized for tracking (silicon) or γ detection (germanium).

As the aim of this work is the study of timing RPCs, the electromagnetic interactions will be described under the perspective of ionization and excitation processes in the following. Sections 2.2 and 2.3 are dedicated to the properties of ionized gases subject to external electric fields; in particular, the case where the field is constant will be implicitly considered, being this a feature of the parallel plate geometries.

[1] Notable exceptions are neutrons and neutrinos.
[2] Ring Imaging Cherenkov.
[3] Transition Radiation Detector.
[4] Parallel Plate Avalanche Chambers.
[5] Resistive Plate Chambers.

2.1.1 Heavy particles

The Bethe-Bloch curve

When a moderately relativistic heavy charged particle traverses a medium, it loses energy mainly through ionizations and excitations of the constituting atoms/molecules. The process can be described in the framework of quantum electrodynamics under the Born approximation [2], resulting in an average energy loss per unit length given by the Bethe-Bloch formula [3]:

$$-\frac{1}{\eta}\frac{dE}{dx} = Kz^2\frac{Z}{A}\frac{1}{\beta^2}\left[\frac{1}{2}\ln\frac{2m_ec^2\beta^2\gamma^2T_{max}}{I^2} - \beta^2\right] \tag{2.1}$$

The contribution of the medium is condensed in the ratio of its atomic to mass number Z/A, the density η and the *mean excitation energy* I. In eq. 2.1 m_e is the electron mass, z the charge of the incident particle in units of the electron charge and β its velocity, γ the relativistic factor and K is a constant given by:

$$K = 4\pi\frac{N_{_A}}{m_ec^2}\left(\frac{e^2}{4\pi\epsilon_o}\right)^2 = 0.307075 \text{ MeV g}^{-1}\text{ cm}^2 \tag{2.2}$$

e is the electron charge, ϵ_o the vacuum dielectric constant and $N_{_A}$ the Avogadro's number. T_{max} is defined as the maximum kinetic energy that can be transferred in an encounter with a free electron, due to momentum conservation:

$$T_{max} = \frac{2m_ec^2\beta^2\gamma^2}{1 + 2\gamma m_e/M + (m_e/M)^2} \tag{2.3}$$

where M is the mass of the particle. The recommended values for the mean excitation energy I have varied with time, but nowadays the values given in ICRU[4] are widely used. Due to the logarithmic dependence of eq. 2.1 on this parameter, rough parameterizations as the described in [5] can be used for many purposes:

$$I = 16Z^{0.9} \text{ eV} \quad \text{for} \quad Z > 1 \tag{2.4}$$

The magnitude $-\frac{1}{\eta}\frac{dE}{dx}$ is usually referred as the 'stopping power' and, remarkably, it depends on the primary particle mainly through β and z, disregarding any influence of its mass. The immediate consequences are: a) once the time of flight of a heavy charged particle along a certain path is determined, and knowing the properties of the traversed material, the average energy loss can be calculated, b) taking advantage of this feature, it is useful to express the energy loss as a function of the kinematic variable $p/Mc = \gamma\beta$ (fig. 2.1) and c) the time of flight and the energy loss of a heavy charged particle are highly redundant observables at intermediate energies.

Except for the case of hydrogen, the curve of stopping power as a function of $\gamma\beta$ shows a minimum at $\gamma\beta \simeq 3$, corresponding to $\frac{1}{\eta}\frac{dE}{dx} \simeq$ 1-2 MeV g^{-1} cm^2 (fig. 2.1). Particles with energy losses close to the point of minimum ionization are denoted as MIPs (Minimum Ionizing Particles).

Close and distant collisions

The average energy loss can be formally written as:

$$-\frac{dE}{dx} = \sum_i \eta_i \sum_n \int_o^\infty Q\frac{d\sigma_{n,i}}{dQ}dQ \tag{2.5}$$

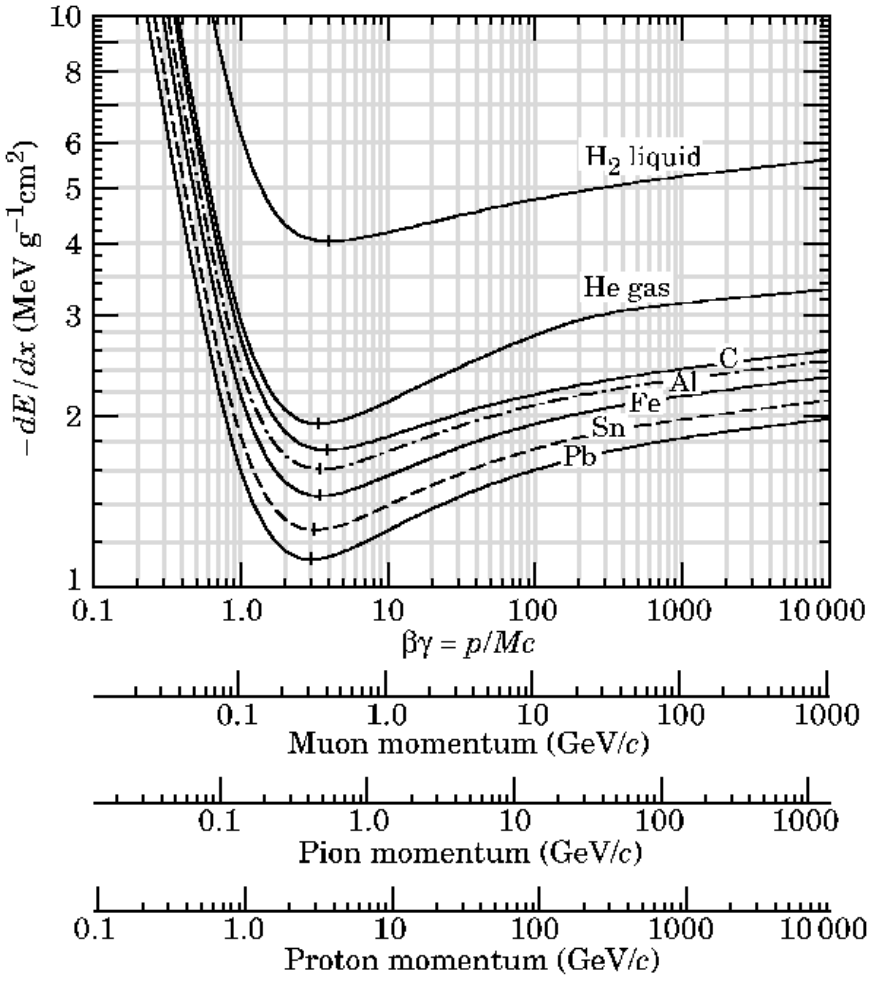

Figure 2.1: Energy loss from the Bethe-Bloch formula for a number of elements and particle species as a function of $\gamma\beta$ [3].

being $\sigma_{n,i}$ the inelastic cross section for leading an atom (or molecule) of type i to a level with an energy $E_{n,i}$ above its ground state, Q the energy transferred and η_i the density of atoms (or molecules) of type i. The derivation of eq. 2.1 from 2.5 is usually performed through the description of two regimes:

- *Distant collisions:* collisions that take place at large impact parameters $b > b_{min}$ (conversely low energy transferred $Q < Q_{min}$). They are responsible for the excitations of the atoms (molecules) of the medium. The scheme of energy levels of the atom (molecule) plays an important role, being synthesized in the average parameter I [2].

- *Close collisions:* collisions that take place at small impact parameters $b < b_{min}$ (conversely, at large energy transferred $Q > Q_{min}$). They are

responsible for ionizations. The binding energy can be neglected and the ionizing particle together with the electron from the medium can be regarded as free particles. For that reason, the scattering amplitudes are obtained from the QED calculation for different spins of the particles. Eventually, close collisions are responsible for the knock-out of energetic electrons (δ-electrons), resulting in large fluctuations of the energy released and therefore deviations from the average formula 2.5.

It can be said that:

$$-\frac{dE}{dx} = \sum_i \eta_i \sum_n \int_o^{Q_{min}} Q \frac{d\sigma_{n,i}}{dQ}\bigg|_{dist} dQ + \sum_i \eta_i \int_{Q_{min}}^{\infty} Q \frac{d\sigma_i}{dQ}\bigg|_{clos} dQ \quad (2.6)$$

The evaluation of 2.6 can be performed analytically in the two regimes and later grouped together, yielding the Bethe-Bloch formula (eq. 2.1). Details on this last step are extensively discussed in [2].

Energy loss curve

It is remarkable the high degree of generality and the accuracy of the Bethe-Bloch formula (an agreement with experimental data at the level of 1% is observed in the range $0.6 < \gamma\beta < 60$ for some cases [3]). However, its applicability is only valid at intermediate energies, failing in both the high and low energy regimes owing to the following reasons:

1. Eq. 2.1 lays on the assumption that the velocities of the atomic electrons can be neglected as compared to the ones of the particle traversing the media. The validity of such assumption becomes weak in the limit of low energies of the primary particle. This effect is accounted for by the so-called *shell correction*, a term of the form C/Z that is usually included in the brackets of eq. 2.1.

2. The electric field transversal to the movement of a particle increases with γ [6], being theoretically possible to ionize at infinite distances whenever γ tends also to infinite. However, any media reacts to an electric field through the polarization of its constituting atoms or molecules, resulting in the screening of the field at large distances that yield smaller losses as compared to the Bethe-Bloch prediction (fig. 2.2). This so-called 'density effects' can be described in the framework of classical electrodynamics [7], [8], and are often parameterized by a term of the form $-\delta/2$ in the brackets of eq. 2.1.

   At even higher energies the radiative losses due to bremsstrahlung start to dominate, growing linearly with E. The energy at which this happens is denoted as *critical energy* E_c.

The stopping power for μ^+ on copper over nine orders of magnitude in momentum is shown in fig. 2.2, including a) the low energy regime where the atomic structure becomes relevant, b) the Bethe-Bloch regime, c) the regime where polarization effects starts to affect the energy loss and, finally, d) the regime where bremsstrahlung radiation dominates.

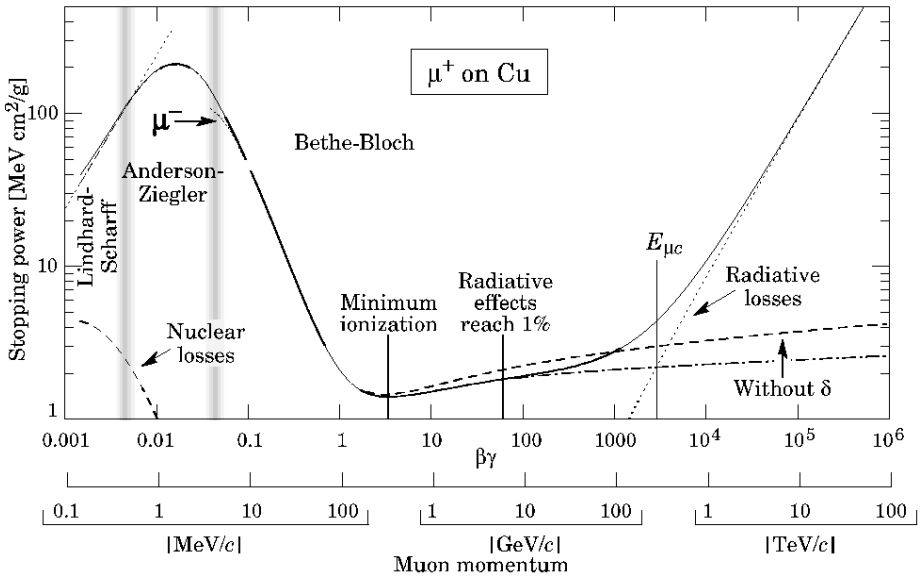

Figure 2.2: Energy loss for μ^+ in copper over 9 orders of magnitude in momentum [3].

Delta rays

It must be stressed that particle detectors are sensitive to the energy deposited on them, not to the energy lost. This subtlety is important in case a sizable amount of energy can be transferred to energetic δ-electrons that are able to abandon the detector before being stopped. As the distance a δ-electron can travel is related to its energy, it is interesting in general to define the '*restricted stopping power*' as:

$$-\frac{1}{\eta}\frac{dE}{dx}\bigg|_{T<T_{cut}} = Kz^2\frac{Z}{A}\frac{1}{\beta^2}\left[\frac{1}{2}\ln\frac{2m_ec^2\beta^2\gamma^2T_{upper}}{I^2} - \frac{\beta^2}{2}\left(1+\frac{T_{upper}}{T_{max}}\right)\right] \quad (2.7)$$

where $T_{upper} = \min(T_{cut}, T_{max})$. Expression 2.7 agrees with 2.1 in the limit where T_{cut} is larger than the maximum energy transferable by momentum conservation, T_{max}.

On the other hand, the energy distribution of δ-electrons with kinetic energy $I \ll T < T_{max}$ can be approximated by [9]:

$$\frac{1}{\eta}\frac{d^2N}{dTdx} = \frac{1}{2}Kz^2\frac{Z}{A}\frac{1}{\beta^2}\frac{1}{T^2} \quad (2.8)$$

and their angle of emission is given, in a free-electron approximation, by:

$$\cos\theta = \frac{T}{p}\frac{p_{max}}{T_{max}} \quad (2.9)$$

that results in emission perpendicular to the particle track, whenever $T \ll T_{max}$. However, elastic scattering in the medium quickly randomizes the direction of motion of δ-electrons [10]. When dealing with electrons, it is customary to define

a practical range $\mathcal{R}_p$, that can be up to 3 times shorter than the total range. For energies below some hundreds of keV, it is well described by [11]:

$$\mathcal{R}_p[\text{g cm}^{-2}] = 0.72 \left(\frac{T}{1 \text{ MeV}} \right)^{1.72} \tag{2.10}$$

Energy loss fluctuations

It must be recalled that the Bethe-Bloch formula (eq. 2.1) provides a *mean* value. As the process of energy loss has a stochastic nature it will show, in general, a characteristic distribution whose mean value is given by eq. 2.1. Due to the sizable probability of emission of high energy δ-electrons, the distribution of energy losses differs from a Gaussian expectation as long as the released energy is smaller than the energy of the particle (*thin media*). According to a classical formulation given by Landau, the energy loss distribution on a thin medium of thickness δx can be written as:

$$\frac{dN}{d\xi} = \frac{1}{\sqrt{2\pi}} e^{-\frac{1}{2}(\xi + e^{-\xi})} \tag{2.11}$$

being ξ the deviation from the most probable energy loss in non-dimensional units:

$$\xi = \frac{\Delta E - \Delta E_{mp}}{K \frac{Z}{A} \frac{\eta}{\beta^2} \delta x} \tag{2.12}$$

Eq. 2.11 is rather distinct from the Gaussian expectation, showing tails towards large values of ξ due to the contribution of one or more δ-rays. The result has practical consequences, indicating that the measurement of the energy lost in thin media by a single track does not represent, usually, a reliable estimate of the average energy loss.

Energy loss in compounds

A mixture or compound can be thought as constituted by pure elements weighted in the right proportion (the so-called Bragg additivity rule):

$$\frac{dE}{dx} = \sum_j w_j \left. \frac{dE}{dx} \right|_j \tag{2.13}$$

and w_j is the fraction of elements of type j in the compound. Care must be taken when applying the Bragg rule to magnitudes like I or δ (the density effect term), as the values of the compound can be totally different owing to the very different electric properties (see [3]).

2.1.2 High energy electrons

In most materials, at the scale of tens of MeV, electrons start to lose energy in matter mainly by bremsstrahlung (at the same scale where e^+e^- production also dominates the photon energy losses). The characteristic distance for these two processes is the radiation length X_o, defined as: a) the distance over which an electron losses in average 1/e of its energy and b) the mean free path for pair production by a high energy photon [3]. It is also a convenient scale for describing high energy electromagnetic cascades. The following parameterization is published in [3]:

$$X_o[\text{g cm}^{-2}] = \frac{716A}{Z(Z+1)\ln(287/\sqrt{Z})} \tag{2.14}$$

and the adequate expression of the Bragg's rule must be used for describing mixtures or compounds. The typical energy loss for electrons and positrons is shown in fig. 2.3 as taken from [3].

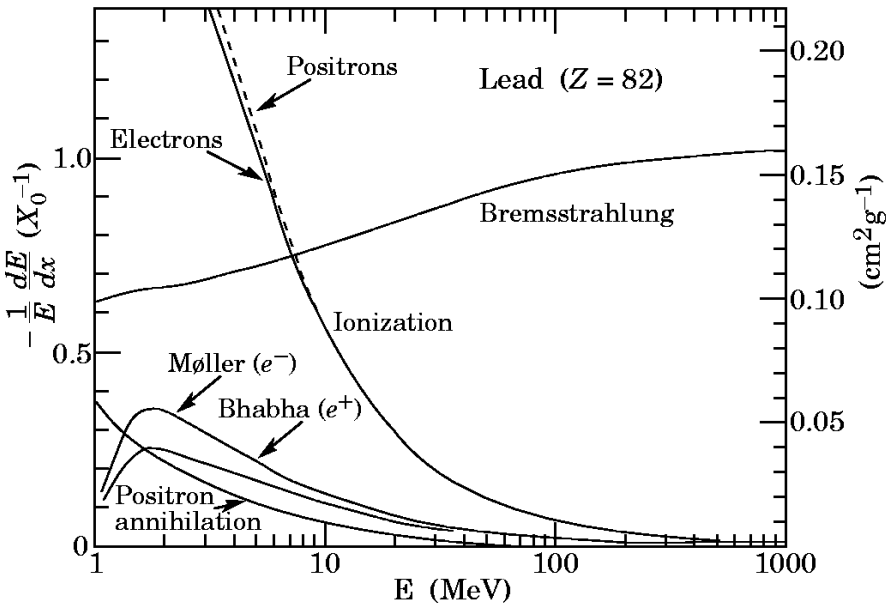

Figure 2.3: Energy loss in units of the radiation length for e^+/e^- in lead, over 4 orders of magnitude in energy. Above 10 MeV the radiative losses by bremsstrahlung already dominate [3].

2.1.3 γ photons

Photons can interact with matter in several manners. From them, the more relevant are usually three:

1. *Photoelectric effect:* at energies comparable to the binding energies of electrons in the atom (up to some keV for the inner shells) the photon transfers all its energy, resulting in an ejected electron with energy equal to that of the photon minus the electron binding energy:

$$E_e = h\nu - K \tag{2.15}$$

   where K is the binding energy and $h\nu$ the energy of the photon.

   The process is strongly enhanced for large values of Z, being the following parameterization suggested in [12]:

$$\sigma_{p.e.} \simeq C\frac{Z^n}{E_\gamma^{3.5}} \tag{2.16}$$

   where n takes values between 4 and 5.

2. *Compton effect:* at intermediate energies, the electrons can be regarded as free, and the kinematics of the interaction can be evaluated by imposing energy and momentum conservation, yielding an electron energy:

$$E_e = \frac{(1-\cos\theta)\alpha}{1+(1-\cos\theta)\alpha}h\nu \tag{2.17}$$

   with $\alpha = \frac{h\nu}{m_e c^2}$ and θ being the angle between the photon and the electron after the interaction. For the purpose of γ-ray detection it is customary to define the Compton edge as the maximum energy carried by the electron, corresponding to $\theta = \pi$. Roughly speaking, the Compton edge represents the maximum energy released in the active medium by Compton interaction.

   Compton scattering can be solved in QED, yielding the Klein-Nishina formula:

$$\begin{aligned}\frac{d\sigma}{d\Omega}\Big|_{Compton} &= Z\left(\frac{e^2}{4\pi\epsilon_o m_e c^2}\right)^2\left(\frac{1}{1+\alpha(1-\cos\theta)}\right)^2\left(\frac{1+\cos^2\theta}{2}\right)\\ &\times\left(1+\frac{\alpha^2(1+\cos\theta)^2}{(1+\cos^2\theta)[1+\alpha(1-\cos\theta)]}\right)\end{aligned} \tag{2.18}$$

3. *Pair production:* when a γ-ray exceeds in energy a value equal to twice the electron mass ($2m_e \simeq 1.02$ MeV) the process of pair (e^+e^-) production (also called γ-conversion) becomes energetically possible. The energy in excess over $2m_e$ is shared in kinetic energy of both the electron and positron. There is no simple expression for the probability of pair production but its magnitude varies approximately as the square of the atomic number of the medium [26].

The strength of the three mentioned interactions as a function of the energy of the photon is shown in fig. 2.4.

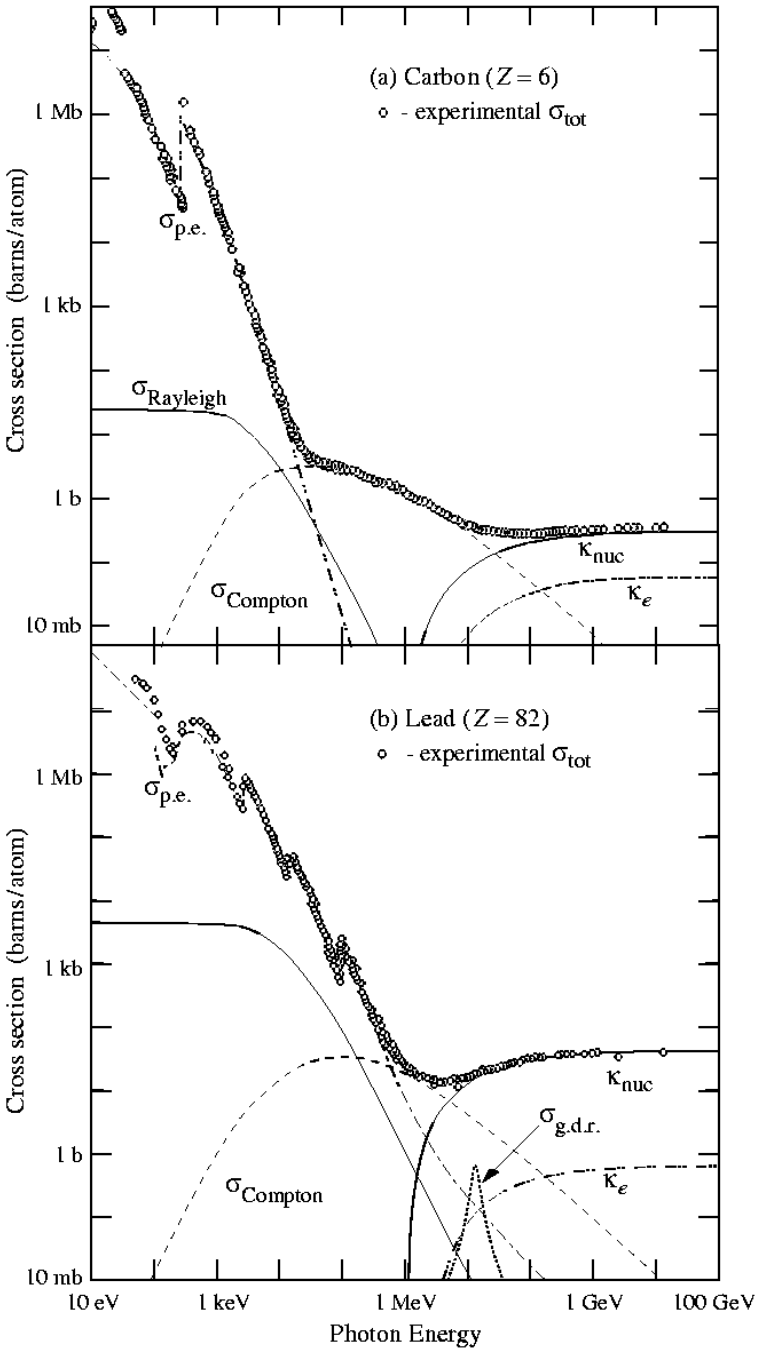

Figure 2.4: Cross sections for photons in carbon and lead [3]. κ_{nuc} and κ_e stand for the probability of pair production in the field of the nucleus and atom, respectively. Other processes show little contributions.

2.2 Avalanches in gases

In 1910 Townsend [14] measured the current between two parallel electrodes when a small number of electrons was released at the cathode, observing an exponential growth as soon as the applied voltage between them was increased above a certain value. Such phenomenon was interpreted as the result of a multiplication process, originated by the drifting electrons and ions, when they achieve the energy required to induce further ionizations.

Townsend's interpretation is nowadays known to be essentially correct, and the term *avalanche* has became popular for describing the increase of current due to the mentioned cascading process. The avalanche phenomenon in gases has been used since then to produce measurable signals out of a relatively small number of primary ionizations, finding a widespread application in the detection of charged particles.

2.2.1 Main processes

The microscopic processes ruling the electromagnetic interactions in gases at low energies are key for describing the avalanche properties. This is so because it is the swarm of low energy secondary electrons and ions which ultimately regulates the avalanche process, and no accurate description can be achieved as long as it is not well described the way they interact with the molecules and atoms of the medium. Currently there are transport codes that predict some of the relevant parameters of the swarm (described later) like for example, MAGBOLTZ [15], IMONTE [16] or HEED [17], and they have found, indeed, remarkable success in interpreting a number of features observed in RPC detectors (see [18] and section 3.2.1).

It is customary to speak about inelastic or elastic collisions, depending whether the kinetic energy of the colliding particles goes or does not go to different degrees of freedom (ionizations, excitations, molecular vibrations...), respectively. Among them, the processes of ionization and excitation are specially relevant; but also photon absorption, electron attachment and ionization by ion impact or photoelectric effect are worth being considered (a detailed discussion can be found at [19]).

2.2.2 Energy distributions of the swarm

In the absence of electric fields, a free charge in a gas will lose its energy by multiple collisions until reaching the average thermal distribution of the constituting molecules and atoms. The kinetic theory of gases provides the thermal distribution of energies[6]:

$$\frac{dN}{d\varepsilon} = \frac{2\sqrt{\varepsilon}}{\sqrt{\pi}(kT)^{3/2}} e^{-\varepsilon/kT} \tag{2.19}$$

with an average energy $\bar{\varepsilon} = \frac{3}{2}kT \simeq 0.04$ eV under normal conditions ($T \simeq 25°C$). Whether this thermal equilibration is still effective or not when an external field is applied, results from the balance between the energy lost by collisions and

[6] Usually denoted as 'Maxwellian'.

the energy regained owing to the electric field during the mean free path of the particle ($eE\lambda$).

The fraction of energy transferred in an elastic electron-molecule (atom) collision is of the order of the ratio between the masses (10^{-5} for Ar), being the ionic losses close to 50% under similar conditions, allowing for a fast thermalization of the last even in the presence of very high electric fields. The case for electrons is very distinct, existing both numerical [20] and analytic [21] descriptions based on the kinetic theory of gases, but taking into account the contribution of the inelastic processes and the electric field. G. Schultz derived the following expression under the assumption that only vibrational and rotational excitations compete with elastic collisions:

$$\frac{dN}{d\varepsilon} = C\sqrt{\varepsilon}\,\exp\left(-\int \frac{3\Lambda(\varepsilon)\varepsilon d\varepsilon}{[eE\lambda_e(\varepsilon)]^2 + 3\Lambda(\varepsilon)\varepsilon kT}\right) \tag{2.20}$$

$$\Lambda(\varepsilon) = \frac{2m_e}{M} + \sum_i \frac{\varepsilon_i \sigma_i(\varepsilon)}{\varepsilon \sigma_e(\varepsilon)} \tag{2.21}$$

where λ_e and σ_e are the mean free path and cross section for elastic collisions, respectively, ε_i is the energy lost to the degree of freedom i (ascribed to rotational or vibrational states in the proposed derivation) and σ_i is the inelastic cross section for that process. The function $\Lambda(\varepsilon)$ stands for the fraction of energy lost in each collision, or *inelasticity*.

For sufficiently small fields such that:

$$[eE\lambda_e(\varepsilon)]^2 \ll 3\Lambda(\varepsilon)\varepsilon kT \tag{2.22}$$

the electron thermalization can take place and its energy distribution becomes Maxwellian. Otherwise, its average energy will be typically larger than the expected in thermal equilibrium.

2.2.3 Relevant parameters of the swarm

The drift velocities v_e and v_i

Electrons and ions drift parallel to the electric field, with a typical value resulting from the average over the distribution of possible energies:

$$v_{e(i)} = \int \cos\theta \sqrt{\frac{2\varepsilon}{m_{e(i)}}} \frac{1}{2\pi} \frac{dN}{d\varepsilon} d\varepsilon \; d\cos\theta \tag{2.23}$$

denoting by θ the angle between the particle velocity and the direction of the electric field[7]. It is customary to expand the energy distribution in the presence of an electric field by using the Legendre polynomials [21]:

$$\frac{dN}{d\varepsilon} = \left.\frac{dN}{d\varepsilon}\right|_o + \left.\frac{dN}{d\varepsilon}\right|_1 \cos\theta + ... \tag{2.24}$$

being $\left.\frac{dN}{d\varepsilon}\right|_o$ the energy distribution in the absence of electric fields.

[7] Eq. 2.23 is nothing but the average of the velocities in the direction of the electric field.

In the limit where the swarm is thermalized and the field is negligible, the evaluation of eq. 2.23 naturally produces a null result, while in the presence of sizable electric fields it can be re-expressed as [10]:

$$v_{e(i)} = \frac{2}{3}\frac{eE}{m_{e(i)}}\int \varepsilon\lambda_e(\varepsilon)\frac{\partial(\sqrt{\frac{m_{e(i)}}{2\varepsilon}}\frac{dN}{d\varepsilon}\big|_o)}{\partial\varepsilon}d\varepsilon \tag{2.25}$$

Expression 2.25 can be analytically solved by assuming a constant value for λ_e and a thermal distribution, producing:

$$v_{e(i)} \simeq \frac{2}{3}\sqrt{\frac{m_{e(i)}e^2}{2kT}}\lambda_e E = \mu_{e(i)}E \tag{2.26}$$

where $\mu_{e(i)}$ is defined as the electronic (ionic) mobility. The mean free path is proportional to the inverse of the gas density; therefore, under the assumption that the gas has ideal behavior, it is expected that $\lambda_e(P) = \lambda_e(P_o)P_o/P$, resulting in:

$$v_{e(i)} = \mu_{e(i)}(P_o)\frac{E}{P} \tag{2.27}$$

and such linear behavior provides, indeed, a reasonable description of the ion drift in gases. At high fields, the calculation of the electronic drift may require the use of the exact non-thermal distribution in the particular case.

The diffusion coefficient D

In a one dimensional medium, a localized cluster of N_o particles diffuses through multiple collisions as:

$$\frac{dN}{dx} = \frac{N_o}{\sqrt{4\pi Dt}}e^{-x^2/4Dt} \tag{2.28}$$

I.e., a Gaussian distribution whose width increases in time as $\sigma_x = \sqrt{2Dt}$. The result can be extended to d dimensions ($d = 1, 2, 3$), providing:

$$\sigma_d = \sqrt{2dDt} \tag{2.29}$$

In fact, the diffusion process is governed by a single parameter, namely, the diffusion coefficient D, that can be obtained according to the kinetic theory of gases [20] as:

$$D = \frac{1}{3}\int \lambda_e(\varepsilon)\sqrt{\frac{2\varepsilon}{m}}\frac{dN}{d\varepsilon}d\varepsilon \tag{2.30}$$

and for the ionic (thermalized) case, the solution of eq. 2.30 is:

$$D_i = \frac{\mu_i kT}{e} \tag{2.31}$$

In the presence of electric fields it is usual to distinguish between the longitudinal and transversal diffusion coefficients, depending on whether the diffusion is considered in the direction of the field or perpendicular to it.

The multiplication coefficient α

Eventually, particles reach enough energy to start to ionize. The first Townsend coefficient α is the characteristic magnitude that describes the process, being related to the inverse of the mean free path for ionization λ. For the case of electrons from the swarm, its value is given by:

$$\alpha = \frac{1}{v_e} \int \lambda(\varepsilon)^{-1} \sqrt{\frac{2\varepsilon}{m}} \frac{dN}{d\varepsilon} d\varepsilon \tag{2.32}$$

There are no general rules for estimating the behavior of the first Townsend coefficient, despite some analytic expressions have been devised under certain conditions [10].

2.2.4 Avalanche propagation

The equations for the evolution of the electron and ion densities in a region where an electric field exists, can be described in terms of the parameters of the swarm v_e, v_i, D_e, D_i, α, following [22]:

$$\frac{\partial n_e(x,y,z,t)}{\partial t} = \alpha n_e |v_e| - \nabla(n_e v_e) + D_e \nabla^2 n_e \tag{2.33}$$

$$\frac{\partial n_i(x,y,z,t)}{\partial t} = \alpha n_e |v_e| - \nabla(n_i v_i) + D_i \nabla^2 n_i \tag{2.34}$$

where the presence of electronegative components has been neglected. The equations account for the multiplication during the drifts of the carriers, plus their spatial diffusion.

In the simple case where N_o electrons were released at instant $t = 0$ at a point placed somewhere in the cathode (taken as zero position):

$$n_e(0) = N_o \delta(t)\delta(x)\delta(y)\delta(z) \tag{2.35}$$

$$n_i(0) = 0 \tag{2.36}$$

and making the simplifying assumptions that the transversal and longitudinal diffusion coefficients are equal, and the parameters of the swarm are constant during propagation, the solution of eqs. 2.33 and 2.34 is given by [23]:

$$n_e(x,y,z,t) = N_o e^{\alpha v_e t} \frac{1}{(4\pi D_e t)^{3/2}} \exp(-\frac{x^2+y^2+(z-v_e t)^2}{4D_e t}) \tag{2.37}$$

Therefore, in a first approach, the avalanche can be described by an exponential growth of the charges $e^{\alpha v_e t}$, diffusing in space with an average radius that grows with the square root of the diffusion time as $r_{_D} \sim \sqrt{D_e t}$.

After collection at the anode (assumed to be separated a distance g from the point where the avalanche started), the average increase in the initial number of particles is given by $m = e^{\alpha g}$, usually referred as the *avalanche gain*.

2.2.5 Avalanche statistics

Primary fluctuations

The number of primary ionizing collisions k produced within a gap of width g follows a Poisson distribution with average $n_o = g/\lambda$ (λ the mean free path for

ionization of the primary particle):

$$P(k) = \frac{n_o^k}{k!} e^{-n_o} \tag{2.38}$$

Also different number of electrons can be ejected in a single ionization, constituting the so-called *cluster size* distribution: according to [24], ionizations releasing more than one electron can amount to 10% of the total in a typical gas like iso-C_4H_{10}.

Multiplication fluctuations

It must be recalled that, as for the interaction of the primary particle, the ionizing probability of the electrons (ions) of the swarm has also a stochastic nature. The relative contribution of the effect is small whenever the number of released electrons (ions) is very large, but will affect the avalanche gain if it contributes in the early stages of avalanche development. When the swarm is thermalized, the behavior of its constituting particles becomes independent from the details of previous interactions[8]. In that case, the distribution of avalanche gains after a certain distance follows an exponential distribution, known as the Furry law [25]. The distribution of gains over a distance g for avalanches initiated by a single electron is, therefore, given by:

$$\frac{dN}{dm} = \frac{1}{\bar{m}} e^{-m/\bar{m}} \tag{2.39}$$

being $\bar{m} = e^{\alpha g}$ the average gain. For increasing fields, deviations from the simple Furry law are expected, a regime where the so-called Polya law proved to be more accurate:

$$\frac{dN}{dm} = \frac{1+\theta}{\Gamma(1+\theta)\bar{m}} \left[\frac{m(1+\theta)}{\bar{m}}\right]^{\theta} e^{-m(1+\theta)/\bar{m}} \tag{2.40}$$

Γ is the Euler Gamma function and θ is a free parameter that depends on the field (at $\theta = 0$ eq. 2.40 coincides with the Furry law).

2.2.6 Streamer propagation

Depending on the conditions, at very high fields the avalanche formation can precede the development of a luminous filament between anode and cathode, resulting from a fast increase of the released charge. Such increase can be ascribed to the onset of new phenomena, different than the normal propagation of the avalanche, and it is usually referred as *streamer*. The nature of such process is not understood in full detail, despite different models have been devised, providing an adequate interpretation of some of the observations [27], [28], [29]. In general, it is accepted that the conditions for a streamer to develop are bound to the distortions of the electric field when the self-field of the avalanche is comparable to the applied field (a concept also denoted as *Space-Charge effects*). Successful quantitative attempts have been made [27], [28], by assuming that the increase of current characteristic of the streamer development is related to

[8] Sometimes it is said that the particles lost their memory.

the presence of short-range UV photons that are able to ionize the gas in regions of high electric fields. The main shortcoming for checking the validity of any realistic description of the streamer process is that calculations rely on estimates of a number of parameters of the swarm, that are usually difficult to access experimentally.

Despite the uncertainties, it is well established since the 60's, thanks to Raether [29], that an experimental limit exists for the maximum gain attainable in wide gap gaseous detectors before the streamer can progress:

$$m = e^{\alpha g} \simeq e^{20} = 5\ 10^8 \tag{2.41}$$

that is called *Raether limit*.

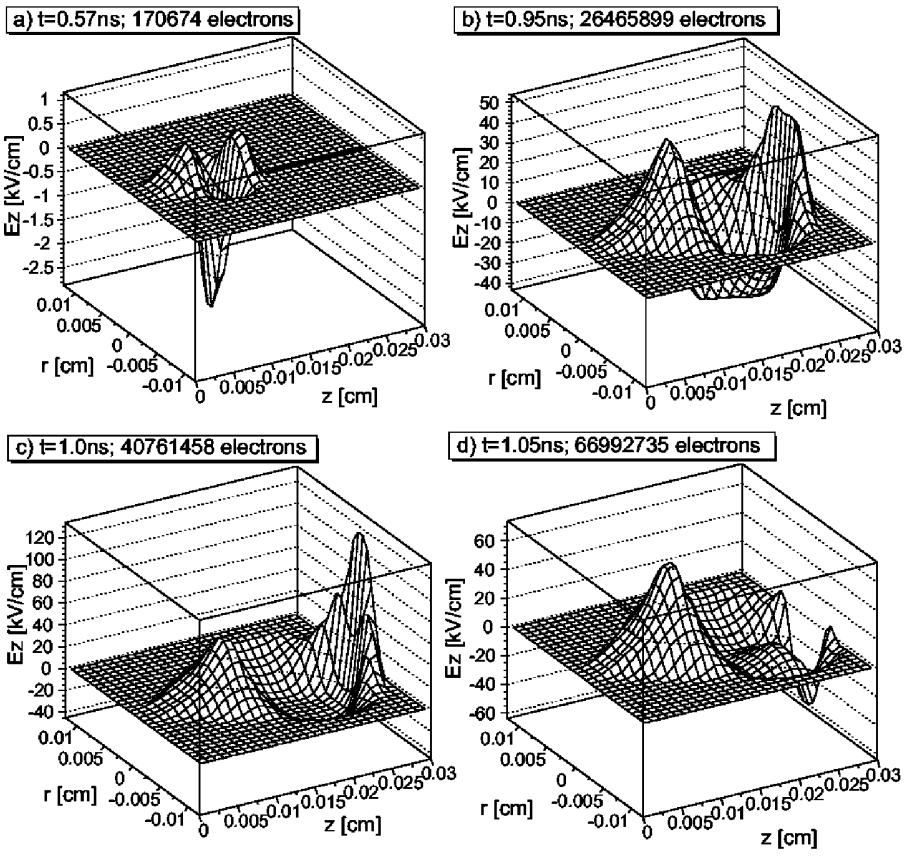

Figure 2.5: Simulated behavior of the longitudinal component of the electric field created by the avalanche, as a function of the position along the gap z and the radial distance r. The avalanche has been started by a single electron at $z = 0$ (cathode) in a gas mixture based on $C_2H_2F_4/SF_6$/iso-C_4H_{10} (85/10/5) at an applied field $E \simeq 93$ kV/cm [24].

Cathode streamer

In fig. 2.5 the simulated behavior of the avalanche self-electric field is shown according to the work of C. Lippmann and W. Riegler [24], that will be used

for illustration. In the streamer models proposed in [13], [27], [28] it is assumed that UV photons are generated during avalanche formation. Being emitted isotropically, they can travel towards the cathode up to the head of the ion tail, where the field is higher, and there induce new avalanches. For this process to end in a streamer, the onset of the Space-Charge regime is required. In such a case, a wave of successive ionizations in the direction of the cathode can progress, resulting in the so-called 'cathodic streamer'.

Anode streamer

A similar process can take place in the electron front. However, it must be noted that the anode streamer does not require from UV photons to propagate. The higher density of electrons in that region results on higher fields as compared to the ion front. In that case, [28] predicts the formation of a streamer arising from the interaction between the electron front of the avalanche and the anode.

The different origin of anode and cathode streamers suggests that both fronts of the streamer (anodic and cathodic) can travel at different velocities. Such behavior has been reported under some conditions [30].

2.3 Breakdown in parallel plate geometries

It is denoted by breakdown a process that produces a high conductivity between cathode and anode, eventually leading to a violent *spark* that results in the drop of the voltage across the gap. Two processes are assumed to be the more frequent ones in leading a detector to the breakdown.

2.3.1 Townsend mechanism

Together with direct ionization of molecules (atoms) of the gas, that is described by the first Townsend coefficient, there are other processes that contribute to the release of secondary electrons. Among them, the more relevant are both the photoelectric effect (from photons emitted during the development of the avalanche) and electron extraction by ion collisions at the cathode. The ejected electrons are accelerated back towards the anode, resulting in the generation of succeeding avalanches.

This feedback mechanism is expected to become self-sustained whenever the average number of electrons ejected at the cathode exceeds the average number of primary electrons released by the primary particle. Assuming an ejection probability δ, and a certain gain $\bar{m}$, the average number of primary electrons n_o is related to the number of electrons ejected at the cathode through:

$$n_\delta = n_o \bar{m} \delta \tag{2.42}$$

Therefore, as long as $\bar{m}\delta \gtrsim 1$, the number of new ejected electrons n_δ coming towards the anode becomes larger than the n_o released by the primary particle. This situation corresponds to the appearance of a self-sustained current, that extends to the whole gap after a certain time, and leads to the breakdown. The condition:

$$\bar{m}\delta \gtrsim 1 \tag{2.43}$$

is denoted as 'Townsend Breakdown Criteria'. Due to the necessity of further avalanches, this mechanism is rather slow as compared with the avalanche formation itself, lasting some tens of μs, depending on the case.

2.3.2 Streamer mechanism

It is an experimental fact that, after a streamer develops, a path of conducting ionized plasma is left through the gap, allowing for the progress of a violent spark between the electrodes, that leads to the breakdown of the applied voltage.

Apart from its different origin, the streamer mechanism is much faster than the Townsend one, as it is started immediately after the first avalanche is produced in the gas. A mixture of the two breakdown mechanisms described is possible. It is, for example, probable that the first stage of the Townsend mechanism precedes the creation of a streamer in, let's say, the 10^{th} generation, that finally causes the breakdown.

It must be mentioned that, in the case of the streamer mechanism, the avalanche statistics can make the conditions for breakdown possible even if the Raether condition is not fulfilled. This phenomenon requires the gases used in detectors to be 'quenched', that is, to have a low light emission.

Chapter 3

Timing RPCs

3.1 Historical introduction

3.1.1 PPCs

A Parallel Plate Chamber (PPC) consists in 2 parallel metallic electrodes operated at high voltage, thus providing an uniform electric field across the volume that they delimit. When a charged particle crosses the space between the electrodes, it creates electron-ion pairs with a certain density; in a later stage, and if the field is high enough, the released electrons are accelerated towards the anode, regaining enough energy for inducing further ionizations in a cascading process called avalanche (see section 2.2). In this simple way it is possible to produce a measurable charge from a reduced number of initial charges. The very fast drifting electrons produce a prompt signal that can be used for timing purposes, whereas the ions drift to the cathode at much smaller velocities, due to their higher mass.

The first application of a parallel plate geometry for timing dates back to 1948, and was called Keuffel Spark Counter after its inventor [31]. It showed a time resolution at the level of 1 ns but, due to the enormous amount of charge released by the spark created, a large recovery time of some milliseconds was required, limiting the rate capability of the device.

The operation of parallel geometries with electrodes covered by high resistivity materials, preventing the voltage breakdown, was pioneered in 1971 [32] and consolidated in 1981 [33] with the advent of the Resistive Plate Chambers (RPCs).

In 1971, the Pestov's group [32] made use of a highly resistive material (glass) for limiting the progress of the spark. The so-called 'Pestov counter' is able to achieve ultimately a time resolution at the level of *25 ps*. However, the counter is characterized by its high technical complexity: i) its gap is as small as 100 μm wide, therefore aiming for a high efficiency it must be operated at around 12 bar; ii) it is required the use of a special kind of glass with $\rho \sim 5\ 10^9$ Ωcm (called 'Pestov glass'); iii) at last, the requirements concerning mechanics are very demanding.

3.1.2 RPCs

The *Resistive Plate Chamber* (RPC)[1] was developed by R. Santonico and R. Cardarelli in 1981 [33] with the intention of overcoming the difficulties inherent to the Pestov counter [32], while keeping its more fundamental virtues (namely, the possibility of working at very high fields by avoiding the breakdown of the detector).

The first RPC consisted in two parallel copper electrodes covered with high resistance plates made of a phenolic resin known as Bakelite, with a volume resistivity $\rho \simeq 10^{10}$ Ωcm. The ensemble delimited a 'wide' gap of 1.5 mm filled with a gas mixture of Argon/iso-C_4H_{10} (iso-butane) in a proportion 1:1 (fig. 3.1 left)[2]. The main advantage as compared to the Pestov counter is that the gas circulates at atmospheric pressure along a wide (1.5 mm) gap. According to the convention used nowadays, it can be said that the detector was operated in streamer mode[3], allowing a high simplification of the electronics (see section 3.1.4).

Under the conditions mentioned, the dark rate of the counter was considerable, contributing to a decrease in the observed efficiency. For avoiding this effect, the plates were painted with linseed oil and, remarkably, this technique has been kept since then for Bakelite-based RPCs.

The signal was measured with pick-up strips, separated from the HV foil through PVC[4], avoiding the use of coupling capacitors. The HV has to be applied through a non-perfect conductor (poorly conductive paper foil) in order to be transparent to the induced signal, otherwise a fraction of it will be lost.

The basic operation principle of an RPC is already described in the original paper and not much has changed since then:

1. The signal induction time, around 10 ns for the electron (prompt) component, is much smaller than the time constant of the RC circuit formed by the resistive plate, $\tau = \mathrm{RC} \simeq \rho\epsilon \simeq 10$ ms [34]. This means that, from the point of view of the signal induced in the read-out electronics, the resistive plate behaves as a perfect dielectric ($R{=}\infty$).

2. From the point of view of the physical phenomena involved, the situation is very similar to the PPC case, just because the resistive plate is essentially transparent to the induced signal. However, operation of PPCs at the typical high fields of RPCs is difficult in practice, because the charge flow required for breakdown is not limited by resistive plates.

3. For avoiding the presence of self-sustained discharges that may arise from the Townsend mechanism (see section 2.3.1), the choice of a standard UV quencher (iso-C_4H_{10}) was adopted.

4. The rate capability of an RPC is ultimately related to the average charge per avalanche and the recovery time of the plate τ or, equivalently, to the average ohmic drop in the resistive plates $\bar{V}_{drop} = \bar{q}/C\phi A\tau$, being C the

[1] It must be said that, in the original paper, the letter C was used for 'Counter', but the more generic word 'Chamber' became later more popular.

[2] Iso-C_4H_{10} is an UV quencher, while Argon is a noble gas well suited for applications with gaseous detectors, due to its high density.

[3] In the original paper, the word 'discharge' is preferred for describing the signal.

[4] Polyvinyl chloride.

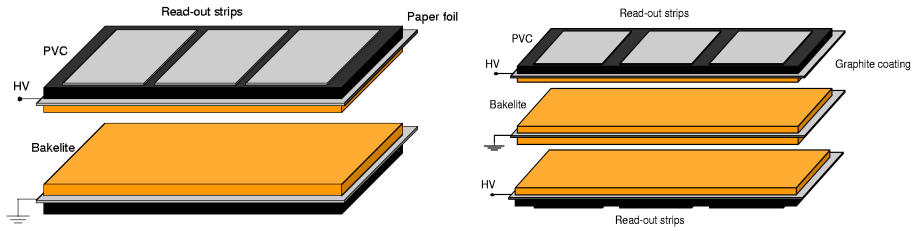

Figure 3.1: Left: example of a 1-gap RPC [33] and right: a symmetric 2-gap RPC [34], both drawn according to their original designs. The HV capacitors are avoided by the use of a PVC layer and a low conductivity paper foil for applying the HV (a graphite coating was used in the 2-gap design). Details are given in text. The dimensions are not realistic, in particular the gap has been enlarged.

capacity of the RPC, ϕ the primary rate and A the area of the plates (section 3.2.7).

5. Regarding timing, the situation is more favorable in a parallel plate geometry ($E \sim$ constant) than in a cylindrical one ($E \sim 1/r$) commonly used for proportional detectors. The parallel geometry allows to extend the 'multiplication region' to all the detector (the field is high enough for inducing an avalanche at any point), while in proportional detectors it is required a propagation time along the 'drift region' before the multiplication can take place, affecting the timing properties. Conversely, the sensitivity to the energy released by the primary particle is much higher in the case of cylindrical geometries as compared to the parallel ones, due to the fact that the multiplication region is well delimited.

In its first design, the RPC technology achieved very promising performances, reaching 97% efficiency and a time distribution of 1.2 ns FWHM, becoming an affordable alternative to the use of plastic scintillators.

3.1.3 Double gap RPC

The double gap structure was introduced in 1988 [34] and the gap width increased up to 2 mm, which is the value commonly used nowadays. The setup was symmetric with the ground electrode in the center and the HV applied over the outer layers (fig. 3.1).

The 2-gap configuration allowed for an increase in efficiency and confirmed that the time resolution was well at the level of $\sigma_T \simeq 1$ ns.

3.1.4 Operation modes

Streamer mode

As said in section 2.2.6, a streamer is a process of a different nature than avalanche multiplication, releasing a high amount of charge as compared to the one of a normal avalanche. Therefore, the rate capability is a potential problem for RPCs operated in streamer mode. Despite this drawback, it has found wide application in experiments that work at low rates, as in the case of BELLE at KEK that operates below 1 Hz/cm^2 [35], or BaBar at SLAC [36].

The benefit of this operation mode is that the read-out electronics is simplified as compared to the avalanche mode. Because of these characteristics, RPCs in streamer mode are specially well suited for cosmic ray experiments as ARGO at YangBaJing [37].

This mode was also called 'spark mode' [38] but it is probably not a good choice: the formation of a spark requires an enormous current that is limited, in fact, by the presence of the resistive plates. So, the term 'streamer mode' became more popular [39].

Avalanche mode

The introduction of the avalanche mode of operation took place in 1993 [40] as an attempt to improve the rate capability by reducing the charge released per avalanche, while using dedicated electronics for amplification (an interesting comparison between streamer and avalanche mode can be found in [38]). For this purpose, a highly electronegative gas (CF_3Br) was used and, since then, a number of different electronegative mixtures were tried, including CH_2FCF_3, $C_2H_2F_4$ and SF_6.

RPCs operating in avalanche mode have found application in high energy physics (like ATLAS or CMS at LHC, see [41], [42] for instance) and are often called 'trigger RPCs', allowing for rate capabilities in the range 100-1000 Hz/cm^2.

The avalanche mode of operation was also called 'proportional mode' [39] which is probably a bit ambitious in view of the following: on one hand, the charge of the collected signal is not proportional to the charge released by the primary particle as it depends on the position of the first cluster; on the other hand, the growth of the avalanche is known to be affected by Space-Charge effect, a regime where the correlation with the charge initially released is very small. Therefore, the more general term 'avalanche mode' prevailed [38].

3.1.5 Multi-gap RPC (MRPC)

A new design appeared in 1996 [43] due to the efforts of M.C.S Williams' group, consisting in a triple set of Bakelite plates separated by gaps of 3 mm, that allowed, according to its inventors, for a similar time resolution as a single-gap 2 mm chamber while reducing the dark current and increasing the efficiency plateau.

It can be roughly expected that the multi gap allows for an increase in the efficiency as:

$$\varepsilon = 1 - (1 - \varepsilon_{_N})^N \tag{3.1}$$

where N stands for the number of gaps and $\varepsilon_{_N}$ denotes the efficiency per single gap. Expression 3.1 is exact under the assumption that, for detection, at least one of the gaps must provide a detectable signal with independence of the others. This assumption is not true, as two independent induced signals falling below the detection threshold can yield a total signal that is above; therefore the efficiency represented by eq. 3.1 represents a lower limit to the one expected in reality. On the other hand, the time resolution slightly increases, in a first approach, as:

$$\sigma_{_T} = \frac{\sigma_{_{T,N}}}{\sqrt{N}} \tag{3.2}$$

which is the expected, if the time response is Gaussian. The details on the approximate statement 3.2 are discussed in chapter 9.

It has been observed repeatedly that the time resolution depends on the gap width, typically improving for small gaps [44]. It can be argued, therefore, that a multi-gap configuration can provide a good timing, as characteristic of narrow RPCs, while keeping the efficiency at high levels, as characteristic of wide RPCs.

Multi-gap technology has a very interesting feature: the inner resistive plates can be left *floating* and they will take in average the voltage drop expected due to electrostatics. The argument is the following: in the electrostatic situation the voltage drop in each of the N gaps is directly $V_N = V/N$. If now a particle ionizes in two neighboring gaps, it can release different charges, inducing different voltage drops in the gaps corresponding to both sides of the plate. In this way the plate is charged up. However, the next avalanche will see a lower field in the gap where more charge was produced, whereas in the other gap the situation will be the opposite. As a result, the charges of the next avalanches that are collected at each side of the resistive plate will compensate from those charges of the previous avalanches, balancing the field in the neighboring gaps. This effect suggests that the grounding of the resistive plates is not expected to be a fundamental issue, as it has been confirmed experimentally.

See fig. 3.2 for typical examples of multi-gap configurations.

3.1.6 Timing RPC (tRPC)

The realization of the importance of the mechanical uniformity of the gap in relation with high precision timing (see chapter 9) together with the development of fast amplification electronics, made possible to operate a multi-gap RPC in avalanche mode with thin gaps of 0.3 mm and glass electrodes, at fields as high as 100 kV/cm. Such step was accomplished in the year 2000 by P. Fonte, A. Smirnitski and M.C.S. Williams [45], opening a new branch in the field. This first development achieved a time resolution at the level of 120 ps, although soon after that, the possibility of going down to the level of 50 ps for small detectors [46] was proved. The applicability of the technology in large size tRPCs was later confirmed [47], providing resolutions comfortably below 100 ps, with reasonable homogeneity. The gas mixture originally used was $C_2H_2F_4/SF_6$/iso-C_4H_{10} (85/10/5) based on results for wide-gap RPCs [48] and called since then 'standard mixture' in the context of timing RPCs. The addition of a small fraction of SF_6 seems to improve the stability, to increase the efficiency 'plateau' and to reduce the amount of streamers. Similar mixtures (90/5/5) have been also tried, showing a slight improvement according to [49].

Soon after the first development, it became popular the use of standard window glass in RPCs, also called soda-lime-silica glass or just float glass [47], [50]. It is widely available, affordable and still with a resistivity $\rho \simeq 10^{12-13}$ Ωcm, allowing for operation at rates up to around 500 Hz/cm^2.

As 'timing RPCs' is the central issue of the present work, its description will be developed in more detail in forthcoming sections. However, most of the characteristics mentioned in the following can be extrapolated to standard RPCs.

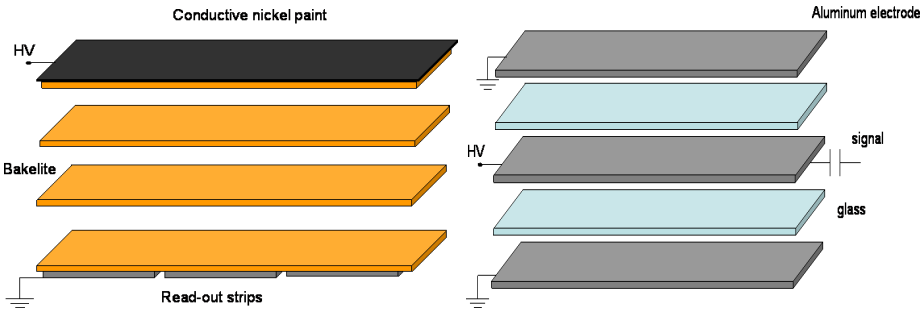

Figure 3.2: Examples of multi-gap RPC. In the left, the original 3-gap design of [43]. In the right, the 4-gap timing RPC prototype studied in chapter 6.

3.2 Timing RPC physics

The RPC field has lived a fast theoretical growth in the past 10 years, allowing for descriptions of different aspects. The results summarized in the following can be grouped in three main topics:

1. *Space-Charge and detector physics:*

   M. Abbrescia [51] (M.C. for charge spectra and efficiency), M. Abbrescia [52] (M.C. implementing Space-Charge in a 'crude' way), P. Fonte et al. [53] (analytic description of Space-Charge), G. Aielli et al. [54] (analytic description of Space-Charge), P. Fonte et al. [55] (analytic description of timing properties), A. Mangiarotti et al. [56] (analytic description of the effect of Space-Charge on timing), C. Lippmann and W. Riegler [57] (full M.C. simulation of RPC physics in 2D including exact calculation of the Space-Charge).

2. *Fluctuations of the applied field:*

   G. Carboni et al., D. González-Díaz et al. [58], [59] (model for the average effect of rate), M. Abbrescia [60] (M.C. for rate effects on RPC performances), A. Blanco et al. [61] (analytic description of mechanical inaccuracies on timing), D. González-Díaz et al. [62] (analytic description of rate effects on timing, M.C. description of charging-up process), C. Lippmann and W. Riegler [63] (M.C. description of rate effects on timing).

3. *Electrostatics:*

   W. Riegler [64] (exact formulas for the weighting field), W. Riegler and D. Burgarth [65] (electrostatic calculation of crosstalk, induction and losses)

3.2.1 Efficiency and primary ionization

The efficiency of an RPC is related to the average number of ionization clusters produced per unit length $n_o/g = 1/\lambda$, being n_o the average number of clusters, g the gap width and λ the mean free path for ionization of the primary particle. In the ideal limit where any cluster is detected, the intrinsic efficiency of the device is reached:

$$\varepsilon_{int} = 1 - e^{-g/\lambda} = 1 - e^{-n_o} \tag{3.3}$$

and, by analogy, the efficiency measured in lab is:

$$\varepsilon_{exp} = 1 - e^{-n'_o} \tag{3.4}$$

The measured efficiency is smaller than the theoretical one because of two main reasons:

1. The lowest value achievable for the threshold of the comparator is limited by the noise level. Therefore, the avalanches that induce signals compatible with noise can not be measured.

2. There is always a probability that the electrons in a cluster are attached and no electron signal is collected.

As a result of these effects, the value of n'_o measured from the efficiency in lab is smaller than n_o that could be estimated, for example, with a simulation code. In particular, it has been observed that n_o is typically a factor 2 bigger than n'_o for different gap sizes [55] when comparing with the value obtained from simulations (HEED [17]). This discrepancy is often interpreted as the fact that, for practical purposes, only a fraction n'_o/n_o of the gap is active. In average, a cluster produced beyond this distance will not reach the threshold. In this natural way it can be introduced the concept of 'dead' and 'active' regions.

It is useful to take an analytic description of the efficiency in lab ε_{lab} [66], [52] based on the assumption that the first non-attached cluster closer to the cathode dominates the behavior of the efficiency:

$$\varepsilon_{exp} = 1 - e^{-(1-\frac{\eta}{\alpha})n_o}\left[1 + \frac{(\alpha-\eta)}{E_w}m_t\right]^{\frac{n_o}{\alpha g}} \tag{3.5}$$

where α and η are the multiplication and attachment coefficients, respectively. $m_t e$ is a charge threshold (related to the threshold of the comparator) and E_w is the weighting field that, according to the Ramo theorem, is related to the size of the induced signal (see section 3.2.6). Eq. 3.5 is just an approximation that proved to describe reasonably well the efficiency of timing RPCs [18], [66] and contains the two effects already mentioned at the beginning of the section. As expected, in the limit $\eta \to 0$ (no attachment) and $m_t \to 0$ (zero threshold) it coincides with the intrinsic efficiency ε_{int}, eq. 3.3.

It was the merit of C. Lippmann and W. Riegler [66] to show that, indeed, the eq. 3.5 (and also detailed M.C. calculations) allows for an explanation of the difference between n_o and the measured n'_o, just resorting to standard physics of gaseous detectors. The analytic expression 3.5 fails when multiple clusters are produced, being inaccurate for wide gap RPCs.

3.2.2 Time response

There is available a model [55] that reasonably catches the main dependencies of the intrinsic time response of an RPC, and whose hypothesis are described in detail in chapter 9. The model allows to obtain the time response function in terms of n'_o (related to the measured efficiency) and the growth coefficient $S = (\alpha - \eta)v_e$ (v_e is the drift velocity):

$$\rho_{_T}(t) = \frac{n'_o}{e^{n'_o} - 1}\frac{e^{(\tau_{th}-St)-\exp(\tau_{th}-St)}}{\sqrt{n'_o e^{(\tau_{th}-St)}}} I_1\left(2\sqrt{n'_o e^{(\tau_{th}-St)}}\right) \tag{3.6}$$

where $\tau_{th} = \ln[m_t(1-\eta/\alpha)]$ and I_1 is the modified Bessel function. The rms[5] (time resolution) can be extracted from eq. 3.6 to be:

$$\mathrm{rms}_T = \frac{K(n'_o)}{S(V)} \tag{3.7}$$

$K(n'_o)$ has an analytic expansion as a function of n'_o that can be found elsewhere [67], whereas its functional dependence is presented in fig. 9.1.

The relevant feature of eq. 3.7 is that the time resolution can be separated in two different contributions: the fluctuation due to the primary and multiplication statistics $K(n'_o)$ that depends on the primary interacting particle on one hand, and the growth coefficient of the gas S that depends on the applied field and the particular gas mixture on the other hand. It must be noted that the two magnitudes n'_o and S are not completely independent[6], but expression 3.7 provides considerable insight in the timing properties of an RPC as a function of the physics involved.

It is apparent in expression 3.6 that the effect of τ_{th} (equivalently, the threshold of the comparator) is just a global shift that will not affect any moment of order larger than one around the mean of the distribution, in particular the time resolution. This effect is well known experimentally [46] and is also reproduced by the numerical calculations of [57].

Limitations for timing

The maximum field applied in a timing RPC is limited by the apparition of streamers, that start to deteriorate the capabilities due to the large charge released. In a first approach, this situation can be identified with the Raether condition $\alpha g \simeq 20$ (eq. 2.41)[7]. Therefore, replacing α in eq. 3.7, it is possible to infer that the *best* time resolution achievable in a given configuration behaves as:

$$\mathrm{rms}_T\big|_{min} \sim \frac{K(n'_o)}{v_e} g \tag{3.8}$$

The dependence on the gap size is also present through the number of primary clusters released n'_o but, being this dependence relatively small (fig. 9.1), the dominant effect is that the time resolution worsens with the increase in the gap size. This effect is well established experimentally [44], showing deviations for very small gaps ($g < 0.3$ mm). A complete picture requires to understand deeply the Space-Charge physics and the Raether criteria.

Eq. 3.6 has tails towards delayed times, becoming Gaussian for high n'_o. In this limit, $K(n'_o)$ behaves approximately as $K/\sqrt{n'_o}$ according to fig. 9.1. Therefore, in the limit where n'_o is large, it is possible to rewrite expression 3.8

[5] Root Mean Square.

[6] For example: if the voltage changes, S will change, but also the efficiency, and therefore n'_o. However, the influence of the voltage over n'_o is only logarithmic while linear over S (see chapter 7).

[7] In fact, the Raether limit was experimentally obtained for wide gaps with widths at the level of cm. The quantitative justification for the limit derived in [29] would be also modified in case of narrow gaps. However, what is required for the argument presented in the text is to assume that $\alpha g \simeq$ ctant represents a practical limit with independence on g, for typical RPC sizes.

in a more transparent way as a function of fundamental variables:

$$\mathrm{rms}_T\big|_{min} \propto \frac{1}{v_e(E)}\sqrt{\frac{\lambda g}{N}} \tag{3.9}$$

being v_e the drift velocity at the field corresponding to the begining of the production of streamers, g the gap size, N the number of gaps and λ the mean free path for ionization.

3.2.3 Time-charge correlation

Equation 3.6 stands for the intrinsic response of the RPC and no attempt is done to describe the extra jitter coming from non-ideal electronics. Besides the unavoidable electronic jitter, a systematic shift of the tof[8] measured at fixed velocity of the primary particle is always present, and it depends on the avalanche size. This 'walk' can be subtracted, if the charge is measured, through a procedure often called in the literature 'the slewing correction'.

There is a part of the time-charge correlation coming from electronics, certainly, but it has been suggested that there is also an intrinsic correlation coming from the avalanche physics [47], an effect not favoured by M.C. calculations [57].

It is not the objective of this work to discuss the nature of the time-charge correlation in timing RPCs. However, it must be said that the slewing correction allows to typically improve the time resolution by 20-60 ps (see table 3.1 at the end of the chapter). An example of how this correlation looks like is shown in fig. 6.15.

3.2.4 Space-Charge

Space-Charge is known to be crucial for interpreting the charge spectra and efficiencies of both standard RPCs [48] and tRPCs [53], [57].

Let's assume the following very naive image: a) the avalanche grows until reaching a critical number of electrons, b) such critical number is related to the situation where the avalanche self-field is comparable to the applied one, resulting in a reduction of the effective field in a large region of the avalanche development (see fig. 2.5), c) further ionizations are highly reduced for a large fraction of the secondary electrons, which drift towards the anode almost unaffected (see fig. 3.3), d) the average field created by the avalanche is proportional to the number of carriers (neglecting diffusion effects):

$$\bar{E}_{avalanche} \propto \bar{n}_e \propto \bar{q} \tag{3.10}$$

On the other hand, according to the assumptions made, the avalanche will grow up to the point when the local field is equal to the applied field E, i.e. $\bar{E}_{avalanche} = E$. This implies that $\bar{q} \propto E$. In a parallel geometry $E \propto V$ and therefore:

$$\bar{q} \propto V \tag{3.11}$$

For low voltages, i.e., before the onset of the Space-Charge regime, the growth of the average charge $\bar{q}$ with V will be the one expected for a proportional counter:

$$\bar{q} \propto e^{\alpha(V)g} \tag{3.12}$$

[8] Time of flight.

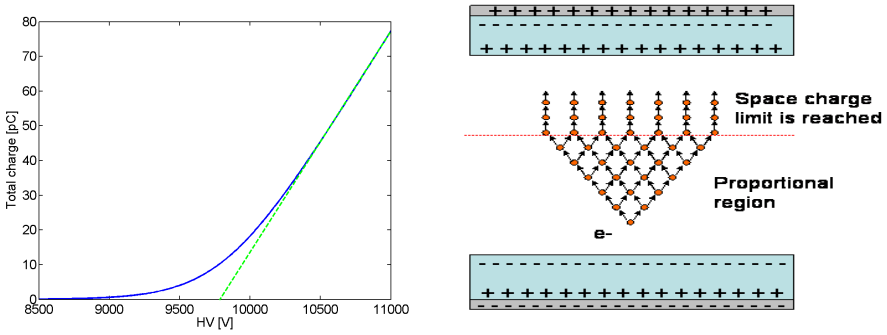

Figure 3.3: Figures inspired in [54], for trigger RPCs. The left picture corresponds to the semi-empirical law $\bar{q}(V) = K \ln(1 + e^{a(V-V_{th})})$ that describes well the exponential and the linear regions observed experimentally. V_{th} is related to the onset of the Space-Charge effect. The dashed line shows the region where the linear behavior is a reasonable assumption. In the right, the Space-Charge effect is illustrated according to the very naive model of text.

For high fields, the behavior of α as a function of V can be approximated by a linear trend [66], so the growth of the average charge with V is well described by an exponential.

Despite its simplicity, the view proposed for describing Space-Charge is in agreement with the observations made on tRPCs [68] (quoted as a transition from an exponential region to a 'sub-exponential' region) and standard 2 mm RPCs [54] [58].

A nice attempt to reproduce the transition from the exponential to the linear regime consists in comparing this situation with a self-regulated system such as a biological population in an environment with limited resources [54]. In this case the role of the 'resources' is played by the field observed by the electrons in the avalanche, which are the active population. The electrons 'eat' electric field up to when it is exhausted and then further growing is stopped. This model predicts in a natural way an exponential 'proportional' regime followed by a 'saturated' regime where the behavior is linear (fig. 3.3).

Space-Charge reduces the released charge by several orders of magnitude as compared to the expected from a proportional regime. Moreover, it allows to reach very high values of α before streamers start to be important, resulting in a very narrow time response (eq. 3.7). For illustration: taking the average value $\alpha \simeq 90/\text{mm}$ obtained in lab at $E = 100$ kV/cm under operation with the standard mixture [69] it would be expected $\alpha g = 25$, yielding for a tRPC working in a proportional regime a total charge given by:

$$\bar{q}_{total} \simeq e\, e^{\alpha g} \simeq 10^4 \text{pC} \tag{3.13}$$

which is orders of magnitude above the typical charges observed in tRPCs (at the level of few pC).

It is known that a parallel geometry does not represent an adequate choice for measuring the energy released by the primary particle, because of the uncertainty in the position of the first interaction. In RPCs, due to the presence of Space-Charge, the correlation between the released charge and the collected one is even smaller, because all the avalanches are doomed to a similar end.

3.2.5 Prompt charge vs induced charge

The charge induced during the drift of the electrons along the gap is denoted as prompt/electronic charge q_{prompt}, a process that takes place typically in the first 3 ns after cluster formation ($v_e \simeq 100$ μm/ns [69], $g/v_e \simeq 3.0$ ns). The drift time of the ions is considerably larger, being at the level of μs. The term *induced charge* $q_{induced}$ is used here to denote the charge induced during both the drifts of the electrons and the ions in the gap.

The total charge released cannot be accounted for before the flow in the resistive plates takes also place (at the scale of its relaxation time). In a natural way, this charge is denoted as the *total charge* q_{total} or simply q.

The average ratio $\bar{q}_{prompt}/\bar{q}_{induced}$ is often evaluated, as it has a clean dependence in the case of a parallel plate chamber in the proportional regime:

$$\frac{\bar{q}_{prompt}}{\bar{q}_{induced}} \simeq \frac{1}{\alpha g} \tag{3.14}$$

indicating that most of the collected charge is induced during the ions drift, as these are mainly produced close to the anode, drifting along the whole gap g. In the presence of Space-Charge the ratio is modified, and different descriptions of this regime can be evaluated (see [53], [54] for instance).

3.2.6 Signal induction

The signal induced in the read-out electronics is usually expressed by following the Ramo theorem [70]:

$$i(t) = \vec{E}_w \cdot \vec{v}_e(t) n_e e \tag{3.15}$$

where n_e is the number of carriers, e the electron charge and $\vec{v}_e$ the drift velocity. Therefore, the measured current is related to the charge drifting inside the gas, through a quantity $\vec{E}_w$ that is called the 'weighting field'. The weighting field is not really an electric field, having units of [L^{-1}]. It is defined as the electric field when the signal electrode is set to a voltage of 1 (no units) and all the other electrodes to 0 (a detailed theoretical discussion can be found in [64]).

In Appendix B it is derived that, for a parallel geometry with infinite plates:

$$q_{total} = \frac{C}{C_{gap}} q_{induced} \tag{3.16}$$

where C is the total capacity of the RPC, $q_{induced}$ is the charge induced during the drift in the gas and q_{total} is the charge released (see previous section). On the other hand, also for infinite plates, the weighting field is given by:

$$E_w = \frac{1}{g} \frac{C}{C_{gap}} \tag{3.17}$$

The exact analytic expression of the weighting field, coming from the evaluation of the generalized Ramo theorem in the presence of resistive materials, can be found exhaustively studied elsewhere [64]. However, expressions 3.16 and 3.17 provide a reasonable description in many practical cases, as long as edge effects are small and the influence of the resistive material can be neglected.

3.2.7 Rate capability

The rate capability depends mainly on the volume resistance of the plates and the average charge released per avalanche. However, as indicated in [38], the surface conductivity must have also a role, and a part of the effect is to enlarge the area affected by the avalanche [60].

A description of the process can be attempted by assuming that the average charge $\bar{q}$ released in an avalanche is deposited on the resistive plate, influencing a transverse area A and inducing an average drop $\bar{V}_{aval} = \bar{q}/C$ (C is the capacity of the glass). The physical process is approximated by an RC circuit coupled to a noise generator (the RPC) with a typical relaxation time $\tau_g = RC \simeq 1$s (see chapter 9 for a detailed description). Let's assume, for simplicity, that at a time τ_g after an avalanche is produced the glass is already recovered and takes its nominal potential. Naming by ϕ the primary rate in units of [L^{-2} T^{-1}] it can be reasoned that the condition for rate effects to start to contribute is:

$$\phi \tau_g A \simeq 1 \tag{3.18}$$

This means that the average occupancy of the area illuminated by the forthcoming avalanches is 1. However, eq. 3.18 does not contain an important ingredient: the average drop per avalanche. For including this effect, let's assume that a certain drop in the voltage ΔV is required for worsening the RPC performances (let's say a voltage drop necessary to induce a 5% drop in efficiency, for example). The average drop per avalanche is $\bar{V}_{aval} = \bar{q}/C$, therefore the condition for not influencing the RPC performances can be written as:

$$\phi \tau_g A \frac{\bar{q}}{C} \lesssim \Delta V \tag{3.19}$$

In particular, the left hand side of eq. 3.19 is the ohmic drop in the resistive plates ($\bar{V}_{glass}$=$\bar{I}R$=$\phi \tau_g A \bar{q}/C$). Working on expression 3.19:

$$\phi \tau_g A \lesssim \frac{\Delta V}{\bar{q}/C} \tag{3.20}$$

$$\phi \lesssim \frac{\Delta V}{\rho d \bar{q}} \tag{3.21}$$

As natural, if the avalanche drop $\bar{q}/C$ is equal to ΔV, the expression 3.18 is recovered. Eq. 3.21 shows the condition for rate effects not to be important; it can be inferred from it that the rate capability of an RPC is governed by the average avalanche charge $\bar{q}$, and the 'column resistivity' ρd (where d is the total thickness of the resistive plates divided by the number of gaps and ρ is the electric resistivity). *In a first approach, the rate capability is independent from the area of influence of the avalanche A.* This is so because a larger area means a higher number of events per affected region, but also a lower drop induced per event, due to the larger capacity.

The above reasoning provides a rule of thumb. However, it can be shown that the *fluctuations* of the field in the gap around its average value depend on A, in fact. Under certain conditions this effect could be even dominant for the RPC performances, and it is discussed in detail in chapter 9.

The maximum rate achievable before the ohmic drop in the plates results in a deterioration of the performances is referred in the following as the *rate*

capability K (in units of flux), keeping in mind that, in a first approach, it scales as:

$$K \propto \frac{1}{\rho d \bar{q}} \tag{3.22}$$

If either the resistivity, the average charge, or the thickness of the resistive plates is decreased by a certain factor, the rate capability will improve by the same amount.

It is very important to realize that an unbiased estimate of the rate capability requires that data were taken during typical times t_{spill} larger than τ_g. This is required for the stabilization of the voltage drop (chapter 9). If the spill is much shorter than the relaxation time τ_g, the voltage drop will be significantly smaller than the corresponding to the stabilized situation, leading to an overestimation of the performances. The effect has been proved in short spills of 0.25 s as commonly used at CERN PS [71].

3.2.8 Type of conductivity

There are natural questions regarding the way the charge flows through the plates. If the conductivity has ionic origin it will decrease in time with the amount of charge delivered, exactly as in the case of a battery, while if the conductivity is electronic it will be stable. The former is the case of Bakelite, whose conductivity seems to be related to the movement of H^+ ions [72]. However, for glass RPCs such a decrease was not seen. This led to some authors to argue that the conductivity is electronic, but 'hopping' [73] in contradiction to the expected ion conductivity [74], [75].

The microscopic characteristics of the resistivity are therefore called to play a role in the stability of the RPC operation along time, directly related to the rate capability and dark current.

3.2.9 Aging

Aging in RPCs has nowadays a number of features, with a reasonably degree of understanding. Most of the effects reported regarding RPC-aging are related to the properties of the resistive plates, but also some of them have to do with the gas mixture. Bakelite, for example, has a resistivity which is typically increasing with time, presumably due to the loss of ionic carriers. This increase can be correlated with the absence of H^+ ions (see previous section) and therefore depends on the drying of the gas. It has been seen that a partial recovery of the resistivity can be obtained via the addition of small amounts of water vapor [76], [77]. This idea has been implemented for CMS chambers showing a high stability of the rate capability [42]. A total recovery seems to be also possible just by inverting the field [78] which is probably not a practical solution.

Another source of deterioration for Bakelite plates is related to the 'curing' of the linseed oil. It is significative the case of the BaBar experiment, where real 'oil stalagmites' were formed in the detectors, decreasing significantly its efficiency by more than 10% [79]. Nowadays, only a very thin and well cured layer of linseed oil is applied. As oil is a potential source of aging effects, some studies are being performed in the direction of non-oil Bakelite RPCs [80].

At last, the necessity of monitoring the concentration of F^- radicals that appear in the mixture after the avalanche process has been pointed out [81].

These radicals may bound forming the very corrosive HF. A particular unfavorable situation would be that of closed gas loops; however, the addition of smalls amounts of water vapor, that react with HF, improves the situation [82].

The situation regarding aging seems to be better in the case of glass RPCs. On one hand, timing RPCs operated in avalanche mode during an equivalent time of 8.5 years at a typical maximum rate of 300 Hz/cm^2 didn't show any degradation for a wide set of configurations as shown in [83] and also [49]. In [83] a small deposit was found at the glass cathode, indicating that some chemical process had taken place, but without influence on the performances.

In the context of glass RPCs, several tests were performed for studying the dependence on environmental factors like humidity or temperature. For the case of wide RPCs, no sizable degradation was found with the temperature [73], but a strong dependence was observed with the percentage of humidity [84], apparently related to the presence of freon in the mixture (CH_2FCF_3 was used in this case) and the formation of HF acid [72]. The effect vanishes when cleaning up the chamber with a flow of ammonia [73].

Putting everything together some controversy is apparent, claiming for a clarification of the influence of water vapour on the formation of HF acid and ageing.

3.2.10 Electronics

Due to the fast tRPC signals, having rise-times at the level of ns (chapter 3.2.5), very fast amplifying electronics are required, with a bandwidth up to 1 GHz. Despite being a crucial part in any fast tRPC development, the detailed description of the acquisition electronics is out of the scope of the present work and therefore only the two designs that have became more popular are briefly discussed: the NINO ASIC[9] of the ALICE group [85] and the TAQUILA board of the FOPI group [86].

The NINO chip has a differential input and it is characterized by its very low power consumption of 40 mW/channel. It implements a measurement of the time-over-threshold (TOT) of the signal, for performing the slewing correction: the TOT width is sampled with a HPTDC of 25 ps bin that allow for a measurement of both the leading and trailing edge. The design proved to be fully adequate, keeping the time resolution of a 10-gap tRPC at the level of 50 ps with a large efficiency plateau.

The TAQUILA board is only a part of the electronic chain, namely, it works with the digital signals after the discrimination stage. It is a 16 channel board started by any of the channels and common-stopped by a free running 40 MHz clock, yielding a very low jitter of $\sigma_T = 12 \pm 2$ ps. The FEE electronics stage rises the jitter up to $\sigma_T = 33 \pm 4$ ps, still within the requirements for operate a timing RPC. The charge for the slewing correction is measured with a QDC.

In the framework of the HADES tRPC project, that is described later, developments are ongoing regarding fast and compact low-noise FEE electronics that use the TOT information for the slewing correction [87].

[9] Application-Specific Integrated Circuits.

3.3 Some timing RPC systems

In this section, the different timing RPC walls, in construction stage or already finished that have been developed so far, are described. Five are the experiments that are applying this technology to the field of nuclear and particle physics: HARP [88], [89], ALICE [90], STAR [91], [92], [93], FOPI [86], [94] and HADES [95], [96], [97] although some others like CBM [98] are foreseen for the future.

3.3.1 HARP

Located at the CERN-PS, the tRPC wall of the HARP experiment has the merit of being the first timing RPC wall to operate in a high energy physics experiment (*and the only one finished so far*). The design and construction of the electronics together with the whole set of cells (368 channels) took *4 months* between December 2000 to April 2001. It is based on the original design of [45], consisting in 4 gaps, 0.3 mm wide, operated at 3 kV/gap, with resistive plates made out of standard float glass (Glabervel) in a double layer configuration, for avoiding geometric losses. It is filled with a gas mixture similar to the 'standard', $C_2F_4H_2/SF_6$/iso-C_4H_{10} in a proportion 90/5/5. Due to the lack of space, it was necessary to machine the glass with a thickness of 0.7 mm over an area of 192×10.6 cm^2. This is the area per tRPC module, being each module divided in 64 pads, grouped in 8 strips per electronic channel. A drawing of the experiment together with a schematic diagram of a module are shown in fig. 3.4.

The requirements in terms of rate capability are not severe, as the typical rates stand below 1 Hz/cm^2. Typical efficiency is at the level of 99% and time resolutions around 150 ps, that can be reduced to 105 ps for a single pad. The requirements of the experiment were $\varepsilon \geq 99\%$ (for an error lower than 1-2% in the determination of the cross-section [88]) and σ_T<200 ps (for PID[10]).

Although rate capability was not a tight requirement, a test was performed at ϕ=2 kHz/cm^2 at CERN-PS, observing a slight deterioration of the performances.

Crosstalk was reported below the level of 10%.

3.3.2 ALICE

The construction of the ALICE tRPC wall was foreseen in 2000 in the framework of the new hadron collider facility at CERN (LHC). It provides the best performances so far. The authors even indicate that they are close to the maximum resolution achievable with the device, due to the fact that the larger contribution to the time jitter comes from the electronics, not from the detector.

ALICE tRPC is a huge project for covering 150 m^2 with 160000 electronic channels and a time resolution below 100 ps, with a high overall efficiency. The cathode is segmented in pads with areas of 9 cm^2 approximately, and the design exploits the multi-gap concept up to a total of *10 gaps* with an applied voltage V = 2.5 kV/gap. Note that the voltage is lower than HARP because the gap is also slightly smaller (0.25 mm) requiring less voltage for getting the typical operating fields of 100 kV/cm. The glass is as thin as 0.4 mm. A layout of a typical cell is shown in fig. 3.5.

[10] Particle IDentification.

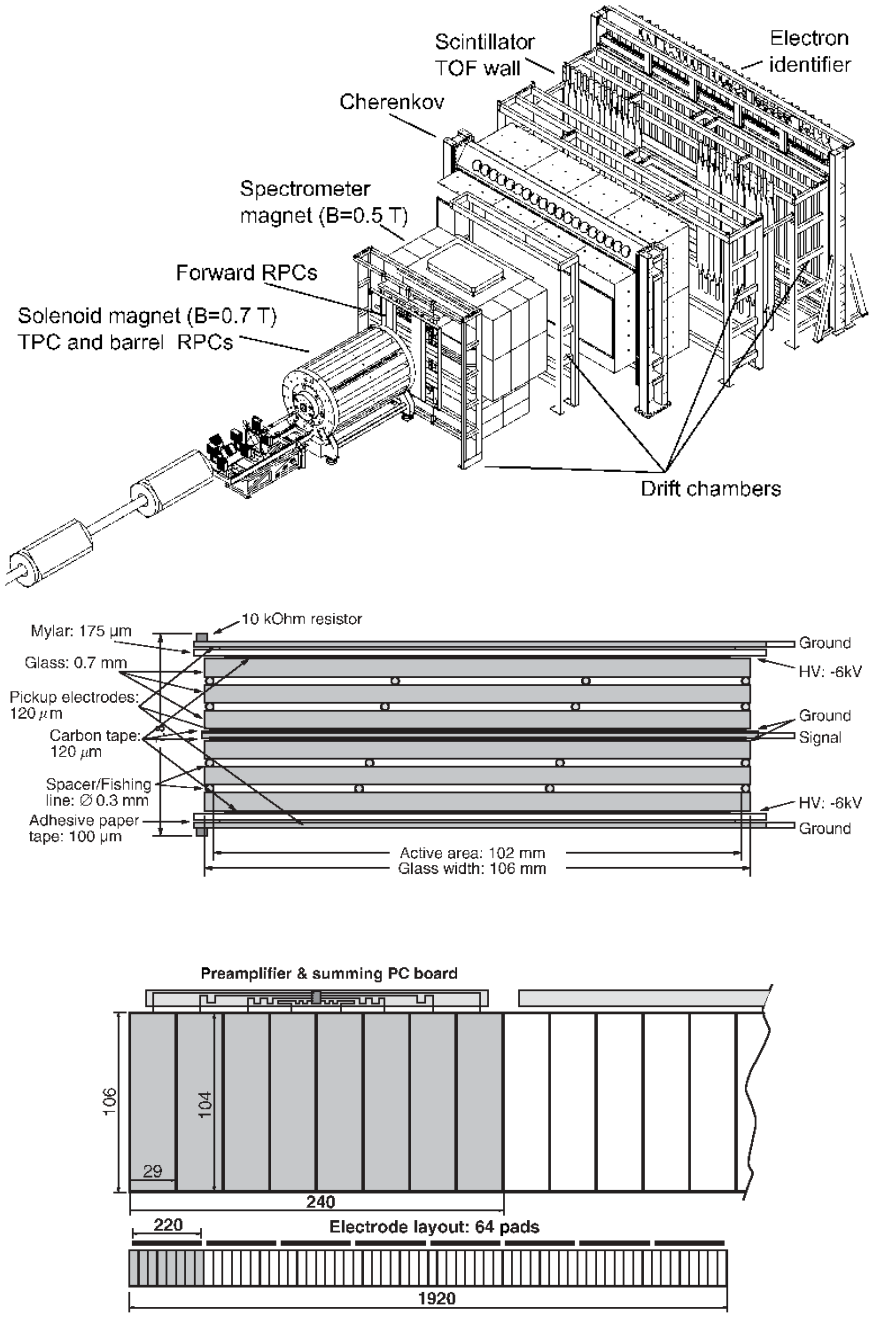

Figure 3.4: HARP spectrometer (up) and detail of the HARP tRPC wall (down) [88].

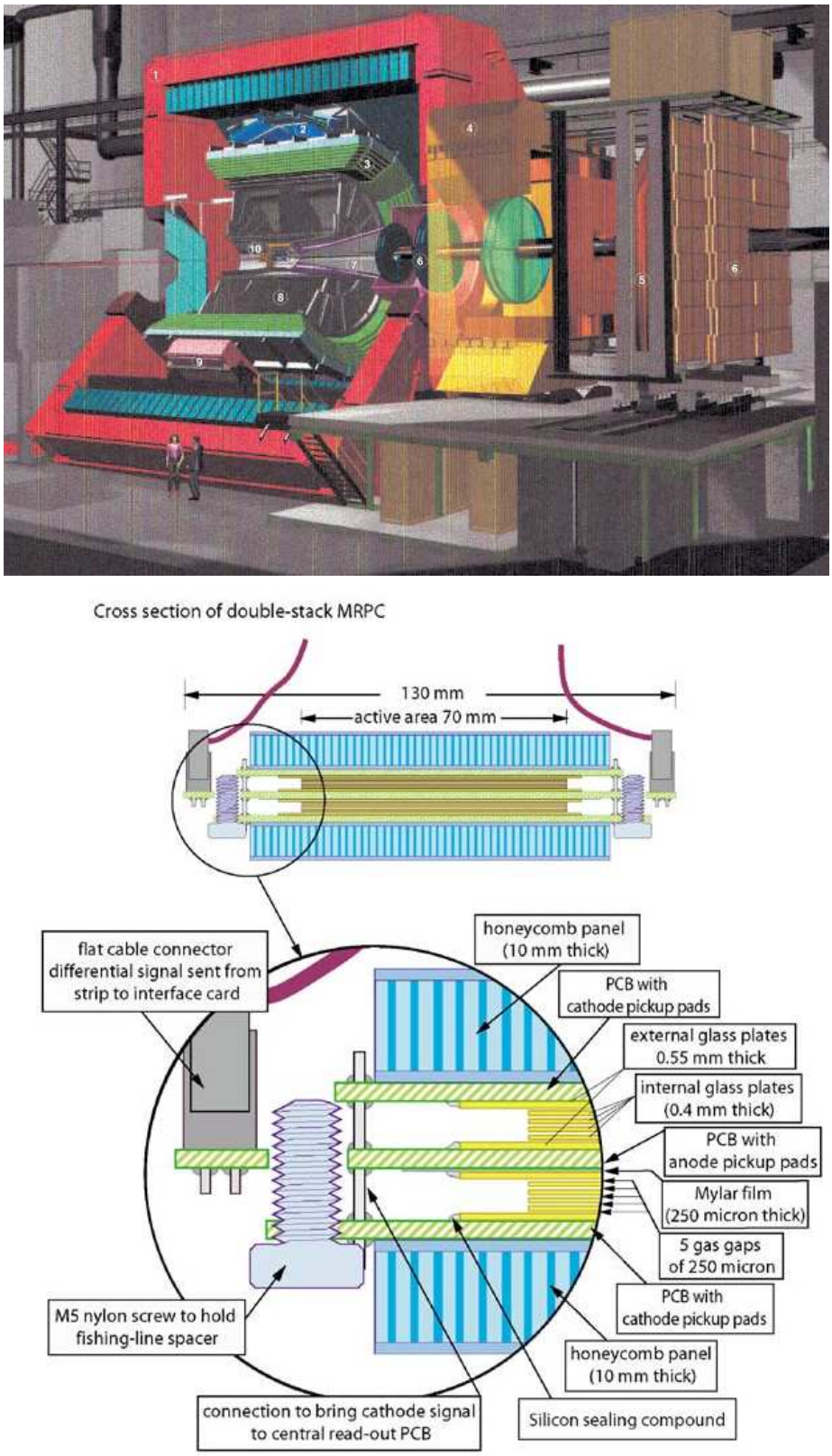

Figure 3.5: ALICE spectrometer (up) [99] and zoom of the Alice tRPC cell (down) [90].

The results of the ALICE tRPC tests have shown to fulfill the commissioning requirements, providing resolutions well below 50 ps and efficiencies up to 99.9%. The rate capability was estimated to be around 1 kHz/cm^2.

3.3.3 STAR

The tRPC wall for STAR at RHIC was born, in fact, at CERN, some of their members coming from the ALICE tRPC group. It is in an advanced stage and one of the final 120 trays foreseen has shown already satisfactory performances. Its main technical requirement is to provide a time resolution below 100 ps over a large area of 60 m^2. The detector is constituted by modules of 9.4×21 cm^2, picking-up the signals in pads of 6.3×3.15 cm^2. It is made out of 6-gap tRPCs of thin glass (0.5 mm) and very narrow gaps of 0.22 mm, allowing for operation at ± 7.5 kV between the electrodes. The efficiency is at the level of 95-97%, plus additional 5% losses due to geometric inefficiency. Regarding time response, 60-70 ps of resolution were achieved, fulfilling the requirements. A picture of the design is presented in fig. 3.6.

According to the authors, measurements performed under a pulsed beam (0.3 ms) at CERN-PS suggest a rate capability higher than 500 Hz/cm^2, providing a safe operating margin for the typical rates around 10 Hz/cm^2 expected for the STAR experiment. Recent 'in-beam' measurements for p-p and d-Au collisions have shown also good performances [93].

3.3.4 FOPI

FOPI detector is located at GSI-SIS in Darmstadt-Germany. There, a tRPC wall is under development to surround the central tracking chamber. It was a multi-step development, from Pestov counter to 4-gap tRPC to 6-gap tRPC (0.3 mm gap), that seems to offer the best performances, reaching efficiencies of 97 ± 3% and time resolutions of 73 ± 5 ps. It uses the standard mixture and is really a multi-strip design in the sense that the pitch between pick-up strips is *as small as 3.44 mm*, being 90 cm long.

Its performance has been tested under different conditions: Co^{60}, proton and deuterium at rates of 50-100 Hz/cm^2, which are a factor 2 larger than the expected in the experiment. An inhomogeneity of the cells regarding systematic shifts of the time distribution has been reported; however, it can be corrected off-line. There are also plans to improve the mechanics [94].

FOPI design has the remarkable particularity that the impedance of the cell coincides with the impedance of the read-out cables and finally the FEE electronics with a value $Z = 50 \pm 1\ \Omega$ [86]. This avoids reflections inside the detector, making easier the handling of the induced signal. A picture of the cells is shown in fig. 3.7.

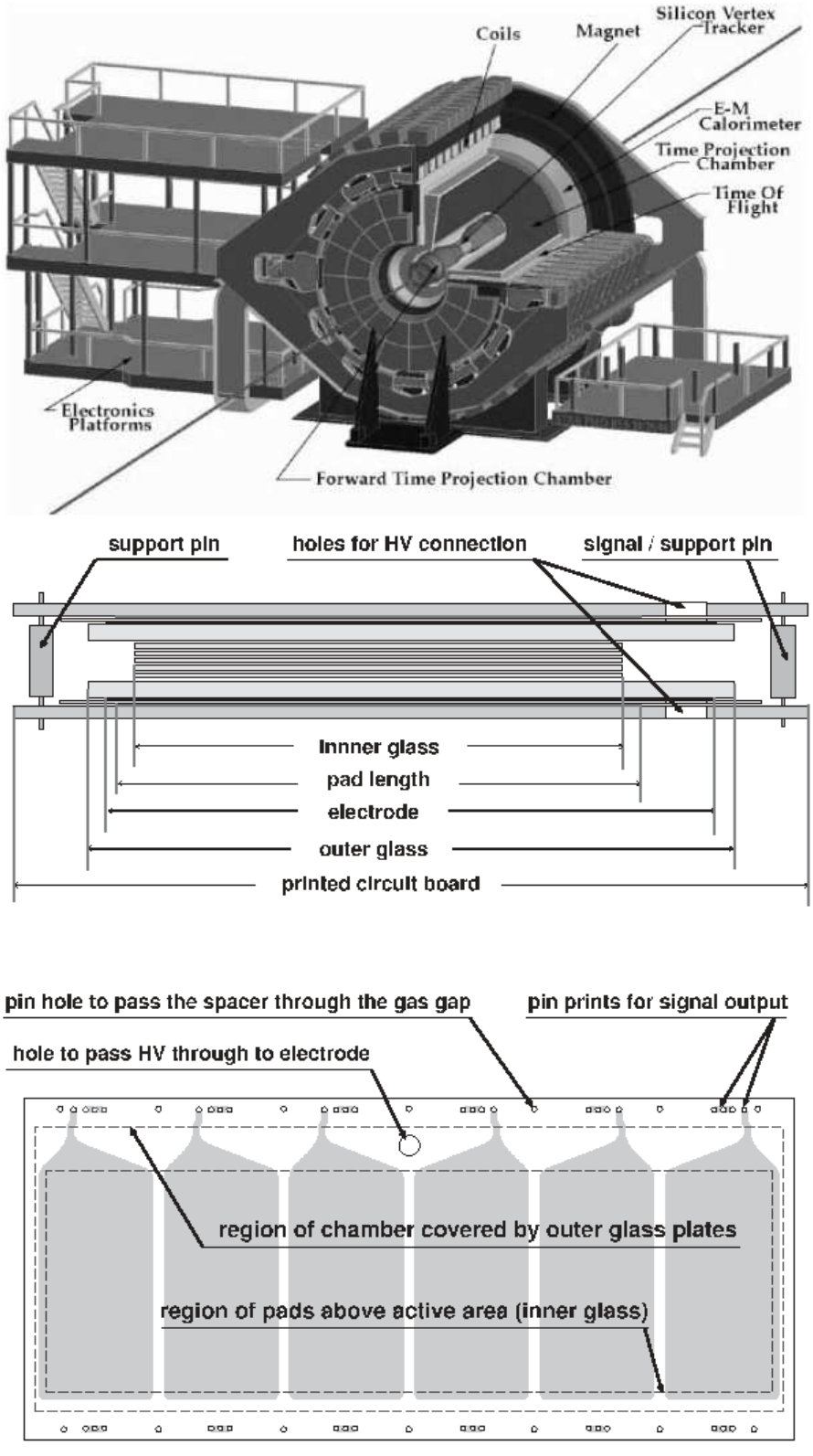

Figure 3.6: STAR spectrometer [100] and the STAR wall [91].

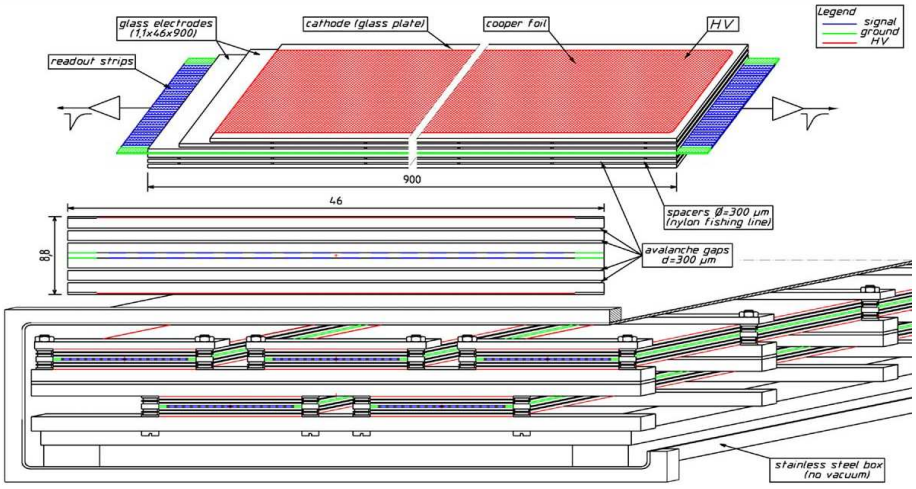

Figure 3.7: FOPI cell [86].

3.3.5 HADES

ESTRELA-HADES also at GSI-SIS is the younger of the timing RPC walls, and it is the topic of the present work. ESTRELA is the acronym for *Electrically Shielded Timing RPC Ensemble for Low Angles* in HADES[11]. Only the main results are summarized here, as an extensive description of the detector will follow: the wall is equipped with 4-gap cells with aluminum electrodes for improving the rate capability, which is a tough requirement for the HADES collaboration. It must be said that HADES spectrometer is already successfully working under light primary beams (see chapter 4). ESTRELA represents an upgrade for providing adequate granularities in order to handle heavy ion collisions up to Au+Au at 1.5 GeV/A.

By design, the cell occupancy is kept at the level of 20% in the case of central ($b < 4$ fm) collisions of Au+Au at 1.5 GeV/A, and time resolutions better than 100 ps-σ together with a high efficiency are required. The maximum operating rates are as high as 700 Hz/cm^2 for the lower polar angles, in the most unfavorable situation (see chapter 5). Such rates are, in fact, close to the operational limit of typical tRPCs (see [47], [90], [96]).

The performances under in-beam illumination with secondaries from C[12] collisions in April 2003 showed the possibility of operate the tRPCs with resolutions below 100 ps and losses of 10% in efficiency at 700 Hz/cm^2. For improving the behavior, and in the framework of the CBM R&D[12] for high-rate tRPCs, a new concept was developed, allowing to increase the rate capability in one order of magnitude, by just a moderate warming of the detector. This is the subject of chapter 8 and can be found in [59].

[11] Incidentally, 'estrela' means 'star' in Portuguese and Galician languages, just because, when the project started, only groups from these two regions were involved, namely LIP-Coimbra (Portugal) and USC-Santiago de Compostela (Galicia/Spain). Nowadays, a number of institutions: JU-Kracow (Poland), GSI-Darmstadt (Germany), CIEMAT-Madrid and IFIC-Valencia (Spain), UP-Leiría (Portugal) have joined.

[12] The R&D programme of the foreseen Compressed Barionic Matter experiment at GSI.

After the 2003 test, 'pros' and 'cons' were found in the design. The main 'pro' is that the cross-talk between neighboring strips was reduced to 0.5% due to the shielding between the cells, as compared to previous results at the level of 80% [47]. The detector also proved to be highly homogeneus over an area of 60×2 cm^2 and, furthermore, the parameters required for performing the slewing correction could be obtained from any position. As the main 'con', it must be mentioned that the shielding requires dead regions between cells, that were estimated to be around 15% percent of the total area for perpendicular tracks. Therefore, the multi-hit capability is guaranteed at the price of some loss in geometric acceptance. The last can be overcame by a double layer configuration [101]. The difficulties of this approach are not negligible: on one hand it increases the number of channels by around 20% due to the necessary overlap, providing, as a benefit, the possibility of self-calibration of the device [97]; on the other hand the material budget is increased and a dependence of the geometric acceptance with the angle of incidence is also introduced. The first problem (the increase in the material budget) is mitigated by the fact that the only detector placed downstream the tRPC wall is a shower detector which proved to be quite insensitive to the amount of material placed upstream. The second problem requires a detailed design guaranteeing that all the particles within the 'relevant angles' of incidence over the tRPC wall are handled. Discussions on these issues are postponed to chapter 5.

A photograph of the prototype tested in April 2003 can be found in fig. 6.1.

3.3.6 Features of tRPC walls

A summary of the main characteristics of each tRPC wall is presented in table 3.1. The table intends to be a comprehensive compilation of data that allows to compare the performances of each timing wall. Some of the fields require explanation: the 'efficiency' do not include geometric inefficiency, it stands for the intrinsic efficiency of the device. In the case of the current HADES prototype the inefficiency is, in fact, dominated by the geometric losses due to shielding. The 'cell size' is defined as the area per pick-up pad/strip and stands for the typical values. The values reported for the 'column resistivity' ρd are based on the estimates given by the authors. The space resolution is usually not published: it is followed the convention of taking one σ for the position resolution along the direction of signal propagation and $w/\sqrt{12}$ in the transversal direction (w is the cell width)[13]. Finally, some of the entries in the table are empty, meaning that the magnitude is considered as recommendable for inter-comparisons but has not been provided by the authors.

The rate capability is difficult to obtain: in the case of HADES and ALICE it has been defined as the rate required for a 5% drop in efficiency, and HARP and STAR are just reasonable estimates from data. Only HADES used long spills with durations above 5 s.

Besides the comments above, not all the measurements were taken under the same conditions. For example: HARP values really come from the final barrel already installed, ALICE represents the performances under spot illumination, STAR tested a single tray under realistic conditions, FOPI is ready to start

[13] I.e., for the resolution in the transversal direction, the rms of a flat distribution across the cell width was assumed.

Detector	HARP	ALICE	STAR	FOPI	HADES
N_{gaps}	4	10	6	6	4
gap size [mm]	0.3	0.25	0.22	0.3	0.3
gas[$C_2F_4H_2/SF_6/C_4H_{10}$]	90/5/5	90/5/5	90/5/5	85/10/5	98.5/1/0.5
electric configuration	cat-an-cat	cat-an-cat	an-cat	cat-an-cat	cat-an-cat
cell size [cm×cm]	22×10.6	2.5× 3.7	6.3× 3.1	90×0.34	60×2
detector size	10 m^2	150 m^2	60 m^2	5 m^2	8 m^2
$N_{channels}$	368	160000	$\simeq$ 30000	5000	$\simeq$ 2100
HV/gap	3.0 kV	2.4 kV	2.35 kV	3.3 kV	3.2 kV
ε	99%	99.9%	95-97%	97 $\pm$ 3%	>95%
plateau length	300 V	2000 V	500 V	600 V	$\gtrsim$ 200 V
σ_T	-	90 ps	120 ps	-	100 ps
σ_T (after slewing corr.)	150 ps	40 ps	60 ps	73 $\pm$ 5 ps	70 ps
cross-talk/neighbor	$<$ 10%	-	-	-	$<$ 0.5%
3-σ tails	-	-	-	$<$ 2%	6%
space resolution [cm^2]	-	-	-	-	0.6×0.6
experiment rates	1 Hz/cm^2	50 Hz/cm^2	10 Hz/cm^2	50 Hz/cm^2	700 Hz/cm^2
dark rate [Hz/cm^2]	$<$ 0.1	-	$<$ 0.3	$<$ 1	2−3
rate capability [Hz/cm^2]	$\leq$ 2000	$\leq$1000	-	-	350
$\rho\ d$ [$10^{12}\ \Omega \times cm^2$]	10 × 0.105	- × 0.04	5 × 0.055	- × 0.15	5 × 0.1
$\bar{q}$	-	2 pC	-	-	-
$\bar{q}_{prompt}$	-	-	-	-	0.7 pC
material budget (x/X_o)	-	-	-	-	12-24%
resistive material	float glass	float glass	float glass	float glass	float glass

Table 3.1: Different timing RPC walls and some of their characteristics.

mass production and HADES is at the second prototype (results on the last prototype are not included here but can be found in [1]).

As a conclusion from table 3.1, the situation of the RPC technology is rather exciting, with several experiments ready to take data. There is a number of different RPC species, and the particular choice is determined by the requirements of the experiment, regarding mainly the required rate capability, granularity (cell size), efficiency, cross-talk, space and time resolution, and material budget. By now, some common features have also emerged: a) float glass is widely used in timing RPCs, b) the gas mixtures adopted are similar, using a certain amount of $C_2F_4H_2$, SF_6 and iso-C_4H_{10} in a proportion around 85/10/5 (the standard mixture), c) the gaps lay in a narrow range from 0.22 to 0.3 mm, allowing for typical fields around 100 kV/cm, d) the rate capability is limited to some hundreds of Hz/cm^2 and e) all the tRPC walls have 4 gaps or more allowing for efficiencies well above 95%.

Chapter 4

Nuclear physics at HADES

4.1 Relativistic heavy ion collisions

There are, at least, two important reasons for studying heavy ion collisions at relativistic energies:

1. To understand the properties of nuclear matter, mainly its Equation of State (EoS).

2. To establish the presence of *in medium* effects on the properties (mass, decay width, reaction cross section) of hadrons surrounded by a dense nuclear medium.

The latter is the paramount scope of the HADES construction at GSI-SIS (Darmstadt, Germany) and in particular of the upgrade to the tRPC wall at low polar angles ($\theta < 45°$). The wall has been devised to study heavy ion collisions up to Au+Au at kinetic energies $E_{kin} = 1.5$ GeV/A and is the subject of the present work.

4.1.1 The Equation of State of Nuclear Matter

With the term nuclear matter it is usually meant an infinite (to neglect surface effects) medium, made of nucleons at global mechanical, chemical and thermal equilibrium, where the contribution to the energy per nucleon W of the Coulomb interaction can be ignored. As such, nuclear matter can be considered mainly a theoretical object. Some cases are (were), however, present in nature, as neutron stars or the early phases of the Big-Bang. On earth, the closest possible situation is the fire-ball formed in central heavy ion collisions: at bombarding energies of 1-2 GeV/A, barionic densities of 2-3 times ρ_o[1] can be reached. Unfortunately, such conditions last merely 15 fm/c and the degree of equilibration achieved in such a short time is open to questions.

Typically, the EoS is represented through the energy per baryon W and expressed as a function of two thermodynamic variables: the temperature T and

[1] $\rho_o \simeq 0.17$ nucleons/fm^3 is the saturation value in the core of heavy nuclei.

the density ρ. It is usually decomposed in a thermal part $W_{_T}$ and a compressional part $W_{_C}$ [102]:

$$\begin{cases} W(\rho,T) = W_{_C}(\rho) + W_{_T}(\rho,T) + W_o \\ W_o = W(\rho=\rho_o, T=0) \\ W_{_C}(\rho) = W(\rho, T=0) - W_o \\ W_{_T}(\rho,T) = W(\rho,T) - W(\rho,T=0) \end{cases} \tag{4.1}$$

The energy per nucleon can be expressed in differential form as:

$$dW = T\,ds - P\,dv \tag{4.2}$$

where v and s are the volume and entropy per nucleon, and the pressure can be therefore expressed as:

$$P = -\left(\frac{\partial W}{\partial v}\right)_s = \rho^2 \left(\frac{\partial W}{\partial \rho}\right)_s \tag{4.3}$$

The EoS is characterized by three fundamental constraints:

1. The value of W_o given by the nucleon mass minus the volume term in the liquid drop mass formula $W_o \simeq (938 - 15)$ MeV/A $= 923$ MeV/A.

2. The condition of stability for ordinary nuclei (i.e. W must have a minimum at $\rho = \rho_0$):

$$\begin{cases} \left(\frac{\partial W_{_C}}{\partial \rho}\right)_{\rho=\rho_o} = 0 \\ \left(\frac{\partial^2 W_{_C}}{\partial \rho^2}\right)_{\rho=\rho_o} > 0 \end{cases} \tag{4.4}$$

3. The value of the compressibility κ [102]:

$$\kappa = 9\left(\frac{\partial P}{\partial \rho}\right)_s = 9\,\rho^2 \left(\frac{\partial^2 W}{\partial \rho^2}\right)_s \tag{4.5}$$

   A high compressibility ($\kappa \lesssim 200$ MeV) will lead to high densities in central heavy ion collisions and the corresponding EoS is called 'soft', while a low compressibility ($\kappa \gtrsim 250$ MeV) will lead to low densities and the corresponding EoS is called 'stiff'.

Historically, the study of particle production in heavy ion collisions was started with the motivation of reaching an independent estimate of κ, but nowadays has a vigorous life of its own with the investigation of possible *in medium* effects (see next section).

Pion production was believed to be a good observable to extract κ [103]: their yield per collision is proportional to the fraction of initial beam energy that is converted into thermal excitation ($\simeq W_{_T}$) and is higher for a stiffer EoS[2]. However, pions interact strongly with nucleons and are easily absorbed,

[2]Smaller densities are reached in the fire-ball and less energy is stored in compressional form $\simeq W_{_C}$.

so their total number is affected also by the details of the expansion phase of the fire-ball.

J. Aichelin ans C.M. Ko had then an idea that changed the scope of the field: the use of sub-threshold K^+ production ($NN \rightarrow K^+\Lambda N$ requires $E_{\rm lab} > 1.6$ GeV) as a promising probe for κ [104]: in fact strangeness is conserved in strong interactions and K^+ absorption (due to the presence of a $\overline{s}$ quark) is negligible in nuclear matter[3]. This idea seemed even more attractive: at sub-threshold energies the production in direct nucleon-nucleon collision is very unlikely, requiring of a two step process involving baryon-baryon or baryon-pion collisions. An experimental confirmation of this cooperative mechanism is given by the almost quadratic dependence of the K^+ multiplicity on the number of participants [105]. For pions, that are above threshold at the same energies, a simple linear dependence is found. The probability of the two steps to happen in cascade is expected to be influenced by the volume of the fire-ball, that is in turn, for a given centrality, affected by κ. This qualitative conclusion has been confirmed by detailed transport model calculations [106]. Unfortunately, this apparently clear situation is obscured by the possibility of *in medium effects* on the K^+ mass, that is predicted to increase with the density inside the nuclear matter (see next section). So, a given value of κ will affect also the K^+ production by changing the *in medium* threshold and introducing more uncertainties in the theoretical calculation. The determination of the EoS from the measured K^+ yield becomes therefore more difficult. Recently, this obstacle has been attenuated by the use of the K^+ multiplicity ratio between a heavy system (Au+Au) and a light one (C+C):

$$\frac{(M_{K^+}/A)_{Au+Au}}{(M_{K^+}/A)_{C+C}} \tag{4.6}$$

Studying the beam energy dependence of this magnitude in the range from 0.8 GeV/A to 1.6 GeV/A, the KaoS collaboration has established that a soft EoS ($\kappa = 200$ MeV) is compatible with data, while a stiff one ($\kappa = 380$ MeV) is not [107].

The value of κ has also important astrophysical consequences. In the core of a neutron star the gravitational force is counterbalanced by the resistance of nuclear matter to compression. So, depending on the EoS, only certain regions of the mass-radius parameter space are possible [108]. In particular, a stiffer EoS ($\kappa \gtrsim 200$ MeV) would allow higher stellar masses ($M \gtrsim 2M_\odot$).

4.1.2 *In medium* effects

A section on the theoretical description of *in medium* effects lays out of the scope of the present work. However, it should be appreciated in the following that a clear dichotomy exists in the theoretical machinery devised to treat pseudo-scalar (π, K) or pseudo-vector (ρ, ω, ϕ) mesons, that are widely used as experimental probes of *in medium* effects.

[3]Strangeness exchange is present and so a complete measurement would require the characterization of K_o production.

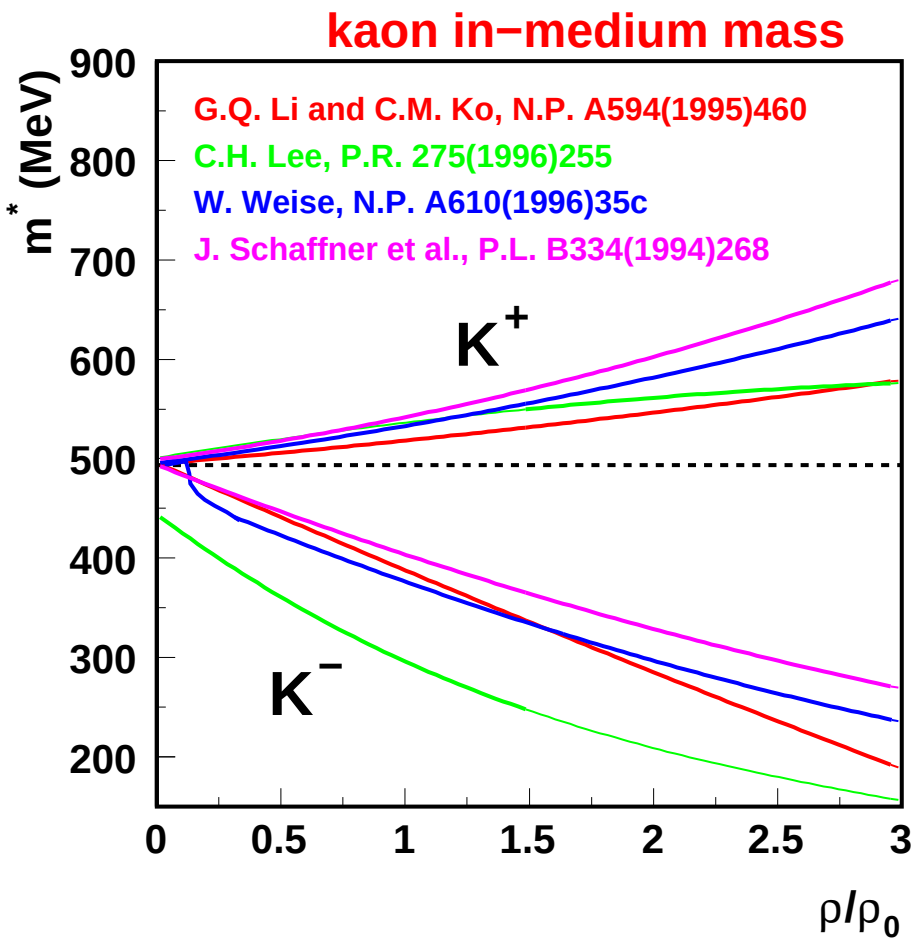

Figure 4.1: Compilation of several calculations for the K^+/K^- effective masses at zero temperature [109].

K^+/K^-

A systematic comparison [109] between different calculations of the *in medium* kaon mass is reproduced in fig. 4.1 for the case of infinite nuclear matter in equilibrium at zero temperature. The effective mass of the K^+ rises with density while that of the K^- decreases, both in an approximately linear way. In more fundamental terms, K^+ and K^- are subject to a repulsive and an attractive potential, respectively. All approaches agree qualitatively and, for example, at $\rho \simeq \rho_0$ a $\simeq 10\%$ rise and a $\simeq 20\%$ drop are predicted for the effective mass of the K^+ and of the K^-, respectively.

ρ, ω, ϕ

Based on arguments dealing with the symmetries of the QCD Lagrangian, G. E. Brown and M. Rho introduced in 1991 what is nowadays known as the Brown-Rho scaling [110]:

$$\frac{m_\omega^\star}{m_\omega} \simeq \frac{m_\rho^\star}{m_\rho} \simeq \frac{f_\pi^\star}{f_\pi} \tag{4.7}$$

where the star indicates *in medium* quantities, f_π is the pion decay constant and m_ρ and m_ω refer to the masses of the corresponding pseudo-vector mesons. They were also able to link the pion decay constant f_π with the chiral condensate [110]:

$$\frac{\langle 0^\star|q\overline{q}|0^\star\rangle}{\langle 0|q\overline{q}|0\rangle} = \left(\frac{f_\pi^\star}{f_\pi}\right)^3 \tag{4.8}$$

For illustration, a recent calculation of the chiral condensate as a function of the density and temperature in infinite nuclear matter at equilibrium is reproduced in fig. 4.2 [113], normalized to the value at $\rho = 0$, $T = 0$. In particular, the decrease of $\langle 0^\star|q\overline{q}|0^\star\rangle/\langle 0|q\overline{q}|0\rangle$ at $\rho \to \infty$ and/or $T \to \infty$ is linked to the partial restoration of chiral symmetry of the QCD Lagrangian. Such a symmetry is broken explicitely by the finite masses of the quarks and spontaneously by the non-zero value of the chiral condensate.

In 1992, Hatsuda and Lee [111] confirmed the conclusions of [110] using *in medium* QCD sum rules to connect hadronic and quark degrees of freedom. A later reexamination of QCD sum rules by F. Klingl, N. Kaiser and W. Weise [112] lead to the discovery that the same rules can be satisfied by a completely different model in which the *in medium* masses are unaffected but widths greatly increase with density and/or temperature. The two scenarios are commonly referred as '*dropping mass*' and '*melting*'.

4.2 Leptonic probes of *in medium* effects

The experimental efforts to establish the presence of *in medium* effects have followed three main approaches: hadronic probes in heavy ion collisions, leptonic probes in heavy ion collisions and elementary on nucleus collisions. Attention is focused here only on the leptonic probes as to their detection the HADES spectrometer is mainly devoted. The main ideas behind lepton spectroscopy can be summarized as follows:

1. The particles are studied through the decay channels of pseudo-vector mesons into e^+e^- or $\mu^+\mu^-$ pairs. This has a double benefit as: a) on one hand the lifetimes of the pseudo-vector mesons are small enough to allow for a strong influence of the high density stages of the fire-ball, while b) di-leptons from the decay interact only feebly with nuclear matter, being possible to determine directly the invariant mass spectra of their parents. Table 4.1 show the main properties of light pseudo-vector mesons.

2. The main disadvantage is the low branching ratio into di-leptonic channels (for the pseudo-vector mesons $\sim 10^{-5}$-10^{-4}). Moreover, many processes can contribute significantly to the background, like π_0, η Dalitz decay and γ conversions for di-electrons, or pion and kaon decay for di-muons.

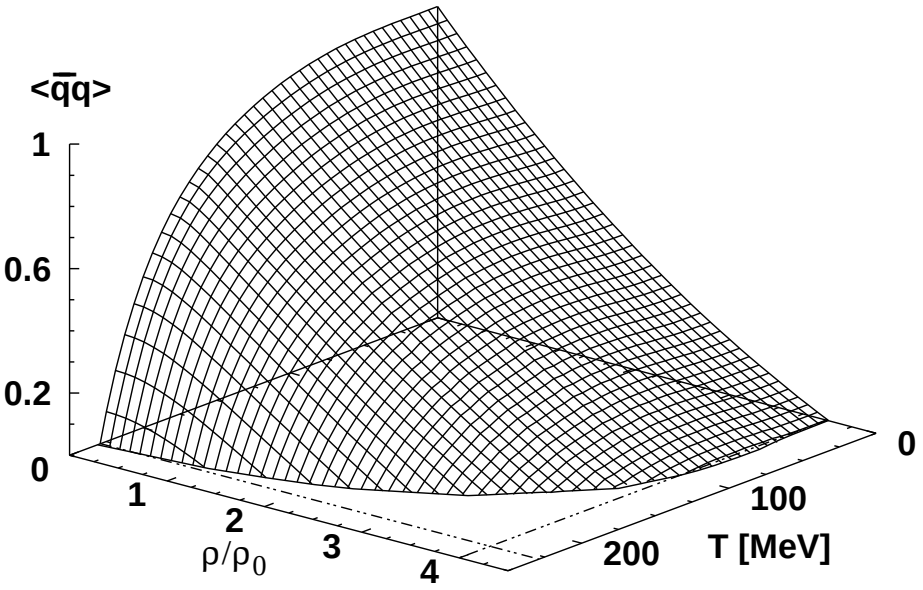

Figure 4.2: Evolution of the normalized quark condensate $\langle 0^\star|q\overline{q}|0^\star\rangle/\langle 0|q\overline{q}|0\rangle$ as a function of density and temperature, taken from [113].

Meson	Mass $[\frac{\text{MeV}}{c^2}]$	Width $[\frac{\text{MeV}}{c^2}]$	$c\tau$ [fm]	Main channel	e^+e^- BR	$\mu^+\mu^-$ BR
ρ	775.8	150	1.3	$\pi\pi$	4.67×10^{-5}	4.55×10^{-5}
ω	782.6	8.49	23.4	$\pi^+\pi^-\pi^0$	7.14×10^{-5}	9×10^{-5}
ϕ	1019.5	4.26	44.4	K^+K^-	2.98×10^{-4}	2.85×10^{-4}

Table 4.1: Light pseudo-vector mesons life times and branching ratios [3].

4.2.1 CERES

A heavy ion program has been running since the 90's at the CERN SPS. The beam energies (50-200 GeV/A) are so high that, indeed, the attention is focused on the search of a possible Quark Gluon Plasma phase. In particular, hadron production is highly above threshold and *in medium* effects are expected to play a minor role on it. However, some evidences have been reported on possible hints of *in medium* effects as discussed in the following.

CERES [114], [115], [116], [117] was optimized to measure e^+e^- pairs in an invariant mass range from $\simeq$ 10 MeV to $\simeq$ 1 GeV. A typical spectra in central Pb+Au collisions at 158 GeV/A is reproduced in fig. 4.3 after combinatorial background was subtracted. The spectrum is unfortunately missing a distinctive feature with a clean interpretation (i.e. a ρ peak displaced at a lower value, for example) and its understanding requires, first, the identification of the contributions from all known usual sources: the Dalitz decays of the π^0, η, η' and ω and the e^+e^- decay of the ρ, ω and ϕ. For this reason a special Monte-Carlo program, called GENESIS, has been developed over the years.

Comparison between data and model is shown in fig. 4.3, indicating a clear excess in the data which, for the invariant mass region 0.2 GeV $\leq m_{ee} \leq$ 0.6

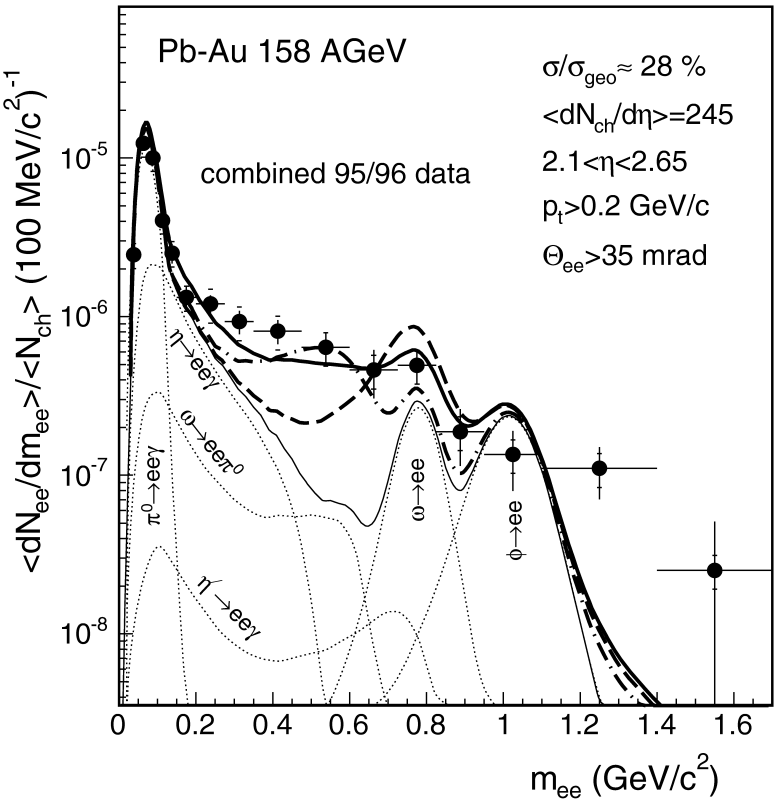

Figure 4.3: Di-electron invariant mass spectrum, after combinatorial background subtraction, obtained by the CERES collaboration for Pb+Au at 158 GeV/A [117]. The thin lines represent the contribution from known sources according to the GENESIS code. The thick lines include the extra contribution of pion annihilation (eq. 4.9) with different assumptions on the properties of the intermediate ρ in the propagator (see text).

GeV, amounts to $2.73 \pm 0.25[\text{stat}] \pm 0.65[\text{syst}] \pm 0.82[\text{decays}]$ [117]. It actually depends on centrality and rises up to $\simeq 4$ if the most central collisions in fig. 4.3 are isolated.

When the same procedure is applied to p+A data, all the spectrum can be described with known sources (fig. 4.4). The last finding suggests to place the origin of the observed enhancement for Pb+Au collisions in a process happening during the lifetime of the fire-ball. The main responsible of the observed discrepancy is believed to be pion annihilation in the dense fire-ball, mediated by the ρ resonance:

$$\pi^+ \pi^- \leftrightarrow \rho \rightarrow e^+ e^- \tag{4.9}$$

Since (4.9) is a two body process, it is expected to be proportional to the square of the pion density in the fire-ball. The observed stronger than linear increase with the number of participants (i.e. centrality) seems to confirm the presence of this mechanism.

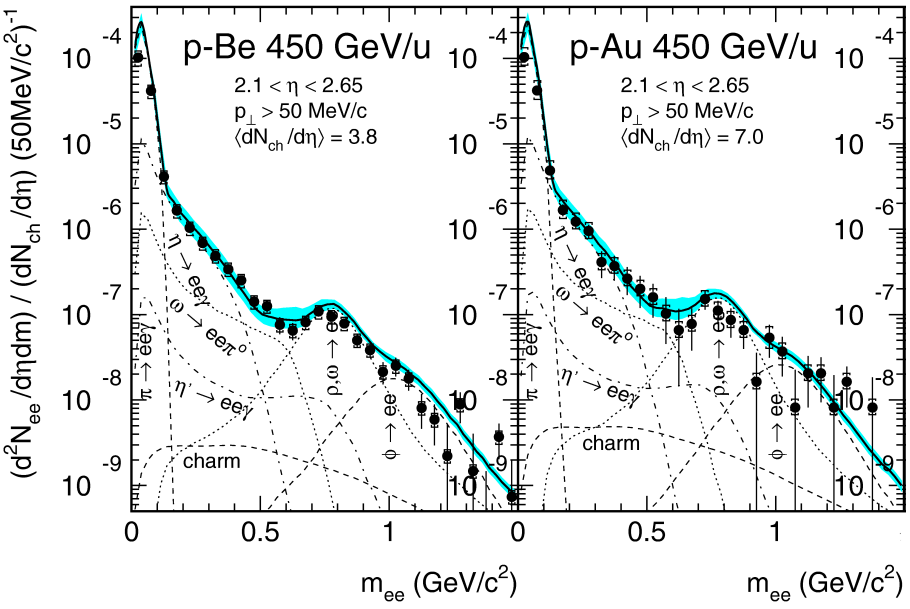

Figure 4.4: The same as fig. 4.3 but for p+B and p+Au at 450 GeV/A [115].

Nevertheless, all attempts to describe reaction 4.9 with the vacuum properties of the ρ meson have failed to explain data (thick dashed line of fig. 4.3) because they predict an increase only in the region of the free ω mass. If a dropping mass scenario is added for the ρ according to the Brown-Rho scaling, the calculations (thick dot-dashed line in fig. 4.3) can reproduce the data. However, the data can also be explained if the ρ *in medium* properties are modified accordingly to the spectral functions approach of [118] (thick continuous line of fig. 4.3), and there is no explicit connection with the Brown-Rho scaling or chiral symmetry restoration. The two scenarios (Brown-Rho scaling, spectral functions) reproduce the localization of the enhancement at intermediate m_{ee}, therefore no clear statement on *in medium* effects can be done. Remarkably, by measuring Pb+Au collisions at 40 GeV/A with an improved setup [116], an enhancement even larger than at 158 GeV/A was found.

4.2.2 NA60

Indications that favor one of the two scenarios for *in medium* effects have been reported by the NA60 collaboration [119], [120], [121], also at CERN SPS. Unlike CERES, di-muon pairs were selected as probes. NA60 is based on a 17 m long muon spectrometer constructed for the NA35/NA50 experiments, separated from the target by a 5.5 m long hadron absorber ($> 70\,X_0$) made mostly of Carbon. Under such conditions, essentially only muons can survive degradation. The final signal distribution after background subtraction is shown in fig. 4.5.

In the analysis of [121], the final excess in the ρ region is isolated by sub-

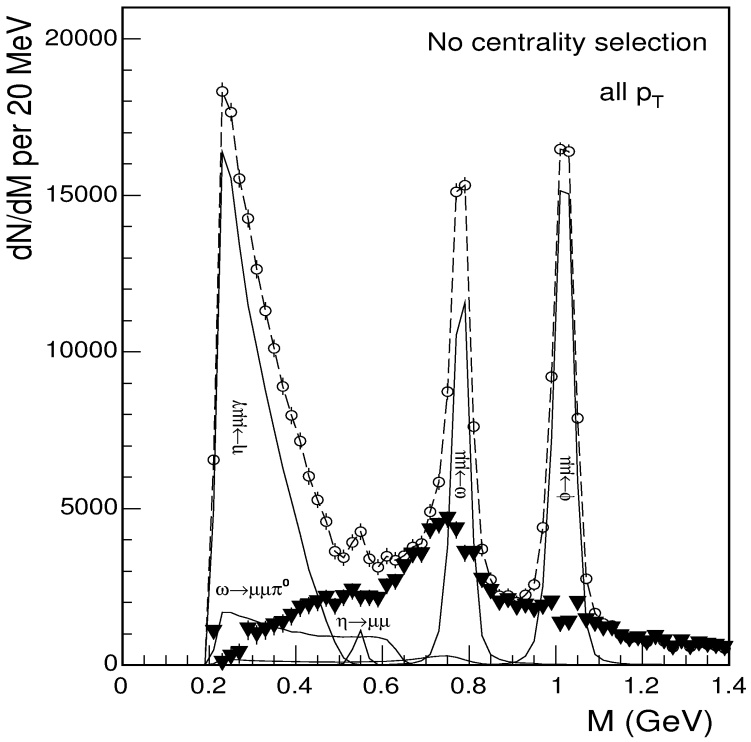

Figure 4.5: Di-muon invariant mass spectrum measured by the NA60 collaboration for In+In collisions at 158 GeV/A [121]. The open symbols are the data after background subtraction. The continuous lines represent the contribution from known sources except the ρ. The close symbols are the difference, yielding a shallow peak at the ρ mass.

tracting, in a conservative way, all known contributions, except the ρ, using the same GENESIS generator as CERES. The evolution of the enhancement with centrality is displayed in fig. 4.6. Two main features can be observed: a) for semi-peripheral collisions there is almost no enhancement as compared with free space (continuous line) and b) for the most central collisions, a strong enhancement is present but c) it remains clearly centered at the value of the ρ mass in free space. Such fact is therefore clearly in favour of a 'melting scenario'.

4.2.3 DLS

At a lower energy scale of the order of GeV, di-electrons from pseudo-vector mesons coming from the fire-ball were studied by the DLS collaboration at BEVALAC in the 90's [122], [123]. Whereas the invariant mass spectra obtained for p+p interactions could be reasonably well described by theoretical calculations neglecting *in medium* effects, a very distinct situation arose even in light systems as C+C and Ca+Ca at 1 GeV/A. Under such conditions neither calculations assuming free di-electron decays nor those including *in medium* effects could describe the observed spectra. In particular, an enhancement above

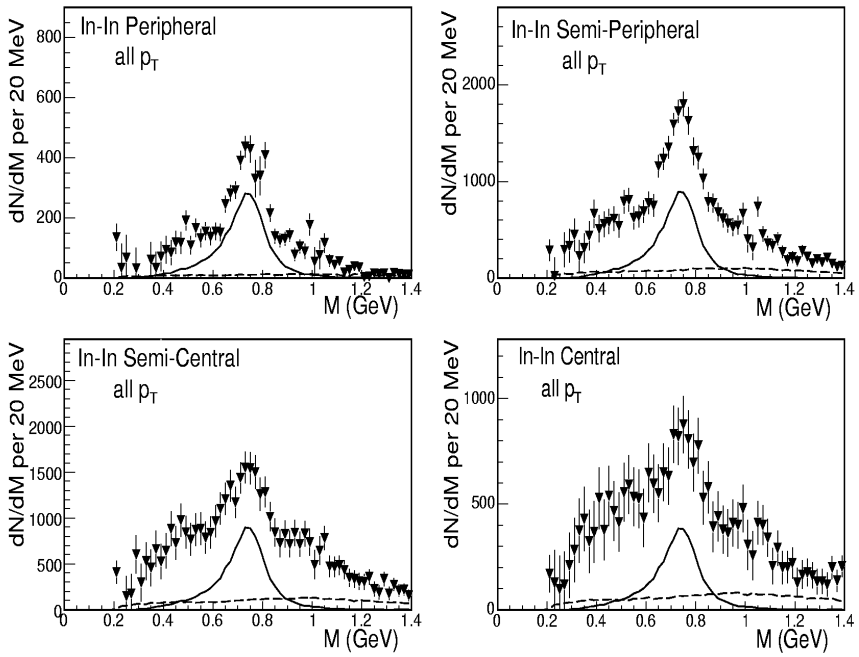

Figure 4.6: Evolution with centrality of the di-muon invariant mass enhancement estimated as for fig. 4.5. The continuous line is the contribution from the ρ with the same properties as in free space. The dashed line is an estimate of the open charm contribution [121].

a factor 2 was seen in the invariant mass region 150-500 MeV according to different transport models [124] (BUU) and [125] (RQMD).

The description given in [125] is shown in fig. 4.7, providing the best theoretical description achieved so far. However, a discrepancy of a factor 2 still remains unexplained in the intermediate invariant mass region. Since years, this unsolved discrepancy between experiment and model has been denoted as 'DLS puzzle'.

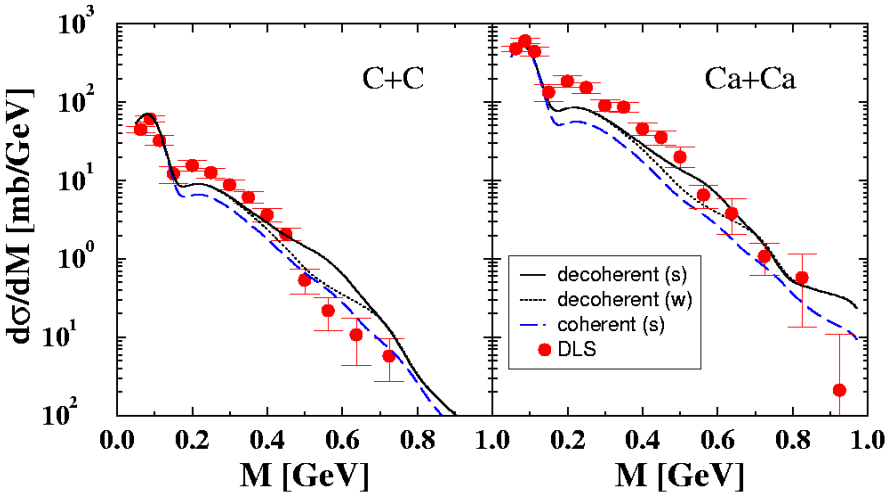

Figure 4.7: Invariant mass spectra obtained from C+C and Ca+Ca collisions at 1 GeV/A by the DLS collaboration, together with different theoretical descriptions [125].

4.3 The HADES experiment

In order to provide an answer to the 'DLS puzzle' and to further study *in medium* effects up to Au+Au collisions at $E_{kin} = 1.5$ GeV/A, the High Acceptance Di-Electron Spectrometer HADES was conceived and built at GSI, Darmstadt, Germany [95], [126]. Therefore, it is a second generation experiment in di-lepton spectroscopy that aims at measuring the invariant mass of the light pseudo-vector mesons ρ, ω, ϕ with precisions as good as $\Delta M/M = 1\%$ (10 times better than DLS) and an acceptance for e^+e^-pairs at the level of $\mathcal{A} = 35\%$ (100 times more than DLS) [95].

A high hadron rejection capability and tolerance to high rates is mandatory provided that the fraction of interesting di-lepton pairs is as small as 1 per million [127]. The technical specifications are that a primary beam intensity of $I = 10^8$ ions/s impinging over a target with a thickness equivalent to 1% interaction probability should be affordable by the experiment in terms of rate capability for Au+Au up to 1.5 GeV/A [95].

Fig. 4.8 shows an schematic view of the HADES spectrometer, where its characteristic hexagonal symmetry can be appreciated.

The story of an ion collision in HADES is as follows: (1) an ion beam comes from the SIS18 at typical energies $E_{kin} \simeq 1$ GeV/A and is deviated to HADES cave (coming from the left on picture 4.8); (2) before and after interacting with the target, a coincidence/anti-coincidence system (start/veto) provides a signal indicating that an interaction took place; (3) the outgoing sub-products cross a threshold RICH blind to hadrons; (4) high precision wire chambers (MDCs) track the particle before the toroidal coils of the magnet; (4) after the magnet, two more tracking MDCs are present and (5) a TOF wall is devised for lepton identification after the magnetic field; (6) at low polar angles a shower detector improves the rejection capability of fast pions.

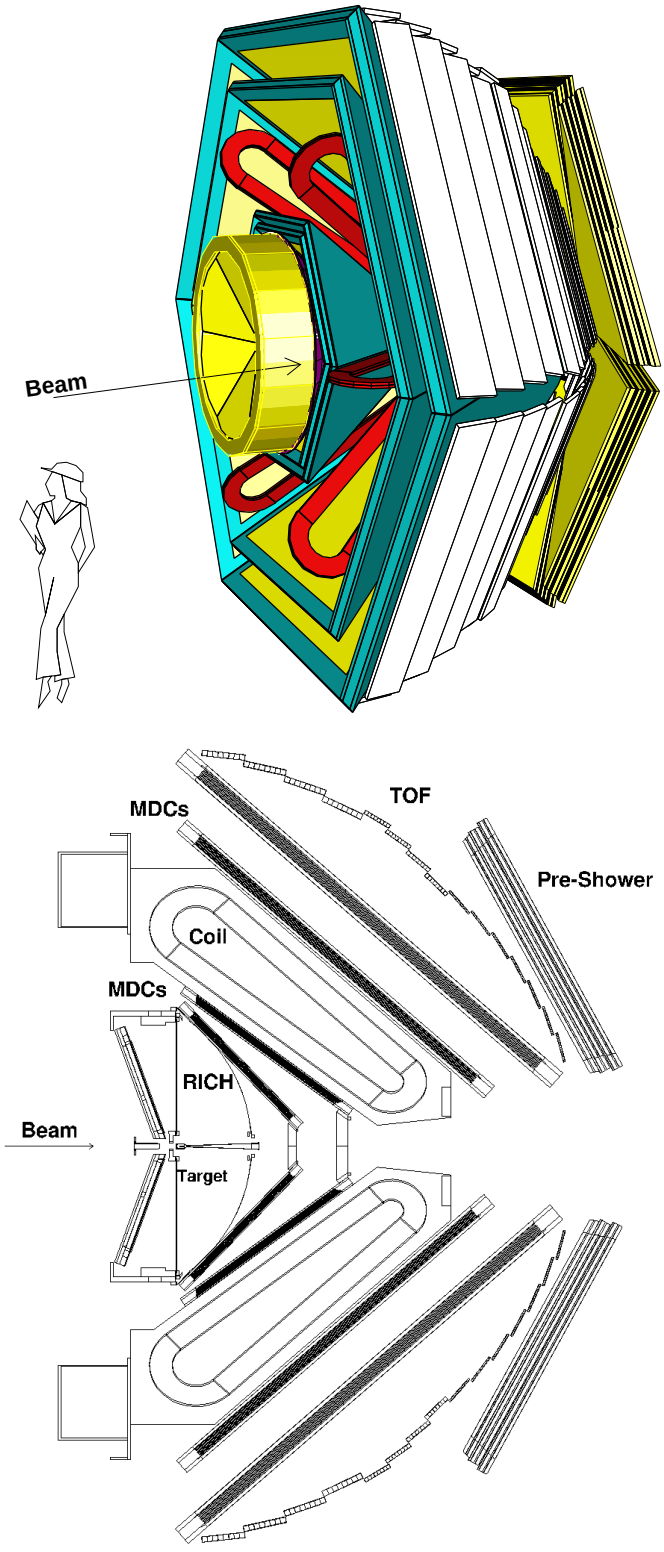

Figure 4.8: Up: 3D view of the HADES spectrometer. Down: side view, indicating the constituting detectors.

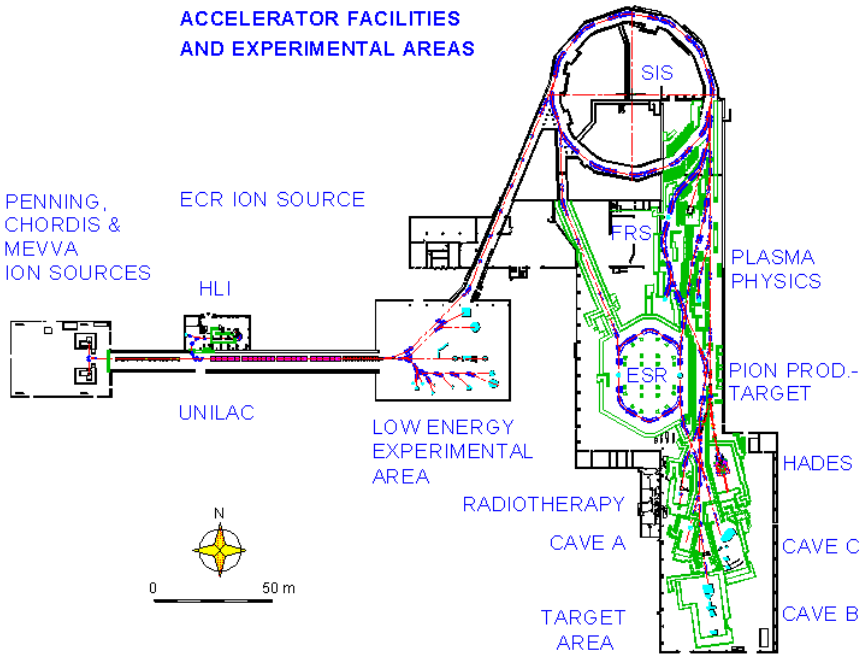

Figure 4.9: GSI's accelerator.

4.3.1 The SIS18 accelerator

The accelerator system consists in a linear accelerator (UNILAC) injecting ions into a 60 meter diameter synchrotron (SIS18), from where the beam can be extracted to the Fragment Separator (FRS), to the Electron Storage Rings (ESR) or to the experimental areas.

The UNILAC was built in 1975 and upgraded in 1999 thanks to the development of a new high current injector, called HSI. It provides an increase in the beam intensity that is able to fill the synchrotron up to almost its *space charge limit* for all ions ($I \simeq 10^{11}$ ions for C beam and $I \simeq 10^{9}$ ions for Au beam). After stripping and charge state separation, the beam from the HSI is matched to the UNILAC, which accelerates the nuclei (without any significant particle loss) up to a few MeV/A, feeding the SIS18.

The SIS18 consists in 24 bending magnets and 36 magnetic lenses, with a vacuum lower than 10^{-11} Torr in the beam line. The acceleration takes place in two resonance cavities diametrically opposed, reaching kinetic energies up to 2 GeV/A in the case of C beam and 1.5 GeV for Au beam. In order to reach the higher energies with Au beams, an exceptional operation is required: a) highly ionized Au atoms ($^{197}Au^{63+}$) are accelerated in SIS18 up to 0.3 GeV, b) then extracted and fully stripped, c) injected into the ESR and cooled by electron cooling, d) finally injected into SIS18 and accelerated up to 1.5 GeV/A. The length of the cycle is 25 s. However, typical operation allows for spills of 5-10 s duration with roughly 50% of duty cycle.

A picture of the current SIS18 is shown in fig. 4.9. There are prospects of an

imminent upgrade towards the so-called SIS100/300 within the project FAIR (Facility for Anti-proton and Ion Research). It will be able to ultimately reach intensities as large as $I \simeq 10^{12}$ ions/spill and energies up to 30 GeV/A for heavy ions [128].

4.3.2 The start and veto detectors

Two identical diamond detectors are placed 75 cm upstream (start) and downstream (veto) the target. The system is aimed at working such that a valid signal on start detector and null on veto results in a valid start signal, that must be delivered faster than 1 MHz[4]. The detector-electronics configuration yields a time resolution as good as 29 ps being rate resistant beyond 10^8 ions/s per channel for meeting the HADES requirements [129]. The detector is conceived to provide a veto efficiency $\varepsilon > 96.5\%$, over an area $A = 2.5$ cm$\times$1.5 cm (larger than the beam spot).

4.3.3 The RICH

The RICH [130] is the first detector found by the products of the primary interaction, as it is located surrounding the target. It is a crucial detector for lepton identification, being totally blind to hadrons while providing a very low multiple scattering and γ conversion probability, due to its gaseous low Z radiator, namely C_4F_{10} (the equivalent thickness x/X_o is at the level of 1%). The low refraction index of the radiator gas provides a threshold for Cherenkov emission $\gamma_{th} = 18.2$, sensitive to electrons with momenta above 10 MeV. On the other hand it is blind to pions up to energies of around $E_{kin} \simeq 2.5$ GeV, which is by far above the maximum kinetic energies available at SIS18. Therefore the hadron blindness is ensured.

The Cherenkov radiation is very softly attenuated by absorption within an UV window corresponding to $145 < \lambda < 190$ nm. The traversing UV photons are reflected on a spherical carbon fiber mirror (2 mm thick) to the back part of the system where they are detected. For this last step, the radiation gas is separated through a CaF_2 window from a multi-wire proportional chamber operated in pure CH_4. It has a pick-up pad structure placed behind a photosensitive CsI layer for enhancing the probability of photon detection. A typical ring-like pattern is at that point registered. For on-line trigger purposes (see section 4.3.7), the full event pattern information of 28272 pads must be transferred within 10 μs (100 kHz), allowing for ring identification capabilities at the level of 90%.

Fig. 4.10 shows a picture of the RICH detector.

4.3.4 The MDCs and the magnet

The Multi-wire Drift Chambers (MDCs) [129] are in total $2 \times 2 \times 6$ chambers, namely, two groups of two MDCs (before and after the magnet), 6 sectors, designed to provide track reconstruction before and after the magnetic field with space resolutions below 140 μm [131]. This extremely high position resolution

[4]Resulting from around 1% primary interactions at the maximum SIS18 intensity.

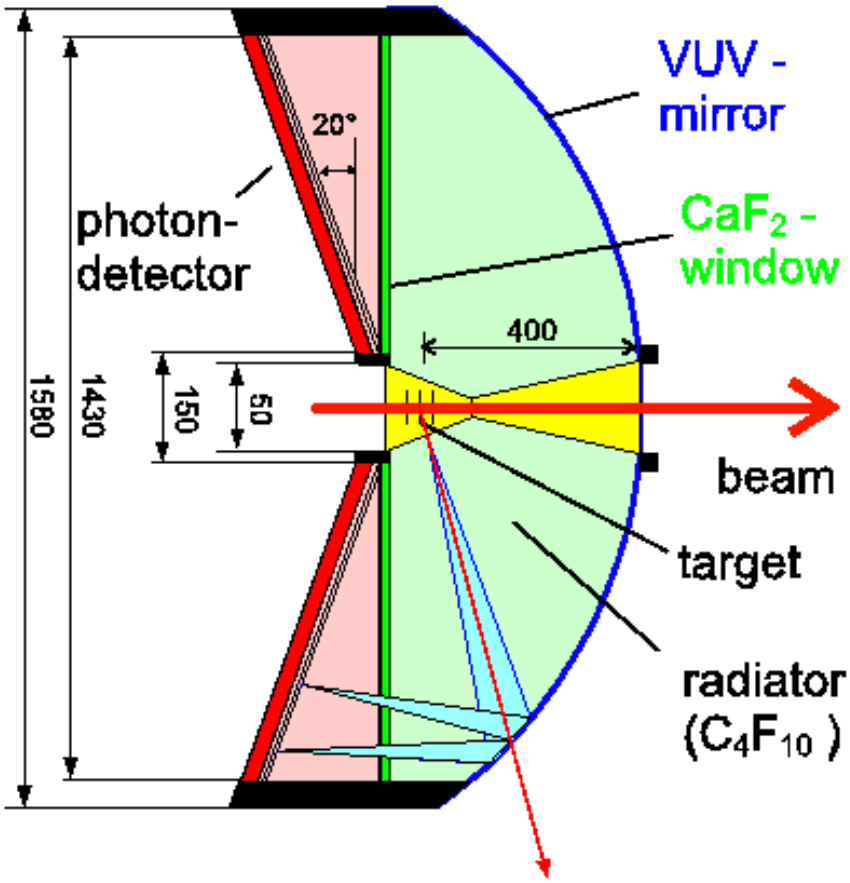

Figure 4.10: The RICH detector.

allows to obtain a momentum resolution $\Delta p/p \simeq 1\%$ and therefore $\Delta M/M \simeq 1\%$ for the invariant mass, fulfilling the requirements of the technical proposal[5].

Each chamber is constituted by six layers of sense wires at different angles, with cell sizes ranging from $5\times5\,\mathrm{mm}^2$ (inner plane) to $14\times10\,\mathrm{mm}^2$ (outer plane). A cell occupancy not larger than 30% was determined from simulated Au+Au central collisions at 1 GeV/A, as is necessary to cope with the ambiguities in track reconstruction.

In order to provide a high momentum resolution it is mandatory to minimize the effect of multiple scattering: it dominates the position resolution for momenta below 400 MeV. An adequate choice of the materials allowed to reduce the thickness of the chambers to $x/X_o = 0.2\%$, comparable with the contribution of the volume of air between the target and the outer MDC. The gas mixture used is based on He/iso-C_4H_{10}.

The MDCs are numbered starting from the target, downstream, therefore

[5]Not all the MDC chambers are fully installed yet and therefore the current momentum resolution is still at the level of $\Delta p/p \simeq 8\%$ [135].

I and II are the inner ones (before the magnetic field) and III and IV stand for the outer ones. In between, a superconducting magnet consisting of 6 coils, produces an inhomogeneous magnetic field which reaches a maximum value of $B \simeq 3$ T near the coils, down to $B \simeq 1.5$ T in the acceptance region.

The field is mostly confined to the region between the two groups of MDC chambers, whose frames are placed in the region corresponding to the shadow of the magnet coils (see fig. 4.8).

4.3.5 The TOF wall

TOF and TOFino are time of flight detectors aimed at providing a high resolution timing for separation of leptons from fast pions, and are required for implementing the multiplicity condition to select different centralities of the primary collisions.

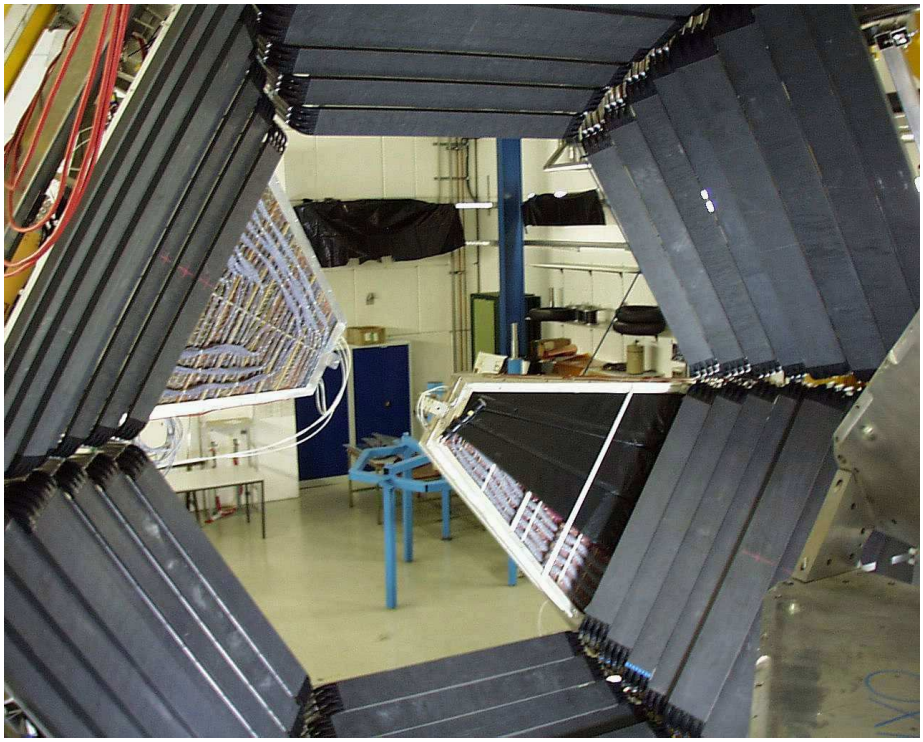

Figure 4.11: The TOF wall.

The TOF detector is made out of plastic scintillator rods (BC408) read at both ends by EMI 9133B photo-multipliers. Therefore, an unbiased estimate of the time of flight and impact position can be obtained, yielding $\sigma_T \simeq$ 100-150 ps and $\sigma_x \simeq$ 1.5-2.3 cm. The pad profile is a 2.0×2.0 cm^2 rectangle for the inner four sets and 3.0×3.0 cm^2 for those at larger polar angle. They are grouped in sets of eight, with eight such sets per sector, covering the laboratory polar angles $45° < \theta_{lab} < 85°$. A photo of the TOF wall is shown in fig. 4.11.

At polar angles below 45° the TOFino detector is temporary placed in order

to fulfill the minimum requirements that allow to explore light environments up to Ca+Ca, providing a reasonable multiplicity trigger still. TOFino is constituted by four scintillator rods with single read-out and time resolution $\sigma_T \simeq 350$ ps [132] after correcting for the position of the interaction (see fig. 4.12).

As said, in order to cope with the high multiplicities present in typical Au+Au collisions at 1.5 GeV/A, the TOFino will be replaced by a tRPC wall with a granularity 80 times larger and time resolutions well below 100 ps, being this the central subject of the present work.

4.3.6 The shower detector

According to [132], fast pions will emulate di-leptons (*fake*) by an amount of 2-3 per event in Au+Au collisions at $E_{kin} = 1$ GeV/A, for a time resolution of $\sigma_T = 100$ ps. The effect is reduced for the large polar angle region, where less than 1 fake per event is expected. Because of this fact, it was decided to place an electromagnetic shower detector behind the TOFino wall, in order to increase hadron rejection.

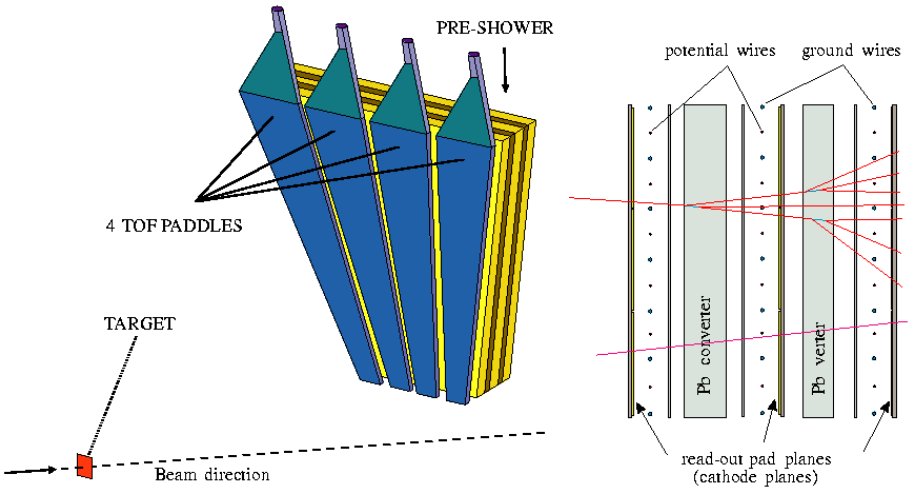

Figure 4.12: The shower detector and the TOFino [133].

Each sector of the shower detector is constituted by three sensitive planes of wire chambers with signal pick-up in pads of squared shapes, ranging in heights from 3 to 4.5 cm. The sizes ensure an occupancy below 5% for Au+Au collisions [133]. Between the active layers, two lead converters of thickness $2X_o$ each are interposed, aiming at inducing an electromagnetic shower with a high probability, but still keeping the probability of hadronic interaction at low levels. The interposition of lead converters defines naturally the so-called Pre-shower, Post-shower1 and Post-shower2 sub-detectors. Chambers are operated in Self Quenching Streamer mode.

The pads of the three modules are projected towards the target, resulting in a one-to-one correspondence between pads in a particular row and column in all three detectors. A 'shower condition' can be defined through the ratio of the

charge collected in each of the two Post-shower detectors to the one collected in the Pre-shower, allowing to identify leptons.

A picture containing the shower detector layout, together with the TOFino, is shown in fig. 4.12.

4.3.7 The trigger scheme

For primary intensities of $I \sim 10^8$ ions/s impinging over a 1% interaction probability target, 10^6 primary collisions per second must be handled. As said, the branching ratio for the di-electron decay of light pseudo-vector mesons is of the order of 10^{-4}, therefore most of the events are of no interest for di-electron spectroscopy. Moreover, processing all the event information corresponding to such a large number of primary collisions is impossible in practice. In order to enhance the 'interesting' events and reduce the collected data to a manageable set, a strategy based on 2 trigger levels is accomplished:

1. The *first level trigger* (LVL1) is given by a valid signal in the start/veto detector together with a multiplicity condition in the TOF+TOFino walls. It is expected from simulation that, in Au+Au collisions, this multiplicity/centrality condition leads to a selection of only 10% of the total number of collisions, reducing the rate of candidate events to 100 kHz.

2. The *second level trigger* (LVL2) performs a selection of lepton candidates by looking at any ring in the RICH that can be matched in an angular window with a hit in the system TOF+shower detector. A conservative window in time of flight is selected and a shower criteria applied [134].

   After the matching, the bending in the magnetic field can be estimated from the position information of the RICH and the shower detector, allowing for a cut in particle momentum; finally, electrons and positrons are combined. This task is performed in the Matching Unit (MU). For not losing events, the LVL2 decision must be taken in less than 10 μs, allowing for a reduction in the candidate tracks up to a factor 100, and yielding an event flow of 100 kHz. Recent results on C+C at 2 GeV/A with a conservative matching window, indicate a reduction of a factor 12, with 92% background rejection and efficiency above 70%.

4.3.8 Off-line analysis

Owing to its hadron blindness, the RICH is the key detector for lepton identification. Whenever it provides a ring, it is matched with a reconstructed track from the inner MDC planes within a certain angular window. Later on, and due to the absence of the outer drift chambers in the physics runs corresponding to the data analyzed so far, the position at TOF and Pre-shower is matched with a valid track. Finally, the shower condition is applied, plus an extra cut in time-of-flight. An illustrative example of this procedure, taken from [135], is shown in fig. 4.13.

The extreme capability of hadron rejection is apparent, being the average multiplicity of the lepton tracks as low as 2×10^{-2} per LVL1 event.

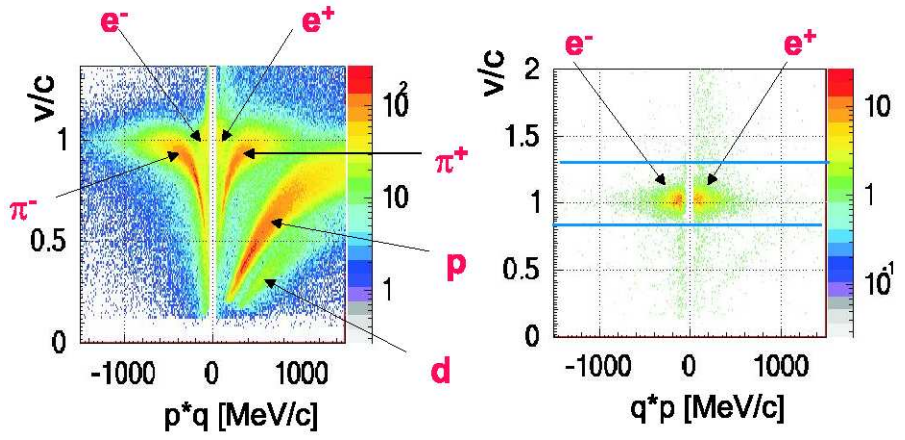

Figure 4.13: Left: β vs p distribution for all the reconstructed particles (LVL1). Right: the same plot after imposing all the cuts for rejecting hadrons. The last cut, namely, a cut in the time of flight of the particles, is graphically shown.

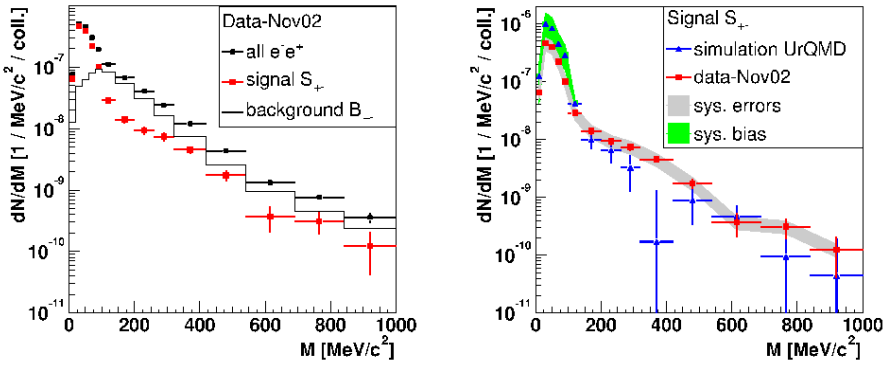

Figure 4.14: Left: contributions of the background and the signal to the invariant mass spectra. Right: invariant mass spectra of di-leptons and comparison with simulation [135].

4.3.9 The background rejection

Once lepton identification has been accomplished, the next step consists in making an adequate combination of e^+e^- candidates. However, a large fraction of the created e^+e^- pairs comes from γ conversion in the target and the RICH radiator but also π_o decays. Such pairs can be identified, in principle, because their relative angle of emission is very small. However, very often one of the leptons of a close pair is strongly bended by the magnetic field, leaving his companion free for randomly combine with other leptons, creating 'fake' pairs. 'The rejection of this combinatorial background is one of the most difficult problems in di-electron spectroscopy' [127], being required to devise adequate algorithms for reducing their contribution. The remaining fakes contribute to the invariant mass spectra as background, that is estimated from the spectra of like-sign pairs

and also using the event mixing technique, being subtracted afterwards.

The first distribution of e^+e^- invariant mass obtained in HADES for C+C collisions at 2 GeV, not corrected by acceptance and efficiency, is shown in fig. 4.14 after the close pair rejection algorithm is performed and the background is subtracted as mentioned above. The signal-to-background ratio is on average 4:1 for $M_{inv} < 100$ MeV/c^2 and 1:2 for higher masses. Latest results can be found in [136].

Chapter 5

The HADES tRPC wall

5.1 Introduction

5.1.1 Coordinate system and notation

The following lines are devoted to introduce the notation that will be thoroughly used within the present chapter. For that, in fig. 5.1 a lateral profile of one of the six HADES sectors is shown, with attention focused on the detectors close to the foreseen tRPC wall, namely: a) the outer drift chamber (MDC IV), b) the large angle scintillator TOF wall and c) the three planes of the shower detector. The values 12° and 45° have been extracted from the geometry implemented in the HADES simulation package[1].

Two reference systems can be distinguished:

1. The 'laboratory' reference system. Its origin is placed at the nominal target position (vertex), with Z defined along the beam axis, being positive in the downstream direction, and Y defined perpendicular to the floor, upwards. The variables referred to that system will be denoted in capital letters and labeled with 'lab'. The HADES geometric acceptance in this reference system can be expressed in spherical coordinates as:

$$18^\circ < \theta_{lab} < 85^\circ \tag{5.1}$$

   together with roughly 360° coverage on the azimuthal coordinate, grouped in six sectors: $30^\circ < \phi_{lab} < 90^\circ$, $90^\circ < \phi_{lab} < 150^\circ$, ... , $-30^\circ < \phi_{lab} < 30^\circ$ $(1, 2, ..., 6)$.

2. The 'local' tRPC reference system. For designing purposes, it is very useful to speak about local coordinates, that will be denoted in lower case, without label, in the following. Taking, for simplicity, the sector 1 ($30^\circ < \phi_{lab} < 90^\circ$), the origin of the local reference system can be defined by the intersection of three planes: a) the Y_{lab}-Z_{lab} plane (y-z plane), b) a plane parallel to the larger face of the shower detector, placed at the tRPC position (x-y plane), and c) the plane perpendicular to the y-z and x-y planes that contains the vertex (x-z plane); the z axis is defined to be

[1] In particular, they were obtained from the limits of the active volume of the TOFino wall that is placed temporary at the tRPC position.

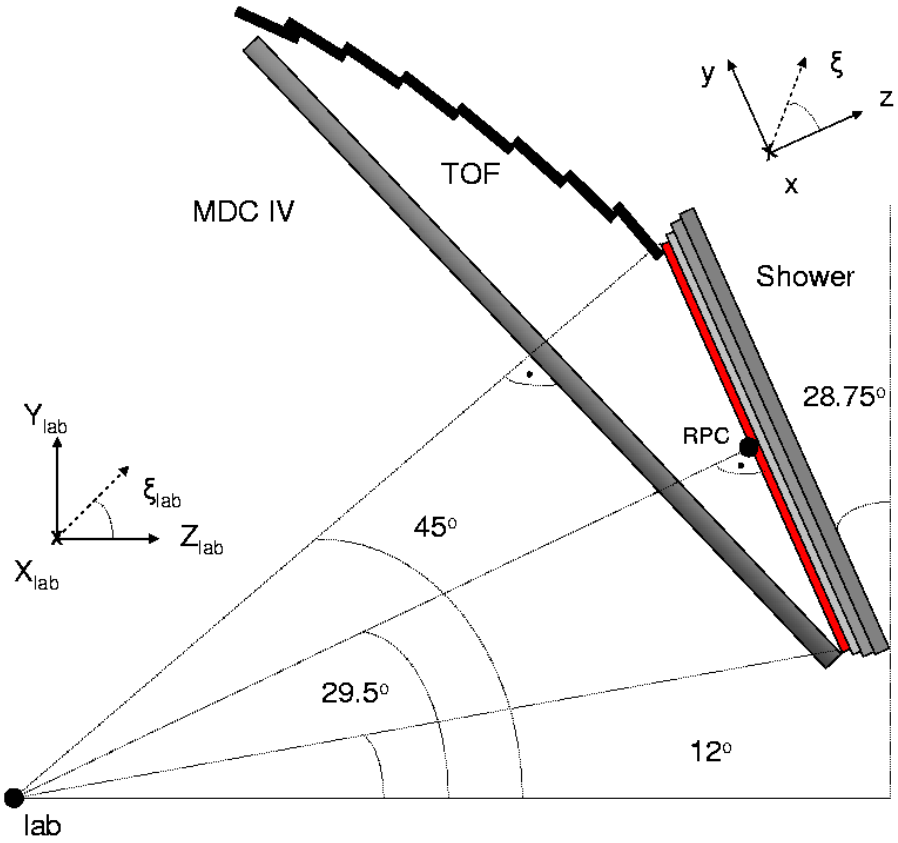

Figure 5.1: Reference system and conventions used in this chapter.

positive in the region tRPC downstream and y is positive in the direction of increasing θ_{lab}.

The origins of the two reference systems are represented by circles in fig. 5.1.

It is shown in the following that the tRPC wall must cover, indeed, polar angles θ_{lab} from 12° to 45° in order to meet HADES geometric acceptance. The small angle 12° (see eq. 5.1) arises from the necessity to measure positive charged tracks that are bent towards low θ_{lab}.

It is very useful to define the angle projected over the y-z plane. This is defined for any track as the angle between the z axis and the projection of the track over the y-z plane. It is denoted by ξ and can be expressed in spherical coordinates as:

$$\tan\xi = \tan\theta \sin\phi \tag{5.2}$$

$$\xi \simeq \theta \sin\phi \tag{5.3}$$

and an analogous definition for the case of ξ_{lab}.

5.1.2 Specifications of the TOF wall

The process of optimization of a large detector can be defined as a multi-variable problem that provides *a feasible compromise between physics requirements and detector performances*. Some of the implications of this observation must be noted:

1. Several designs and even technologies may fulfill the same physics requirements, providing different choices for optimization.

2. Optimization can evolve in time owing to any change in the physics requirements or in the detector performances.

3. The key word in any realistic design is *feasibility*. An optimum solution must be, implicitly, feasible.

For understanding the process of optimization followed in this work, it must be recalled that the physics requirements were discussed elsewhere, along earlier studies about the feasibility of the HADES spectrometer itself [95], [132], [139], but also more recent discussions will be explicitly mentioned when necessary. Such physics requirements will *not* be revisited in this work, but simply compiled within the following paragraphs.

The design of the HADES-TOF wall at low angles must be optimized for handling the highest rates and multiplicities foreseen at the HADES spectrometer, for the maximum energies available at SIS18[2]. On one hand, this means that the wall must be operational for Au beam intensities up to $I = 10^8$ ions/s impinging over a Au target with 1% interaction probability, according to the technical proposal [95] (a requirement that was later relaxed down to $I = 2\ 10^7$ ions/s, because of technical reasons [140]). On the other hand, the detector must have enough granularity to cope with the highest multiplicities foreseen (central Au+Au collisions[3] with a kinetic energy $E_{kin} = 1.5$ GeV/A [4]). Technical specifications [95] suggest an occupancy per cell at the level of 20%, but later on it was adviced to go below 10% for lepton detection [141]. Requirements concerning granularity and rate capability are completely different in essence: while the first one can be always virtually met by increasing the total number of cells, the second one must be provided by the TOF technology used: for glass timing RPCs, rates higher than 500 Hz/cm^2 in long spills are hardly reachable without a sizable degradation of the performances, and *more cells will not improve the situation*.

Other 'important' requirements that the TOF wall must fulfill are:

1. High time resolution ($\sigma_T \simeq 100$ ps) for separating e^+e^- pairs from fast pions [132], [139].

2. Robust multi-hit capabilities.

3. High geometric acceptance, close to 100%.

[2] The performances at higher energies, as expected in SIS100, are briefly discussed at the end of the chapter.

[3] 'Central' is defined in the following by the condition $b < 4$ fm for Au+Au collisions, corresponding to the 5-10% of more central events.

[4] 1.5 GeV/A is the larger energy attainable for heavy systems at SIS18, 2 GeV/A can be achieved in lighter systems due to the larger Z/A ratio.

4. High intrinsic efficiency, close to 100%.
5. Highly unbiased multiplicity estimate for centrality selection on the primary collisions.
6. It must not affect the detectors placed tRPC downstream.
7. It must fit to the available space.
8. It must be equipped with fast, low noise, compact and robust FEE for operating a large number of channels under stable conditions (the status of the electronics can be found elsewhere [87]).

At last, other 'interesting' features of the TOF wall would be:

1. Low cross-talk.
2. Easy cabling.
3. Possibility of providing isochronicity of the tRPC cells through intercomparisons between them.
4. Possibility of providing isochronicity of the tRPC cells through intercomparisons with other high resolution timing detectors (Start detector and/or TOF wall at large angles).
5. Moderate tails towards delayed times.

The results concerning the estimate on the timing required for lepton identification can be found in [95], [132], [139]. There, a value for $\sigma_T = 100$ ps is derived, based on studies with Au+Au central collisions. For the sake of consistency, some basic figures about particle identification capabilities based on tof will be provided: the time of flight of a particle traveling along a distance L is related to its momentum through:

$$t = \frac{E}{pc} L = \frac{L}{c} \sqrt{1 + \left(\frac{mc}{p}\right)^2} \tag{5.4}$$

When measured over the same distance L, the tof of two particles (1, 2) with masses m_1 and m_2 will differ by an amount δt, according to:

$$\delta t = \frac{L}{c} \left(\sqrt{1 + \left(\frac{m_1 c}{p}\right)^2} - \sqrt{1 + \left(\frac{m_2 c}{p}\right)^2} \right) \tag{5.5}$$

Let's assume that the tof measurement is performed by a detector with a Gaussian time response of width σ_T: the degree of admixture $k = \delta t / \sigma_T$ can be therefore defined. It is shown in fig. 5.2 that, as long as $k \gtrsim 2$, it is possible to resolve the contributions of both peaks. If, for illustration, the criteria for belonging to each respective population is defined at the intersection between both distributions, the detection efficiency and degree of admixture can be obtained:

$$k = 2 \qquad \text{eff} = 84\% \qquad \text{admixture} = 16\% \tag{5.6}$$

$$k = 4 \qquad \text{eff} = 97.5\% \qquad \text{admixture} = 2.5\% \tag{5.7}$$

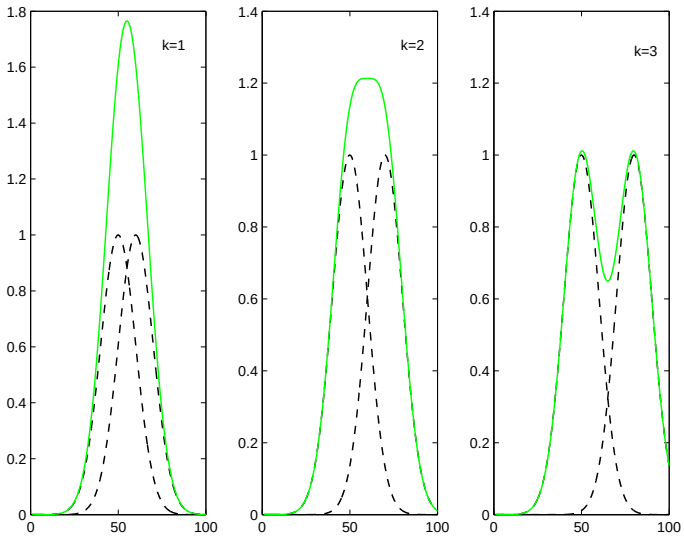

Figure 5.2: Example of the admixture of two Gaussian distributions as a function of the mathematical definition of admixture $k = \delta t/\sigma_T$.

that are, indeed, complementary probabilities. Eq. 5.5, together with the admixture $k = \delta t/\sigma_T$, allows to define the momenta $p_{threshold}$ at which a certain degree of admixture is present, as a function of the time resolution of the detector, for different species of interest (fig. 5.3). The interpretation of the admixture acording to eqs. 5.6, 5.7 is true whenever the populations of both species are the same, that is not the present case. A final evaluation of the PID capabilities requires to perform a full simulation [95],[139].

5.1.3 Simulation

In the following, the event generator URQMD(1.2) [142] was used for describing nucleus-nucleus collisions, and the outgoing products are propagated through the HADES spectrometer (implemented with the HGeant/Geant transport code [137], [138]), finally producing a distribution of particles over a plane at the tRPC wall position. This 'virtual' plane has been defined to be parallel to the plane of pads of the Pre-shower detector, but having a larger active area and being placed few cm upstream in the direction perpendicular to the Pre-shower. The choice of this 'virtual' plane is natural since: a) both detectors will be mechanically attached to the same frame and b) the tRPC+Pre-shower set must provide the same acceptance that the Pre-shower alone; therefore, the active area of the tRPC was chosen to be larger than the one of the Pre-shower, in a first approach, and later reduced as much as possible to fit to the Pre-shower acceptance (section 5.2.1).

Depending on the purpose, different simulations were performed:

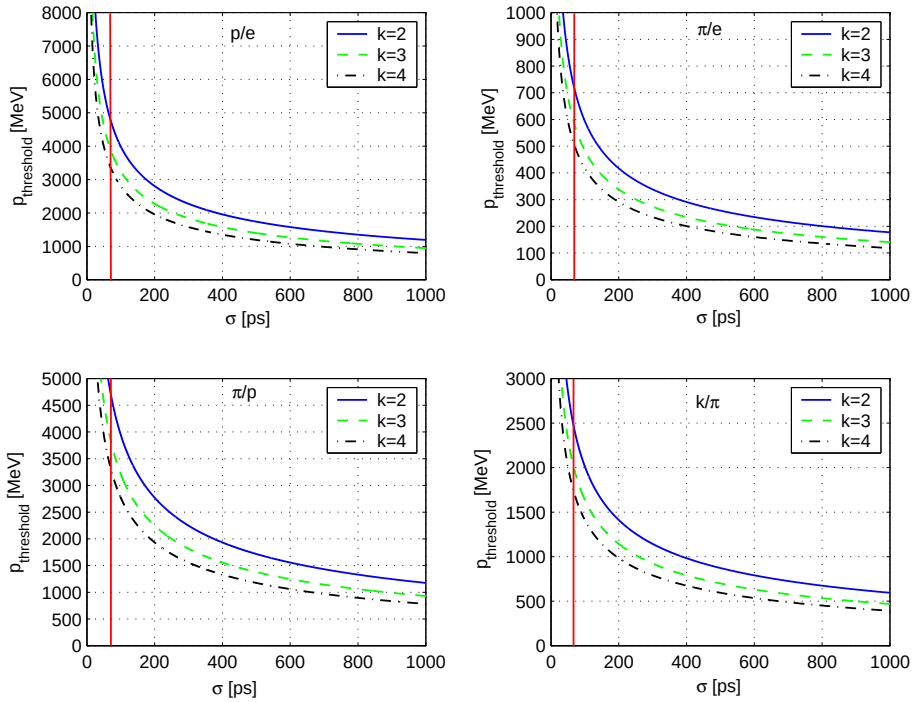

Figure 5.3: Threshold momenta as a function of the time resolution for HADES-TOF lever arm ($L \simeq 2.3$ m), considering different degrees of admixture and different typical cases. The vertical line stands for $\sigma_T = 80$ ps.

For *physics studies*:

1. 10^3 central ($b < 4$ fm) Au+Au collisions[5], $E_{kin} = 1.5$ GeV/A, magnetic field scaled down to $B = 0.72 B_{max}$, with B_{max} providing a maximum value of $B \simeq 1.5$ T in the acceptance region[6]. The target is considered to be point-like and the geometry of the spectrometer is the standard one (no misalignments), being denoted as 'ideal geometry' from now on.

2. 10^3 minimum biased Au+Au collisions at an intensity $I = 2\ 10^7$ ions/s, point-like target of thickness equivalent to 1% interaction probability, $E_{kin} = 1.5$ GeV/A, $B = 0.72 B_{max}$, ideal geometry.

   'Minimum biased' means that the collisions are considered at all possible impact parameters, weighted proportionally to b.

For studies on *geometric acceptance*:

1. 10^6 e^+e^- pairs were generated, according to an isotropic distribution in the laboratory system ($0 < \theta_{lab} < 90$) and flat in $1/p$ from $p = 100$ MeV to 1000 MeV (mass of the ϕ) and propagated along a magnetic field $B = 0.72 B_{max}$.

[5] Approximately $2\ 10^5$ tracks over the tRPC.
[6] $B = 0.72 B_{max}$ is the typical field used so far in HADES.

In order to explain the reasons for selecting this distribution, let's define $\Delta\eta$ as the variation in angle suffered by a particle having momentum p in a magnetic field B. As shown in [143], [144], in a first approach both magnitudes are related through:

$$p \propto \frac{1}{2\sin(\Delta\eta/2)} \simeq \frac{1}{\Delta\eta} \tag{5.8}$$

Therefore, an uniform distribution in $1/p$ provides roughly all possible deflections $\Delta\eta$ within the HADES acceptance, with equal weight for all of them.

In the following, the three simulations described will be denoted as *central*, *minimum biased* and *all tracks*.

The software digitizer

Usually it is denoted by *digitizer* a 'dictionary' that allows to go from the distribution of particles over a detector, as obtained from a physics simulation package, to a realistic situation, after taking into account the detector response (see fig. 5.4).

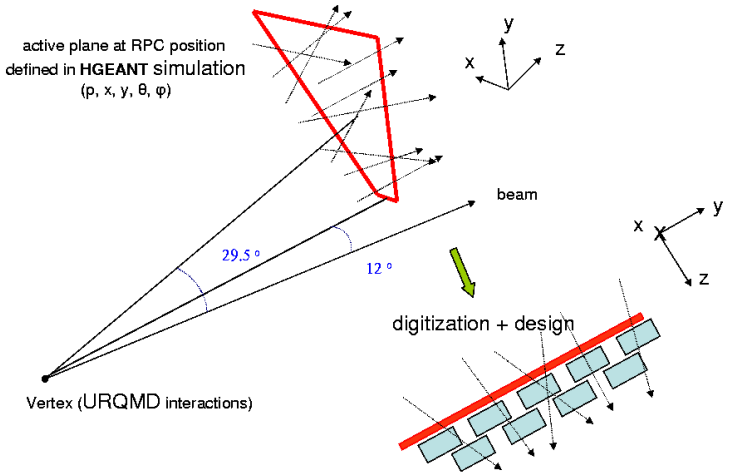

Figure 5.4: Scheme of the 'simulation plus digitization' in its present stage. It must be noted that digitization and design are performed in a single step.

The digitizer assumes that each tRPC cell is constituted by 4 gaps with an efficiency $\varepsilon = 0.75/\text{gap}$ (for MIP's [68]) with independence from the position of the cell, the inclination of the particles, and the primary ionization. These assumptions can be considered as reasonable due to the small dependence of the performances on the primary ionization (see section 3.2.4), and assuming that edge effects can be neglected.

The efficiency was assumed to be $\varepsilon = 1/\text{gap}$ for hadrons and $\varepsilon = 0.75/\text{gap}$ for leptons in order to provide a 'worst case' scenario regarding lepton detection. The time and position resolution were not implemented in the digitizer for present purposes, and they will be explicitly mentioned when necessary.

5.2 Characteristics of the tRPC wall

5.2.1 Determination of the tRPC wall acceptance

The geometric acceptance of the HADES spectrometer at the tRPC position has been defined by generating *all possible tracks* over it, as described in previous section, imposing the condition that such tracks provide a valid hit in all the MDCs[7] and the Pre-shower (ideal MDC and Pre-shower response is therefore assumed).

The distribution obtained over the tRPC is shown in fig. 5.5. As said, the tRPC area has been chosen in simulation to be larger than the active area of the Pre-shower detector. In the left side of fig. 5.5, the distribution of *all tracks* over the tRPC can be seen, while, in the right side, the same distribution is shown after imposing the condition of having a valid hit in the 4 MDC planes and the Pre-shower, therefore defining the limits of the geometric acceptance at the tRPC position.

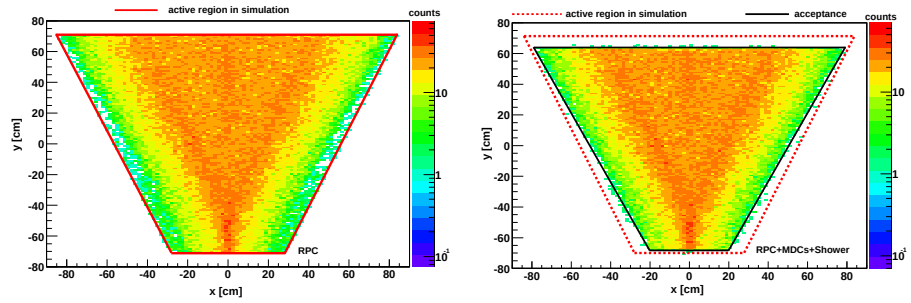

Figure 5.5: Left: figure showing the area illuminated for acceptance estimates under a primary distribution that contains all the possible tracks within the spectrometer. Right: the same distribution as in left but requiring a valid hit in all the drift chambers and the Pre-shower, providing an estimate of the acceptance at the tRPC position (thick line).

In order to account for possible, unavoidable, displacements of the HADES detectors, it may be required to adopt the conservative assumption of covering an area larger than the true tRPC acceptance. For evaluating such possibility, the HADES geometry obtained from the November 2002 beam time after alignment of the detectors[8], was implemented in simulation and the acceptance obtained is shown in fig. 5.6 (left) together with the estimate for the case of ideal geometry. The only effect of such misalignments seems to be related, indeed, to a small decrease of the geometric acceptance at the tRPC position: therefore the ideal geometry provides a conservative upper limit to the acceptance.

Fig. 5.6 also shows (lines) the acceptance estimated from Au+Au central collisions at 1.5 GeV/A, defining essentially the same acceptance that fig. 5.5. In particular, the distribution of *all tracks* has lost the azimuthal symmetry. This effect can be explained by a sizable magnetic kick over the azimuthal angle that bends the low p tracks towards the middle of the sector. The depletion at low polar angles θ_{lab} in the case of the Au+Au distribution is created by the

[7] This is done by requiring a hit in each of the 6 wire planes of the 4 MDC chambers.
[8] Software alignment.

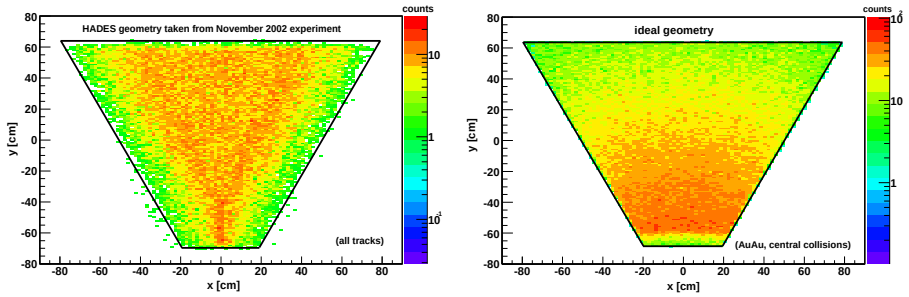

Figure 5.6: Left: distribution of *all tracks* over the tRPC plane for the HADES geometry present in the November 2002 experiment. Also shown (lines) the geometric acceptance estimated for the ideal geometry (statistics are a factor 3 smaller than in fig. 5.5). Right: distribution corresponding to Au+Au central collisions after imposing the condition of valid hit in MDCs+Pre-shower. The distribution obtained lays in the acceptance (lines), as expected.

presence of the MDC frames.

The dimensions of the HADES geometric acceptance obtained from fig. 5.5 are shown in fig. 5.7, together with its position in the 'laboratory' reference system. For design purposes, the following convention is adopted: *the geometric acceptance is defined at the plane of the foreseen last gap of the tRPC in the downstream direction.*

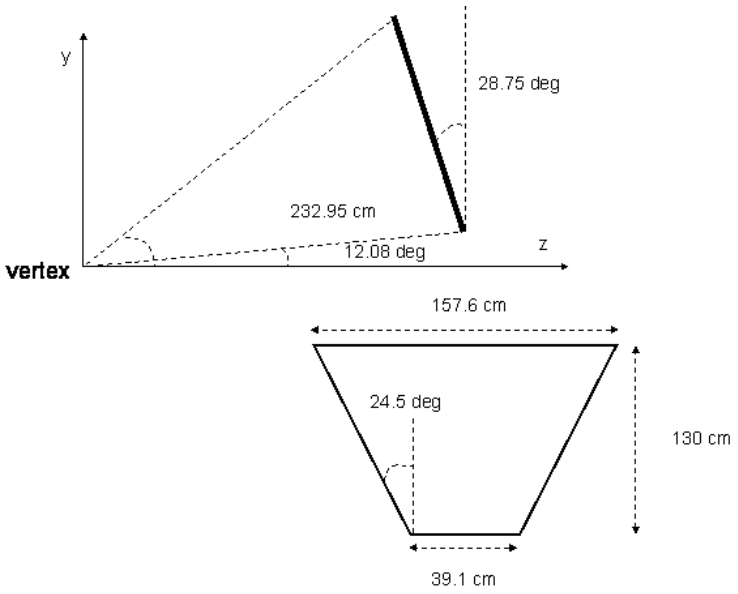

Figure 5.7: HADES acceptance at the tRPC in the laboratory reference system.

There is a natural question on how to distribute the cells over the tRPC acceptance. The coverage can be accomplished, for example, with a) vertical or b) horizontal strips, or c) squared cells, d) having different orientations with

respect to the impinging particles, placed on e) one or f) several layers. Here, using the knowledge accumulated in previous studies [139] and [145], an approach based on an array of long cells extended along the x direction will be followed. The benefits are, among others, a high homogeneity of the distribution of particles over the cell, due to the approximate azimuthal symmetry, and the possibility of placing the FEE (Front End Electronics) under the shadow of the magnet coils (the region close to the slanting sides of the trapezium that defines the acceptance).

Having this in mind, the distributions of interest over the tRPC, regarding occupancies and primary rates, will be expressed as a function of the y coordinate, after integrating (or averaging) over the x coordinate. As mentioned, the expected large homogeneity of the distributions of particles as a function of x justifies the approach.

5.2.2 Rate of particles

The primary intensity considered is $I = 2\ 10^7$ ions/s, corresponding to the maximum value expected in HADES for a heavy ion environment. The interaction probability in the target is set to 1% according to HADES proposal [95] and primary minimum biased Au+Au collisions at 1.5 GeV/A are transported. The rate expected at the tRPC wall as a function of y (averaged over x) is shown in fig. 5.8.

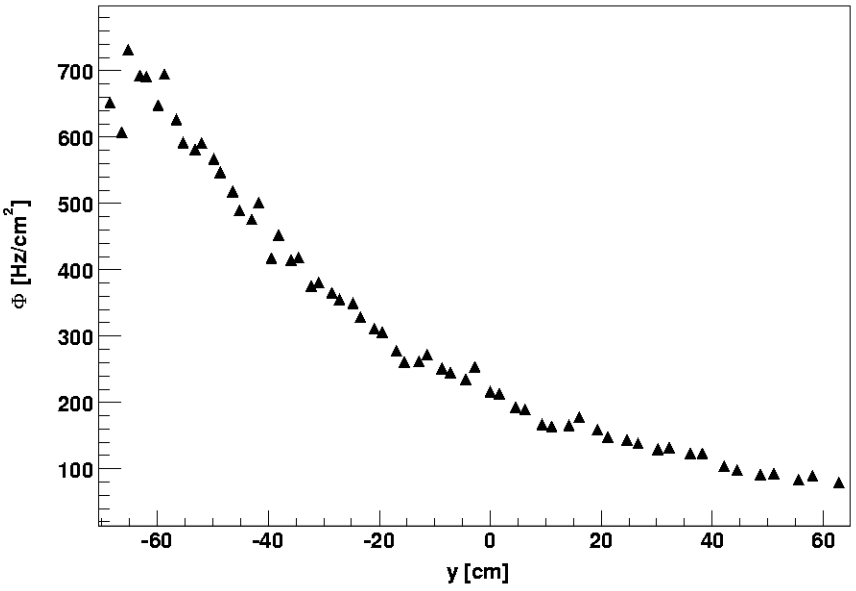

Figure 5.8: Rate over the tRPC wall for the most unfavorable environment expected in HADES: minimum biased Au+Au collisions, E_{kin} = 1.5 GeV/A, $I = 2\ 10^7$ ions/s, P_{int}=1%, B =0.72 B_{max}. A maximum value $\Phi = 700$ Hz/cm^2 is reached at the lower polar angles.

It can be observed that the distribution is peaked towards low values of y (low polar angles θ_{lab}) due to the Lorentz boost. The strong dependence of the

rate with y[9], suggests that different kind of tRPCs could be used within the same experiment [98], for the coverage of different polar angles.

According to previous works on glass timing RPCs (for instance [47], [147]) and chapter 6, the expected maximum rate ($\Phi \simeq 700$ Hz/cm^2) is already at the limit where glass timing RPCs can offer good performances. The implications of such a worsening are quantitatively discussed in the next sections.

Frequency of particles

Besides the rate limitation, that has to do with the accumulation of charge over the resistive plates (see section 3.2.7), working at high rates also results in an increased probability of piling-up of the tRPC signals. For an estimate of the effect, it must be recalled that the tRPC signal extends in time up to around $\Delta T_{signal} \sim 1$ μs, mainly due to the ion tail. Therefore, if the frequency of hits over the tRPC cell is higher than $1/\Delta T_{signal} \sim 1$ MHz, the pile-up becomes sizable, resulting in a worsening of the timing performances. For the highest rates expected at low polar angles ($\Phi = 700$ Hz/cm^2) and the typical cell sizes foreseen for that region (around 15×2 cm^2) [10], the frequency of hits is kept as low as 0.020 MHz, that guarantees a safe operation with pile-up at the level of 2%. In case of higher frequencies of hits, the possibility of filtering out the ion tail should be considered.

5.2.3 Occupancy

The average number of tracks over the tRPC acceptance per primary interaction per unit length (namely, the occupancy density) along the y direction is shown in fig. 5.9. It has been obtained for the highest multiplicity scenario expected in HADES under current SIS18: central Au+Au collisions at $E_{kin} = 1.5$ GeV/A, yielding $N = 30 \times 6$ charged particles over the tRPC wall.

According to fig. 5.9, HADES requirements of 10-20% occupancy per cell can be fulfilled, at low y, by strips having widths in the range 3-6 mm. A similar approach has been followed by FOPI experiment, where the pick-up electrodes are segmented by long strips of 3.44 mm pitch; however, the large cluster sizes observed require dedicated multi-hit studies [148]. The cluster sizes can be reduced virtually to one by working with electrically isolated tRPC cells, but the feasibility of producing long cells with sub-cm widths is mechanically questionable.

So, it was decided to keep the cell width at the cm scale, and the required occupancy levels can be met by an additional segmentation of the sector in small sub-sectors or petals (in fig. 5.10 different possibilities are illustrated). Moreover, the advantages of a moderate segmentation (therefore wider cells), are considerable, as shown in sections 5.2.4 and 5.3.2.

Each segmentation produces an inefficient region due to the separation between the tRPC petals, that reduces the geometric acceptance; therefore a large number of petals is not advisable. On the other hand, by symmetry, an even-fold segmentation places an inefficient region at the middle of the sector, a zone where a fraction of the low momentum particles is strongly focused at the

[9] A factor $\times 10$ reduction is observed from the lower value of y ($\theta_{lab} \sim 12°$) to its maximum value ($\theta_{lab} \sim 45°$).

[10] See next sections.

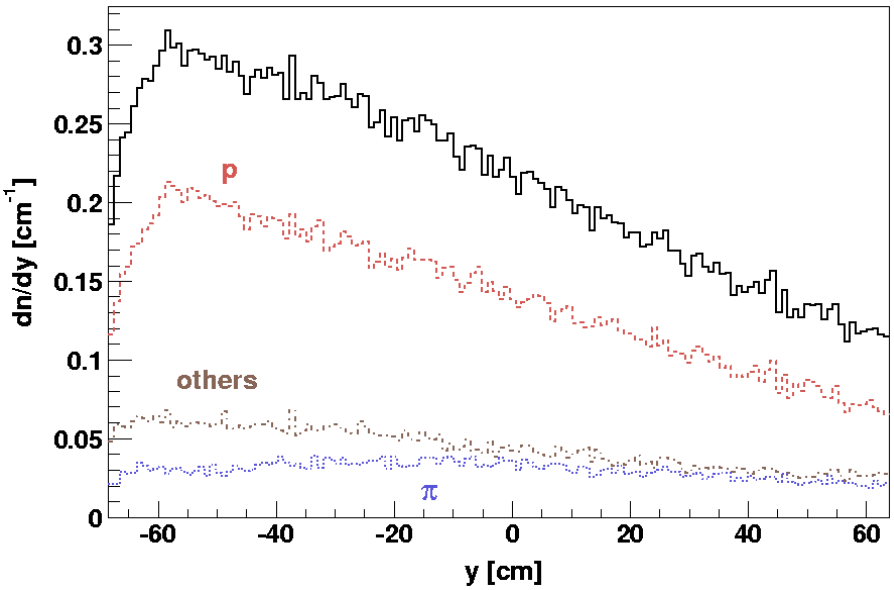

Figure 5.9: Occupancy density on the tRPC wall (full line) for the highest multiplicity environment expected in HADES: central Au+Au collisions ($b < 4$ fm), $E_{kin} = 1.5$ GeV/A. The contributions of protons (dashed), pions (dotted) and others (dash-dotted) are shown, being the latter dominated mainly by electrons. The reduction of the number of protons at low y is caused by the MDC frames.

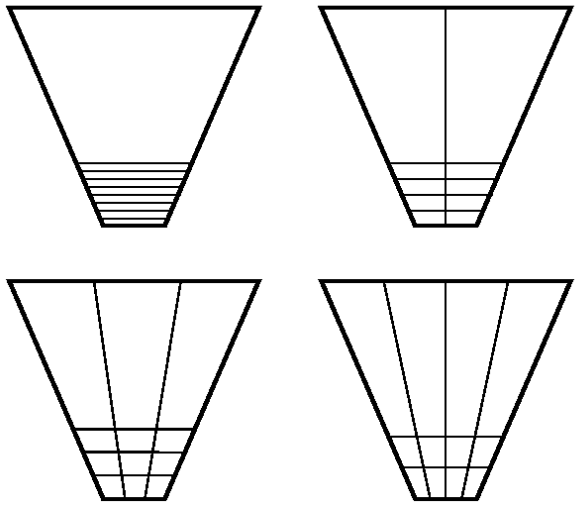

Figure 5.10: Natural segmentations in 1-4 petals, that keep constant the area of the cell and provide, in a first approach, equivalent occupancies (and granularities) of the tRPC wall.

tRPC plane (see section 5.2.4 and also [143]) due to the inhomogeneities of the magnetic field.

The interpretation of the occupancy

For low occupancies, and assuming that the positions of the particles over the tRPC are not correlated among themselves, the statistical distribution of tracks over a region Δy at the tRPC follows Poisson statistics. Therefore, by taking the average occupancy of the cell $n = \frac{dn}{dy}\Delta y$, the probability that the cell is empty (P_o), that it has 1 hit (P_1), etc, can be defined:

$$P_o = e^{-n} \simeq 1 - n \tag{5.9}$$

$$P_1 = ne^{-n} \simeq n(1-n) \tag{5.10}$$

$$\dots$$

$$P_k = \frac{n^k e^{-n}}{k!} \simeq \frac{n^k}{k!}(1-n) \tag{5.11}$$

Due to expression 5.9, the probability that the cell is occupied (1-P_o) is often approximated by the average occupancy n. While the last has no upper bound, the former is a true probability, taking values between 0 and 1.

Number of electronic channels

In a one layer design, once the maximum assumable occupancy is imposed by the experiment requirements, the number of required cells becomes a fixed number; it is just a geometric (and technical) problem to chose the adequate arrangement and the shapes of the cells. Furthermore, the details of the occupancy density become irrelevant for calculating the total number of electronic channels.

Let's assume, for illustration, the numbers coming from the simulation of central Au+Au collisions at 1.5 GeV/A: $N = 30$ charged particles over each sector of the tRPC wall. It must be recalled that simulations at a lower energy $E_{kin} = 1$ GeV/A and $b = 0$ provide $N = 20$ [139], [145]. If the occupancy is set to 20% being uniform over the wall, the number of required cells can be obtained as:

$$N_{cells} = 6 \text{ sect} \times 20/0.2 = 600 \quad \text{Au+Au, } b = 0 \text{ fm, 1.0 GeV/A} \tag{5.12}$$

$$N_{cells} = 6 \text{ sect} \times 30/0.2 = 900 \quad \text{Au+Au, } b < 4 \text{ fm, 1.5 GeV/A} \tag{5.13}$$

Using a double-end read-out for having unbiased estimates of the time-of-flight, *1800 electronic channels* would be required (and 1200 at 1 GeV, in qualitative agreement with earlier proposals [139] (1440 channels) and [145] (1320 channels)).

5.2.4 Number of petals

Different possibilities of segmentation will be discussed, through the study of three effects: *volume effects*, *double hits* and *azimuthal magnetic deflection*. The first two are general issues, while the third is characteristic of the HADES magnetic field.

Volume effects

The requirements that allow to neglect the thickness of the detector for occupancy calculations can be extracted by looking at the situation illustrated in fig. 5.11. An active volume with dimensions $d \times D \times w$ (thick, long, wide) and an average angle of incidence ξ, projected over a plane parallel to the face $d \times w$, have been assumed. In that simple case, the *volume effects* can be evaluated through the ratio of the particles impinging from the side to the particles impinging on the surface:

$$n = \frac{dn}{dy} w \tag{5.14}$$

$$n_{side} = \frac{dn}{dy} d|\tan\xi| \tag{5.15}$$

$$\frac{n_{side}}{n} = \frac{d}{w}|\tan\xi| \tag{5.16}$$

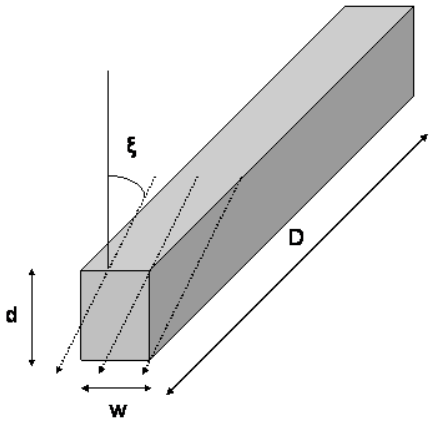

Figure 5.11: Simplified situation where the volume effect, namely the fraction n_{side}/n, can be directly evaluated.

It has been assumed that the only 'volume' contribution comes from the face $d \times D$, that is enough for the present discussion and true in general for long cells ($D \gg w$). As a consequence, when $n_{side}/n \gtrsim 1$, the increase in the granularity will not help to reduce the occupancy, being dominated by the particles impinging from the side.

In HADES, a value for ξ can be obtained from geometric considerations, as most of the hadrons travel through almost straight lines due to their large momentum. Fig. 5.12 shows the behavior of the projected angle ξ as a function of the local tRPC position y:

$$\tan\xi = \frac{y}{L} \tag{5.17}$$

being L is the distance from the target to the center of the sector.

The geometric expectation given by eq. 5.17 is shown in fig. 5.13, together with the observed y vs ξ distribution for central Au+Au collisions at 1.5 GeV/A. Most of the particles are very close to the geometric prediction, being slightly

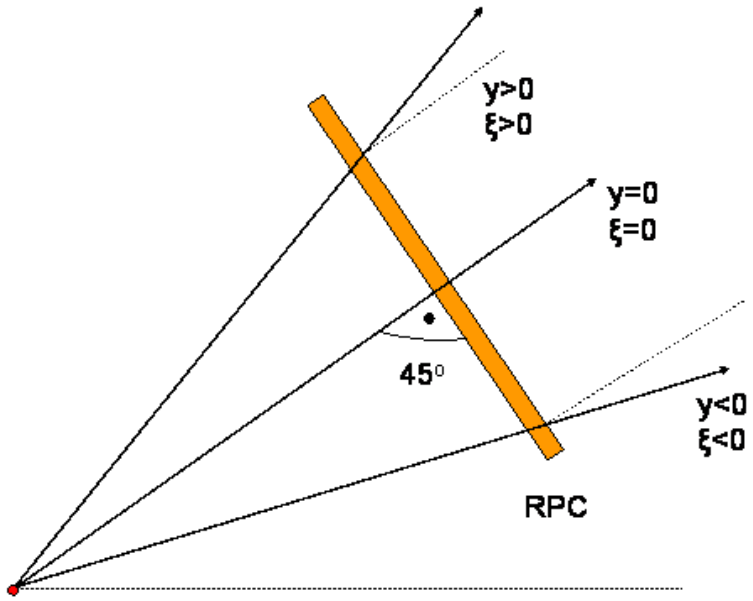

Figure 5.12: Figure showing the direct relation between the angle projected on the y-z plane (ξ) and the local position y over the tRPC.

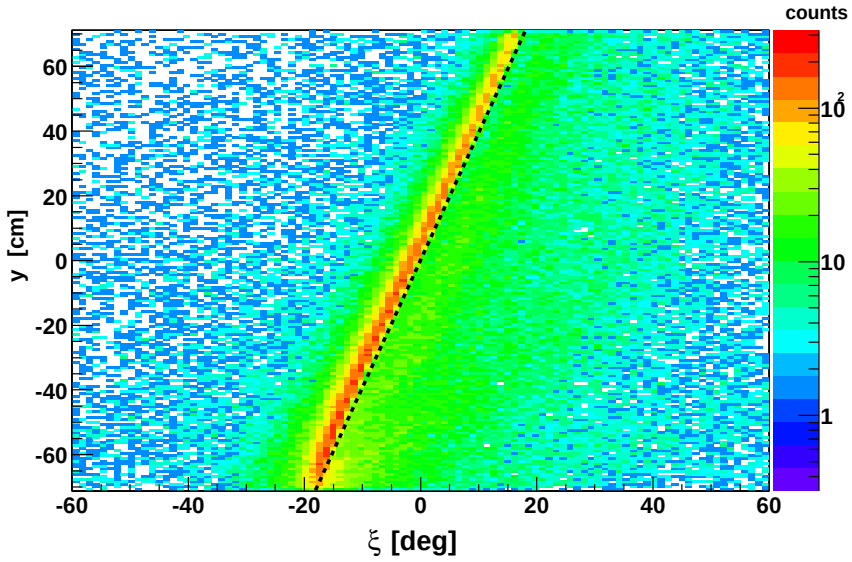

Figure 5.13: Local coordinate y as a function of the projected angle ξ for central Au+Au collisions at 1.5 GeV/A. Most of the particles lay close to the geometric expectation in the case of straight tracks (dashed line).

deflected towards low values of ξ, corresponding to an average downwards deflection $\Delta\xi \simeq -1.5°$. The points scattered out of $\tan\xi \simeq \frac{y}{L}$ are mainly leptons and particles produced out of the vertex.

Let's assume, for illustration, that the design is performed to provide an occupancy $n = 20\%$; then, a) according to fig. 5.9, the cells must have the following widths at low y: $w = 0.6$ cm for a 1-fold segmentation, $w = 1.2$ cm for a 2-fold segmentation and so on; b) at low y, $\xi \simeq -20°$ is obtained from fig. 5.13; c) the active thickness is assumed to be $d = 0.72$ cm (four 0.3 mm gas gaps and three 2 mm plates). With these values, the volume effect can be quantified for different configurations through the magnitude n_{side}/n, as shown in fig. 5.14.

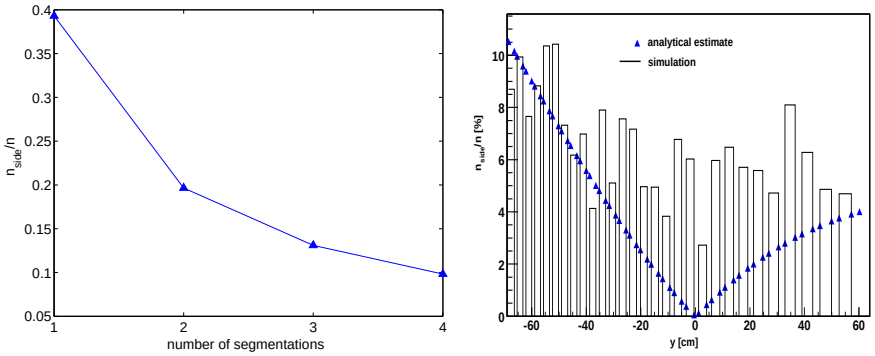

Figure 5.14: Left: n_{side}/n (volume effect) as a function of the number of segmentations (the occupancy was set to $n = \frac{dn}{dy}\Delta y = 20\%$). Also shown (right) the comparison between the evaluation of formulas 5.16, 5.17 and the simulated values of n_{side}/n for the layout proposed in section 5.3.1.

For a 1-fold segmentation and 20% occupancy, the volume contribution is already 40%, being around 10% for a 3-fold segmentation. The magnitude of the effect for a 3-fold segmentation, with the cell sizes proposed in section 5.3.1, is also shown, together with the result of the evaluation of eq. 5.16 (triangles), indicating a reasonable mutual agreement, not exceeding the volume effect a 10%.

The volume effect can be reduced by inclining the detector cells such that straight tracks coming from the vertex are impinging perpendicularly at any position of the TOF wall. This option would lead to a completely different assembling of the cells in the gas box as compared to the one proposed here, but must be considered as a reasonable choice.

Azimuthal deflection in the magnetic field

By construction, HADES magnetic field is aimed at providing a momentum kick along the polar angle. However, a residual azimuthal kick is present, tending to focus (de-focus) the particles to (from) the middle of the sector[11], depending on their charge. This effect has been recently characterized in some detail [143], providing an explanation of why both the focusing and the de-focusing processes

[11] y-z plane.

lead to an enhancement of the lepton population close to the middle of the sector at the tRPC position.

For illustrating the effect, the distribution of particles along the x direction is shown in fig. 5.15 at the lower polar angles (-66 cm $< y < -65$ cm, $\theta_{lab} \simeq 12°$), as it would be expected for central collisions and for a $1/p$ di-lepton distribution.

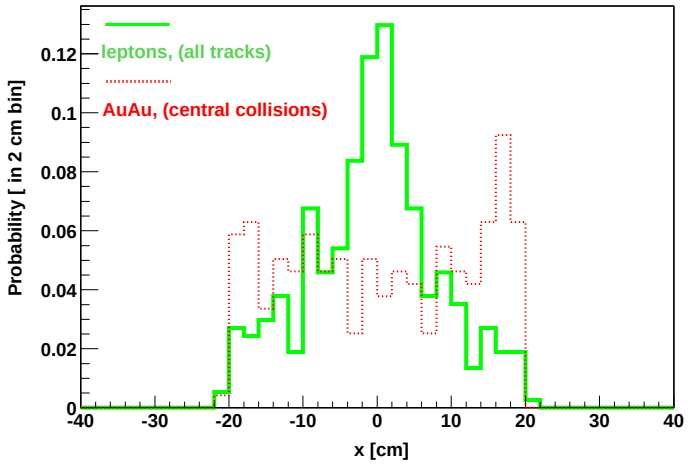

Figure 5.15: Distribution over x at $\theta_{lab} = 12°$, obtained for leptons and central Au+Au collisions. The figure shows the focusing observed for leptons (mainly positrons in the plotted region) towards the middle of the sector, while a large homogeneity is present in the events coming from Au+Au central collisions.

While the distribution corresponding to central collisions is roughly uniform, as expected due to the azimuthal symmetry, the leptons tend to focus towards the middle of the sector, due to the azimuthal magnetic kick. Therefore, to avoid possible losses of geometric origin, a segmentation in an even number of petals is not advisable.

Influence of the propagation time

It is very important to take into account that a particle is not detected until the avalanche signal has been induced and propagated along the cell up to the FEE electronics. If a different particle arrives to the cell before the collection of the signal has finished, such a signal will be distorted[12]. Otherwise, the second particle will arrive to the same cell but will not affect the first. This represents a favorable situation whenever the particle of interest is faster than a typical particle from the bulk, as is the present case. Therefore, when dealing with leptons, the scenario provided by the occupancy given in fig. 5.9 is expected to be more favorable.

The situation can be described from a simple point of view, in order to evaluate the effect: a) two particles arrive to the cell separated in time by Δt and b) the distribution along the cell is homogeneous. Let's consider that

[12] Let's note that for a velocity of propagation $v_{prop} = 2/3c$ and a typical cell size $D = 20$ cm the propagation time from one of the cell ends to the other is 1 ns.

the first particle arrives at a position x and that the distance traveled by the corresponding induced signal when the second particle arrives is $\Delta x = v_{prop}\ \Delta t$ (v_{prop} is the velocity of propagation of the signal). Under these assumptions, the probability that the second particle impinges on a region where the signal induced by the first has already arrived, can be regarded as the probability of having a clean signal from the first, without any kind of interference coming from the second. Such probability can be written as a function of the probability that both signals interfere (P_{interf}) according to:

$$1 - P_{interf}(x, \Delta t, D) = \frac{1}{D}[\Delta x\ \Theta(D - (x + \Delta x)) + \Delta x\ \Theta(x - \Delta x)] + \frac{1}{D}[(D - x)\ \Theta((x + \Delta x) - D) + x\ \Theta(\Delta x - x)] \quad (5.18)$$

with Θ being the step function, x the position of incidence of the first particle and D the length of the cell. The integral interference probability P_{interf} of eq. 5.18 for all the positions of the first particle can be obtained as:

$$1 - P_{interf}(\Delta t, D) = \frac{1}{D}\int_o^D (1 - P_{interf}(x, \Delta t, D))\, dx = \frac{1}{D^2}\left[\int_o^{D-\Delta x} \Delta x dx + \int_{\Delta x}^{D} \Delta x dx + \int_{D-\Delta x}^{D} (D - x) dx + \int_0^{\Delta x} x dx\right] \quad (5.19)$$

that results in the simple expression:

$$P_{interf}(\Delta t, D) = \left(1 - \frac{v_{prop}\Delta t}{D}\right)^2 \quad (5.20)$$

Naturally, the interference probability increases with D, providing a strong argument against very long cells (low segmentations). For illustration, the magnitude $P_{interf}(\Delta t, D)$ is shown in fig. 5.16 for the low polar angle region and different segmentations, assuming $\Delta t = 0.1$, 0.25, 0.5 ns.

Eq. 5.20 must be averaged over the time distribution of the species of interest, yielding $\bar{P}_{interf}(D)$. Therefore, the effective occupancy can be defined, in general, as:

$$n_{eff} = n\bar{P}_{interf}(D) \quad (5.21)$$

If $\bar{P}_{interf}(D) \to 1$ all the hadrons contribute to the effective occupancy.

Algorithm for recovering double hits

In general, leptons with high *tof* are always present, corresponding to low momentum and therefore large deflections (see fig. 5.18, for instance). In such a situation, it exists a chance that the lepton signal is completely hidden, because a fast hadron crossed the same cell. This case will be referred as 'total interference'. Therefore, the concepts of 'total' and 'partial' interference can be defined, as described in fig. 5.17, and denoted by $P_{interf[2]}$ and $P_{interf[1]}$, respectively[13].

In fig. 5.17 (up), it exists partial interference and, as a result, induced signals coming from different particles are collected at both tRPC ends, providing a biased estimate of the position. Fortunately, HADES has two accurate means

[13] In previous section, the interfering probability was referring to the case of partial interference $P_{interf[1]}$.

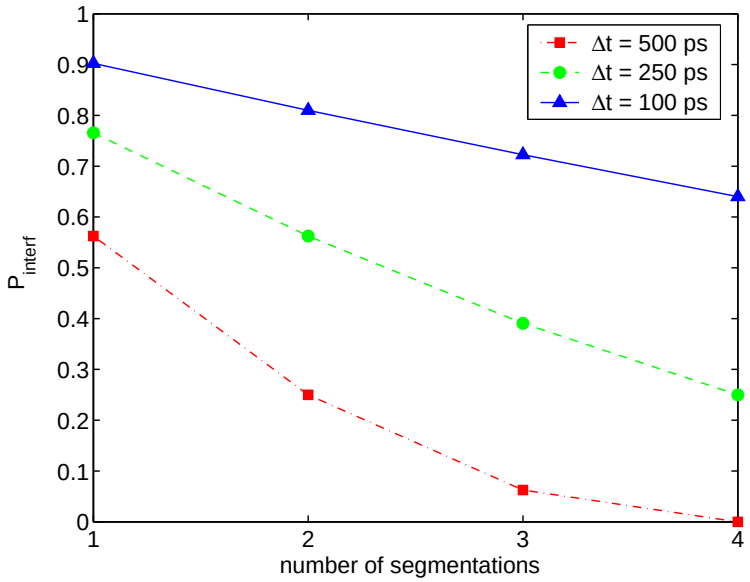

Figure 5.16: Probability of interference expected at low polar angles as a function of the number of segmentations (therefore the cell length), and the *tof* difference Δt.

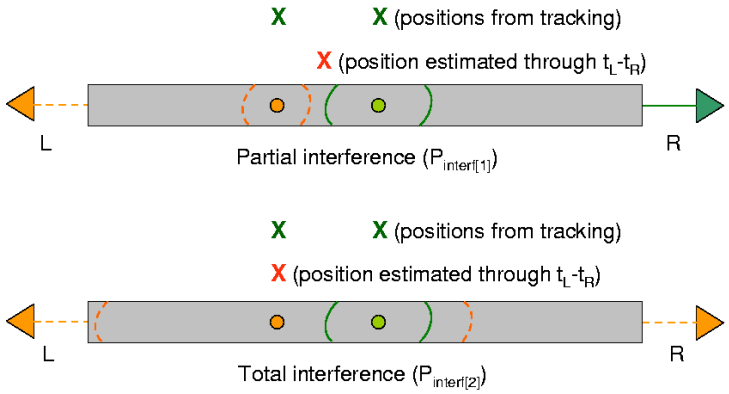

Figure 5.17: Partial (up) and total (down) interference. The arcs show the wave front of the induced signal at fixed time. The position reconstructed by the tRPC (biased) is shown, together with the ones resulting from an ideal auxiliary detector system.

for determining the true position over the tRPC: the MDC tracking system and the Pre-shower detector (that is attached to the tRPC). Therefore, a partially interfering double hit can be identified by the typical pattern described in fig. 5.17 (up) (I.e.: a mismatch between the position estimated from the tRPC, $x_{RPC} = (t_L - t_R)v_{prop}/2$, and the two positions reconstructed by the tracking. Incidentally, the biased tRPC position lays always between the two reconstructed positions, making a clean pattern).

If the true positions of the double hits are known with the help of external

information, the times of flight of the two particles (t_1, t_2) can be estimated through:

$$t_1 = t_R - \frac{D - x_R\big|_{ext}}{v_{prop}} \tag{5.22}$$

$$t_2 = t_L - \frac{x_L\big|_{ext}}{v_{prop}} \tag{5.23}$$

$$\sigma_T^2 = (\sigma_T\big|_{RPC})^2 + \left(\frac{\sigma_x\big|_{ext}}{v_{prop}}\right)^2 \tag{5.24}$$

with x starting from the left end of the cell. Assuming a propagation velocity $v_{prop} = \frac{2}{3}c$ (section 6.5.3) and a reasonable value of $\sigma_x\big|_{ext} < 1$ cm[14], a contribution of 50 ps is obtained when accounting for the resolution of the tracking system (still smaller than the intrinsic tRPC resolution).

It must be noticed that, in case of double hits, the charge information is corrupted[15]. However, a time resolution $\sigma_T = 100$ ps can be obtained even in the absence of slewing correction as shown in section 6.4.2. Therefore, the expected time resolution for double hits is:

$$\sigma_x\big|_{ext} \lesssim 1 \text{ cm} \rightarrow \sigma_T \sim 100 \text{ ps} \tag{5.25}$$

Note that, if the algorithm for recovering double hits can be implemented in practice, it would suggest, against the conclusion of previous section, to build very long cells so that the probability of partial interference $P_{interf[1]}$ is enhanced and the total interference $P_{interf[2]}$ reduced virtually to zero. However, it is advisable at the present stage to try to minimize interference and keep the length of the cells at reasonable values.

The time of flight of leptons

The fact that the e^+e^- pairs travel at the speed of light indicates that their time of flight and momentum are correlated only due to the deflection in the magnetic field. Before studying such correlation it is necessary to remove from the sample of lepton tracks those with unreasonable times of flight due to erratic paths along the magnetic field that are, anyway, hard to reconstruct for the tracking system. The more critical cases can be identified by looking for correlations between tof-ξ_{lab} and tof-$\Delta\xi$ ($\Delta\xi$ is defined as the difference between the projected angle in lab at the tRPC position and the projected angle at vertex): looping leptons or those with very long paths are identified as disconnected regions in any of these two representations (fig. 5.18 up). Furthermore, fig. 5.18 (up-right) indicates that particles with zero deflection ($\Delta\xi = 0$) can have very large times of flight, an effect that can be only explained by the erratic movement of low momenta electrons in regions of high field, yielding $\Delta\xi = 0$ just by chance. Such leptons were removed from the sample through the cuts indicated by the lines in fig. 5.18.

[14] The nominal precision of the HADES tracking system is at the level of 0.1 mm at the plane of the drift chambers.

[15] Large shaping times of some tens of ns are commonly used for charge measurements, therefore resulting, in case of double hits, in the analog sum of the charges produced by both particles.

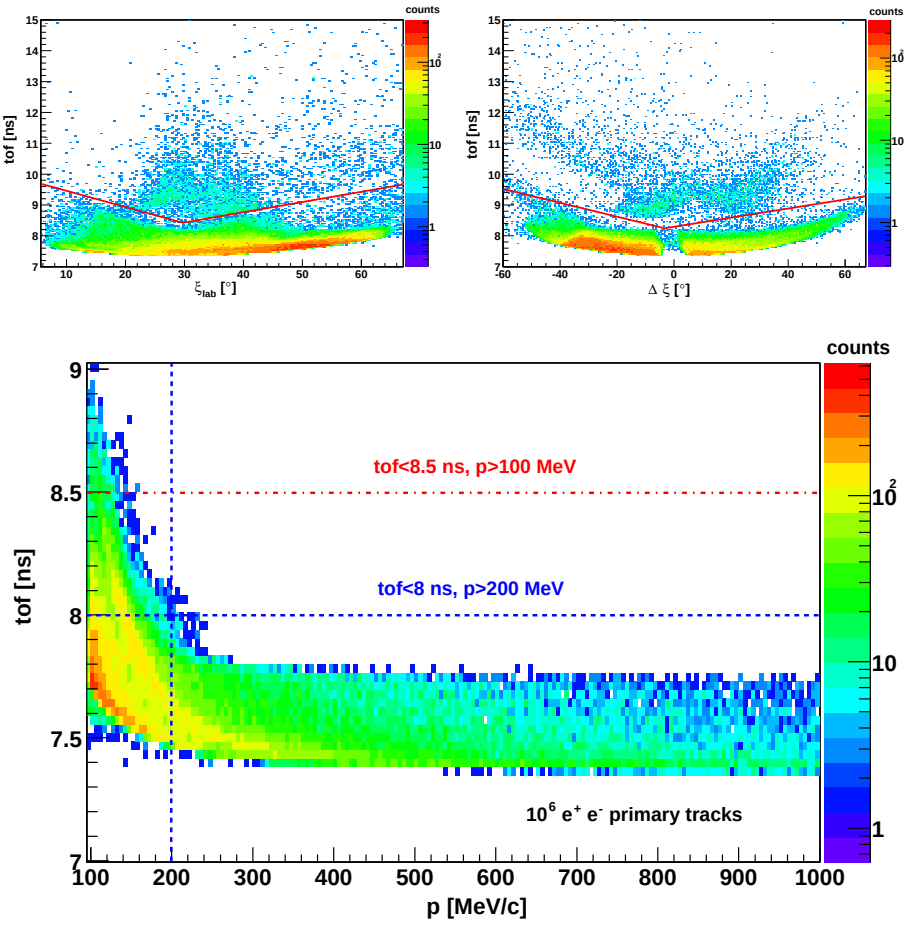

Figure 5.18: (Up-left) Time of flight of e^+e^- pairs as a function of the projected angle in the 'lab' system. (Up-right) Time of flight of e^+e^- pairs as a function of the variation between the projected angle at the tRPC and vertex. (Down) Relation between time of flight and momentum for e^+e^- pairs.

Finally, the plot 5.18 (down) shows the correlation between tof and p for e^+e^- pairs (the two observed branches at low momentum correspond to the different paths of e^+ and e$^-$ within the spectrometer). The following observations can be made: a) most of the leptons with momentum $p > 100$ MeV have $tof < 8.5$ ns (not more than 1.1 ns later than the fastest lepton) while b) $p > 200$ MeV implies $tof < 8.0$ ns (less than 0.6 ns later than the fastest lepton). Fig. 5.18 has been obtained for the typical field applied in the spectrometer, but the relations a) and b) will also hold, in general, for lower fields.

5.3 Design

5.3.1 1-layer layout

According to the arguments presented, a 3-fold segmentation with cells electrically isolated, each of them featuring a width that provides an homogeneous occupancy $n \simeq 20\%$ in the most unfavorable scenario expected in HADES, constitutes a reasonable choice, because of the following reasons:

1. The electric isolation provides robust multi-hit performances by construction (cross-talk levels below 1% were obtained for the first prototype tested in 2003, as shown in chapter 6).
2. The width of the cells can be kept at the level of $\Delta y \simeq 2$ cm for the lower polar angles, fulfilling the occupancy criteria ($n \simeq 20\%$) and providing enough stiffness.
3. The volume effect, n_{side}/n, produced by inclined particles is as small as 10% (fig. 5.14).
4. The shorter lengths as compared to the case of single segmentation reduces significantly the probability that a coincident particle interfere with the lepton signal. Moreover, the probability of having a clean lepton signal is better than 90% for the configuration presented (see next sections).
5. There are no geometric losses in the efficiency towards the middle of the sector.

Length of the columns

Due to the azimuthal symmetry of the experiment, the distribution of secondary particles is rather homogeneous over x. However, an exact symmetry in ϕ_{lab} does not imply total homogeneity in x, as can be inferred by looking at fig. 5.19, where the occupancy densities over the inner and the outer columns are shown.

A decrease in the length of the inner column such that $D_{inner} = 0.93 D_{outer}$, provides the same occupancy over the three columns (fig. 5.19 right). Despite the small difference, this feature is included in the proposed design.

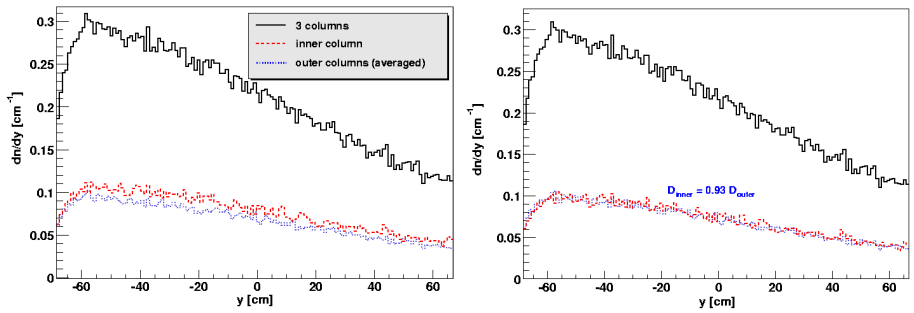

Figure 5.19: Left: contribution to the occupancy for each of the columns, assuming an exact 3-fold segmentation. Right: contribution to the occupancy for each of the columns, after the re-scaling $D_{inner} = 0.93 D_{outer}$.

Design parameters

As said, once the occupancy is fixed, the cell sizes can be obtained. A possible configuration is shown in fig. 5.20, with the cell sizes chosen to fulfill the occupancy requirements by means of commercially available aluminum profiles (for instance, [146]).

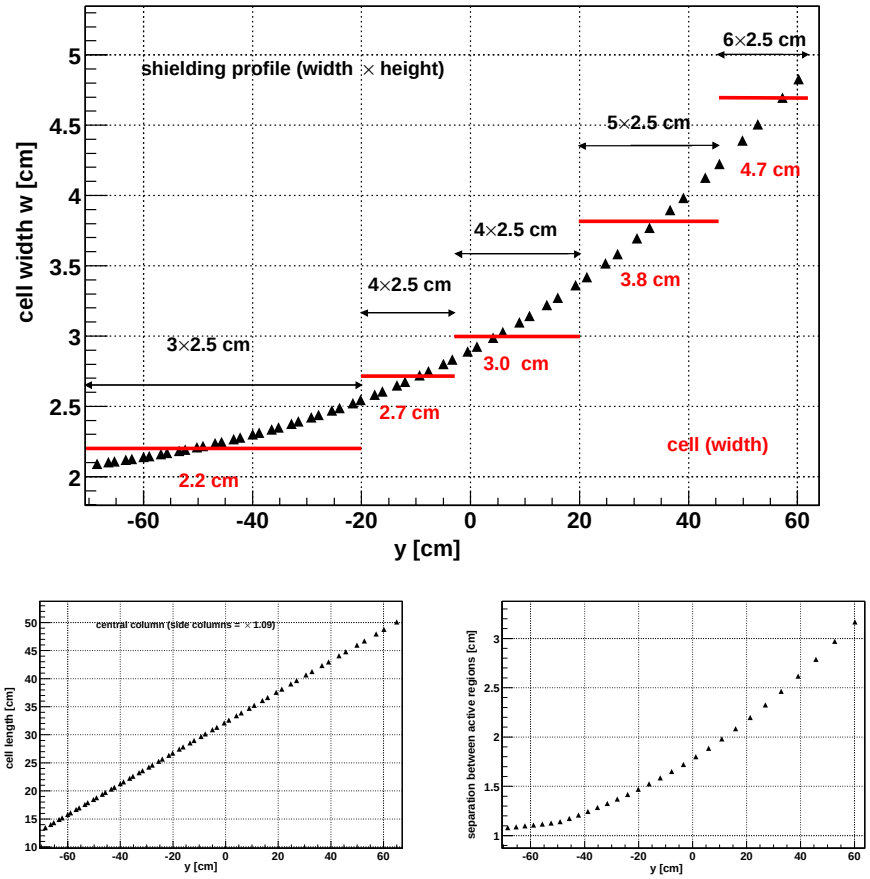

Figure 5.20: Up: cell width as a function of y for keeping the occupancy at 20%. Down-left: cell length for the central column. Down-right: separation between the active region of the cells along the y direction.

Double hit probabilities

The magnitudes used for evaluating the design are defined in the following:

1. P_o: probability that the cell is empty when a lepton arrives.
2. P_1: probability that the cell is occupied by one particle when a lepton arrives.
3. P_{clean}: probability that the cell is occupied by one particle too slow to affect a lepton. A clean lepton signal will be collected in that case.
4. $P_{interf} = P_{interf[1]} + P_{interf[2]}$: probability that the cell is occupied by one particle fast enough to interfere with a lepton signal.
5. $P_{interf[1]}$: probability that the cell is occupied by one particle fast enough to modify the lepton signal collected in one of the cell ends. The two tracks can be partially recovered off-line.
6. $P_{interf[2]}$: probability that the cell is occupied by one particle so fast that modifies the lepton signal collected in both ends. The lepton is lost.
7. $P_{>1}$: probability that the cell is occupied by more than one particle (disregarding their arrival times). In this case, it will be assumed, conservatively, that the lepton signal is lost.
8. $P_{lost} = P_{interf[2]} + P_{>1}$: probability that a lepton is lost.

Now it must be recalled that, leptons with $p > 100$ MeV have times of flight $t < 8.5$ ns and, similarly, $p > 200$ MeV implies that $t < 8.0$ ns. Aiming at a conservative estimate, the double hit probabilities defined in previous paragraph have been evaluated for a 'dummy' coincident lepton with time of flight $t = 8.5$ ns ($p > 100$ MeV) and equal probability of impinging at any position x along the cell. The resulting probabilities are shown in fig. 5.21 for the case of Au+Au collisions at 1.5 GeV/A.

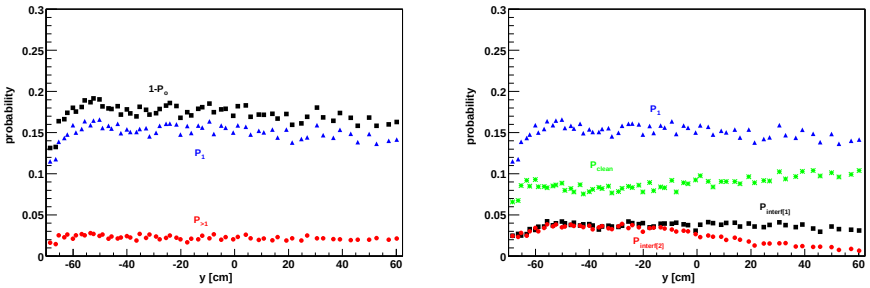

Figure 5.21: Left: probability that the cell is occupied 1-P_o, that it has 1 particle when the lepton arrives P_1, and that it has more than 1 particle $P_{>1}$. Right: different possibilities when the cell is occupied by one particle P_1, namely: a) P_{clean} (the lepton is cleanly detected), b) $P_{interf[1]}$ (both induced signals interfere), c) $P_{interf[2]}$ (the lepton signal is hidden by a fast particle and is lost). A costant arrival time $t = 8.5$ ns is assumed for the coincident lepton.

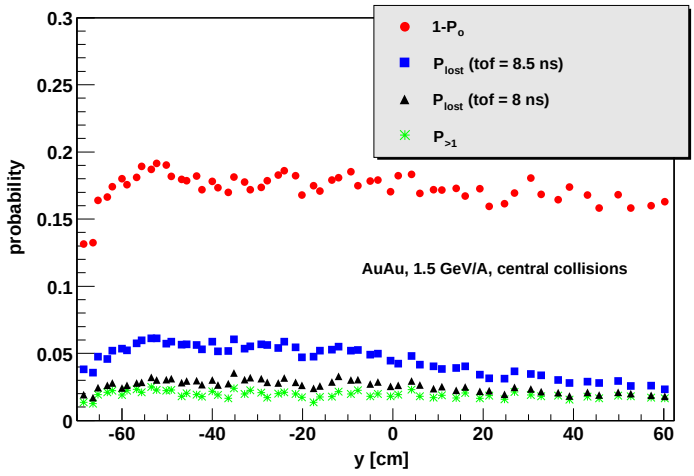

Figure 5.22: Probability that the cell is occupied (1-P_o) for the proposed design as a function of the local coordinate y (circles). Also shown the probability that the lepton signal is lost for different times of flight 8.0 ns (triangles) and 8.5 ns (squares). The asterisks show the practical limit to lepton detection, given by the probability of having simultaneous coincidence in the same cell between the lepton and more than 1 track coming from the bulk of particles.

The probability of losing the lepton is shown in fig. 5.22 for two different times of flight (8.0 ns, 8.5 ns). The main conclusion is that, for leptons with $tof = 8.0$ ns ($p > 200$ MeV), the probability of not being detected tends to:

$$P_{lost} = P_{interf[2]} + P_{>1} \simeq P_{>1} \simeq n^2 \sim 0.04 \tag{5.26}$$

that represents a practical limit to lepton detection under the conservative assumption that leptons in coincidence with more than 2 tracks are unrecoverable in a given cell. The final lepton detection performances are presented in the next section.

Expected detection probability

It is useful to define the total detection probability for leptons, $\mathcal{D}$, as the combination of three strongly uncorrelated factors:

1. The *intrinsic efficiency* ε. It is a property of the detector itself and stays at the level of 99% for 4-gap tRPCs [88], under low rates. The decrease of the efficiency as a function of rate has been parameterized in chapter 6 under typical HADES conditions, providing, approximately:

$$\Delta\varepsilon \simeq -1.5\% \frac{\phi}{100 \text{ Hz/cm}^2} \tag{5.27}$$

Assuming the operating rates obtained from the simulation of Au+Au collisions at the highest intensities (fig. 5.8), it is possible to extrapolate the behavior of ε as a function of y to that conditions, as shown in fig. 5.23. An increase of a factor 2 in the rate capability can be easily obtained

by a proper selection of the glass (different float glasses are compiled in [59]), still featuring a decrease of around 5%.

2. The *geometric acceptance* $\mathcal{A}$. The main geometric losses come from the regions between neighboring petals/columns (along the y direction) and also from the regions between the neighboring cells (along the x direction), both due to the space required for the shielding profiles. On one hand, it has been estimated that the active region of the columns can be kept within a separation of 0.5 cm, still providing electric isolation; the resulting inefficiency due to that regions can be straightforwardly evaluated for the most unfavorable case of perpendicular incidence, representing less than 2.5% losses in the HADES acceptance (fig. 5.23). On the other hand, the inefficient region due to the separation of the cells can be as high as 15% for perpendicular incidence, as estimated in section 6.5.1. The latter is the main inconvenient of a 1-layer design.

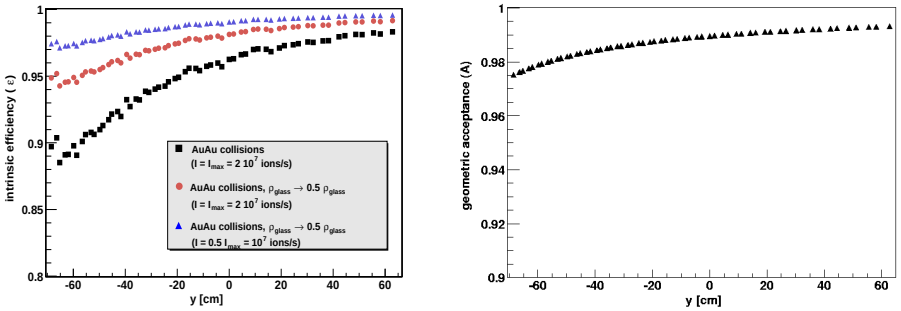

Figure 5.23: Left: behavior of the intrinsic efficiency from eq. 5.27 extrapolated to Au+Au collisions at the highest intensities expected. An increase of a factor 2 can be roughly achieved by an adequate choice of the glass, therefore increasing the efficiency up to a 95%. Right: geometric losses in the region between neighboring petals for perpendicular incidence, in the case of a 3-fold segmentation in columns.

3. The *ideal lepton detection probability* $\mathcal{L}$. It is provided by the chosen design and stands for the probability that the lepton signal is collected when considering the occupancy of other particles within the same tRPC cell. It depends on the time of flight of the leptons and can be obtained through the probabilities defined in previous sub-section. The final result is plotted in fig. 5.24 for the proposed design under Au+Au central collisions at 1.5 GeV/A, assuming for the coincident lepton $tof = 8.5$ ns ($p \gtrsim 100$ MeV) and $tof = 8.0$ ns ($p \gtrsim 200$ MeV).

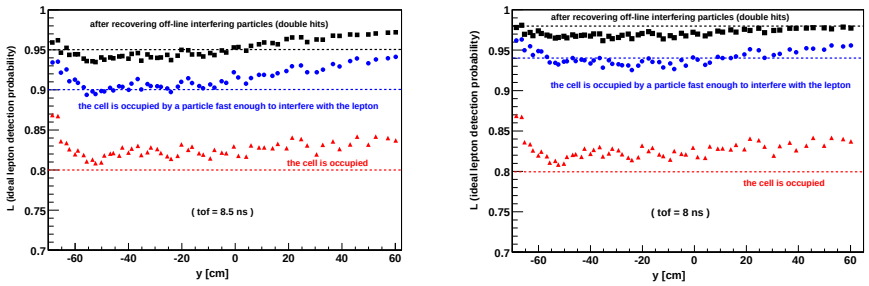

Figure 5.24: Lepton detection probability, $\mathcal{L}$, in case of ideal detector response for different times of flight (8.5 ns and 8.0 ns), corresponding to momenta above 100 MeV and 200 MeV, respectively. In more than 90% of the cases a clean signal is collected, while $\simeq 5\%$ of the double hits can be additionally recovered off-line with the procedure described in section 5.2.4.

5.3.2 2-layer layout

As said, a 1-layer layout constituted by electrically isolated cells requires some spacing between the active volumes of each cell for placing the necessary shielding. Such an approach has been implemented through the use of aluminum profiles, and the results are shown in section 6; they indicate that the loss in geometric acceptance can be almost 15% for perpendicular incidence, even in the very tight configuration chosen, where the active regions were separated by only 3 mm.

The overlap between layers

For avoiding dead regions, the use of a double layer configuration is proposed. The overlap required is given by the angle of incidence of the particles at the tRPC position (see fig. 5.25). It has to be taken into account that optimizing the detector for certain angles of incidence will bias the sample of detected particles, depending on their momentum. For avoiding this drawback, a general solution is proposed: the overlap was determined in such a way that all the possible tracks within the spectrometer that come from the vertex and have a momentum between 100 MeV and 1000 MeV go through at least 4 tRPC gaps (providing $\varepsilon \gtrsim 99\%$). The distribution for generating *all tracks* has been described in section 5.1.3, allowing to obtain all the possible angles of incidence ξ as a function of the local coordinate y (fig. 5.26). Therefore, the maximum and minimum angles ξ at each position y within the tRPC wall provide the required overlap (see fig. 5.25):

$$b_{downwards}(y) = (d+h)\tan\left[\xi_{min}(y)\right] \tag{5.28}$$

$$b_{upwards}(y) = (d+h)\tan\left[\xi_{max}(y)\right] \tag{5.29}$$

where d is the active thickness of the detector (region comprised between the two outermost gaps of each 4-gap cell, $d = 0.72$ cm) and h the separation between active volumes of different layers (assumed to be 1 cm due to mechanical constraints).

A y vs ξ scatter plot is shown in fig. 5.26 (left) for *all tracks*, compared with the distribution coming from Au+Au central collisions at 1.5 GeV/A (right),

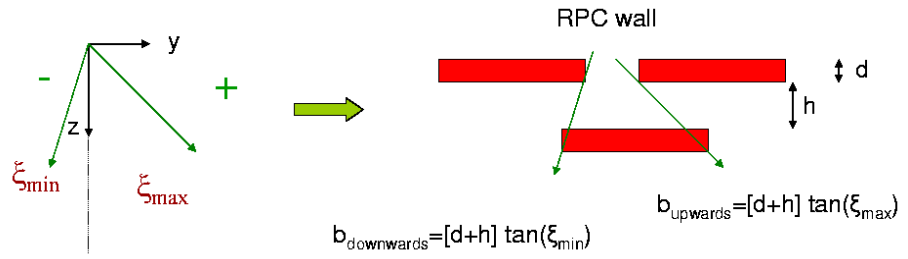

Figure 5.25: Relation between the extreme values of the angle of incidence at the position of the tRPC wall and the required overlap.

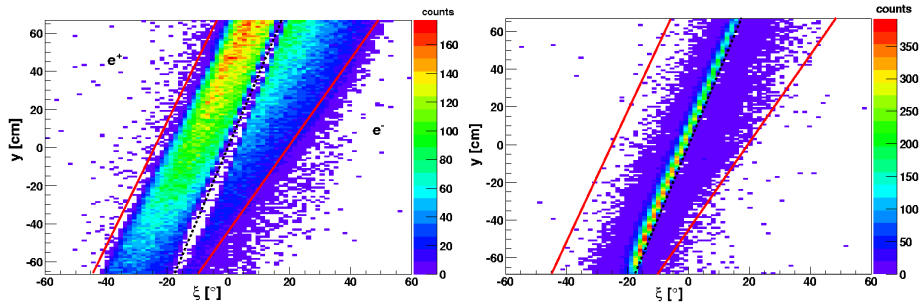

Figure 5.26: Relation between the position of the cell y and the angle of incidence ξ. It has been obtained for *all tracks* coming from target (left) and for Au+Au central collisions at 1.5 GeV/A (right) after imposing that the tracks come from the vertex. As expected, the physical distribution (right) is contained in the non-physical distribution of all the tracks (lines).

imposing the condition that the particles come from the vertex. Clearly, the 'physical' Au+Au distribution is contained in the distribution of *all tracks*, as expected (see lines).

Due to the asymmetric distribution of the angles of incidence, the overlap is better characterized by an overlap 'upwards' and 'downwards' (in y direction) as shown in fig. 5.27 (up). For simplifying the design, a convenient parameterization is also shown: in the lower part of the sector, the change in the overlap as a function of y can be implemented as a global shift of 1 mm of all the cells in one layer every 10 cm along the y direction.

Evaluation of the overlap

The overlap configuration can be evaluated by MC. In this case, the efficiency per gap was set in the digitizer to be $\varepsilon \simeq 0.75$ according to the experimental values. Being just a pure geometric optimization that depends mainly on 2 variables (y, ξ), it is not required to generate events through a full simulation: it proved to be very convenient to randomly generate tracks at the surface of the detector at different angles of incidence ξ and position y, allowing to determine the efficiency of the tRPC wall over a large region in the y vs ξ space. The results are shown in fig. 5.27 (down) indicating the regions where more than 4 gaps are crossed $\varepsilon \gtrsim 99.5\%$ (left) and also $\varepsilon \gtrsim 95\%$ (right). By comparison with

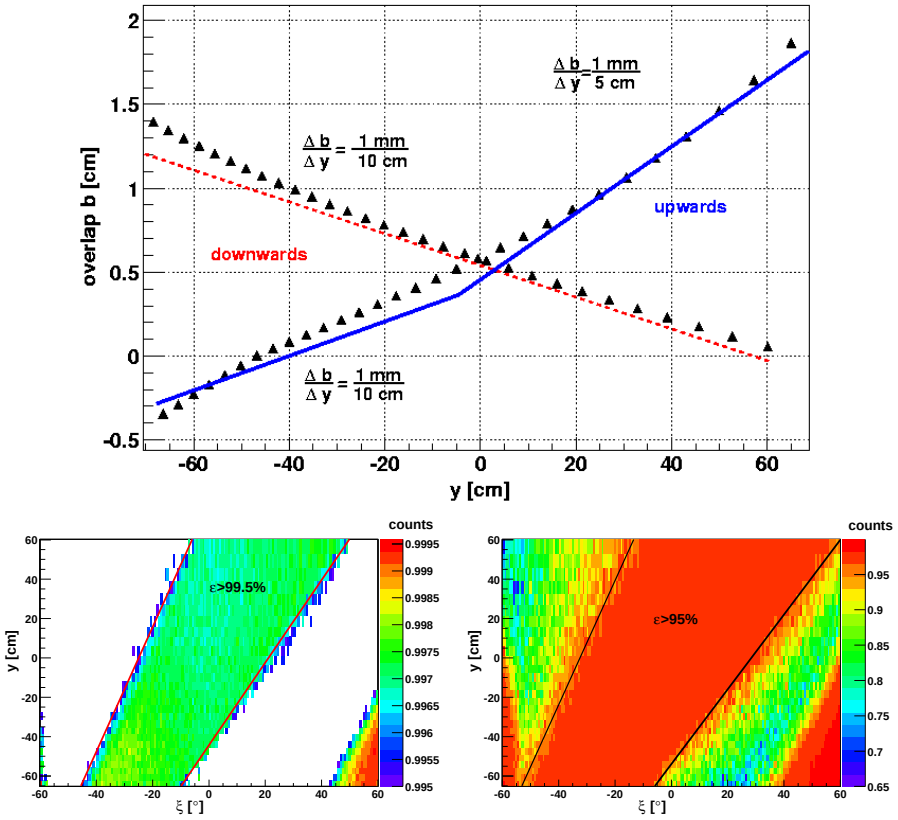

Figure 5.27: Up: overlap (downwards and upwards) as a function of the local coordinate y, together with the very convenient parameterization chosen. Emulated efficiency, showing the 99.5% efficient region, corresponding to 4 gaps crossed (left) and 95%, corresponding to approximately 3 gaps crossed (right).

fig. 5.26 (left), it can be seen that the region with $\varepsilon > 99.5\%$ in fig. 5.27 (lines) is conservatively larger than the region of interest.

Efficiency performances

From the discussion of previous sections, a convenient design was made based on figs. 5.20 (cell dimensions) and 5.27 (overlap between layers), that is presented in table 5.1. For illustration, the arrangement of the cells is shown only for one of the six columns/petals, taking as reference the acceptance of figure 5.5; it corresponds to the column/petal placed in the second layer, right hand viewed from the target. For simplicity, the use of commercially available aluminum profiles was imposed, yielding only six groups of cell sizes. The other five columns/petals are analogous to the one in table 5.1, and the relative positioning of the two layers fulfills the overlap determined in figure 5.27.

cell	y[cm]	x[cm]	D_{inf}[cm]	D_{sup}[cm]	cell w [cm]	tube w [cm]	α [°]	β [°]
1	0	6.6	13.0	13.7	2.2	3.0	7.8	24.5
2	3.5	7.0	14.1	14.8	2.2	3.0	7.8	24.5
3	7.0	7.5	15.2	15.9	2.2	3.0	7.8	24.5
4	10.6	8.0	16.4	17.1	2.2	3.0	7.8	24.5
5	14.1	8.5	17.5	18.2	2.2	3.0	7.8	24.5
6	17.6	8.9	18.6	19.3	2.2	3.0	7.8	24.5
7	21.2	9.5	19.8	20.5	2.2	3.0	7.8	24.5
8	24.7	9.9	20.9	21.6	2.2	3.0	7.8	24.5
9	28.2	10.4	22.0	22.7	2.2	3.0	7.8	24.5
10	31.8	10.9	23.1	23.8	2.2	3.0	7.8	24.5
11	35.3	11.4	24.3	25.0	2.2	3.0	7.8	24.5
12	38.8	11.9	25.4	26.1	2.2	3.0	7.8	24.5
13	42.4	12.3	26.5	27.2	2.2	3.0	7.8	24.5
14	45.9	12.8	27.6	28.3	2.2	3.0	7.8	24.5
15	49.4	13.3	28.7	29.8	3.2	4.0	7.8	24.5
16	54.7	14.0	30.5	31.3	2.7	4.0	7.8	24.5
17	59.7	14.7	32.0	32.9	2.7	4.0	7.8	24.5
18	64.8	15.4	33.7	34.5	2.7	4.0	7.8	24.5
19	69.8	16.1	35.3	36.1	2.7	4.0	7.8	24.5
20	74.9	16.8	36.9	37.9	3.0	4.0	7.8	24.5
21	80.2	17.5	38.6	39.5	3.0	4.0	7.8	24.5
22	85.4	18.2	40.2	41.2	3.0	4.0	7.8	24.5
23	90.7	19.0	41.9	43.1	3.8	5.0	7.8	24.5
24	96.9	19.8	43.9	45.1	3.8	5.0	7.8	24.5
25	103.2	20.7	45.9	47.1	3.8	5.0	7.8	24.5
26	109.3	21.5	47.9	49.1	3.8	5.0	7.8	24.5
27	115.5	22.4	49.8	51.1	3.8	5.0	7.8	24.5
28	121.6	23.2	51.8	53.3	4.7	6.0	7.8	24.5
29	128.4	24.1	54.0	55.5	4.7	6.0	7.8	24.5

Table 5.1: Arrangement of the cells in the proposed design. The adopted conventions are defined in fig. 5.28. It must be noted that y and x refer to the local coordinates but with y starting at the bottom of the geometric acceptance.

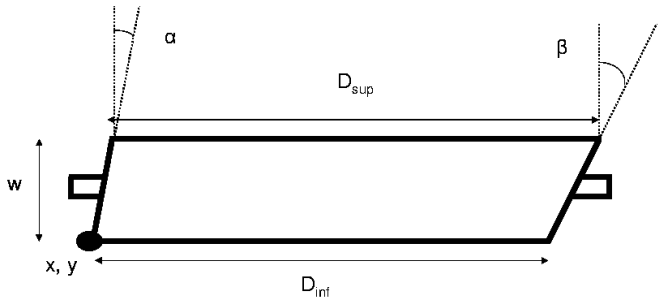

Figure 5.28: Conventions used in table 5.1.

Therefore, the final number of cells required is:

$$N_{cells} = \quad 29 \text{ cells} \times 6 \text{ petals} \times 6 \text{ sectors} \quad = 1044 \quad (5.30)$$

$$N_{channels} = \quad 29 \text{ cells} \times 6 \text{ petals} \times 6 \text{ sectors} \times 2 \text{ sides} \quad = 2088 \quad (5.31)$$

The lepton detection capabilities of the design can be evaluated: taking the conservative numbers for the intrinsic efficiency $\varepsilon \gtrsim 95\%$ (worst scenario), the geometric acceptance $\mathcal{A} \gtrsim 98\%$ (worst scenario), and the design value $\mathcal{L} \gtrsim 95\%$ ($p > 100$ MeV), a value for the total lepton detection probability for leptons with momentum above 100 MeV $\mathcal{D}(p > 100$ MeV) can be obtained as:

$$\mathcal{D} = \mathcal{L} \times \mathcal{A} \times \varepsilon \gtrsim 88.5\% \tag{5.32}$$

and for the detection of lepton pairs:

$$\mathcal{D} = (\mathcal{L} \times \mathcal{A} \times \varepsilon)^2 \gtrsim 78.2\% \tag{5.33}$$

determined for Au+Au central collisions, $b < 4$ fm and $E_{kin} = 1.5$ GeV/A [16]. If further improvements related to the moderate increase of the temperature of the glass are finally accomplished, ε could be increased up to a value close to 99% (see the encouraging results [73], [59] and [1]). On the other hand, the ideal detection probability for leptons $\mathcal{L}$, for $p > 200$ MeV, is at the level of 97%, as long as double hits can be recovered with the algorithm proposed in section 5.2.4.

First level trigger performances

The first level trigger performances will be affected by the level of occupancy of the cells (some tracks are lost) but also by the overlap (tracks can produce more than one valid signal). Both effects are taken into account by the digitizer and, therefore, the multiplicity measurements can be evaluated and compared with the true multiplicity. This is done in fig. 5.29 for Au+Au central collisions (all sectors), indicating that a small increase with respect to the true multiplicity takes place, indeed, at the level of 20%. Despite this, the ratio σ_N/N is roughly constant and therefore the effect can be corrected by re-defining the trigger condition, without losing performances. The result of fig. 5.29 and the previous remark point to the fact that, in central Au+Au collisions, the initial fluctuations due to the characteristics of the interaction have a dominant role on the multiplicity distribution measured, reducing the impact of design choices.

5.3.3 3-D design

A detailed picture of the 3D design corresponding to the lower polar angles is shown in fig. 5.30, together with some of the cells that have been recently tested in November 2005 [1]. The asymmetric overlap is visible in the drawing. The natural way-out of the cables towards the FEE (placed at the sides of the gas box) is summarized in fig. 5.30 (down).

[16] Also $B = 0.72 B_{max}$, point-like target at origin and ideal HADES geometry is assumed.

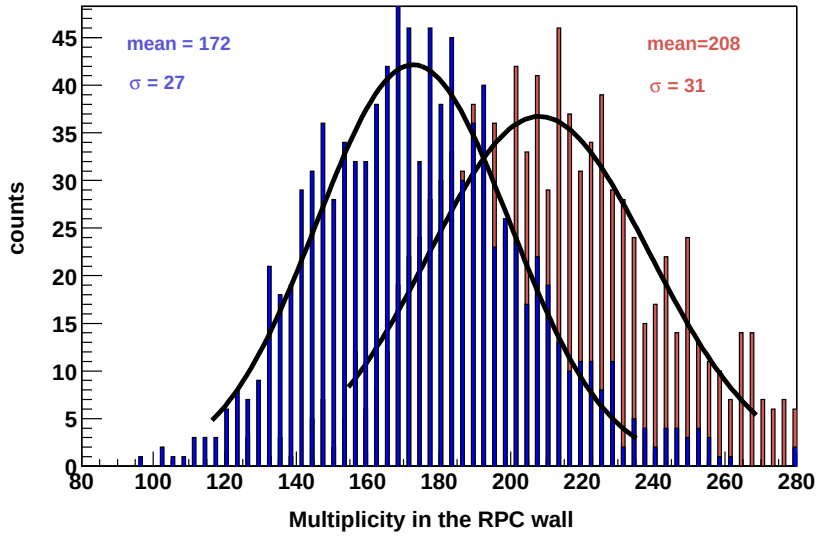

Figure 5.29: Simulated multiplicity at the tRPC wall (all sectors) as expected for the proposed design (rightmost distribution), under central Au+Au collisions at 1.5 GeV/A. The true multiplicity is given by the leftmost peak. Both distributions are fitted to a Gaussian, showing a slight increase in the first case due to the overlapping regions that produce double-counting.

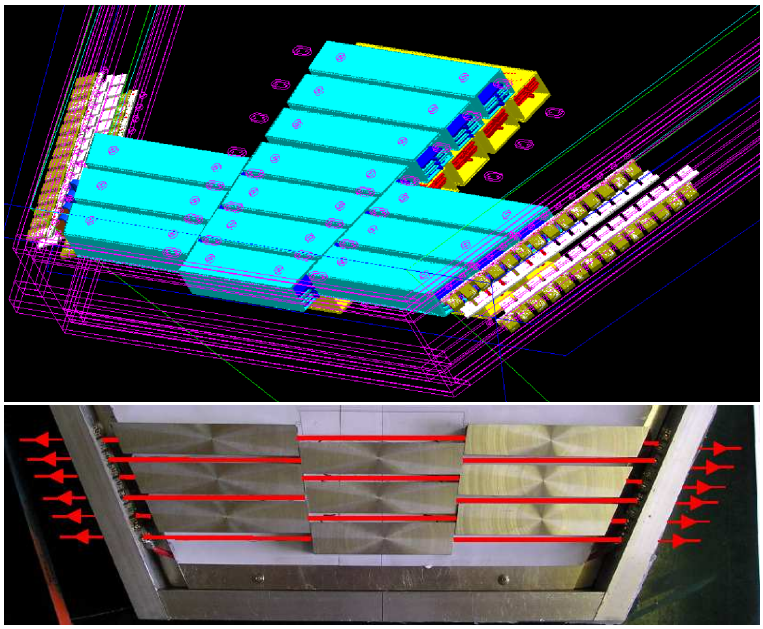

Figure 5.30: Up: 3D drawing of a detail of the proposed design at low polar angles. In the lower part, the shielding profiles that surround the detector cells are shown, indicating also the distribution of the signal cables.

5.4 Other issues

5.4.1 Evaluation of the impact over other detectors

Geometric constraints

[17]Geometric integration is a crucial issue. Moreover, most of the details regarding the final shape and dimensions of the gas box and also of the electronic channels, even the dimensions of the screws or the thickness of the gas box, the materials used, etc... were discussed along countless meetings of the members of the ESTRELA project. A full description of all these topics is out of the scope of the present work. On the other hand, geometric integration constitutes a boundary (or compromise) between physics requirements and practical feasibility; therefore, a part of the arisen problems must be discussed, even if rather superficially, here. More on geometric integration can be found at [149].

There are three major geometric constraints:

1. For not coming into conflict with MDC IV frame at the lower polar angles, the tRPC gas box must be not thicker than 10 cm. Fortunately, in the proposed 2-layer configuration, constituted by 4-gap cells + shielding, the thickness can be kept at the level of 8-10 cm without big effort. Moreover, the proximity of the frame of the MDC IV and the tRPC gas box is not likely to represent any potential mechanical problem, due to the high robustness of both elements.

2. There was a problem due to the high proximity between the TOF photomultipliers and the tRPC gas box at intermediate polar angles ($\theta_{lab} \simeq 45°$). The two main alternatives considered for providing a safe separation from them were: a) to perform a downstream displacement of the set tRPC+shower detector or b) to cut the gas box; both solutions result in the decrease of the geometric acceptance. The two possibilities were evaluated based on CAD designs [149], that provided the specifications for the minimum cut and also the minimum displacement required for overcoming the problem (fig. 5.31).

   The acceptance was estimated as described in section 5.2.1 for both proposed solutions, yielding a similar loss in geometric acceptance (evaluated at the nominal tRPC position for easier comparison), at the level of 3-4%, distributed in the region of $\theta_{lab} = 40\text{-}45°$. Due to the similar consequences of both approaches, it was decided to cut the gas box because of practical reasons. The cut gas box together with a CAD picture of the geometric integration in HADES are shown in fig. 5.32.

[17] In collaboration with H. Álvarez-Pol.

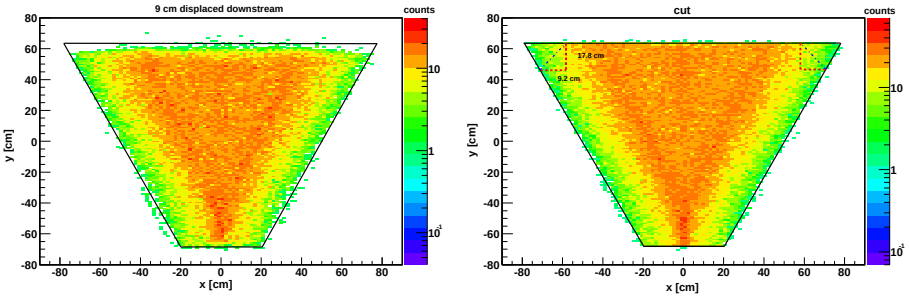

Figure 5.31: Figures showing the losses in the acceptance at the nominal tRPC position for two different approaches: a) downstream displacement of the set tRPC+shower detector (left), 9 cm along the direction of the rails where the frames are placed (this is the only movement allowed), and b) cut in the region where the TOF photomultipliers are present (right).

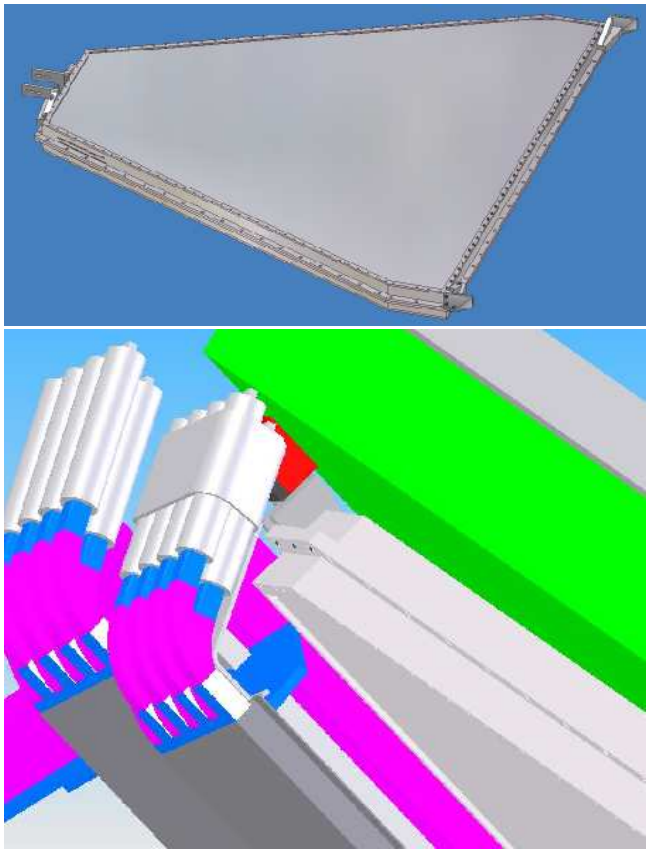

Figure 5.32: Up: gas box used in November 2005 tests, featuring a cut in the region close to the TOF photomultipliers. Down: detail of the region where the gas box and the TOF photomultipliers are closer. The cut in the gas box is needed for avoiding that the two detector systems are inter-penetrated.

3. The room for the FEE electronics: FEE will be placed at a region that is shadowed by the magnet coils. This region results from the projection of the coils over the tRPC position, and is of no interest from the point of view of the acceptance. However, after fulfilling all the mechanical constraints[18], the available room renders as small as $\mathcal{V} \simeq 4 \times 3 \times 1$ cm^3 per channel. It was decided to place the FEE board parallel to the slanting sides of the gas box, allowing for an easier cooling of the electronics[19]. In that case, the available area per channel is approximately 1×4 cm^2 in the low polar angle region (see fig. 5.33).

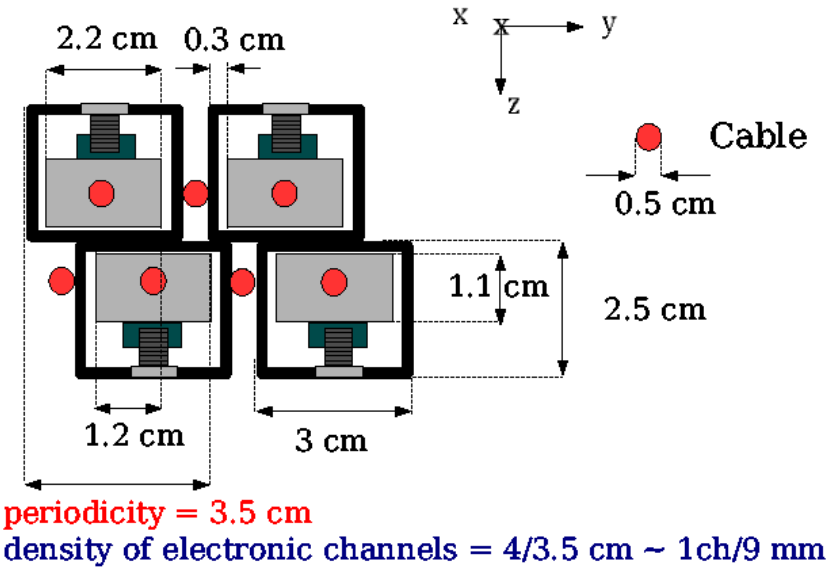

Figure 5.33: View of the tRPC cells, projected over one of the slanting sides of the sector. The distribution of cells corresponds to the design proposed at the lower polar angles, where the density of channels is higher.

In order to fit to the available space it was decided to place some of the necessary electronic components, as voltage regulators, DAC thresholds, test signals and trigger logic in a different board that is placed in an orthogonal fashion (fig. 5.34) still placed mostly under the shadow of the magnet.

The electronic boards are denoted by DBO (Daughter board) and MBO (Mother board), respectively. The first performs amplification, discrimination and charge measurement[20] while the second ensures the distribution and stabilization of the power supply, the distribution of the thresholds of the comparators and the test signals, and a basic trigger logic that must be used for the multiplicity trigger of the experiment. Details on this approach can be found in [87].

[18] Mainly arising from the sizes of the filtering capacitors and the necessary structure for interfacing the signal to the FEE itself.

[19] For example, with fans blowing from $\theta_{lab} = 12°$ to $\theta_{lab} = 45°$ or vice-versa.

[20] Through the time over threshold of the integrated signal.

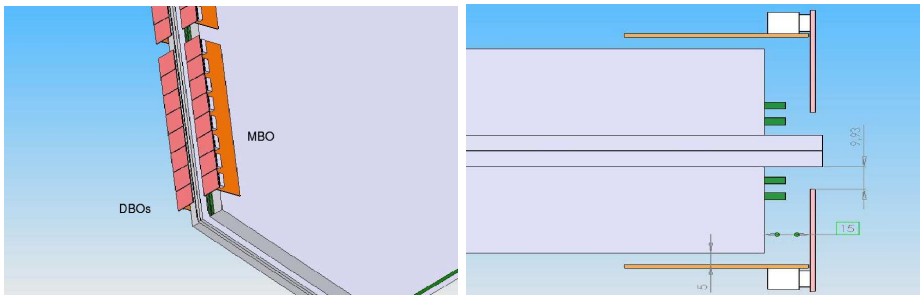

Figure 5.34: Drawings showing the positioning of the MBO+DBO setup with respect to the gas box. The two pins in the right of the gas box interface the signal from the inside.

Therefore, the area of the gas box must be large enough to cover the HADES acceptance at tRPC position (fig. 5.7), but respecting the TOF photomultipliers, and having a total thickness smaller than 10 cm in order to not touch the MDC IV frame. Last, but not least, it must provide enough room towards the limit of the sector for placing the electronics.

Shower detector performances

The shower condition. As said in section 4.3.6, the shower detector provides hadron rejection by producing an electromagnetic shower on two lead converters of $2X_o$ thickness each. Whether a tRPC wall placed in front of it will alter or not its performances must be studied.

The development of the shower is sampled by three planes of wire chambers featuring the so-called Pre-shower, Post-shower[1] and Post-shower[2]. Let's denote by Q the charge collected at the Pre-shower and Q_1, Q_2 the charges released in the Post-shower[1] and [2], respectively. Two different conditions for discriminating an electromagnetic shower that are currently used in HADES data analysis, were studied:

Condition 1:

$$\frac{Q_1}{Q} > 2 \quad \text{or} \quad \frac{Q_2}{Q} > 2 \tag{5.34}$$

Condition 2:

$$\frac{Q_1}{Q} > P_1(p) \quad \text{or} \quad \frac{Q_2}{Q} > P_2(p) \tag{5.35}$$

where $P_1(p)$ and $P_2(p)$ are polynomials of third order, and provide a shower condition that depends on the reconstructed momenta of the particle. Also different algorithms for estimating the charge Q_i were studied (called alg_1 and alg_2)[21].

For evaluating the influence of the tRPC wall over the performances of the shower detector, a wall made of solid glass was defined in simulation, with a thickness ranging from 1.4 to 2.6 cm[22]. The primary distributions used differed slightly from the used in previous sections: a) Au+Au, $b = 0$ fm, $E_{kin} = 1$

[21] They were used for data analysis before and after November 2001, respectively.
[22] Equivalent to 7-13 glass layers 2 mm thick.

GeV/A and b) isotropic distribution in the c.o.m.[23] of di-leptons coming from the decay of the ϕ meson, boosted to a beam energy E_{kin}=1.5 GeV.

The radiation length. Both the development of an electromagnetic shower and the deflection of a charged particle due to multiple scattering in a medium are related to the radiation length X_o. These two effects are expected to modify the shower detector performances, as a function of the total number of radiation lengths of the material placed in front (x/X_o):

1. If an important fraction of the electromagnetic shower development takes place already at the tRPC wall, conditions 5.34 and 5.35 can change.

2. The final distribution of angles after multiple (electromagnetic) scattering is given, approximately, by a Gaussian distribution with sigma $\Delta\theta$ given by:
$$\Delta\theta = \frac{13.6\text{MeV}}{\beta cp}\sqrt{x/X_o}\,[1 + 0.038\ln(x/X_o)] \tag{5.36}$$
according to [3]. If the number of radiation lengths in the tRPC wall is very large, the scattered angle can result in a wrong estimate of the charge in the pads of the Post-shower detectors and even the loss of the particle within the acceptance of the shower detector.

The equivalent thicknesses in radiation lengths of the detectors under study are, approximately:

$$\left.\frac{x}{X_o}\right|_{TOFino} \simeq \frac{0.5}{42.4} = 0.012 \tag{5.37}$$
$$\left.\frac{x}{X_o}\right|_{RPC} \lesssim \frac{2.6}{12.3} = 0.21 \tag{5.38}$$
$$\left.\frac{x}{X_o}\right|_{Post-shower} = 2 \tag{5.39}$$
$$\tag{5.40}$$

What matters for the following discussion are orders of magnitude: therefore, the aluminum used for the electrodes ($X_o \simeq 8.9$ cm) and the glass ($X_o \simeq 12.3$) are regarded as if they were the same material.

There is a significant increase in the fraction of radiation lengths for the tRPC wall as compared to the current TOFino wall ($\times 20$) but still much smaller than the 2 radiation lengths of any of the Post-shower lead converters. This points to a small effect over the shower conditions 5.34 and 5.35.

On the other hand, larger scattered angles are also expected as compared to the TOFino wall, but still at the level of $\Delta\theta \lesssim 3.5°$ for $p > 100$ MeV (eq. 5.36). This fact, added to the high proximity between the shower detector and the tRPC, suggests that the influence of the multiple scattering is small.

Results. The PID capabilities are compared in fig. 5.35 for the present TOFino wall (dashed) and a 1.8-2.6 cm thick wall made of glass. The result is rather conclusive: the influence of the material budget in front of the shower

[23] Center of mass frame.

detector has little influence on its PID capabilities, despite a marginal worsening at low momenta for hadrons. This, in fact, improves the situation, by reducing the amount of fakes.

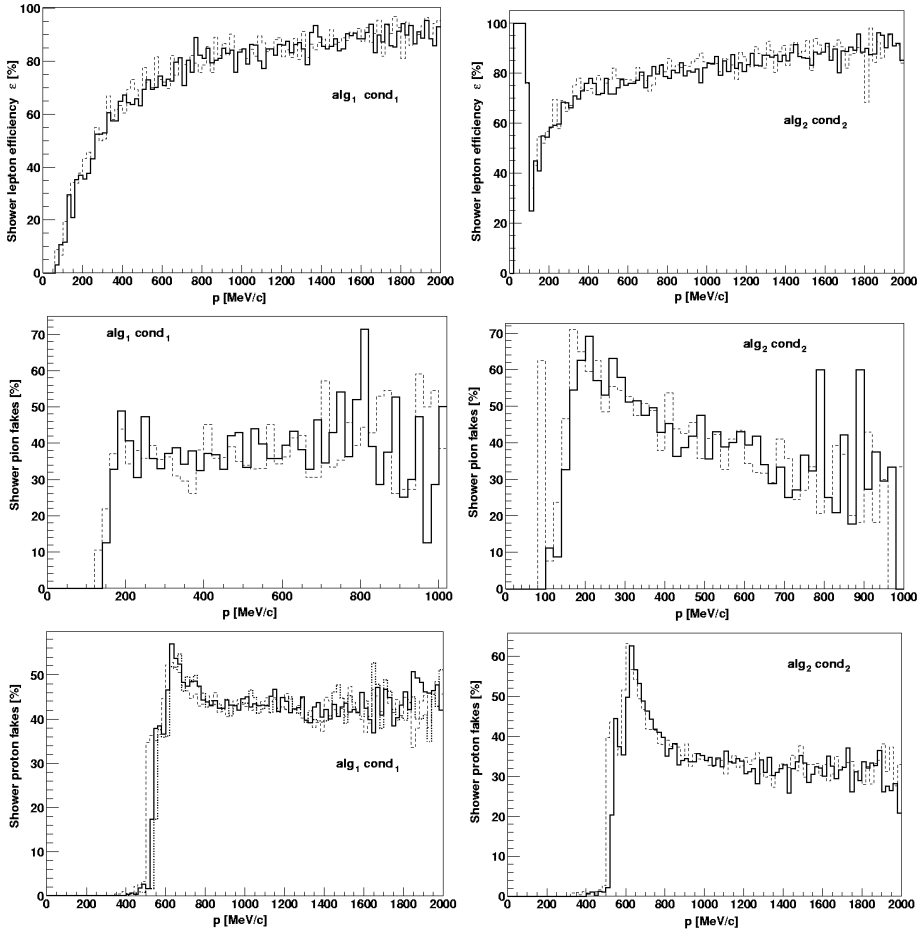

Figure 5.35: Shower identification efficiency and fake probability (namely, shower PID capabilities) for leptons, pions and protons by using different algorithms for estimating the charge Q (alg_1 or alg_2) and also different 'shower' conditions ($cond_1$ or $cond_2$). The two lines shows the responses for the TOFino (dashed) and for a wall of glass 1.8 cm thick (thick line). Also shown is the influence of a thickness of 2.6 cm on the proton fake probability (alg_1, $cond_1$), where a tiny effect can be appreciated at low momenta.

In fig. 5.36 the fraction of tracks that crossed the tRPC but could not be matched to any hit in the Pre-shower are shown, and compared with the TOFino case. The influence on the Pre-shower inefficiency for lepton detection is at the level of a few percent.

As a conclusion, the replacement of the TOFino by the tRPC wall does not seem to perturb significantly the performances of the shower detector.

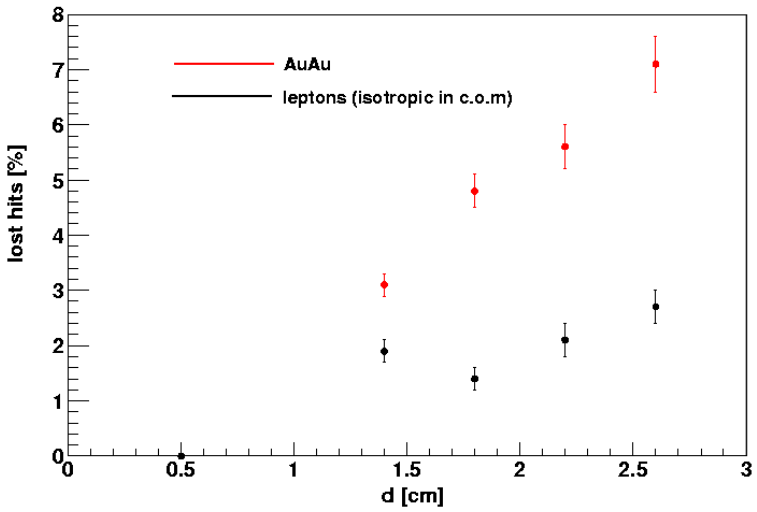

Figure 5.36: Decrease of the fraction of tracks that show a valid hit in the tRPC wall and Pre-shower, with respect to the case of the TOFino (0.5 cm of plastic scintillator). The situation for hadrons coming from Au+Au interactions (upper set of points) and leptons (lower set of points) is compared.

5.4.2 Au+Au 8 GeV/A

[24]In view of the possible application of HADES within the foreseen SIS100 facility, some studies were performed regarding Au+Au and C+C collisions at 8 GeV/A. In particular, the situation corresponding to the maximum energy attainable at SIS18 (1.5-2 GeV/A) was compared with the typical expected at SIS100 (8 GeV/A). The primary rate over the tRPC is shown in fig. 5.37 for the same beam intensity and interaction probability as considered for SIS18 ($I = 2\ 10^7$ ions/s, 1% interaction probability). The observed increase of a factor 3 would require a considerable increase in the tRPC rate capability.

However, the more constraining requirements at SIS100 are related to the granularity of the detector, due to the higher multiplicities as compared to the present SIS18. Simulated occupancy densities for Au+Au and C+C environments at typical energies of both facilities are shown in fig. 5.37. The observed increase of a factor 4 in the cell occupancy is expected to make the present design hardly usable for 8 GeV/A Au+Au collisions at SIS100; nevertheless, the enhancement in the region $\theta_{lab} \simeq 40°$ is only a factor 2 larger than in the case of 1.5 GeV/A, for which the present design has been optimized.

On the other hand, the 8 GeV/A C+C environment produces occupancies smaller than Au+Au at 1.5 GeV/A by a factor 5. More simulations are required to settle the range of applicability of HADES-tRPC in the new SIS100 facility, but from present results it seems to be suited for studying intermediate systems like CaCa or NiNi (more detailed results can be found in [150]).

[24] In collaboration with M. Golubeva.

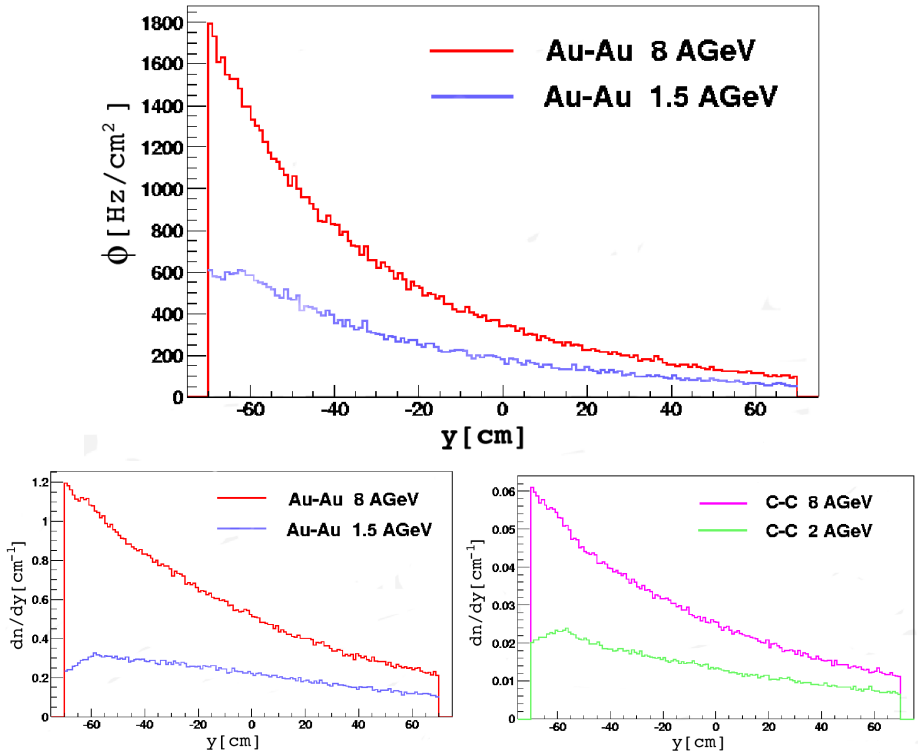

Figure 5.37: Up: simulated rate over the tRPC as a function of y for minimum bias Au+Au collisions at I= 2 10^7 ions/s and $P_{int} = 1\%$. Down: simulated occupancy over the tRPC as a function of y for central Au+Au ($b < 4$ fm) and C+C ($b < 3$ fm). In all the cases, the energies correspond to typical SIS18 and SIS100 energies.

5.5 Conclusions

In this chapter, a design aimed at covering the low polar angle region of HADES $18° < \theta_{lab} < 45°$ has been presented. The granularity, together with the intrinsic efficiency of the detector and the geometric acceptance have been designed to provide a detection probability for leptons around $\simeq 90\%$ even in the worst scenario expected at SIS18 (central Au+Au collisions, $E_{kin} = 1.5$ GeV/A), with a highly unbiased measurement of the multiplicity for first level trigger purposes in that case. The cell sizes are set so that the occupancy per cell (double hit probability) is homogeneous along the whole wall, at the level of $n \simeq 20\%$. For that, each sector is divided in 3×2 petals, allowing for reasonable cell sizes.

The array is constituted by 1044 4-gap tRPC cells electrically isolated. For avoiding the dead regions due to the shielding, a 2-layer scheme has been chosen, with overlaps determined by the requirement that all possible tracks coming from target and impinging over the tRPC wall cross at least 4 gaps. This scheme provides a very high geometric acceptance, dominated by the losses in the regions between adjacent petals ($\mathcal{A} \gtrsim 98\%$ of the total HADES acceptance for $18° < \theta_{lab} < 45°$).

Some of the more relevant constraints regarding geometric integration have

been discussed, together with the solutions for each case.

Preliminary studies on the feasibility of the present tRPC wall within the forthcoming SIS100 accelerator have been discussed, suggesting that operation at intermediate nuclei masses is possible, but further simulations are required.

The maximum expected rates at HADES in Au+Au collisions at 1.5 GeV/A ($\Phi = 700\,\mathrm{Hz/cm^2}$) are slightly above the ones affordable by ordinary glass timing RPCs. A practical solution to this potential problem, based on the moderate warming of the glass, is given in chapter 8.

A much more detailed document, including full mechanical integration and detailed design, constitutes the Technical Design Report of the ESTRELA-HADES project and it can be found elsewhere.

Chapter 6

Performance of HADES tRPCs

6.1 Introduction

A previous work of the group of P. Fonte [47] showed the viability of building timing RPCs of large sizes (160×5 cm^2), with a time resolution in the range 50-75 ps σ and an efficiency above 95% up to rates of 140 Hz/cm^2, showing a reasonable homogeneity along the detector length. The performances were slightly worst than previous designs [46] based on small cells, possibly due to the higher mechanic complexity and also to the increase in the propagation distances. However, the overall performances shown in [47] could be considered as a proof of principle for a timing RPC wall based on long cells.

It must be recalled that, for the measurements performed in [47], a pulsed monochromatic pion beam was used at CERN PS (0.3 s per spill, spaced a few seconds) of $E_{kin} = 3.5$ GeV ($\gamma\beta \simeq 30$)[1]. Despite the relative success of the development, some drawbacks and questions were already posed by the authors:

1. *Cross-talk*: cross-talk above 80% between neighboring cells was observed.

2. *Favorable environment*: the tRPC operation was facilitated due to the use of a mono-energetic beam. Typical experiments in particle and nuclear physics deal with a broad range of energies and particle species, resulting in different ionizations. This represents a potential source of problems, that could result in an undesirable increase of streamers or a lower efficiency, if not both[2].

3. *Pulsed beam*: the short duration of the beam spill (0.3 s) is smaller than the typical time constant of float glass, $\tau_g \sim$ s. It is shown in chapter 9 how this fact introduces a bias in the observed performances, impeding a direct extrapolation to equal instantaneous rates but longer spills[3].

[1] Above the MIP's dip. Due to the very slow growth of the Bethe-Bloch ionization curve, they are denoted as MIPs in [47].

[2] An increase in the fraction of streamers would worsen the tRPC rate capability. The problem can be solved by decreasing the applied voltage but then the tRPC performances are partially sacrificed.

[3] Typical spills in HADES are 5-10 s long.

6.1.1 Cross-talk

A detailed study on electromagnetic propagation on resistive plate chambers can be found in [65]. There it is argued that, for high lengths, a tRPC cell can be considered as an inhomogeneous transmission line[4]. In such a case, if the pick-up strips are not interconnected and a fast amplifier with low input resistance is used, the *modal dispersion* of the signal propagated increases with the distance from the amplifier, resulting in a perfectly bipolar cross-talk signal (zero induced charge). This observation is in agreement with the measurements of [47] (D=160 cm), where a large bipolarity is observed on the cross-talk signals, not transporting sizable charge.

The effect is different from the one observed in configurations with segmented electrodes, where the same avalanche induces current (and net charge) over two or more pick-up strips at the same time. In fact, a general situation will have contributions with both origins (induction during avalanche formation and induction during signal propagation) .

In [47], around 80-90% of the hits induced cross-talk on the neighboring cell. As a consequence, the effective occupancy of the system is increased, rising doubts about the possibility of application in a *multi-hit environment*[5]. For illustration, let's consider the average number of hits in a cell per primary interaction (occupancy) to be n, and let's also assume that the distribution of the number of hits over the cell follows a Poisson distribution (see section 5.2.3), the cross-talk probability is denoted by P_{cross} and N is the number of neighbors per cell. Then, the probability that a cell is empty (able for detection) is given by:

$$P_0 = e^{-n} \tag{6.1}$$

If N neighbors are inducing cross-talk with a probability P_{cross}, the effective occupancy of the cell will increase, yielding:

$$P_0 = e^{-n(1+NP_{cross})} \tag{6.2}$$

Typical design criteria is $n = 20\%$ and $N = 2$ (see chapter 5). Therefore, for 80% of cross-talk, a decrease in P_0 from 82% to less than 60% will be expected.

As said, the *immediate* effect of cross-talk is to artificially increase the occupancy. However, there is another more 'subtle' effect that takes place even if cross-talk is not high enough to trigger the comparator. In that case, the occupancy will not be increased, but cross-talk will still introduce fluctuations on the signal base-line of the neighbor cell, possibly modifying the timing of a hit that arrives slightly after.

A way to reduce cross-talk effects was suggested by FOPI collaboration [86]; they minimized the signal reflections below 2% by setting the detector impedance to $50 \pm 1\ \Omega$, exactly as for the electronic stage. Even if impedance matching does not make cross-talk disappear, it reduces its influence. However, impedance matching is not an easy option in a situation where different cell widths (namely, different impedances) are involved.

[4] I.e., the faster components of a signal induced on the tRPC electrode have amplitudes changing significantly within a given propagation line of length D (i.e.: $\lambda \lesssim D$). In particular, for GHz components, and assuming a propagation velocity $v_{prop} = 2/3c$, the cell can be considered as a transmission line if $D \gtrsim 20$cm.

[5] I.e., several neighboring cells firing simultaneously within the same primary collision.

For reducing the cross-talk, a versatile and robust solution is proposed in this work, based on the electric isolation of the tRPC cells [101]. In this case there is also a price to be paid: the presence of dead regions due to the electric isolation between cells require a dedicated design in order to provide a high geometric acceptance (see section 5.3.2 for details).

6.2 Experimental setup

6.2.1 The prototype

In spring 2003, a first tRPC prototype constituted by 3 cells was tested [96], [97], resembling the expected final ones to be installed at the HADES spectrometer (fig. 6.1) . The cells had 4 gas gaps in a symmetric configuration and were made out of standard float glass (electrically floating [43]) and aluminum electrodes, placed inside rectangular *shielding profiles* in order to reduce the cross-talk. The approximate dimensions were $60 \times 2 \times 1.1$ cm^3 (long/wide/thick). They were inspired in the design proposed in chapter 5: the cell length was of the order of the maximum length expected (50 cm), for testing homogeneity, mechanics and signal propagation; the width was of the order of the thinnest cell expected (2.2 cm); the thickness of the cell had its main contributions coming from the glass and aluminum plates ($60 \times 2 \times 0.2$ cm^3), that were chosen as a compromise between thickness and mechanical stiffness. For practical reasons, the gas mixture used was 98.5% $C_2H_2F_4$ + 1% SF_6 + 0.5% iso-C_4H_{10} at atmospheric pressure and ambient temperature, being slightly different from the so-called 'standard mixture' (85% $C_2H_2F_4$ + 10% SF_6 + 5% iso-C_4H_{10}). The choice was shown to have little effect on the performances (a short discussion on the main effects of the variation of the gas properties is presented in chapter 7).

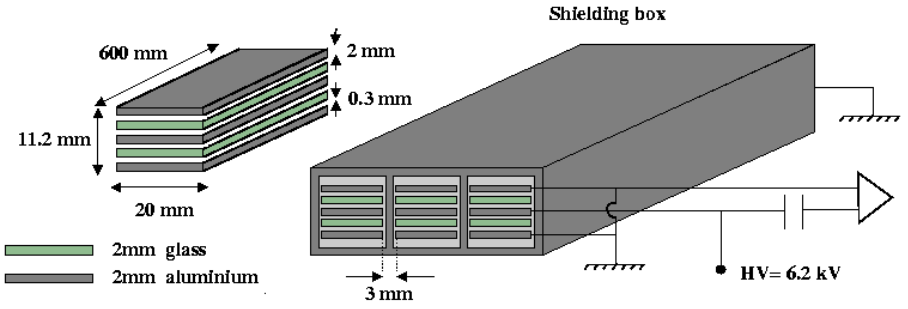

Figure 6.1: Drawing of the tRPC prototype tested in 2003 in HADES cave.

Regarding the electric configuration, the outer aluminum electrodes are grounded while the inner one is fed at 5.2-6.8 kV, thus providing a V/gap in the range 2.6-3.4 kV. A schematic drawing of the prototype is shown in fig. 6.1.

The previous description is general and does not include a number of small differences between the 3 tRPC cells tested:

1. tRPC *I*: glass electrodes. 1.9 cm wide.
2. tRPC *II*: aluminum electrodes. 1.7 cm wide.
3. tRPC *III*: aluminum electrodes. Twice the density of spacers (test of the mechanics). 1.9 cm wide.

The cells were insulated from the walls of the shielding profiles with PVC tape. For tRPC *II* (inner), a copper strip was interposed in a 'sandwich' tape+copper+tape, whose read-out is shaped, amplified and sent to an ADC. The idea of this configuration was to estimate the effect of the signal induced to the walls as compared with the induction over the electrodes. This effect is a kind of 'edge effect' described in [101] as *loss of induced charges*, and could be of importance when the avalanche is produced close to the shielding walls (see section 6.6.1 for the analysis of these data).

A front and side picture of the prototype is shown in fig. 6.2. Each cell is carefully accommodated inside the shielding profile to avoid unnecessary stress over the glass. Inside the gas box, a capacitor of 1 nF is placed in order to filter the signal induced, that is later on interfaced to the outer part of the box, where the Front End Electronics (FEE) is directly attached.

6.2.2 The acquisition system

The description of the FEE stage is shown in fig. 6.3 (more details can be found elsewhere [151]). The tRPC signal goes through 2 amplification stages and then it is split for discrimination (timing) and buffering (charge measurements).

The FEE board is terminated at 50 Ω, and referred to the ground of the box itself (common ground). The double-end lecture ($t_L = t_{Left}$, $t_R = t_{Right}$) allowed for a position independent estimate of the time of flight and position of the impinging particle:

$$t = \frac{t_L + t_R}{2} - t_o \tag{6.3}$$

$$x = \frac{t_L - t_R}{2} v_{prop} \tag{6.4}$$

where v_{prop} is the velocity of the induced signal and t_o the reference time.

The FEE was placed at one end of the gas box, and the furthermost end of the cell delivered the signal through a long cable up to the part where the FEE is placed[6]. The analog tRPC signal and the digital signal from the comparator are then delivered to a 2249W Lecroy ADC (200 ns window) and a fast 2228 Lecroy TDC (50 ps bin) based on the CAMAC standard.

The cell is not adapted to the FEE electronic stage, resulting in the appearance of reflections with periodicity $2D/v_{prop}$ (D=60 cm is the cell length), which are able to re-trigger the comparator several times before falling below threshold, therefore perturbing the system. For avoiding these spurious contributions but also possible re-triggerings coming from the ion tail, a dead-time of 1μs is implemented in the comparator. At the typical operating voltages of around 3 kV/gap, the threshold of the comparator was set close to 10 mV.

[6] See chapter 5 for a description of the cabling in the latest design.

Figure 6.2: Front view of the 3-cell prototype. The left-most cell was replaced by one having glass electrodes (RPC I). In the lower photograph the tRPC cells are shown before placing inside the shielding profile.

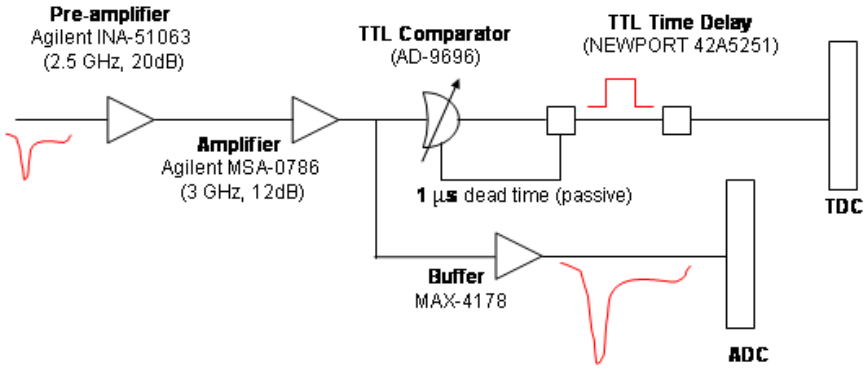

Figure 6.3: Figure showing the full electronic chain. Further details can be found in [151].

6.2.3 The trigger system

1. *The position within the spectrometer*: for this test, it was decided to cover a region at the lowest polar angles of the foreseen tRPC wall, because of the higher rates expected there (fig. 5.8). A drawing showing the orientation of the experimental setup in HADES can be seen in fig. 6.4; finally, the tRPC was placed at approximately 20° from the beam line, taking as reference the nominal target position.

2. *The telescope*: the trigger line was defined with the help of two fast Bicron scintillators (BC-420) with dimensions $8\times2\times3$ cm^3, placed orthogonally at both sides of the tRPC gas box as shown in fig. 6.4. They are denoted by $scin_1$ (tRPC upstream, perpendicular to it) and $scin_2$ (tRPC downstream, parallel to it), defining a trigger area of, approximately, 2×2 cm^2. In order to reduce the probability of random coincidences, a third coincidence with a scintillator of cylindrical shape and radius $r = 1.25$ cm ($scin_3$) was required, providing the trigger condition T:

$$T = T_1 \otimes T_2 \otimes T_3 \tag{6.5}$$

   The reference scintillators 1 and 2 allow to obtain a time resolution as good as $\sigma_{_T} = 35$ ps for MIPs [47], and they were placed in a symmetric configuration with respect to the tRPC gas box, a decision discussed along the following points.

3. *The on-line positioning*: it was made use of a telescope mount [152] whose orientation could be defined remotely by fixing 2 angles (declination and right ascension), that allow to define a straight line for astronomic observations. The setup was modified from its original purpose, as illustrated in fig. 6.4 and 6.5, and the rotations along the 2 angles were used to define a trigger line pointing to the target. This situation, where the trigger line points to the target, was identified by chosing different orientations and looking for that one yielding the maximum number of triggers.

4. *The reference scintillators*: for avoiding effects due to the time spread of the bulk of particles, the intrinsic time response of the two reference scintillators was estimated by placing them as close as possible. It was imposed a soft quality cut for selecting 'good scintillator events', namely cuts 1 (position) and 2 (charge) according to the conventions of section 6.4.1. The scintillator time response obtained under these conditions is shown in fig. 6.6, yielding a combined resolution $\sigma_{_T}\big|_{scin} = 50$ ps (namely, $\sigma_{_T}\big|_{scin} = \sqrt{35^2 + 35^2}$ ps) in accordance with [47].

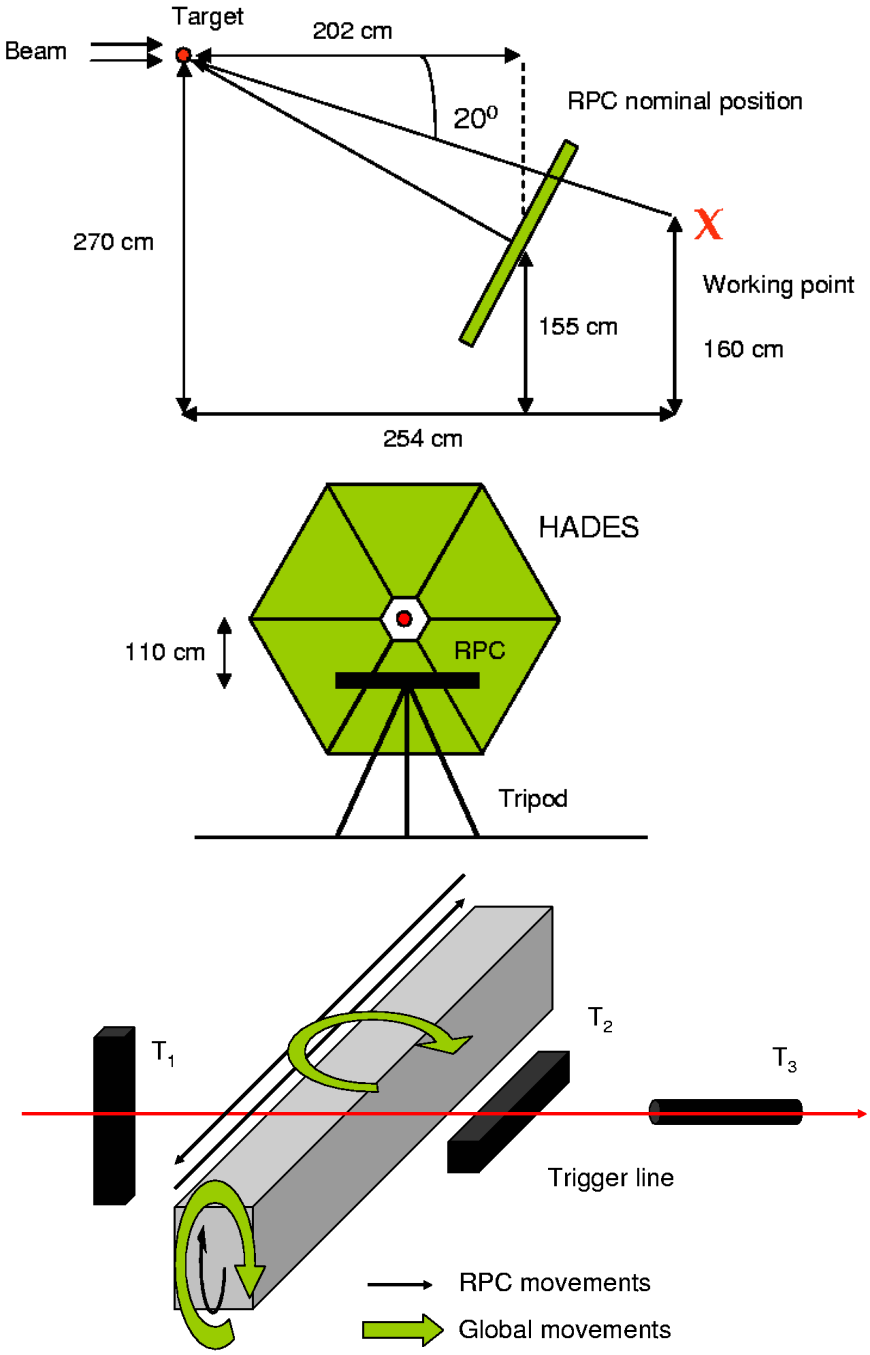

Figure 6.4: Up: position of the setup relative to the HADES spectrometer. Down: scheme of the different movements that are allowed within the setup used. 'Global' stands for common movements of the telescope and the tRPC, whereas 'RPC' stands for independent movements of the tRPC.

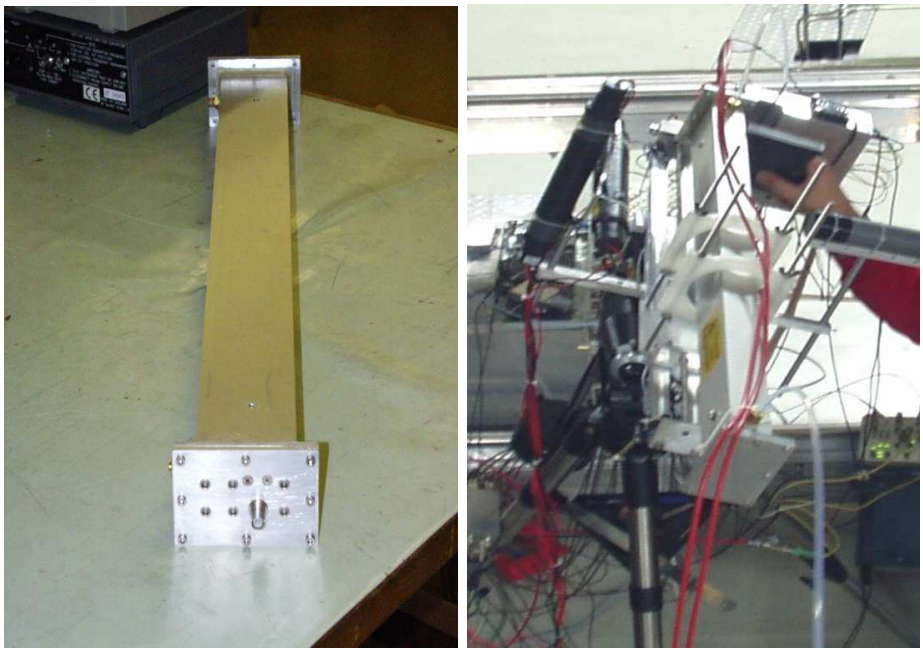

Figure 6.5: tRPC gas box (left) and in-beam setup (right). In the latter, the telescope mount is shown, after adapted to handle the gas box and the trigger line defined by the reference scintillators. Also shown the fast rectangular scintillators $scin_1$ and $scin_2$ (black, tRPC upstream) and the cylindric one $scin_3$ (grey, tRPC downstream). In the final configuration the fast scintillators were placed symmetrically respect to the gas box, as shown in fig. 6.4.

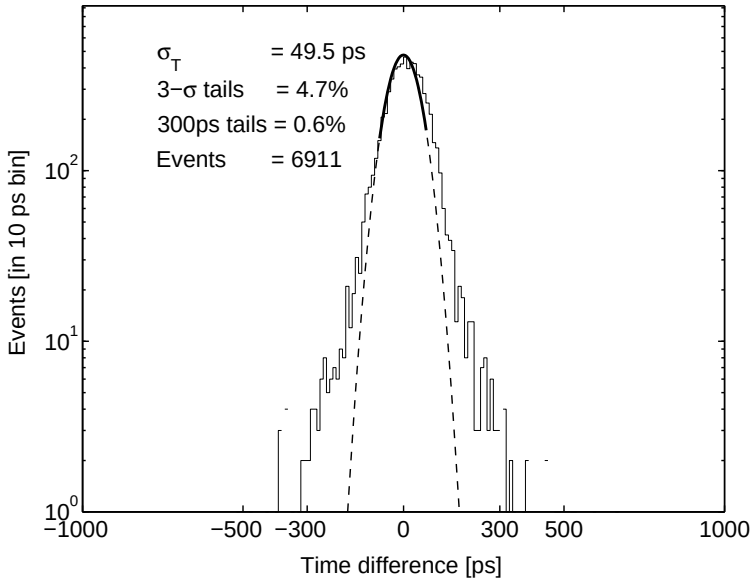

Figure 6.6: Time response of the reference scintillators.

5. *The time distribution of the bulk of particles*: a typical *tof* distribution of the particles impinging over the tRPC is shown in fig. 6.7. It has been obtained with the reference scintillators, measuring over a distance of 18 cm between scintillator centers. The condition of a valid hit in the tRPC has been also imposed.

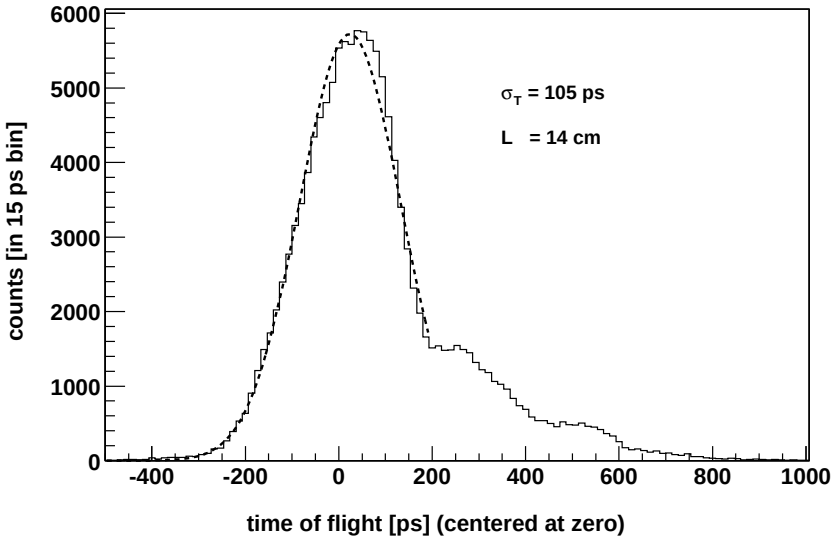

Figure 6.7: Time of flight spectrum measured with the reference scintillators for a separation of 18 cm between centers. The distribution has been shifted to have the zero at the position of the peak.

The time spread of the bulk of particles was much larger than the intrinsic tRPC time response, requiring a dedicated setup for the estimate of the timing performances. For that purpose, a symmetric configuration is chosen, being the reference scintillators placed symmetrically at the same distance from the tRPC (making in total $L = 18$ cm between centers). In that case, the average *tof* between them can be compared with the *tof* measured between one scintillator and the RPC, providing a highly unbiased estimate of the time resolution:

$$\Delta t_{scin-RPC} = (t_{_{RPC}} - t_1) - \frac{t_2 - t_1}{2} = t_{_{RPC}} - \frac{t_2 + t_1}{2} \qquad (6.6)$$

$$\sigma_{_T}^2 = \sigma_{_T}\big|_{_{RPC}}^2 + \frac{1}{4}\sigma_{_T}\big|_{scin}^2 \qquad (6.7)$$

and the intrinsic time response of the tRPC, $\sigma_{_T}\big|_{_{RPC}}$, can be determined from the measured $\sigma_{_T}$ and the combined resolution of the reference scintillators $\sigma_{_T}\big|_{scin} = 50$ ps.

In the following sections it is shown that the peak in fig. 6.7 corresponds, actually, to particles traveling at the speed of light. Therefore, the times

lower than zero must come from the time resolution of the reference scintillators. As indicated in the figure, a value of $\sigma_T \simeq 100$ ps is obtained from a direct fit, indicating that some extra contribution may be present in the timing reference, when measuring in that situation ($L = 18$ cm between centers). When substituted in eq. 6.6, the difference between considering $\sigma_T\big|_{scin} = 50$ ps or $\sigma_T\big|_{scin} = 100$ ps on the estimate of the tRPC resolution is around 10-15 ps, for typical measured values of $\sigma_T = 85$ ps[7]. In the following, the conservative convention of taking, as reference, the nominal scintillator resolution at zero distance $\sigma_T\big|_{scin} = 50$ ps (fig. 6.6) will be adopted.

6.3 The particle environment

The beam of primary nuclei was constituted by C nuclei at $E_{kin} = 1$ GeV/A, expected to impinge over a C target with a thickness equivalent to an interaction probability of 5%. However, a proper focusing of the beam over the target could not be guaranteed.

Measurements of the time distribution of the particles were performed by placing the scintillators at different distances (0, 4, 14, 20, 31 cm), allowing for an estimate of the distribution of velocities of the particles. For that purpose, a Gaussian fit at the maximum of the *tof* distribution was performed, and the time at maximum and width of the distribution were represented in fig. 6.8 as a function of the distance between scintillators. Fig. 6.8 shows a linear trend, as expected, indicating that the Gaussian fit provides a reasonable estimate of the maximum. Moreover, the fit yielded a propagation velocity of $\beta = 0.97 \pm 3$ for the particles at the peak. It is also shown how the width of the scintillator time response increases fast with L (distance of separation) from the value $\sigma_T = 50$ ps, measured at $L = 0$ cm, up to $\sigma_T = 200$ ps, at $L = 30$ cm, due to the different particle velocities. This observation justifies the use of a symmetric trigger, as described in previous section.

6.3.1 β and $\gamma\beta$ distributions

Once β is estimated at maximum, it is possible to obtain the β distribution of all the particles and compare with the expectations from simulation. For the latter, 3 scintillating plastics of 3 cm thickness and an area of 40×40 cm^2 were simulated at the position of the experimental setup, according to fig. 6.4, with a separation of 18 cm between centers. The large used areas provide high statistics over the region of interest, reducing enormously the computing time. For the generation of C+C collisions at 1 GeV/A averaged over all possible impact parameters, URQMD(1.2) was used [142]. The distribution generated was propagated through the HADES geometry implemented with the transport code HGeant/Geant [137], [138].

The output of the simulation was evaluated for two scenarios:

1. Distribution expected over the tRPC (minimum biased).

[7] Decreasing the effect for higher values.

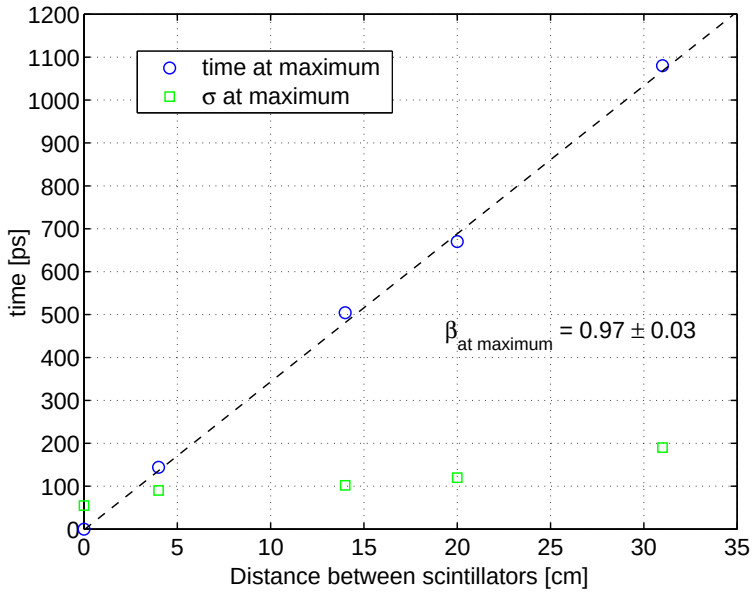

Figure 6.8: Time of flight at maximum as a function of the distance between the scintillator edges. The time at zero distance is defined as zero. From the slope of the fit, the velocity of propagation of the particles populating the peak of the time distribution can be obtained. Squares show the width (σ) of the time distribution indicating a broadening due to the different particle velocities.

2. Distribution expected over the tRPC after fulfilling the trigger requirements (valid signal in the three scintillating plastics), and convoluted with a scintillator time response of $\sigma_T\big|_{scin} = 50$ ps.

The comparison between data and simulation is shown in fig. 6.9. The two curves to be directly compared are the full and dashed ones. In the measured data (full line) there is an excess towards $\beta = 1$, that can be attributed to leptons from secondary processes (as γ conversion), resulting from a bad focusing of the beam. Some features are common to simulation and data: both distributions are cut at $\beta \lesssim 0.4$ due to the energy lost in the first two scintillators; on the other hand, a prominent peak is present at $\beta \sim 0.7 - 0.8$ that is dominated by protons according to simulation, and presumably also in data. In both cases, the correlation observed between the charge released and the reduced momentum $p/M = \gamma\beta$ is in qualitative agreement with a Bethe-Bloch distribution at low values of $\gamma\beta$, as expected for heavy particles (fig. 6.10), while large values of β are much more scattered regarding energy deposition, suggesting that they are dominated by electrons and positrons. The large population of leptons would also point to the observation of rates higher than expected, an effect discussed in the next section.

It must be stressed that fig. 6.9 also indicates that there are differences between the minimum biased distribution of hits over the tRPC and the distribution of triggered events. Whereas this fact avoids to estimate the tRPC response for particles with $\beta < 0.4$, it does not introduce any important bias regarding the distribution of events that truly impinge over the tRPC. In other

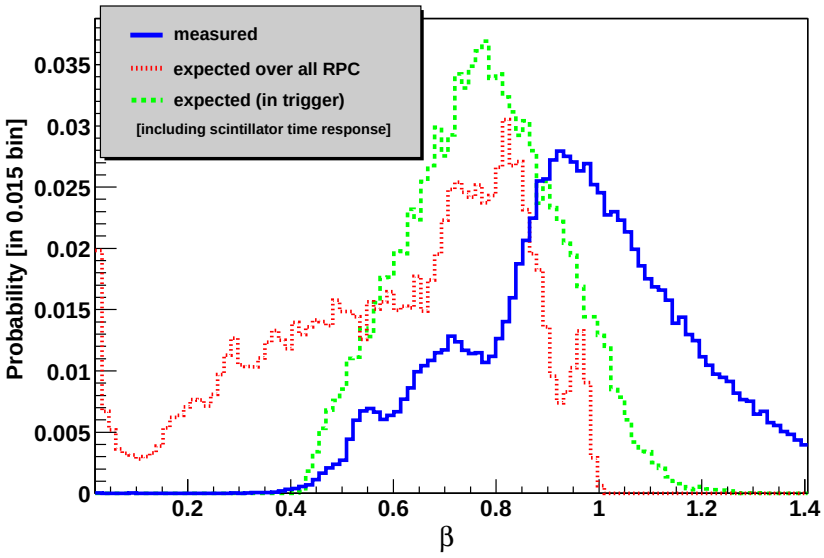

Figure 6.9: β distribution obtained with the reference scintillators and comparison with simulation performed under trigger conditions and minimum biased.

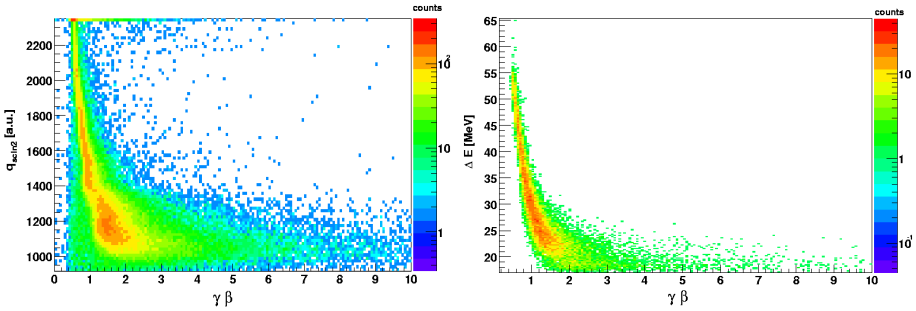

Figure 6.10: Charge in scintillator 2 as a function of $\gamma\beta$ (left). In the right, the energy deposition is shown as a function of the $\gamma\beta$ of the particles, as expected from simulation (the scintillator time response is included).

words, expectedly, highly ionizing particles with $\beta < 0.4$ are detected in the tRPC, despite the trigger selection removes them.

At last, the average beam intensity was monitored during the runs and therefore the expected rate over the tRPC could be evaluated by taking the nominal interaction probability at the carbon target, $P_{int} = 5\%$. This is shown in fig. 6.11 for typical cases: a) measured (see next section), b) simulated, c) simulated in Au+Au, 1.5 GeV/A central collisions for the lower polar angles, with $P_{int} = 1\%$.

The high rates observed when compared with simulation can be explained by assuming a bad focusing, that would result in an increase of secondary electrons

from interactions along the HADES structure. This interpretation is qualitatively supported by fig. 6.9 and fig. 6.10.

In fact, the experimental situation was very convenient for testing purposes: the rates were so high that they reached the maximum values expected in HADES, whereas the distribution of $\gamma\beta$ of the primary particles (and therefore, their ionizations) is reasonably similar to the expected C+C environment (fig. 6.9).

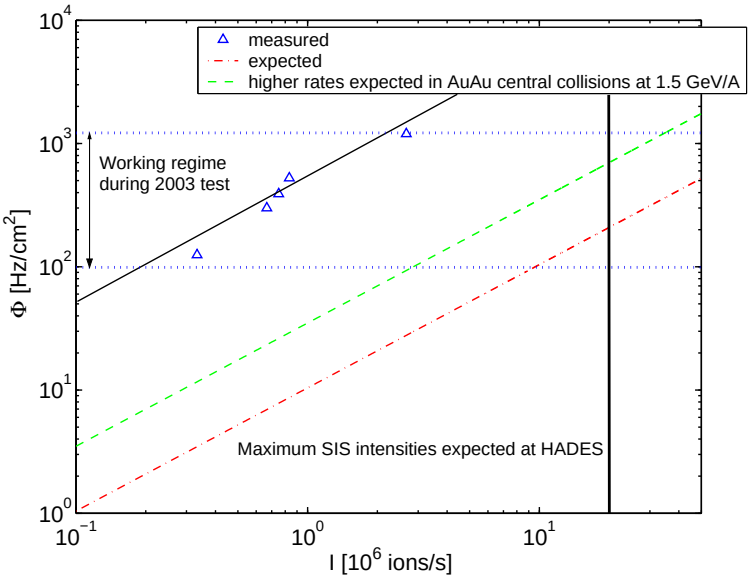

Figure 6.11: Relation between the rate measured and the SIS18 intensity for C+C collisions at 1 GeV/A. The large discrepancies point to a bad focusing. Also shown the expectations for the maximum HADES rates over the tRPC for Au+Au collisions at 1-5 GeV/A at low polar angles. A linear fit to the measured points is also shown.

6.3.2 Primary rate

At the high rates present during the tests, the DAQ system showed a saturation due to its dead-time. Therefore, the use of an auxiliary scaler (Caen 145 quad scaler) was required for unbiased rate estimates (obtained with scintillator *3*). On the other hand, the fact that the beam was pulsed, with roughly 50% duty cicle, and the necessity of a certain number of spills for a reasonable amount of data, indicates that monitoring rate variations within a given run is important. On top, the exact time of each triggered event is known through a free running clock integrated in the acquisition system. For rate estimates, it is convenient to represent the average number of triggered events per spill as a function of the rate over the tRPC. In principle, both magnitudes must show a linear correlation but, due to the DAQ dead-time, a better fit is achieved by using a second order polynomial[8] (fig. 6.12). The parameters from the fit together with the clock

[8] For consistency, the independent term is set to zero in the fit, imposing that both variables tend to zero.

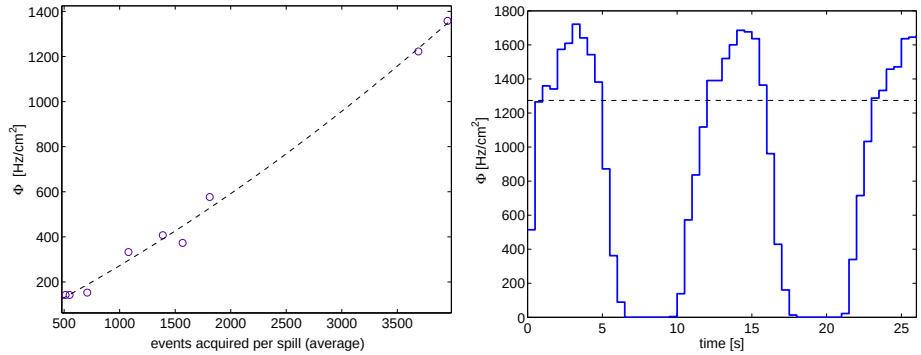

Figure 6.12: Left: curve showing the correlation between the average number of events per spill and the primary rate. Right: spill structure.

allow to monitor the rate and spill structure within a given run, as shown in fig. 6.12 for one of the more intense illuminations ($\Phi = 1240$ Hz/cm^2 in average). The average spill duration is around 6 s.

6.3.3 Spill time profile

It is important to understand the characteristics of the spill profile as a function of time. The two more frequent cases are shown in fig. 6.13[9].

Both sets of data correspond to an average rate of $\Phi \simeq 1200$ Hz/cm^2. The first (left) shows a relatively uniform distribution of the spill while in the second there is a rate reduction with the spill time. Despite the differences, the analysis performed in the following sections has proved to be quite insensitive to the shape of the spill.

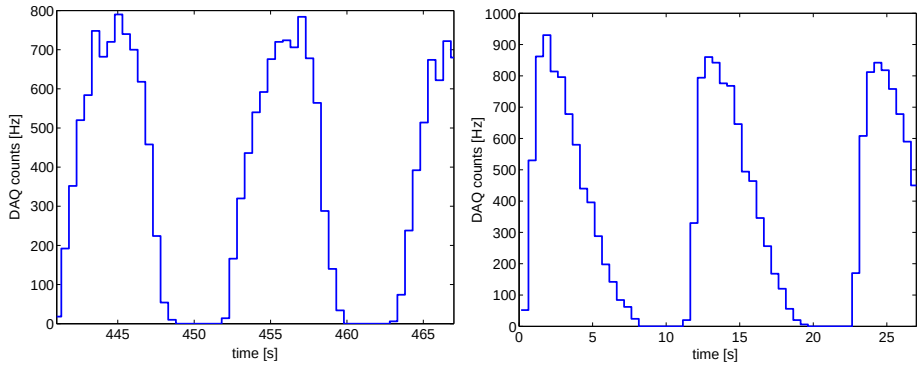

Figure 6.13: Two different spill profiles for the same average primary rate of $\Phi \sim 1200$ Hz/cm^2.

[9]Unstable runs with highly variable rates were also observed, standing for less than 5% of the total. They are disregarded.

6.4 Analysis

Around 2 millions of events were taken under different conditions, and the influence of the variables V (voltage), Φ (rate) and x (position) over the three tRPC cells was studied. Moreover, dedicated runs with high statistics were performed at fixed values of these parameters, allowing studies on *multi-hit* capabilities, performances for *highly ionizing particles*, *signal losses* and *self-calibration*, that are the subject of some of the following sections.

Unless specified, the cuts used are mainly related to the reference scintillators, denoted as *external cuts* (see next section). They must be performed in order to reject random coincidences, inclined particles or edge effects, that would worsen the scintillator time response. These cuts allow for the best timing performances of the reference scintillators, yielding the distribution shown in fig. 6.6, with $\sigma_T = 50$ ps.

Attention is focused on the following observables: σ_T, 3-σ tails, ε, q_{prompt} and $P_{streamer}$ (time resolution, events out of $\pm 3\sigma$ from the time at maximum, efficiency, prompt charge in 200 ns and fraction of streamers, respectively).

6.4.1 Cuts

External cuts (reference scintillators)

1. Overflows in the TDC as well as pedestals in the ADC for the signals of any of the scintillators are removed.

2. Particles within $\pm 2\sigma$ around the peak of the scintillator position distribution are selected, determined through the time difference between both scintillator ends. The cut reduces the fraction of inclined tracks (see fig. 6.14). In the following, y and x are used for referring to the position in $scin_1$ and $scin_2$, respectively.

3. Particles within $\pm 2\sigma$ around the peak of the charge distribution are selected. The cut allows to get the best timing, allowing to reduce edge effects in the scintillators, that very likely produce small amounts of light. See fig. 6.14.

Internal cuts (tRPC)

1. After external cuts, the overflows in the TDC and the charge pedestals in the ADC contribute to the measured inefficiency of the detector and they are removed[10].

This set of cuts is called *soft cuts*. An improvement was seen on timing properties (specially a drastic reduction in timing tails) by performing a cut in the tRPC position at $\pm 1\sigma$ around the peak. The improvement can be ascribed to the presence of a small fraction of inclined tracks or random coincidences in the trigger. This set of soft-cuts plus one on the tRPC position is denoted by *hard cuts*; the last are used only in section 6.6.2 in order to provide an idea of the nature of the tails.

[10] The difference between time efficiency and charge efficiency was very small, having a contribution coming from cross-talk events.

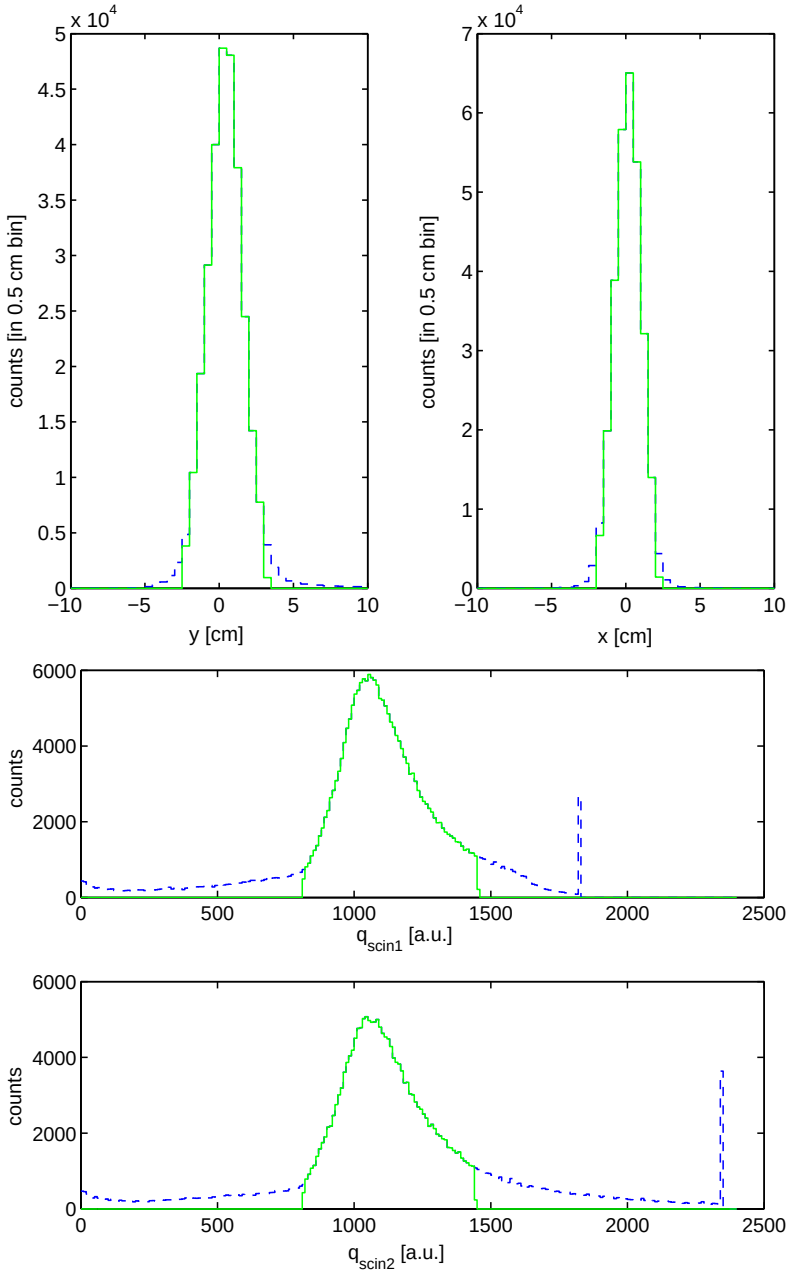

Figure 6.14: Up: quality cuts performed on the scintillator position distribution (in continuous line is the selected region). Down: quality cuts performed on the scintillator charge distribution (in continuous line the selected region). They are shown after the pedestal has been subtracted and the distributions re-scaled for showing an equivalent gain.

6.4.2 q-t correlation

As usual for tRPCs, the most important correlation was observed between the measured time $\Delta t_{scin-RPC}$ (eq. 6.6) and the avalanche prompt charge q_{prompt}. The correction for these 'avalanche size' effects allowed, in the present case, for an improvement of 20-30 ps in the resolution. Such a correction is denoted as *slewing correction* and here it was performed, if nothing is said, as follows:

1. The charge distribution is divided in 12 bins and the average is performed over $\Delta t_{scin-RPC}$ and q_{prompt} in that regions.
2. The time-charge points obtained are interpolated by 1^{st} order polynomials.
3. The average time as a function of the charge, parameterized as described above, is subtracted from the measured time.

The procedure is represented in fig. 6.15, and typical time distributions before and after the 'slewing correction' are shown in fig. 6.16 for tRPC I at V=3.1 kV/gap and $\Phi \simeq 100$ Hz/cm^2.

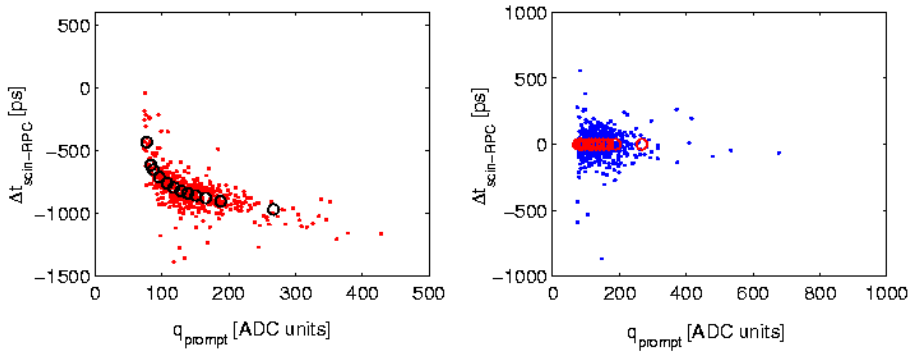

Figure 6.15: Typical charge-time correlation measured (left). The right plot shows the same figure after applying the 'slewing correction'.

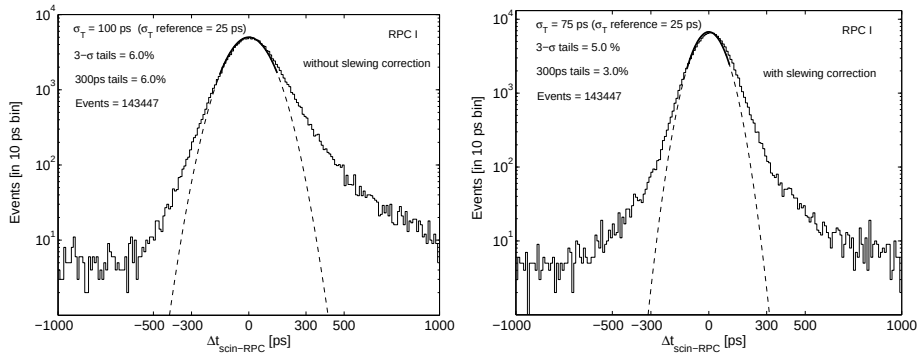

Figure 6.16: Typical time distribution before (left) and after (right) slewing correction.

6.4.3 Time walks

Electronic walks must be conveniently monitored for long term operation [153]. In the present setup, runs were short enough so that the effect of walks was generally small and it was not necessary to correct for it. However, systematic shifts towards large times and small charges were observed, being correlated with the arrival of each spill (fig. 6.17). The effect is important for the higher rates studied, and it is shown in chapter 9 that it can be ascribed to the charging-up time of the resistive plate, that takes place at the scale of seconds.

Incidentally, the correlation appears in data also as a time-charge correlation and its effect is therefore reduced after the 'slewing correction' is performed.

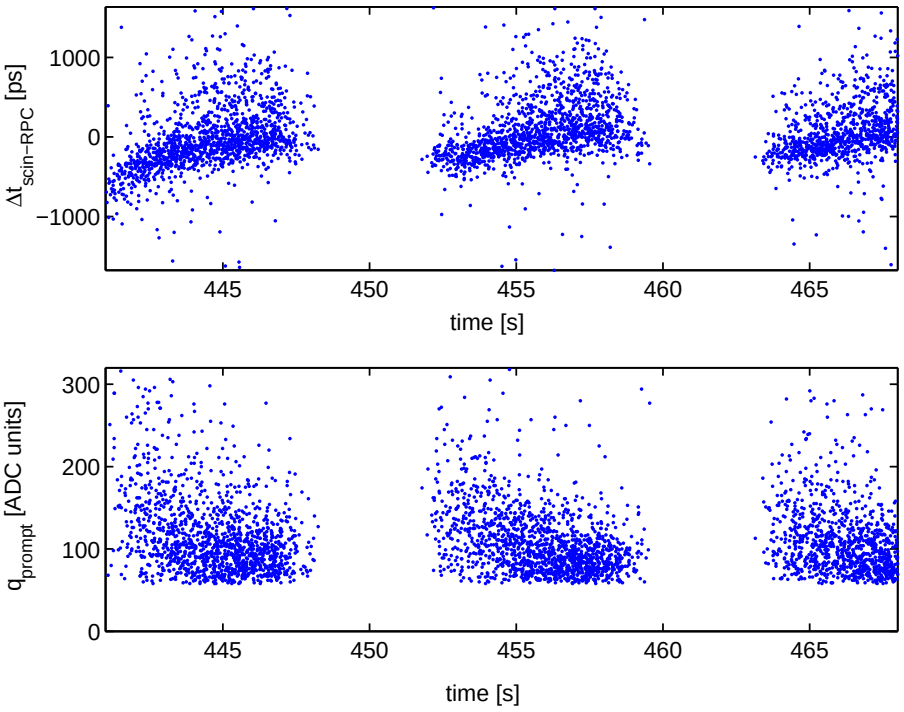

Figure 6.17: Effect of the arrival of the spill over the charge and the time of flight measured, as a function of the irradiation time. The average rate was $\Phi = 1200$ Hz/cm^2 and $V = 3.1$ kV/gap.

6.5 Detector performances

6.5.1 Intrinsic efficiency

For a determination of the intrinsic tRPC efficiency, it is useful to study the behavior of the efficiency as a function of the position (x, y) in the reference scintillators. The study was performed for tRPC *II*, V=3.1 kV/gap, $\Phi \simeq 100$ Hz/cm^2 (the lowest rates studied) without *any* cut. The 2-D profile of the triggered events, together with the efficiency profile, are shown in fig. 6.18. The high statistics of the run allow to state the following facts:

1. Fig. 6.18 down: the profiles of the three tRPCs can be clearly seen in the 2 dimensional scan, showing inefficient regions due to the shielding between cells.

2. Fig. 6.18 up: the trigger line was not crossing exactly the center of the tRPC *II* (as intended), but shifted around 1 cm.

3. Fig. 6.18 up: the position distribution of the triggered events had a major contribution coming from a region $A \simeq 2 \times 2$ cm^2, that would be expected if all the selected particles travel in straight line and the position resolution of the scintillator is not contributing. The presence of sizable tails out of these regions indicates that, with some probability, inclined tracks fulfilled the trigger requirements.

In fig 6.19, an enlightening 1-D plot of the efficiency as a function of the position in scintillator 1 (y) is presented.

From the central peak, an intrinsic efficiency above $\varepsilon = 95\%$ per cell can be inferred. The peaks with high detection probability out of the inner ± 1 cm are due to inclined tracks that cross tRPC *I* or *III*; on the other hand, the valleys with efficiencies around $\varepsilon = 60 - 70\%$ are produced by the dead regions of around 3 mm required for the shielding profiles. It is observed that, due to the presence of inclined tracks in the trigger, the inefficient region extends along $\simeq 2$ cm per side. If only straight tracks were selected, the expected dead region would be as small as 3 mm (see fig. 6.1), showing a clean zero value for the efficiency.

Despite the large intrinsic efficiency, the overall tRPC efficiency obtained for all the triggered events is $\varepsilon = 75\%$, dominated by the dead regions. Due to the fact that the inefficient regions are shared with the neighbors, the following convention was adopted: the *tRPC cell efficiency* is estimated by considering only the contribution of one half of the inefficiency measured (in the absence of cuts). In this way, an estimate of the *tRPC cell efficiency* of $\varepsilon \simeq 87\%$, including geometric effects, is obtained, as compared with the *intrinsic tRPC efficiency* at the level of $\gtrsim 95\%$. The estimate of the intrinsic efficiency requires of enough statistics to perform a meaningful study as a function of the scintillator position and, moreover, does not represent a true estimate of the efficiency of this tRPC system. Therefore, the *tRPC cell efficiency* is preferred in the following.

The intrinsic efficiency determined is still smaller than the values close to 99% measured with similar detector configurations ([153], for instance). It must be recalled that, with the setup used and due to the presence of a small fraction of inclined tracks, it was not possible to get an unbiased measurement of the intrinsic efficiency, but rather a lower limit.

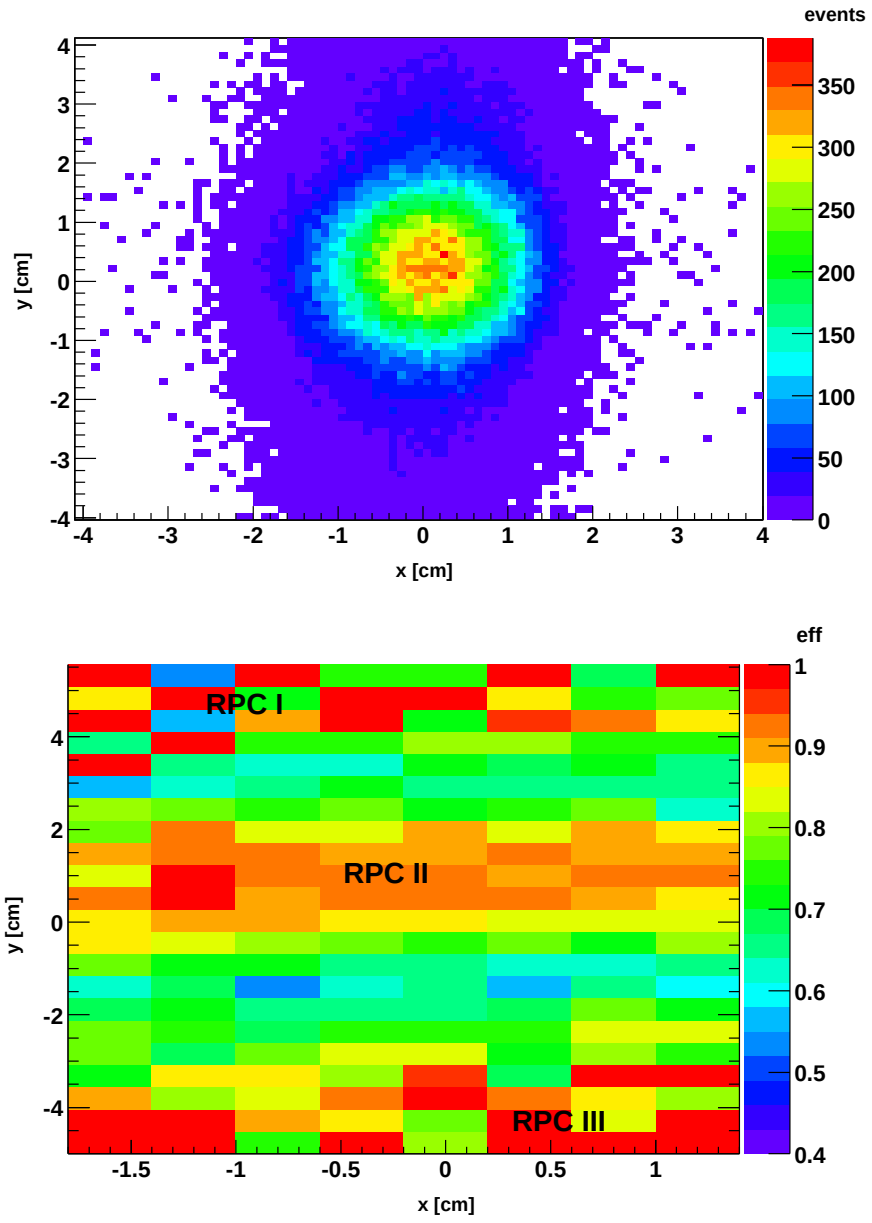

Figure 6.18: The upper picture shows the distribution of the triggered events as a function of the position x (scintillator 2) and y (scintillator 1). In the lower picture, the efficiency profile is shown, suggesting the presence of three tRPCs with dead regions between them.

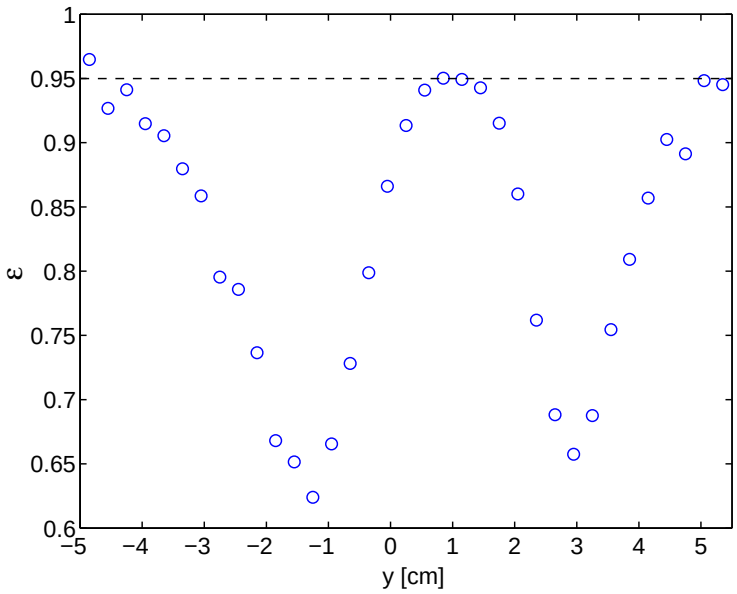

Figure 6.19: Efficiency distribution as a function of the y position along the vertical scintillator ($scin_1$). The maximum of the triggered events is at $y \simeq 0$.

6.5.2 Scan in voltage: *working point*

The 'cell efficiency' and time resolution for tRPC I as a function of the HV per gap are shown in fig. 6.20 for $\Phi \simeq 100$ Hz/cm^2. A small improvement of the time resolution with the applied voltage is visible, as expected, whereas the tRPC cell efficiency increases up to a plateau at around $\varepsilon = 87\%$, dominated by geometric losses.

The streamers begin to be sizable as soon as the efficiency plateau is reached, an effect that could be due to the small concentration of SF_6 in the gas mixture used. However, a contribution below 5% seems to be still affordable regarding performances.

For the dedicated studies on tRPC performances described in the following chapters, the working point was set to $V = 3.1$ kV/gap, where the efficiency plateau begins and the fraction of streamers is still small.

6.5.3 Scan in position: *homogeneity*

Velocity of propagation of the induced signal

The position of the impinging particle can be obtained through the time difference between the left and right ends of the tRPC (eq. 6.4). In the present setup it was possible to shift the tRPC perpendicularly to the trigger line via a motorized translation stage, that allows precisions below the mm. The known displacements of the tRPC could then be compared with the expected from time difference measurements. According to eq. 6.4, the velocity of propagation of the tRPC signal along the electrodes can then be obtained from the measured position as shown in fig. 6.21, yielding $v_{prop} = \frac{2}{3}c$ with residuals below 2 mm.

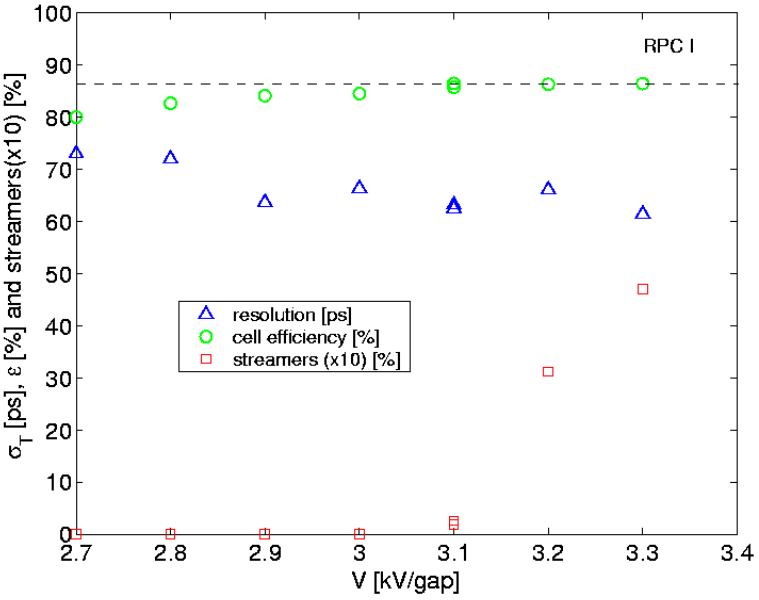

Figure 6.20: Plot showing the cell efficiency and the time resolution for tRPC I (glass electrodes). The efficiency plateau observed at high voltages is dominated by geometric losses. On the other hand, a contribution around 5% of streamers seems to exert no effect.

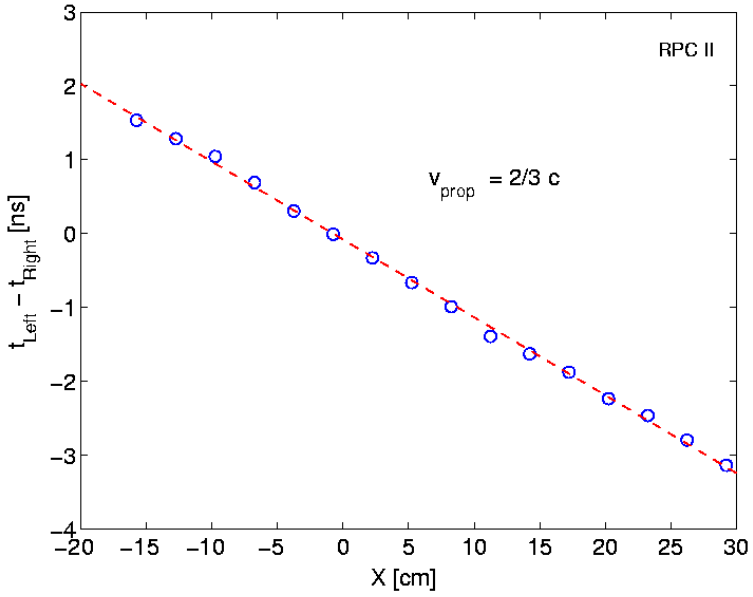

Figure 6.21: Time difference (left-right) for the tRPC *II* as a function of the position. The slope of the linear fit allows to extract the velocity of propagation of the signal, providing $v_{prop} = 2/3c$.

Position resolution

If the trigger area is small enough, the illumination over the tRPC can be considered as 'point like' for practical purposes, and the spread of the time difference between left and right provides an unbiased estimate of the tRPC position resolution. Indeed, the 'point like' condition can be interpreted as the limit where the trigger area is significantly smaller than the tRPC position resolution.

The histogram of $t_{Right} - t_{Left}$ is plotted in fig. 6.22, showing a highly Gaussian behavior with $\sigma = 60$ ps. It must be recalled that, when plotting the time difference between both tRPC ends, the fluctuations due to avalanche formation, that are common, are subtracted. Therefore, the resulting time distribution becomes rather independent from the details of the avalanche formation, being dominated by the electronic jitter $\sigma_{T,el}$:

$$\sigma_{pos} \sim \frac{v_{prop}}{2}\sigma_{T,el} \tag{6.8}$$

The value obtained from fig. 6.22 for the combined electronic jitter[11], 60 ps, is larger than the one measured in laboratory under 'point like' illumination $\sigma_{T,el} \simeq 30-40$ ps. The reason for the discrepancy can be attributed to the large trigger area.

Finally, by using eq. 6.4 and the velocity determined in previous section, the position resolution translates into $\sigma_{pos} = 60$ ps $\times\, v_{prop}/2 = 6$ mm (in fact, the rms of a flat trigger distribution extending over 2 cm is 5.5 mm, suggesting a contribution of the trigger area to the measured position resolution).

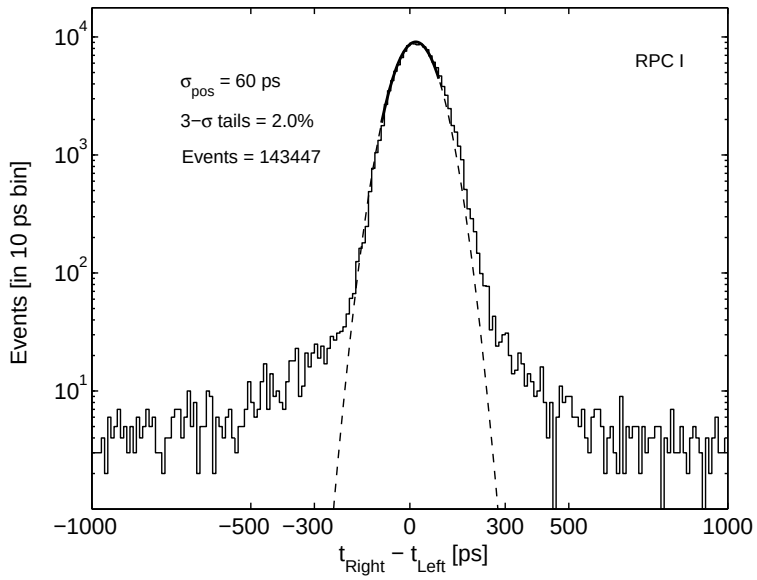

Figure 6.22: tRPC position distribution. The width of the distribution provides an upper limit to the position resolution, $\sigma_{pos} \lesssim 6$ mm.

[11] Combined jitter of the two electronic channels.

Homogeneity

The homogeneity of the main features of the tRPC is of great importance for a long detector, allowing for a direct evaluation of the construction concept. The time response before and after the slewing correction is showing in fig. 6.23, featuring a highly homogeneous behavior for both (all the points are scattered by less than 10 ps around the average value). The fraction of streamers and the average prompt charge are represented in fig. 6.24.

A small decrease in the fraction of streamers is visible towards the inner region of cell *III*, at the level of a 3%; despite being reasonable this could be a signature of non-perfect mechanics for that cell. Due to the influence of the streamers, the average prompt charge is also slightly different in the inner region than close to the edges. However, according to fig. 6.20, a 5% of streamers is perfectly assumable.

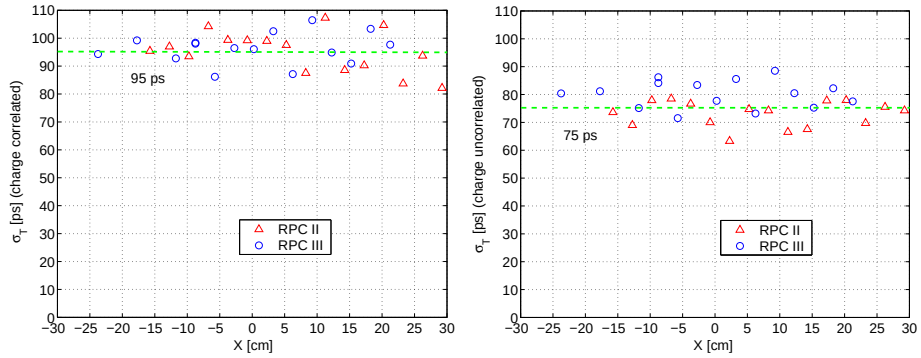

Figure 6.23: Figure showing the time resolution before (left) and after (right) the slewing correction. Such a correction allows, typically, for an improvement around 25 ps, being rather uniform along the detector.

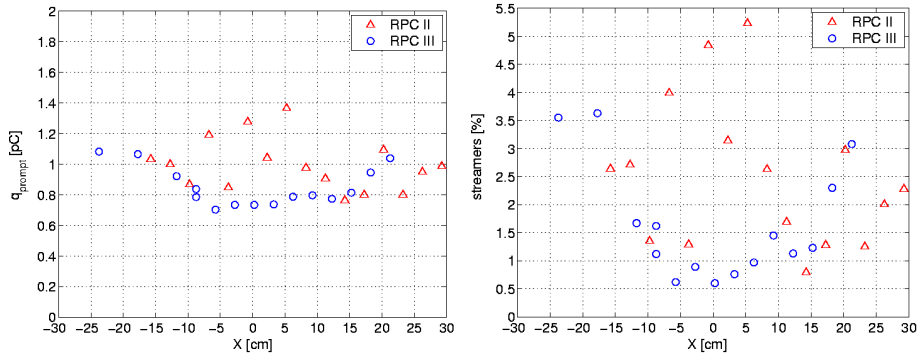

Figure 6.24: Average prompt charge (left) and fraction of streamers (right) for tRPC *II* and *III* as a function of the position. In the absence of streamers the value for the induced charge is $q_{prompt} \simeq 0.7$ pC and it is increased in 30% if they are present.

6.5.4 Scan in rate: *robustness*

The degradation of the performances, due to the accumulation of charge in the resistive plate, is a central feature of tRPCs. For showing the effect, all runs have been grouped together in fig. 6.25, showing the cell efficiency ε, time resolution σ_T and 3-σ tails for different $V = 3.1 - 3.4$ kV/gap. The performances are also represented as a function of the equivalent rate in units of the maximum rate expected in the HADES experiment ($\Phi = 700$ Hz/cm^2), that corresponds to the lower polar angles (see fig. 5.8). Denoting by Φ the primary rate, the curves can be roughly parameterized as straight lines:

$$\varepsilon = 87\% - 1.5\% \frac{\Phi}{100 \text{ Hz/cm}^2} \tag{6.9}$$

$$\sigma_T = 67 \text{ ps} + 4.7 \frac{\Phi}{100 \text{ Hz/cm}^2} \tag{6.10}$$

$$3\text{-}\sigma \text{ tails} = 6.7\% + 0.6\% \frac{\Phi}{100 \text{ Hz/cm}^2} \tag{6.11}$$

A much more detailed analysis on rate effects, together with a theoretical interpretation can be found in chapter 9.

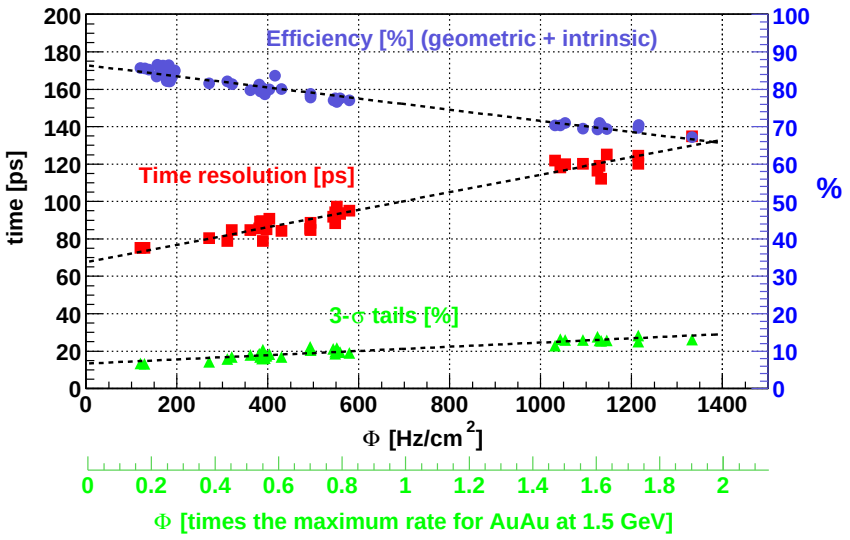

Figure 6.25: Behavior of the tRPC performances as a function of the primary rate. Also shown the equivalent rate in times the maximum rate expected in HADES at the tRPC wall position.

6.6 Specific issues

6.6.1 Induction to walls

Simulation

One drawback of the use of shielding profiles is the loss of signal due to induction to the walls. In the present prototype, it was tried to minimize the geometric losses, therefore the transversal distance from the cell to the walls was reduced down to 1 mm. For evaluating the influence of the walls, dedicated simulations (fig. 6.26) were performed for the same geometry as cell *II* (taken from [154]).

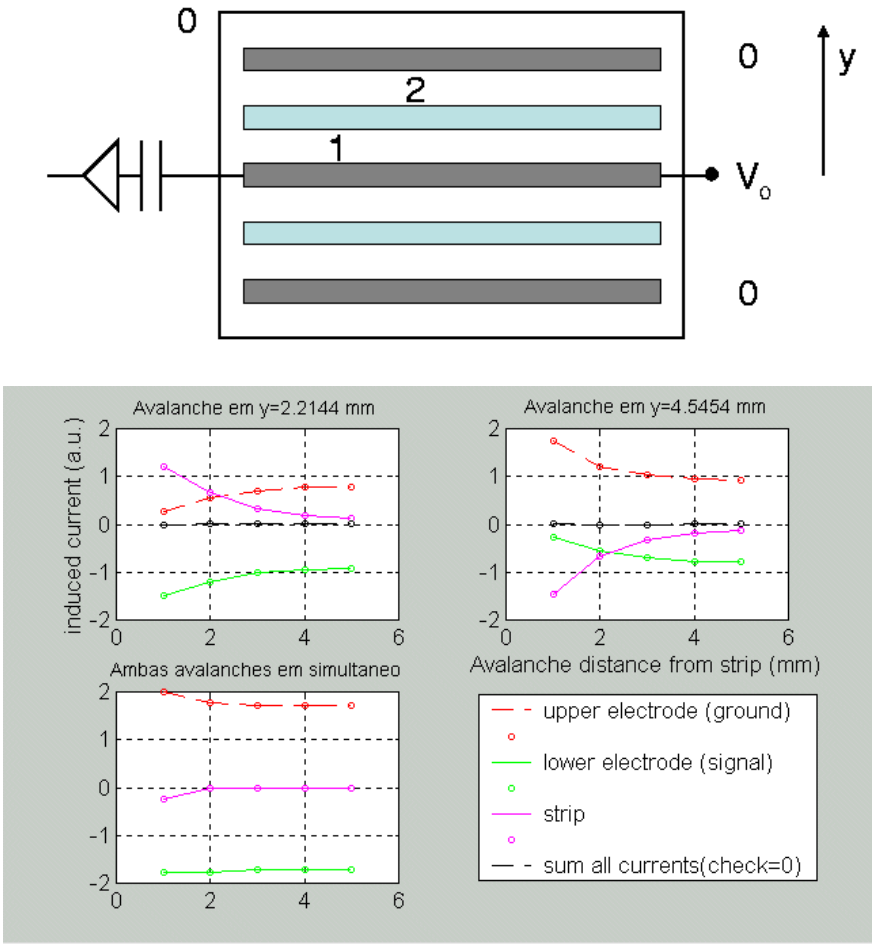

Figure 6.26: Up: configuration over which the weighting field is calculated. Down: results of the induced current, taken from [154], as obtained with the Femlab software [155]. The current is in arbitrary units: lines can be identified by its asymptotic behavior towards the center of the cell (ground is 1, strip(wall) is 0, signal is -1). The first two plots correspond to the induction of avalanches from different gaps, whereas the last corresponds to the case of two avalanches at the same time.

The study was done for the first 2 gaps (the other 2 are symmetric) as a function of the transversal separation from the wall (placed at distance=0), taking, for illustration, a charge at a distance $y = 2/3g$ from the cathode. In fig. 6.26, the expected induced current, $I = \vec{E}_w \cdot \vec{v}_d$ (see section 3.2.6) is represented in arbitrary units. The wall is referred as 'strip' because the charge has been measured through pick-up strips covering the wall (see next sub-section).

Being the glass a symmetry element, the weighting field of the wall shows different signs depending on the gap, and therefore it is expected that the current induced can show different signs. If all the gaps produce the same charge, the induction to the walls is balanced, and the net effect is small.

Data

As said, pick-up strips were placed over the shielding walls for evaluating the signal losses to the surroundings. For most of the avalanches, the signals induced over the strips are typically much smaller than in the case of direct induction over the electrodes, therefore the signal has been shaped and largely amplified for providing measurable values.

First, correlations of the charge in the strip with the time measured in the main cell were studied. Naturally there is an effect, that comes from the q-t correlation itself, but once the slewing correction is performed no residual correlation remains between the charge in the strip and the measured time.

Another possible effect is the loss of events that would be detected normally but fall below threshold after inducing in the shielding walls. For evaluating this, the shape of the charge pedestal of the strip (obtained from events uncorrelated with the trigger) must be compared with the shape of the charge distribution of the strip for those triggered events that have not been detected. If the induction to the walls causes an efficiency loss, it should result in a difference between both distributions. The result of the analysis is presented in fig. 6.27. The charge induced to the walls is shown for all the triggered events (dot-dashed line), together with the charge pedestal of the strip (continuous) and the charge distribution of the strip for non-detected events in the tRPCs (dashed). Differences in shape between the dashed line and the continuous line would indicate the presence of events that have not being detected in the tRPC cell but induced a sizable current on the walls. The figure is very conclusive: no effect above 1% seems to be responsible for efficiency losses, even in the very tight configuration chosen here, with walls placed 1 mm close to the tRPC cells.

Still remains the question of how the ADC deals with the negative induced charges. It is natural to expect that a negative charge will lead to an entry below the pedestal, and indeed that effect is present in fig. 6.27 (up). At last, the correlation between the charge induced to the walls and the charge induced to the electrodes is shown in fig. 6.27. Two branches are visible when the charge collected in the tRPC cell increases; this fact likely indicates that, as expected, both polarities are induced over the shielding walls.

To conclude: the induction to the walls, despite being measurable, could not be correlated with any degradation of the tRPC performances.

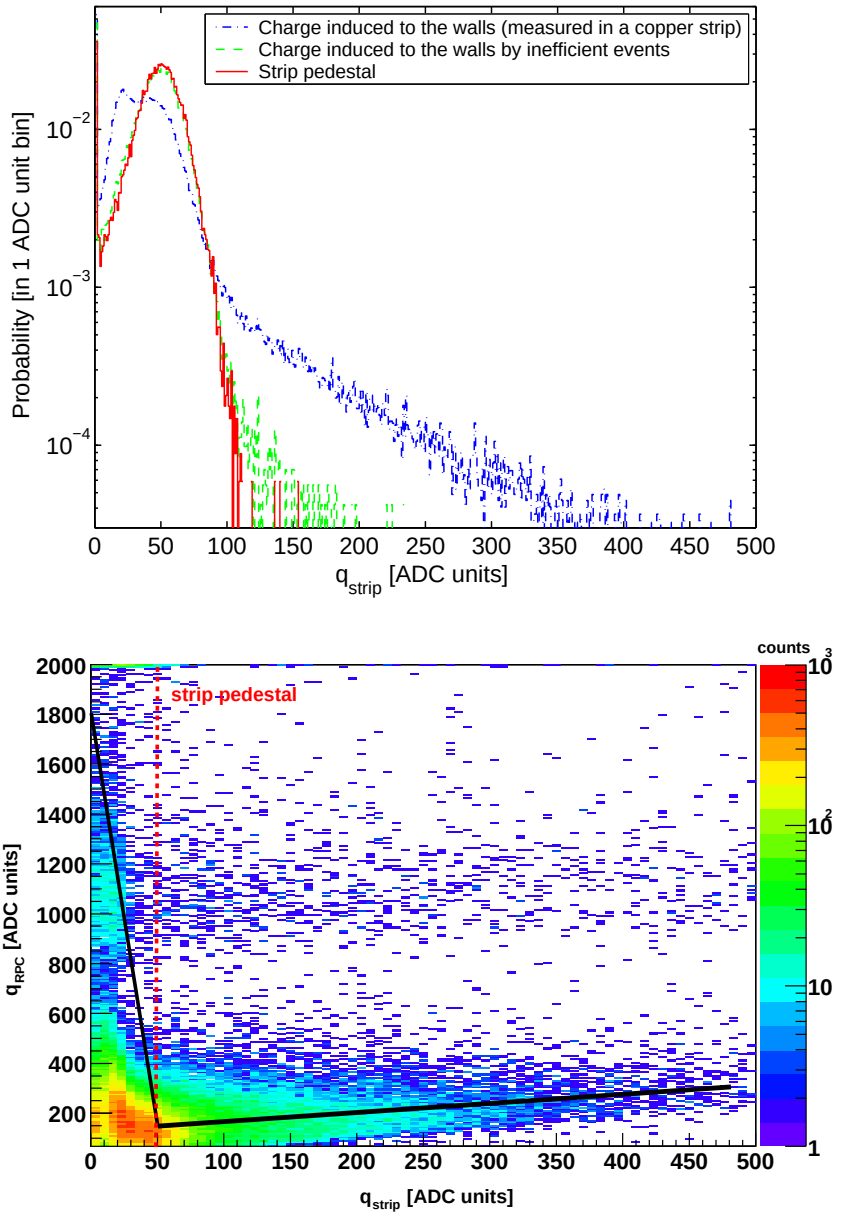

Figure 6.27: Up: charge induced to the walls by all the avalanches (dot-dashed) and non-detected events in the tRPCs (dashed) together with the charge pedestal of the strip (continuous). Down: correlation between the charge induced to the walls and the charge induced to the electrodes, showing two branches. This fact can be considered as an indication of the presence of two different polarizations of the induced signal.

6.6.2 Timing tails

As the timing tails of this prototype are significantly larger than other similar designs [47], a dedicated study was devoted to this feature. It was observed that a fraction of the timing tails appeared also as tails in the tRPC position distribution. As the position distribution is largely independent from the details of the avalanche formation (section 6.5.3), this is an indication that a fraction of the tails have a geometric origin, most probably coming from inclined tracks. Therefore, the influence of a cut in the tRPC position at $\pm 1\sigma$ around the center of the position distribution (called *hard cuts* in section 6.4.1) was studied.

The results are represented in fig. 6.28, showing a drastic reduction on tRPC *III* tails from 7.1% to 1.2%, in better agreement with previous works [47] and recent results on similar prototypes [1]. In the case of tRPC *II*, a sizable amount of tails remains after the *hard cuts*, an effect that can be considered as an indication there is room for improving the mechanics. In particular, tRPC *II* had half the density of spacers than tRPC *III*.

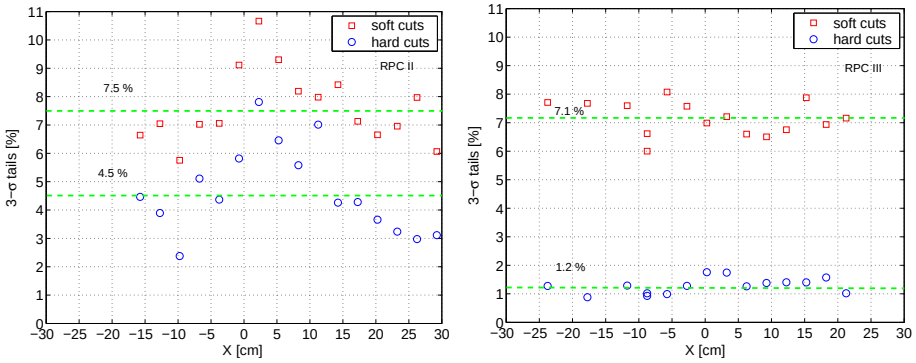

Figure 6.28: 3-σ tails of tRPC *II* and *III* with soft cuts (only external) and hard cuts (extra cut in tRPC position). The improvement is significative.

6.6.3 Multi-hit capability

The feasibility of working in a multi-hit environment is discussed in this section. For that purpose, it was evaluated the influence of cross-talk during signal propagation, that may degrade the tRPC performances when several cells are fired at the same time.

On one hand, it is relevant to know how often a tRPC cell, out of the trigger line, registers a valid time but zero charge, which is the signature of a cross-talk signal correlated with an event crossing the main cell. But, at the end, the multi-hit capabilities are given by the performance of a cell when a hit is simultaneously registered in its neighbor ('coincident' hit). If there is no change in the tRPC response for that case, it will prove that the effect of cross-talk has no practical consequences. For easier treatment, the cell situated across the trigger line is denoted as 'main' while 'neighbor' to any other.

In the present experimental situation, the light beam used (carbon) provided small occupancies of the tRPC cells, requiring a large amount of data in order to provide reasonable statistics for evaluation of multi-hit performances.

As said, a *cross-talk event* is defined by the conditions $q \leq q_{pedestal}$ (zero-charge) and $t < t_{overflow}$ (valid time). With the shielded configuration proposed, cross-talk is kept at a very low level of around 0.5% per neighbor. In particular, the cross-talk of cell I over II is 0.16% whereas II over I is 0.4% and II over III is 1.1%, indicating a slight asymmetry of the effect.

Looking at the time differences (left-right) in the 'neighbor' cell, the position distribution of the induced cross-talk along the 'neighbor' can be represented for signals triggered at a fixed position position in the 'main' cell (center), as shown in fig. 6.29 (left). The distribution of the cross-talk induced extends up to twice the detector length (±60 cm) that could be due to reflections in the detector. Also, in fig. 6.29 (right) the fraction of cross-talk for different positions of the trigger along the 'main' cell is represented. Within the poor statistical significance of the figure (less than 20 events contribute per point) it seems that a slight increase is seen, in fact, towards the center of the cell as it would be qualitatively expected from the calculations of [65].

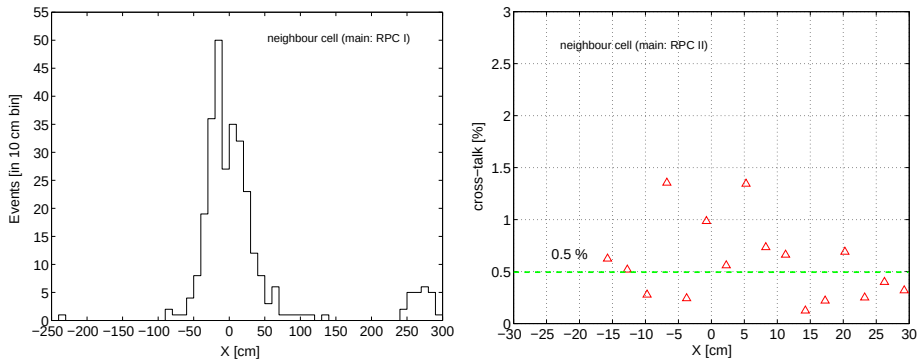

Figure 6.29: Position distribution of the cross-talk induced, obtained through to the time difference at the 'neighbor' cell (left). In the right, the cross-talk probability is shown as a function of the position in the 'main' cell.

For a better understanding of cross-talk, the charge spectra in the 'main' cell is shown in fig. 6.30, together with the 'coincident' hit probability and the 'cross-talk' probability as a function of charge.

The study is performed at $V = 3.1$ kV/gap and $\Phi \simeq 100$ Hz/cm^2 for tRPC cell I and II as the 'main' cell and II and I the 'neighbors', respectively. It is clearly seen a high correlation of the cross-talk with large charge events in the 'main' cell (increasing from 0.1% to 10% with the charge of the avalanche). As expected, the 'coincident' hit probability does not depend on the charge in the 'main' cell. A slight asymmetry on the detector gain is also apparent, being the presence of streamers more likely in cell II, but still below 1%. This can be ascribed to the fact that tRPC I has glass electrodes while tRPC II has metallic ones, being the first more sensitive to rate effects, due to the larger total resistance. Such an effect would result in a decrease of the effective voltage in the gap and, therefore, a lower gain.

At last, the performances are evaluated for the case where two hits are present simultaneously in the 'main' and 'neighbor' cell[12] ('coincident' hit). In

[12] 'Simultaneously' must be understood in the sense of 'within the TDC time window' (1μs).

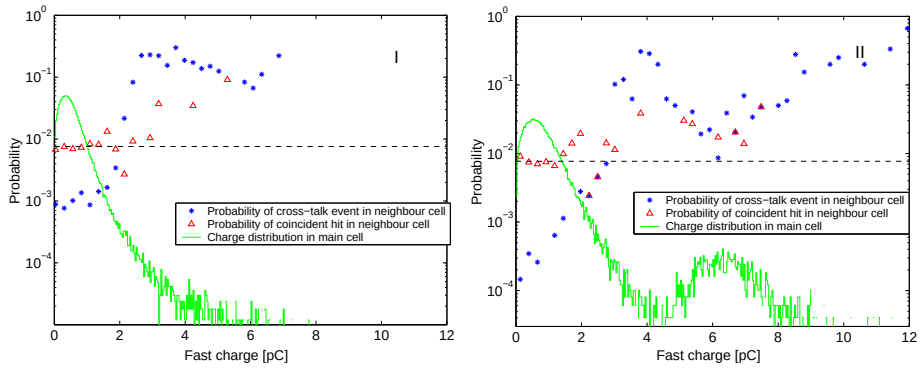

Figure 6.30: Charge spectra for cells I and II in the trigger line ('main' cell) together with the 'coincident' hit and 'cross-talk' probabilities on the 'neighbor'.

order to study the nature of the 'coincident' hits, their position distribution in the 'neighbor' cell is shown in fig. 6.31 (tRPC I is the 'main' cell and II is the 'neighbor'). In the absence of correlation between the 'coincident' hits, and due to the expected largely homogeneous irradiation along the x direction (see chapter 5), a homogeneous distribution of 'coincident' hits should arise. Instead, a shallow peak is shown at $x = 0$, correlated with the trigger position. The same study was performed for the cell II in the trigger line ('main') not showing a peaked distribution. This suggests that the effect is not due to a physical process of the bulk of particles but more likely to inclined tracks that cross both cells ('main' and 'neighbor') in the same triggered event. However, in order to be safe from trigger correlated effects, those events are removed from the sample (fig. 6.31), and the remaining ones are kept for multi-hit studies.

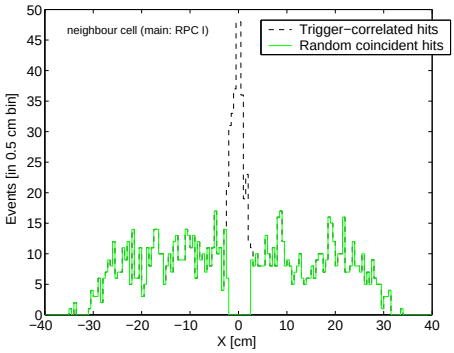

Figure 6.31: Distribution of 'coincident' hits in the 'neighbor' cell. The events at $x = 0$ are correlated with the trigger position, probably due to inclined tracks that cross the 'main' and 'neighbor' cell simultaneously. They are removed from the analysis (dashed line).

The time response for this situation (*truly 100% multi-hit*) is plotted in fig. 6.32 for cell I, not showing any significative degradation. The same analysis was carried out for cell II, and a small degradation seems to be present, in fact, slightly increasing the presence of tails. Results are compiled in table 6.1.

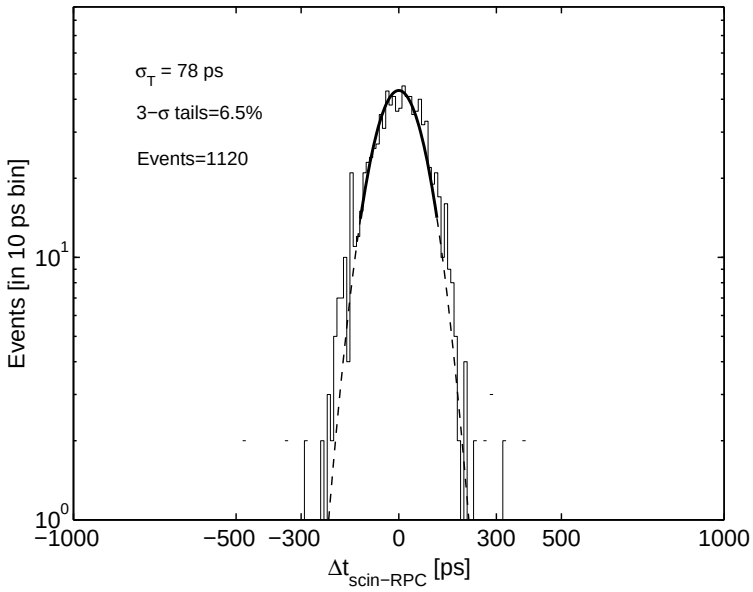

Figure 6.32: Time distribution under multi-hit conditions ('neighbor' cell is firing). The almost unaltered time response as compared with the single-hit situation (see table 6.1) suggests that the cell design provides robust multi-hit capabilities. The contribution of the reference time (25 ps) is included.

It should be noted that a hit in the 'neighbor' cell can influence a simultaneous hit registered in the 'main' cell only in the case that it arrives first. For evaluating this, $\Delta t_{scin-RPC}$ (eq. 6.6) in the 'main' cell is plotted as a function of $\Delta t_{scin-RPC}$ in the 'neighbor' (fig. 6.33) not showing any left-right asymmetry.

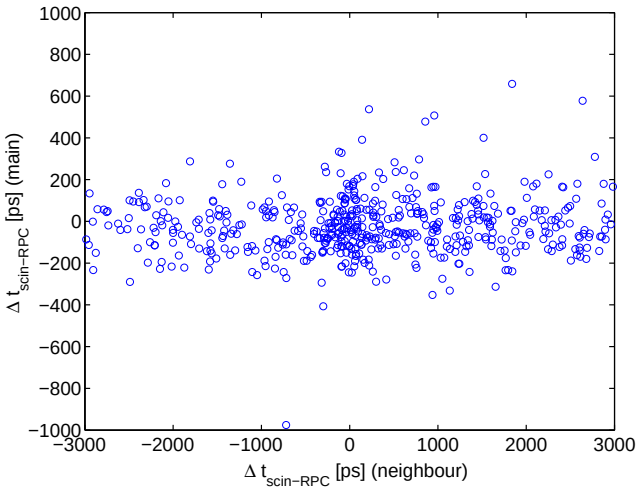

Figure 6.33: Time in 'main' cell as a function of time in 'neighbor' for 'coincident' hits. If some effect is present it must appear an asymmetry in the early branch of $\Delta t_{scin-RPC} < 0$ ('neighbor') as compared to the late.

	Cross-talk			Coincident hit				
main RPC	$I \rightarrow II$	$II \rightarrow I$	$II \rightarrow III$	fraction	σ_T	σ_T^*	tails	tails*
I	0.16%	-	-	0.94%	70 ps	74 ps	5.0%	6.5%
II	-	0.4%	1.1%	0.87%	82 ps	81 ps	6.0%	10.0%

Table 6.1: Results of the evaluation of the multi-hit performances. The star(∗) denotes the result obtained under multi-hit conditions; without star stands for the result under single-hit conditions (the contribution from the reference time has been subtracted).

6.6.4 High and low ionizing particles

It is of interest to analyze the time response for fast and slow particles separately. The presence of the latter may limit the performances in similar physical environments. On one hand, the dependence of the time response with primary ionization is relatively modest (see eq. 3.7); however, on the other hand, large primary ionizations may result in an excess of streamers, having important consequences on the rate capability and the overall tRPC performances.

For this study, 'slow' particles are defined as having $\beta < 0.75$ and 'fast' as $\beta > 0.75$. The separation is done because at that velocity a significative difference in the primary ionization is visible in the reference scintillators (figs. 6.9 and 6.10). With this definition, only 4% of the triggered particles can be considered as 'slow' in the present environment. For not biasing the study, the quality cut on the scintillator charges was performed only towards small charges, otherwise the events under study would be strongly suppressed[13]. Applying this modified quality cut and selecting fast particles, it was obtained for tRPC *II* $\sigma_T = 82$ ps and 3-σ tails = 6.0%, in agreement with the value reported in table 6.1 where the quality cuts had been performed as usual. This is due to the fact that performing a cut at low β is roughly equivalent to cut large scintillator charges. When selecting the slow particles $\beta < 0.75$, a slight worsening of $\sigma_T = 90$ ps and 3-σ tails = 6.0% is observed (see table 6.2).

Natural sources of the difference observed in the time response between fast and slow particles can be either a systematic effect in the scintillator response as a function of the charge released, or the tRPC response itself. However, the small observed increase has no practical consequences and will not be discussed here. Incidentally, the time response for streamers has been studied, and is summarized in table 6.2. Despite the sizable worsening appreciated, it may be of interest for future applications, because the time resolution is still at the level of 100 ps[14].

At last, the tRPC prompt charge was studied as a function of the velocities of the impinging particles, determined with the reference scintillators, and it is shown in fig. 6.34. As a consequence of operation in Space-Charge regime, only a small correlation is present between the average prompt charge and the velocity (ionization) of the particles.

[13] Due to the larger charges released by low β particles.

[14] A direct extrapolation to the operation in streamer mode is, however, not possible, due to the very low thresholds used in avalanche mode as compared to that case.

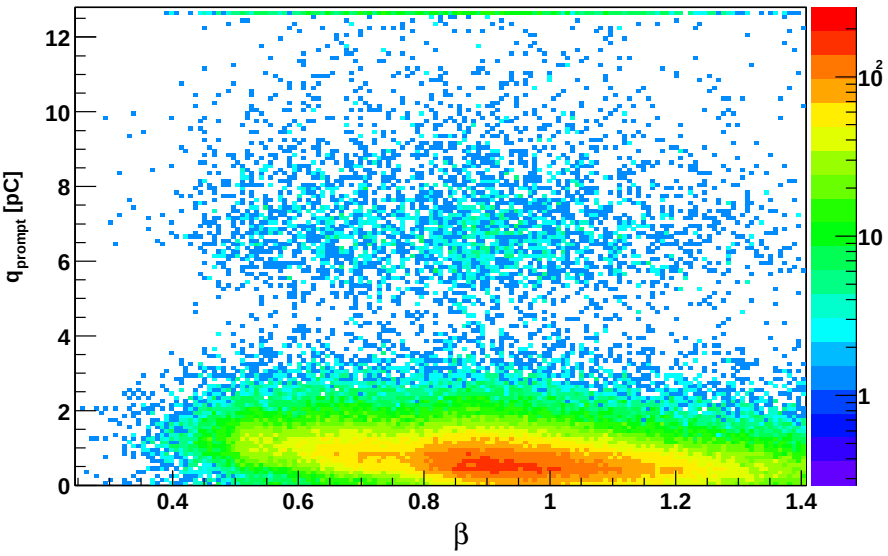

Figure 6.34: Prompt charge as a function of the particle velocities, determined with the reference scintillators. The streamer region appears as a disconnected region at $q_{prompt} > 4$ pC.

As said, more critical would be that the large primary ionizations result in an excess of streamers. This is studied in fig. 6.35, indicating that, in fact, a noticeable increase of the fraction of streamers is present towards small values of β, but still reasonable.

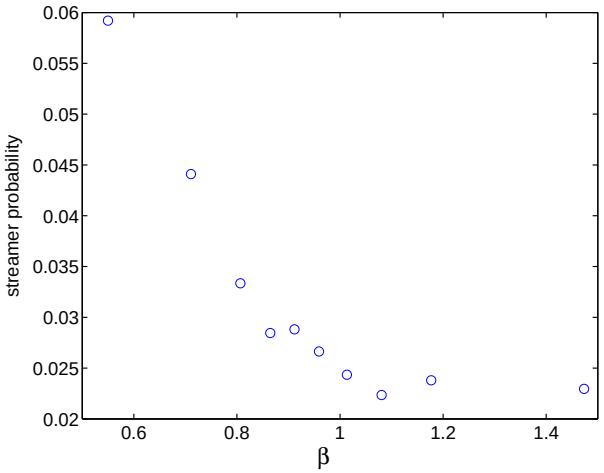

Figure 6.35: Fraction of streamers in the tRPC as a function of the particle velocities, determined with the reference scintillators. The increase towards low velocities is apparent.

	$\beta > 0.75$		$\beta < 0.75$		Streamers	
main RPC	σ_T	tails	σ_T	tails	σ_T	tails
II	82 ps	6.0%	90 ps	6.0%	107 ps	4.0%

Table 6.2: Time response for fast and slow particles.

6.6.5 Calibration (slewing correction)

Calibration from a reference point

In timing RPCs, the measured time must be corrected for the time-charge correlation that is always present. Additionally, in any system, all timing signals must be guaranteed to be isochronous by adequate comparisons among themselves. All these procedures together will be called *calibration*.

If the tRPC has a high homogeneity, it is expected that the calibration parameters can be obtained from any position and used elsewhere. Along the previous sections the slewing correction has been routinely performed as an average over charge slides (section 6.4.2). Despite being an accurate method, it is hard to parameterize. On the other hand, the q-t correlation is well described by a two-segment linear fit when representing 't vs log(q)':

$$t = t_1 + b_1 \log(q) \quad \text{if} \quad q < q_c \tag{6.12}$$

$$t = t_2 + b_2 \log(q) \quad \text{if} \quad q \geq q_c \tag{6.13}$$

In fact, this method for applying the slewing correction has proved to be as accurate as the 'standard method' used in previous sections. Therefore, it was tried with this simple description and the parameters were taken from a reference position ($x = -7$ cm) to perform the slewing correction at any other position along the detector. Different calibration procedures are summarized in (fig. 6.36), all showing a reasonable homogeneity of the time resolution after the calibration.

The parameters obtained from the logarithmic 2-piece linear fit are represented in fig. 6.37 as a function of the position. There is still a 4th independent parameter that accounts for the overall time offset that is of no interest and essentially constant.

It is remarkable that b_2 and q_c are rather homogeneous, whereas b_1 is more fluctuating, due to the smaller amount of events in the region $q < q_c$. The simple parameterization proposed can be of interest for on-line purposes.

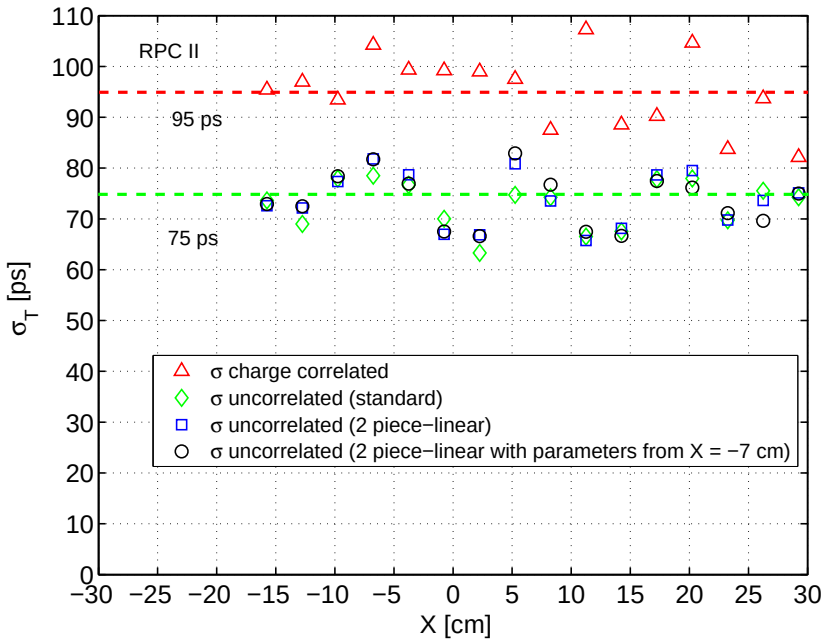

Figure 6.36: Time resolution before and after calibration. There are shown different approaches that lead to similar results.

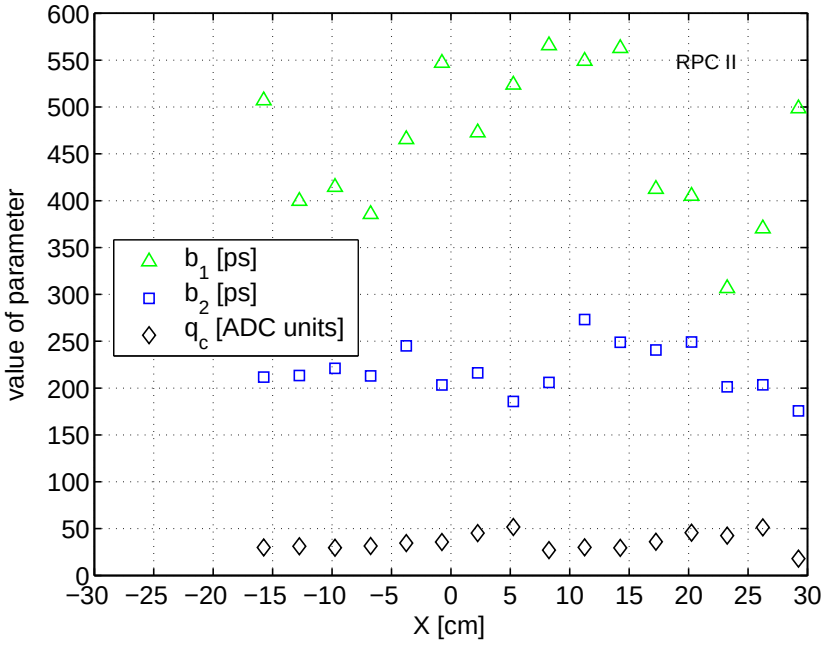

Figure 6.37: Calibration parameters as a function of the position.

Self-Calibration

'Self-Calibration' is defined as the procedure that allows to get the calibration parameters from two tRPCs that share information. In particular, this is the situation when a certain overlap exists between the tRPC cells so that an impinging particle can cross two of them during its flight. In the present case, the second tRPC had to be emulated. For that, the time difference between the times measured with two different tRPCs in two different runs is represented in fig. 6.38[15].

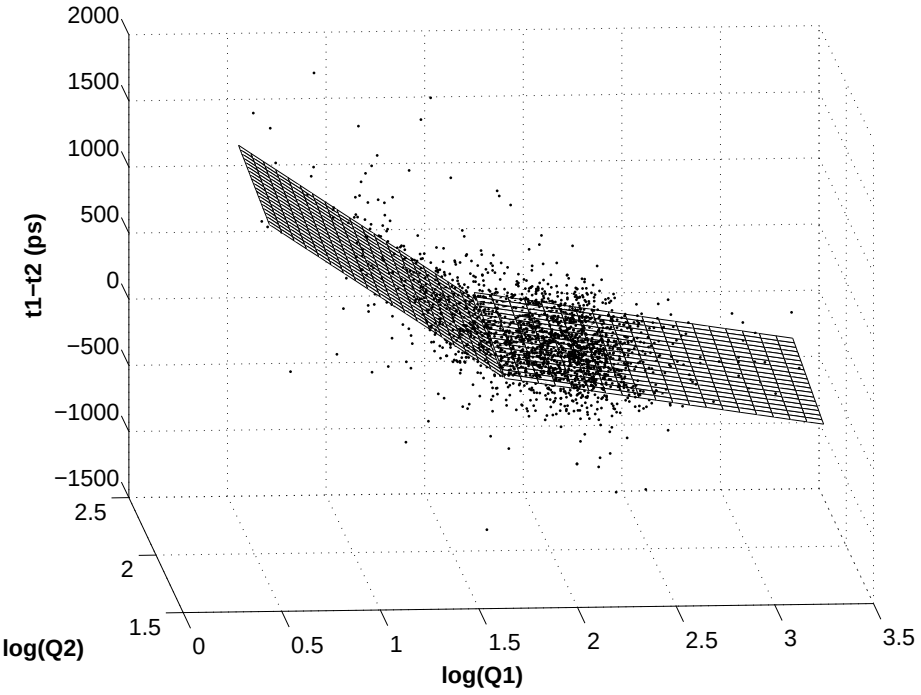

Figure 6.38: Two dimensional picture used for obtaining the calibration parameters in a system RPC-RPC.

Let's take the time and charge information from two different tRPCs, denoted as RPC_1 and RPC_2. In order to derive the time-charge calibration for RPC_1, for instance, only a narrow range of Q_2 is kept close to the maximum of the charge distribution and the points $\Delta t(Q_1, Q_2)$ are fit by a mosaic of two bilinear patches, yielding the required linear correction segments for RPC_1. The parameters for the self-calibration procedure were used at different positions of RPC_1 (in this case tRPC *III*), yielding the output shown in fig. 6.39.

Therefore, it seems possible to use this procedure in the HADES tRPC wall, where overlapping regions are present. In practice, if there is an external way to select 'reference' particles with a well defined time of flight, as photons or leptons, the isochronicity can be obtained even in the absence of overlapping re-

[15] This is a reasonable approximation to the situation where two cells detect the same particle, because in timing RPCs the time response of two overlapping cells is, indeed, largely uncorrelated.

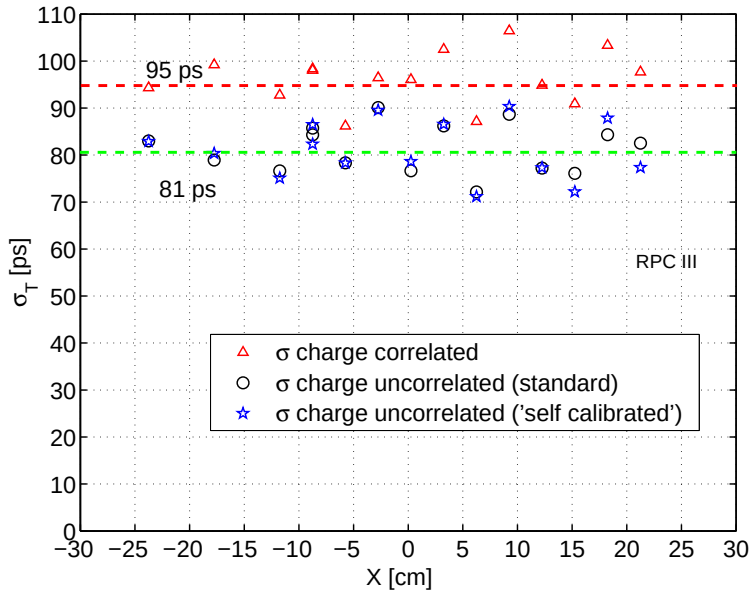

Figure 6.39: Result of the self-calibration procedure for tRPC *III*.

gions. The proposed method is, however, straightforward, having the advantage of being completely stand-alone.

6.7 Conclusions

The feasibility of operating a timing RPC wall in a multi-hit environment, with secondaries coming from nuclear collisions has been shown. The timing resolution of the prototype was at the level of $\sigma_T = 75 - 85$ ps, featuring an intrinsic efficiency above 95% and a robust design, with high homogeneity of the timing properties.

The prototype allows for operation at the higher rates expected in HADES with 10% degradation in efficiency and 25 ps worsening in time resolution. However, further developments, as proposed in chapter 8, are expected to improve the behavior at the highest rates.

Timing tails at the level of 6% are present mostly towards delayed times, not representing a problem for lepton identification in HADES. A study has been performed on the nature of the tails, suggesting that the situation can be improved in the future, reducing them down to 1-2%.

The presence of shielded cells is a robust solution, reducing the cross-talk to less than 1%, mainly triggered by streamers. The necessary shielding requires the presence of geometric voids that reduced the efficiency down to 87% for perpendicular incidence. It is because of this reason that, aiming for a complete geometric coverage, the final design will have 2 layers (section 5.3.2).

Chapter 7

Measurement of the growth coefficient

7.1 Introduction

As mentioned in section 3.2.2, the available models for describing RPC time response agree in that it is governed by the growth coefficient $S = \alpha^* v_e$ [55], [66]. The star stands for 'effective', being $\alpha^* = \alpha - \eta$, i.e., the first Townsend coefficient after corrected for electron attachment, and v_e is the electron drift velocity. S depends only on the properties of the gas and the applied voltage, and it is hence an intrinsic time scale directly determined by the growth dynamics of the avalanche. In fact, before Space-Charge starts to influence the multiplication process, the number of primary carriers grows, in average, as:

$$N_e(t) = N_o e^{St} \tag{7.1}$$

where N_o is the number of primary electrons that contributed to the avalanche. The larger the coefficient is, the faster the avalanche grows and the earlier it reaches the threshold of the FEE comparator. Incidentally (as intuitive) the faster an RPC is (in the sense of S being large) the narrower its time response function and so the better the timing. This assertion is discussed in detail in chapter 9.

For an adequate interpretation of a part of the results discussed in this thesis, it was necessary to determine the behavior of S as a function of the applied voltage for a number of mixtures. Two ways for doing it can be found in literature:

1. The values of α^* and v_e are obtained from simulation packages, as for example MAGBOLTZ [15] (v_e) and IMONTE [16] (α, η).

2. Using the fact that a linear electronic system does not affect the growth coefficient of an exponential signal [151], S can be measured after the amplification stage just by setting two thresholds at different voltages and measuring the delay between the outgoing digital signals. The method requires that Space-Charge is not important at the level of the comparator.

It must be said that currently a controversy exists regarding some of the parameters of the swarm obtained from simulation and data [57].

An elegant, although indirect, way of evaluating the timing properties of an RPC consists in studying the behavior of the time resolution σ_T as a function of the peak delay t_o of the time distribution [156], [157]. It is natural to expect that both magnitudes are related as, in fact, the currently available models suggest [156]; therefore the σ_T vs t_o plots allow to evaluate the RPC time response with some independence of the parameters of the swarm. A typical σ_T vs t_o plot is used, for example, in chapter 8, where the relation is expected to be independent from the value of S. The main short-coming of the approach is that it requires to know the overall offset of t_o and, for this, an estimate of S *is necessary to some extent.*

7.2 The experimental technique

For the measurements, two fast amplifiers and two comparators were required and, therefore, they were retrieved from the FEE described in section 8.2.2.

The RPC signal was split and delivered to two electronic channels with comparator thresholds set at different levels. If the signal is discriminated in the exponential regime, it is then verified that:

$$m_{t_1} = N_o e^{St_1} \tag{7.2}$$

$$m_{t_2} = N_o e^{St_2} \tag{7.3}$$

$$\ln(m_{t_1}/m_{t_2}) = S(t_1 - t_2) \tag{7.4}$$

For simplicity, $m_{t_1} = 2\, m_{t_2}$ was chosen and a factor $\ln 2$ is regained. The setup used consisted in an UV lamp illuminating the cathode of a 1-gap RPC (0.3 mm wide) through a quartz fiber (fig. 7.1). For reducing the internal reflections, the impedance of the detector was matched to the impedance of the FEE. It is very important to ensure that the intensity of the lamp is not high enough to perturb significantly the field in the region of the gap under illumination. In order to eliminate any dynamic effect, S was measured at fixed voltage as a function of the intensity of the lamp: when the value stabilizes, it indicates that the perturbation of the field produced by previous avalanches is negligible.

An overall offset due to cabling is present, being required to periodically determine it by setting both thresholds to the same value. This is the more delicate point: if there is some environmental noise or walks in the channels, the offset may change within the same run, making difficult to get a precise measurement. Such instabilities were observed.

The distribution of t_1-t_2 measured was recorded with a fast TDS7104 oscilloscope (Tektronix), and the average extracted. This is done several times, aiming for an estimate of the error of the measurement.

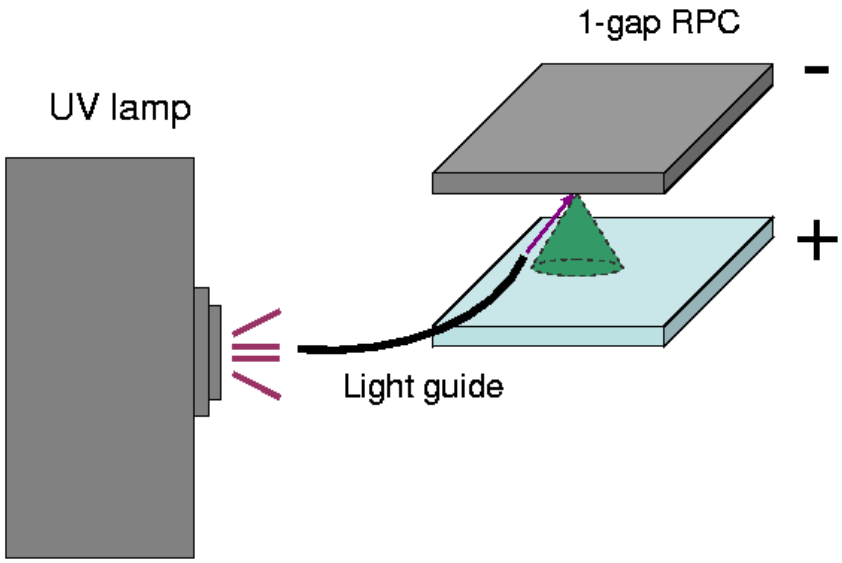

Figure 7.1: Setup used for the measurement of S. The light from the lamp is collected with the guide and driven to the RPC cathode.

7.3 Results

The proposed study consists in determining the growth parameter S for different gas mixtures as a function of the applied voltage. Two of the mixtures considered had been previously used for the studies presented in chapters 8 (Freon/SF_6, 80/20) and 6, 9 (Freon/SF_6/iso-C_4 H_{10}, 98.5/1/0.5) but also Freon/SF_6 at 90/10 and pure iso-butane were measured for comparison. Results are shown in fig. 7.2.

It was observed that above a certain field, owing to the appearance of streamers, the drop in the resistive plates prevents further growth of S. Therefore, the values of S are represented up to the point where the voltage drop starts to be important, showing a roughly linear behavior. It must be stressed that the largest achievable value of S represents an important quality figure for a timing gas.

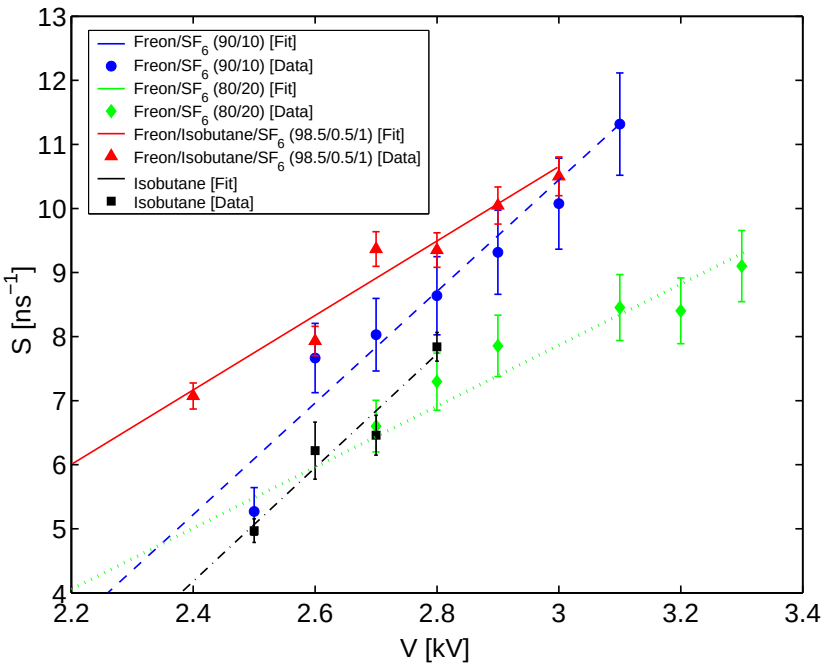

Figure 7.2: Avalanche growth coefficient S measured as described in text for different mixtures. Although the error bars are large, all the curves seem to indicate a linear behavior. The best fit is also shown.

7.4 Conclusions

The avalanche growth coefficient S has been measured for a number of mixtures, suggesting a linear behavior, in qualitative agreement with the expectation from simulation [57]. The behavior of S vs V is in agreement with values measured before for the standard mixture (see [57] for example), indicating that S changes little for small variations of the gas concentrations around the standard mixture. An excess of SF_6 seems to worsen the performances (in accordance with [49]) and iso-butane shows the worst timing properties of the mixtures studied. However, the statistical significance of the data is poor in the present setup and further investigation is required after improvements on the stability of the system.

The following parameterizations were obtained:

$$S[\mathrm{ns}^{-1}] = (8.4 \pm 1.0)V[\mathrm{kV}] - 14.8 \pm 2.8 \quad \mathrm{Fr/SF_6}\ (90/10) \tag{7.5}$$

$$S[\mathrm{ns}^{-1}] = (4.3 \pm 1.0)V[\mathrm{kV}] - 5.3 \pm 2.7 \quad \mathrm{Fr/SF_6}\ (80/20) \tag{7.6}$$

$$S[\mathrm{ns}^{-1}] = (6.0 \pm 1.2)V[\mathrm{kV}] - 7.2 \pm 3.1 \quad \mathrm{Fr/Is/SF_6}\ (98.5/0.5/1) \tag{7.7}$$

$$S[\mathrm{ns}^{-1}] = (8.4 \pm 2.4)V[\mathrm{kV}] - 15.8 \pm 6.6 \quad \mathrm{Is} \tag{7.8}$$

A better characterization of the studied gases, in view of a realistic application, would require to determine the ionization mean free path λ (equivalently, the average number of ionization clusters per gap $n_o = g/\lambda$), that is not accessible with the present setup.

Chapter 8

Increase of rate capability with T

8.1 RPC behavior at high rates

8.1.1 The DC model

It is well known that the rate limitation of RPCs is related to the total resistance of the plates. Roughly speaking this means that, when an avalanche is produced inside the detector, the field is locally perturbed during a characteristic time $\tau_g \sim RC$ (R and C are the resistance and capacity of the plates, respectively). The perturbation affects the forthcoming avalanches, and mimics, in average, a situation where the electric field is lower than the applied one. It has been shown in the introduction (section 3.2.7) that, in a first approach, it is enough for describing rate effects to consider the average ohmic drop in the resistive plates, according to the Ohm's law [158]:

$$\bar{V}_{gap} = V - \bar{I}R \tag{8.1}$$

that can be rewritten as:

$$\bar{I} = A_g \varepsilon \phi_i \bar{q} \tag{8.2}$$

ϕ_i stands for the irradiation over the RPC in units of $[\mathrm{L}^{-2}][T^{-1}]$, ε is the probability of inducing an avalanche per incoming particle, A_g is the illuminated area and $\bar{q}$ the average charge released per avalanche[1].

When working with MIPs, ε is close to 100%. However, in the particular case of illumination with 1 MeV γ photons it is typically as small as 1% [158]. Besides that, the characteristic charge spectra of γ's for multi-gap RPCs does not exhibit a shallow peak as in the case of MIPs, being rather exponential instead (fig. 8.4). As the minimum threshold reachable in the comparator is limited by the noise level, it is difficult to avoid that an important fraction of the avalanche spectra is not detectable in that case.

The remark is important because quite often, and in particular for the measurements performed along this chapter, Na^{22} or Co^{60} γ-emitters are used for

[1] For simplicity, the total charge is denoted just by q and the prompt charge by q_p in the following.

testing RPCs. It is not the purpose of this chapter to provide an estimate for ε, thus the impinging rate times the efficiency is simply re-defined as the *primary rate* over the RPC $\phi_p = \varepsilon\phi_i$, i.e., *able to produce an avalanche*:

$$\bar{I} = A_g \phi_p \bar{q} \tag{8.3}$$

So, eq. 8.1 can be expressed as:

$$\bar{V}_{gap} = V - \phi_p \rho d \bar{q} \tag{8.4}$$

where d is the resistive plate thickness per gap and ρ its resistivity.

On the other hand, in the absence of dynamic effects in the plates and once the properties of the gas (P, T, gas admixture) and the size of the gap are fixed, the average charge is related to the voltage in the gap through a *characteristic curve*:

$$\bar{q} = F(V_{gap}) \tag{8.5}$$

that can be extrapolated to a dynamic situation as:

$$\bar{q} \simeq F(\bar{V}_{gap}) \tag{8.6}$$

This relation establishes a 'feedback' in the drop process given by eq. 8.4. Let's assume for illustration that V is constant and the only free parameters are ρ, ϕ_p and d. Therefore, working on expression 8.4:

$$\bar{V}_{gap} = V - \phi_p \rho d F(\bar{V}_{gap}) \tag{8.7}$$

$$\frac{V - \bar{V}_{gap}}{F(\bar{V}_{gap})} = G(\bar{V}_{gap}) = \phi_p \rho d \tag{8.8}$$

$$\bar{V}_{gap} = G^{-1}(\phi_p \rho d) = f(\phi_p \rho d) \tag{8.9}$$

As a conclusion, if the performance of the RPC is ruled by the average effective field $\bar{V}_{gap}$, then any RPC observable O is just a function of $\phi_p \rho d$ for a constant applied field: $O|_V = O|_V(\phi_p \rho d)$. This is denoted as the *DC model*.

As the rates attainable are imposed by each particular application, the only quantity left for optimization is the 'column resistivity' ρd. Therefore, to operate an RPC at high rates requires to reduce ρd as much as possible within practical limitations (for a complete discussion on what 'practical' means see, for instance, [98]).

It is convenient to define the *relative rate capability* as $\kappa = \frac{\rho_o d_o}{\rho d}$ so that $O|_V = O|_V(\phi_p/\kappa)$: if κ is increased by a factor N, then the RPC can work at N times the nominal operating rate with equivalent performances (this is, indeed, a natural definition for the relative rate capability).

Unfortunately, the simple DC model could be not everything. An RPC observable may be also sensible to the fluctuations of the field in the gap, i.e. to $\mathrm{rms}_{V_{gap}}$ [60], [61]. This represents a delicate point, as the time resolution is a second moment and therefore *a direct estimate of the fluctuations*.

Along the present chapter, the RPC behavior is studied by assuming that the DC model is accurate enough to reproduce the observables, and a dedicated study of the fluctuations is given separately in chapter 9. In order to apply the DC model it will be useful to follow the descriptions of [54] and [58] for trigger

RPCs, and the observations on timing RPCs [56], [68], and therefore assume that the 'characteristic curve' $\bar{q}$ vs V_{gap} of a tRPC under strong Space-Charge is reasonably well described by a linear trend:

$$\bar{q} = a(V_{gap} - V_{th}) \tag{8.10}$$

V_{th} stands for the voltage at which Space-Charge starts to dominate; below it, the RPC enters in the proportional regime, so the gain goes exponentially to zero and the RPC is 'switched off'. Inserting the relation 8.10 in eq. 8.7:

$$\frac{\bar{q}}{a} + V_{th} = V - \phi_p \rho d \bar{q} \tag{8.11}$$

and solving the equation:

$$\bar{q} = \frac{a(V - V_{th})}{1 + a\phi_p \rho d} = \frac{\bar{q}(V, \phi_p = 0)}{1 + a\phi_p \rho d} \tag{8.12}$$

inspired by G. Carboni et al. [58].

8.1.2 RPC behavior under temperature variations

It is known that the resistivity of many ion conductors follows the Arrhenius-Rasch-Hinrichsen law [74]:

$$\ln \rho = a + \frac{b}{T} \tag{8.13}$$

which can be conveniently represented for narrow temperature ranges as:

$$\rho = \rho_{T_o} 10^{(T_o - T)/\Delta T} \tag{8.14}$$

In particular, the relation has been proved for glasses that contain a certain fraction of some alkali metal [74]. It is expected that standard float glass shows an ion conductivity related to the flux of Na^+ ions. They are present in the form of NaO_2 (sodium dioxide or soda) with typical concentrations of 15% (SiO_2 (75%) + NaO_2 (15%) + CaO and others (10%))[74]. As expected, the glass used for the construction of the tRPCs tested along this chapter has a resistivity that follows the law 8.14, as shown in fig. 8.1 (taken from [59]).

According to the ideas developed in previous sections, it seems that it can be made use of the exponential decrease of the resistivity with the temperature to exponentially increase the rate capability $\kappa = \frac{\rho_o d_o}{\rho d}$. This fact has been already demonstrated by C. Gustavino et al. [73], in the case of trigger RPCs working with MIPs (cosmic rays) over 16 °C variation, showing no aging up to 30 °C variation. In this work, an extension to timing RPCs of this earlier work is proposed, varying the temperature in 42 °C.

It must be taken into account that, when changing moderately the temperature or pressure of a gas, its density scales as:

$$\eta \propto \frac{P}{T} \tag{8.15}$$

On the other hand, the properties of ionized gases are known to depend on the reduced electric field E/η (see chapter 2). For coping with changes of the density of the gas, the reduced voltage is defined as:

$$V^* = V\frac{\eta_o}{\eta} = V\frac{P_o}{P}\frac{T}{T_o} \tag{8.16}$$

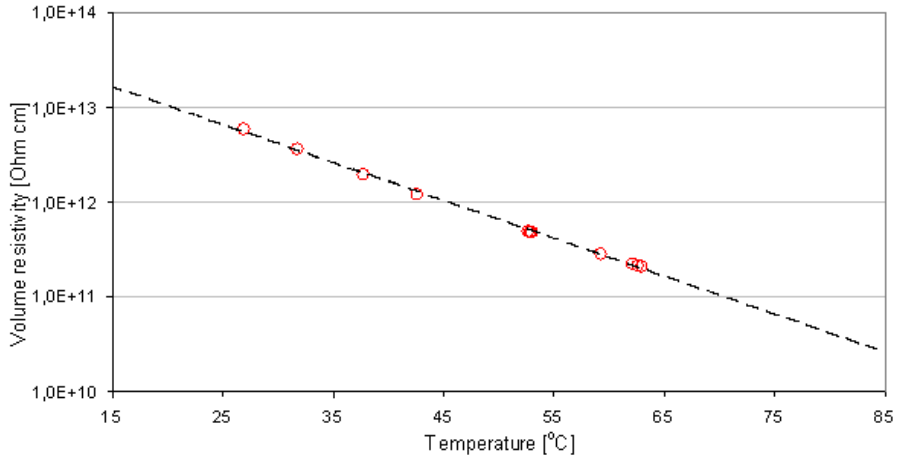

Figure 8.1: Resistivity as a function of the temperature for the glass used. The behavior is described by $\rho = \rho_{T_o} e^{-(T-T_o)/\Delta T}$, with $\rho_{T_o} = 10.5\ 10^{12}$ Ωcm, $T_o = 293$ K, $\Delta T = 25$ K.

and, by analogy:

$$\bar{q} = a(V^*_{gap} - V_{th}) \tag{8.17}$$

$$V^*_{gap} = (V - A_g \phi_p \bar{q} R)\frac{\eta_o}{\eta} \tag{8.18}$$

For taking into account the variation of the gas density when changing T, the reduced voltage applied V^* has been kept constant along the measurements. In this way, the RPC performances are not expected to change, as long as the ohmic drop in the glass is negligible.

Equation 8.12 can be now re-written as:

$$\bar{q} = \frac{a(V^* - V_{th})}{1 + ad\phi_p \rho(T)\frac{\eta_o}{\eta}} \tag{8.19}$$

The chamber was operated at a pressure slightly above the atmospheric one, for allowing the circulation of the gas. In the following it is assumed that P is not changing importantly during the data taken. Therefore:

$$\bar{q} = \frac{a(V^* - V_{th})}{1 + ad\phi_p \rho(T)\frac{T}{T_o}} \tag{8.20}$$

as a function of V (applied field), ϕ_p (primary rate) and T (temperature). Using eq. 8.18, the behavior of the reduced voltage in the gap can be also derived:

$$V^*_{gap} = V_{th} + \frac{(V^* - V_{th})}{1 + ad\phi_p \rho(T)\frac{T}{T_o}} \tag{8.21}$$

and the relative increase of the rate capability as function of the temperature is given by:

$$\kappa = \frac{\rho(T_o)}{\rho(T)}\frac{T_o}{T} \tag{8.22}$$

8.2 The experiment

8.2.1 Goal

Merging the ideas discussed in previous sections, one could aim to describe the behavior of a timing RPC under temperature variations of some tens of degrees, and check that the increase in the rate capability matches the expected from the measured behavior of the glass resistivity (fig. 8.1). The observables studied are the time resolution σ_T, peak time t_o, efficiency ε, prompt charge $\bar{q}_{prompt}$ and dark counting rate. The time difference between both ends of the detector allows for a direct determination of the position x, that is also used in the following.

The ultimate goal is to show that the operation of a timing RPC under modest variations of the temperature is feasible and that an improvement on the rate capability up to an order of magnitude in 25 °C can be achieved (according to fig. 8.1), while keeping unaltered the performances.

8.2.2 Setup

The tRPC chamber was described in section 6.2.1, in particular tRPC *I* (glass electrodes) has been used. The HV scheme is shown in fig. 6.1, varying from 2.6-3.2 kV/gap, and the gas mixture was constituted by $C_2H_2F_4$ and SF_6 (80/20). The FEE boards were developed in the framework of the HADES experiment [159], and they were put at both ends of the cell for providing the position and the time of flight of the impinging particles.

The main differences between the FEE used here and previous designs [151], were that a) the dead-time of 1 μs at the level of the comparator was implemented through 2 flip-flops and a digital delay, b) the electronic components had been also updated to a Philips BGA-2712 pre-amplifier and a dual comparator AD96685, c) the topology was completely different owing to HADES space constraints. A picture of the FEE board is shown in fig. 8.2 and details can be found in [159].

The analog signal was buffered after amplification and later shaped before going to a 2249W Lecroy ADC that provided the charge integrated over 200 ns. For the digital part, a 2228 Lecroy TDC with 50 ps bin width was used. All modules are CAMAC based. The threshold of the comparator was set to 10 mV.

The tRPC gas box was placed inside a sleeve that could be heated at will. For providing an adequate and controlled heating system it was made use of the well known PT100 sensors (Platinum Resistance Thermometers). They are affordable, easy to use, and allow to measure temperature variations in the scale of a fraction of degree, as it was required. A picture of the setup is shown in fig. 8.3.

High primary rates over the tRPC were achieved by illumination with a Na^{22} source together with a Co^{60} source of similar intensity, both 'point-like'. According to [160] Na^{22} decays in a β^+ process, following:

$$Na^{22} \rightarrow Ne^{*22} + e^+ + \nu_e \tag{8.23}$$

$$Ne^{*22} \rightarrow Ne^{22} + \gamma(1.274) \tag{8.24}$$

and the resulting γ spectrum contains photons coming from positron annihilation ($E = 0.511$ MeV) and from Neon de-excitation ($E = 1.274$ MeV).

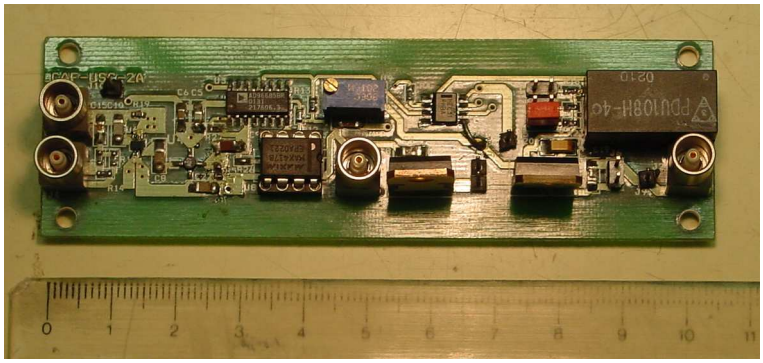

Figure 8.2: Picture showing a 2-channel board as the one used for these tests. The larger component is the digital delay, regulators are visible in the lower-right part. The small chips towards the left of the board (input signal) are the amplifiers.

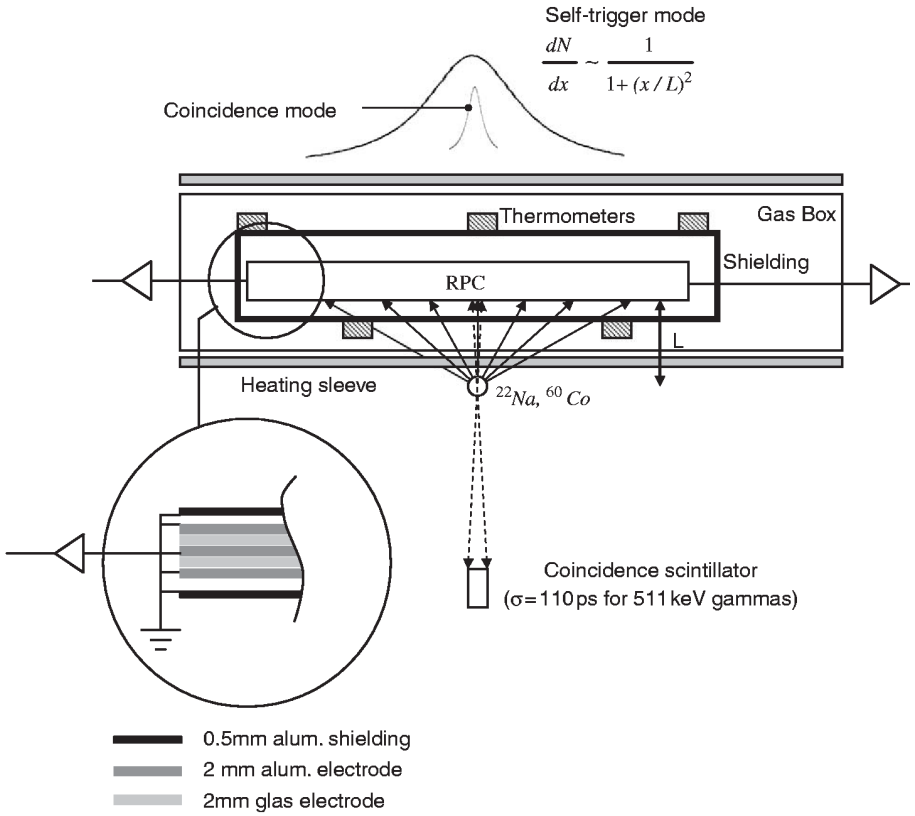

Figure 8.3: Scheme showing the experimental setup. It allows for a measurement in self-trigger mode (for efficiency) or in coincidence mode (for timing) using as reference a fast scintillator with a resolution of 110 ps σ for 1 MeV γ-photons.

Co^{60} is a β^- source whose daughter nuclei decays through a double transition with almost 100% branching ratio. The emited photons are not completely colinear but follow an angular distribution peaked at 180° [160]:

$$Co^{60} \rightarrow Ni^{*60} + e^- + \bar{\nu}_e \tag{8.25}$$

$$Ni^{*60} \rightarrow Ni^{60} + \gamma(1.173) + \gamma(1.332) \tag{8.26}$$

Four different sources with different activities $\mathcal{A}$ and distances L to the tRPC were used:

1. Source 1: $\mathcal{A} = 0.61$ mC (Co^{60}) + 0.46 mC (Na^{22}), $L \simeq 5$ cm.
2. Source 2: $\mathcal{A} = 0.61$ mC (Co^{60}) + 0.46 mC (Na^{22}), $L \simeq 5$ cm + 2.5 cm.
3. Source 3: $\mathcal{A} = 0.46$ mC (Na^{22}), $L \simeq 5$ cm.
4. Source 4: $\mathcal{A} = 0.046$ mC (Na^{22}), $L \simeq 5$ cm.

Due to the exponential charge spectrum observed (fig. 8.4), it was not possible to reach an efficiency plateau. This must be compared with the case of MIPs where, in 4-gap tRPCs, a shallow peak is visible in the charge distribution and the efficiency 'plateau' is well defined (see [68] and also chapter 6).

It must be said that, for the case of 1 MeV γ-photons, the tRPC efficiency is related to the electron extraction probability (mainly Compton) from the electrode, that brings the following consequences:

1. The angular and energy distributions of the ejected electrons give an extra contribution to the time jitter, which is not present in the case of MIPs [161], suggesting that:
$$\sigma_{T(\gamma s)} > \sigma_{T(mips)} \tag{8.27}$$
2. The absolute efficiency is dominated by the extraction probability in the electrode and not by the ionization probability in the gas. This implies:
$$\varepsilon_{(\gamma s)} \ll \varepsilon_{(mips)} \tag{8.28}$$
3. Due to the low energy of the extracted Compton electron, it will be very likely stopped before crossing the following gap. On the other hand, under strong Space-Charge, the collected charge q is rather independent from the primary ionization. Therefore, for a 4-gap tRPC:
$$\bar{q}_{(\gamma s)} \sim \frac{1}{4}\bar{q}_{(mips)} \tag{8.29}$$

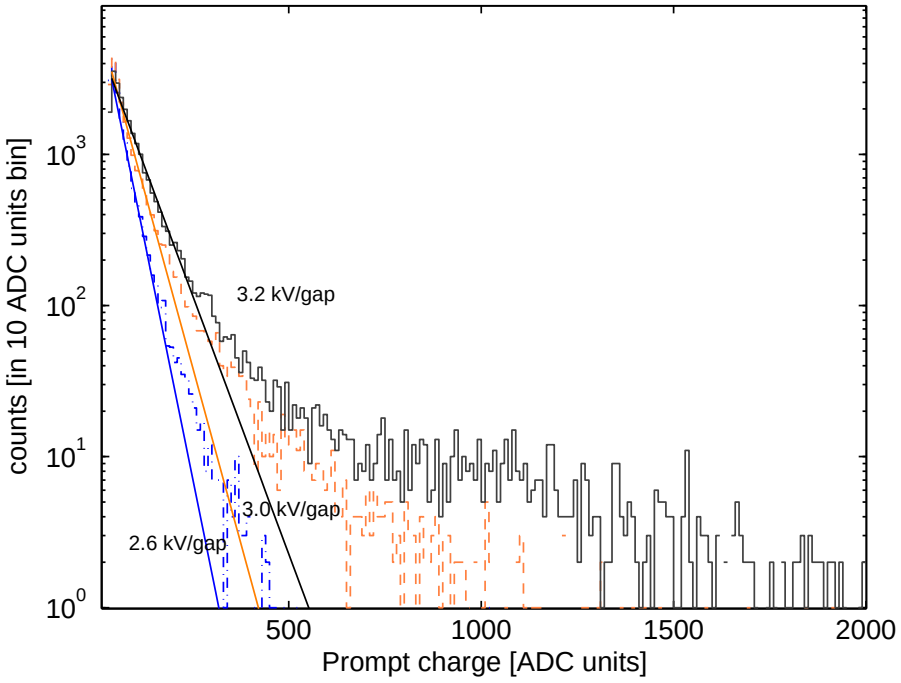

Figure 8.4: Charge spectra for different applied voltages and $\phi_p < 20$ Hz/cm^2 ($V^*_{gap} \simeq V^*$). The fit is performed over the first 600 ADC channels. The exponential fit describes very well the observed spectra (note that the scale is logarithmic); however, for high voltages, a small population of streamers can be observed. At q_{th}=30 a peak is present, caused by the threshold of the comparator.

8.2.3 Data acquired

55 different runs were performed in order to study the effects of rate, temperature and voltage over the reduced average voltage in the gap $\bar{V}^*_{gap}$ or, equivalently, the detector gain. These runs are grouped as follows:

- 4 sets of runs for every source (1, 2, 3, 4) at a fixed reduced voltage $V^* = 3.2$ kV/gap for 7 temperatures (21, 27, 33, 37, 43, 55, 63 °C). **28 runs**.

- 3 sets of runs for 2 different sources (3, 4) at 9 values of the reduced voltage V^* (2.6, 2.7, 2.8, 2.9, 3.0, 3.1, 3.2, 3.3, 3.4 kV/gap) and 2 temperatures (21, 33 °C). **27 runs**.

The current was monitored after any temperature variation, for guaranteeing that the thermal equilibrium was reached (the current stabilizes). It could be estimated that the thermal equilibrium was reached at a short time scale of minutes. However, it is known that some *conditioning* is needed at the time scale of hours [162] that reduces the contribution of parasitic currents. Owing to practical limitations, the studies are restricted to the thermal equilibrium stage and it was not tried to reach a full conditioning of the tRPC. In any case, the dark rate estimated in the absence of a full conditioning represents an upper

limit to the dark rate, being still much smaller than the typical working rates (see section 8.3.4).

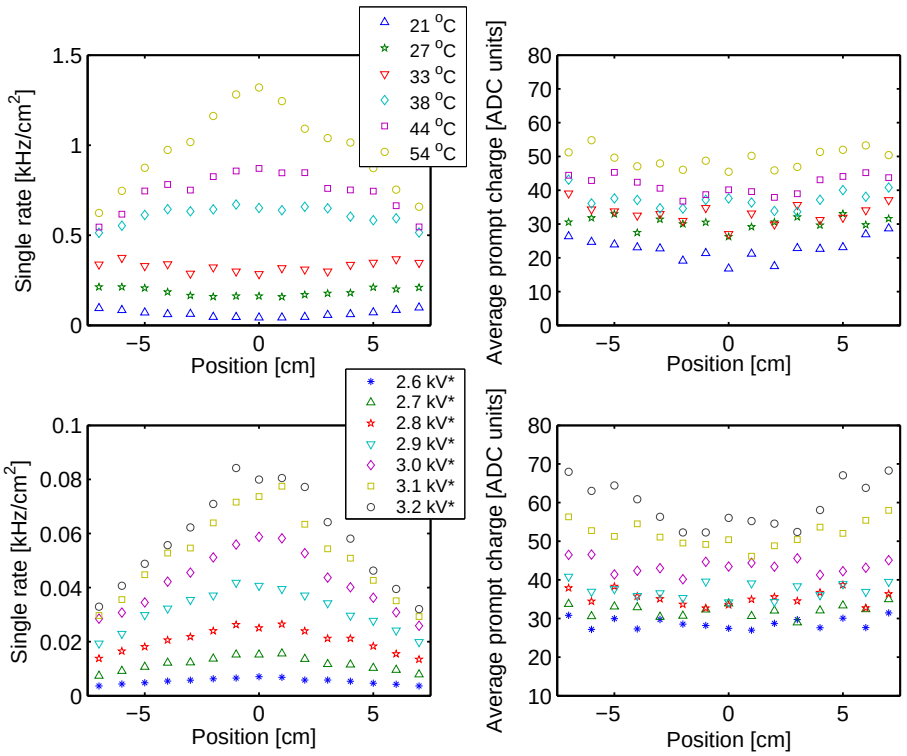

Figure 8.5: Data taken for source 1 (more intense) at $V^* = 3.2$ kV/gap at different temperatures: rate (up left) and prompt charge (up right). Also shown the data for source 4 (less intense) at T=21 °C and different voltages: rate (down left) and prompt charge (down right).

Examples of the data taken are shown in figs. 8.5 and 8.6. The 'single' rate stands for the rate in self-trigger mode (the tRPC is triggered by any avalanche that fires the threshold of the comparator). The tRPC cell was 60 cm long, so that its position distribution extended up to roughly ± 30 cm (see for instance fig. 8.14); however, only the inner region (± 7.5 cm), where the uncertainties on the primary rate are smaller, was studied in the following. It is shown in fig. 8.5 how the effect of the increase in temperature is huge for the single rate (in source 1, a *factor 15* recovery is seen in the counting rate when going from 21 to 54 °C); however, the variations in the average prompt charge are rather modest (around a factor 2). The explanation for this apparent inconsistency lays in the fact that the shape of the charge distribution is exponential and, as a consequence, the efficiency is very sensitive to even very small variations of the gain.

In fig. 8.5, some central features are illustrated: when looking at source 1 at fixed temperature, a dip around the position of the source (x=0) is seen; this is not strange if the field is significantly reduced due to the drop in the glass plates. When the temperature is increased, the field in the gap starts to recover, and both the single rate and average prompt charge grow. Also by looking at

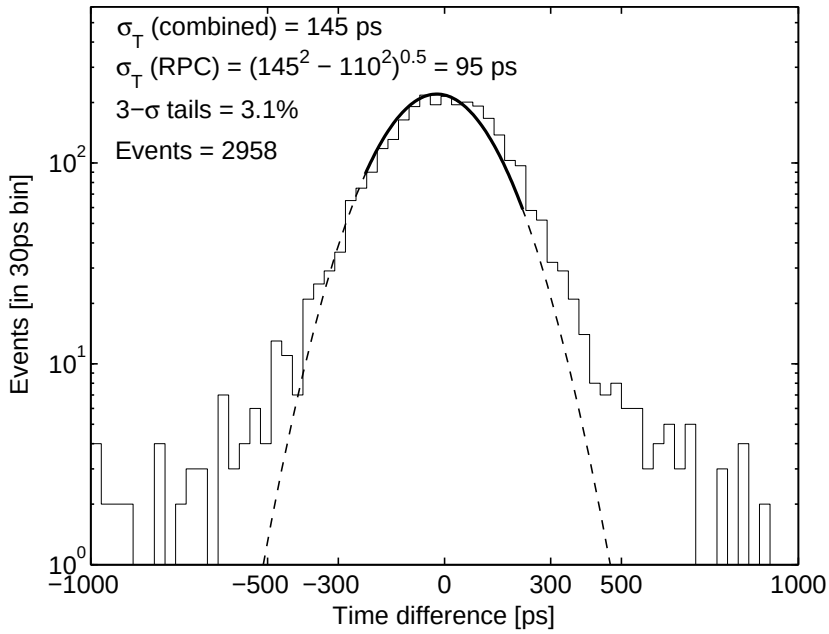

Figure 8.6: Typical time of flight distribution obtained using a scintillator reference of 110 ps σ. The time-charge correction has been already applied. As compared to MIPs (chapter 6) the σ of the distribution is significantly larger (around 90-100 ps). The distribution shown corresponds to $V^* = 3.2$ kV/gap, T=21 °C, source 4 (low rate).

source 4 (less intense, $V^*_{gap} \simeq V^*$) it can be realized that the charge and single rate increase at once as a function of the reduced voltage V^*, as expected.

It has to be noted that, for some of the runs, the position distribution appeared globally shifted by 1-2 cm, typically. This corresponds to a difference in time of 100-200 ps between channels and can be ascribed to electronic walks. It was subtracted after imposing that all the distributions were centered at $x = 0$.

Fig. 8.6 shows the typical time resolution obtained in case of illumination with 1 MeV γ photons by using a reference scintillator with a time response width of 110 ps. The resulting tRPC response is at the level of 90-100 ps σ.

8.3 Single rate

8.3.1 Determination of the primary rate profile

Due to the absence of a 'plateau', the efficiency was defined by using as reference the counting rate observed at a certain operating voltage, in the limit $V^*_{gap} \simeq V^*$ (low drop). For this purpose, the weaker source, 4, at $V^* = 3.2$ kV/gap was used. However, it was required to make a partial use of the effect to be measured, because even for the source 4 the voltage drop in the plates was not negligible. So, the temperature was increased up to reach a situation where the observed rate becomes independent from it, that can be considered as an indication that the drop in the plates is not affecting the measurements ($V^*_{gap} \simeq V^*$), and the observed profile was taken as reference.

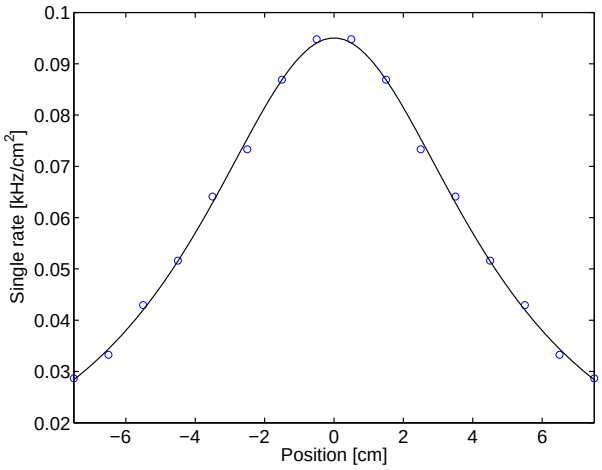

Figure 8.7: Rate profile for source 4 at the reference voltage $V^* = 3.2$ kV/gap. The operating temperature was increased up to 44 °C to guarantee that the ohmic drop in the glass is negligible. Data are fitted to the functional dependence of eq. 8.30.

It can be deduced that the profile of a point-like source illuminating a strip-like detector at a distance L is described by a Cauchy-Lorentz distribution. Therefore, the primary rate profile over the tRPC, for each source k=1, 2, 3, 4, can be compactly expressed as:

$$\phi_{p,k}(x) = \frac{N_k}{2\pi L w} \frac{1}{1 + (x/L)^2} \tag{8.30}$$

where N_k is the total number of counts per unit time that would be observed for source k over an infinite strip-like detector, and w is the width of the tRPC (1.9 cm). The primary rate profile of source 4 in the absence of drop in the plates, together with the best fit to eq. 8.30 are plotted in fig. 8.7, providing $N_4 = 4.8$ kHz, $L = 4.2$ cm. Once N_4 and L are determined, the values for N_1 and N_3 can be obtained just re-scaling by the counts measured by the reference scintillator[2].

In the case of source 2 (source 1 displaced 2.5 cm apart from the tRPC) the decrease of solid angle had to be included [163]:

$$\varepsilon_\Omega = \frac{\arctan[\frac{w}{2(L+2.5)}]}{\arctan[\frac{w}{2L}]} \tag{8.31}$$

Therefore:

$$N_2 = N_1 \varepsilon_\Omega \tag{8.32}$$

[2]These sources (1, 3) are so intense that it was not possible to obtain the tRPC primary rate in the absence of voltage drop in the glass, so the information of the scintillator was used. The problem of this approach is that, apart from Na^{22}, the source 1 has also photons coming from Co^{60} that have, in principle, a different detection efficiency. It is still possible to use the scintillator information as long as the ratio of the scintillator to the tRPC efficiency is similar for Na^{22} and Co^{60} sources. This approach is reasonable due to the small dependence of the shape of $\lambda_{int,\gamma}(E)$ (attenuation mean free path for photons) with respect to the material, in the Compton region [3].

Source	N_k[kHz]	L[cm]	ε_Ω
1	90	4.2	1
2	57	6.7	0.63
3	46	4.2	1
4	4.8	4.2	1

Table 8.1: Sources used, together with its normalization factor, distances to the tRPC and geometric correction.

DAQ dead-time

The rates studied were so high that the DAQ system was limited by its dead-time. To overcome the problem an external reference, a Caen 145 quad scaler, was used for translating from the DAQ counting rate to the real tRPC counting rate.

FEE dead-time

There is still a tiny effect to be accounted for: the tRPC counting rate in the scaler is slightly biased by the dead-time of the FEE itself (1μs). A correction must be applied by following [12]:

$$N_{real} = \frac{N}{1 - N\tau} \tag{8.33}$$

being N the frequency of events measured by the scaler and τ the dead-time of the FEE. This expression is exact for a *non-paralyzable* measuring device [12], as is the case for the dead time of the comparator[3]. The correction given by eq. 8.33 is in practice not larger than 5% for the highest rates.

The values finally obtained for N_k are summarized in table 8.1 and the primary rate profiles for each source are shown in fig. 8.8, together with the data taken at different temperatures.

8.3.2 A model for the efficiency to γ rays

It can be developed a simple model that contains all the relevant features of a timing RPC irradiated with γ photons, based on the assumptions described next:

1. The DC model describes the behavior of $\bar{q}$, $\bar{q}_p$ and ε.
2. In the regime studied, the average total charge $\bar{q}$ is proportional to the reduced voltage in the gap V^*_{gap}.
3. The prompt charge spectrum $\frac{dN}{dq_p}$ is well described by an exponential:

$$\frac{dN}{dq_p} = \frac{1}{\bar{q}_p} e^{-\frac{q_p}{\bar{q}_p}} \tag{8.34}$$

[3]Non-paralyzable means that the detection device is not registering any other event during a fixed dead-time after the first event arrives.

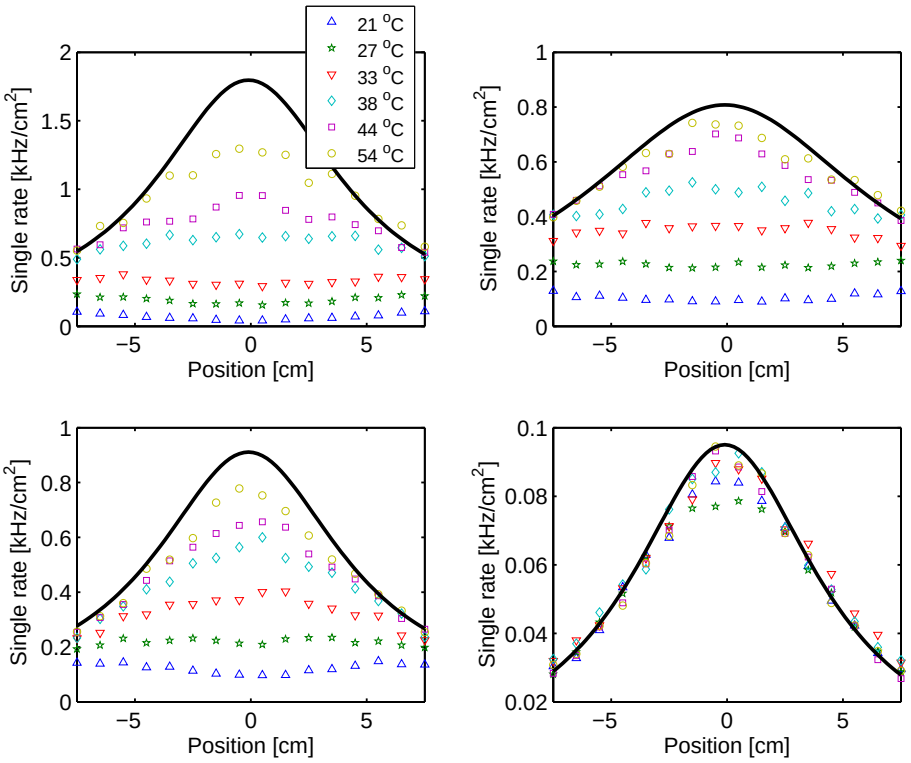

Figure 8.8: Figures showing the data taken for the 4 sources used (1, 2, 4 and 3, read clockwise from the upper-left corner) and different operating temperatures. The reduced applied voltage was V^* =3.2 kV/gap. The continuous line shows the rate over the tRPC in the absence of ohmic drop in the glass (determined as explained in the text). The data tends asymptotically to the curves when T increases, as expected.

Under this hypothesis, the observed primary rate ϕ_p is related to the true primary rate Φ_p (able to produce an avalanche) through a constant $\varepsilon_o < 1$, that accounts for the part of the spectrum that falls below threshold:

$$\Phi_p = \phi_p / \varepsilon_o \tag{8.35}$$

that, in the case of an exponential spectrum can be written as:

$$\Phi_p = \phi_p e^{\frac{q_{th}}{\bar{q}_{p,o}}} \tag{8.36}$$

being $\bar{q}_{p,o}$ *the charge at 3.2 kV/gap*, where the efficiency is referenced, and q_{th} is the charge at threshold, after subtracting the ADC pedestal. See fig. 8.9 for a clarification of this issue.

Remarkably, eq. 8.34 has the same form as the Furry law [25]. This is the empirical law for the fluctuations of an avalanche started by an electron inside a gaseous detector, when the applied field is low enough to allow for an equilibrium of the secondary electrons (see chapter 2). It may turn to be useful to deeply understand the underlying physical processes in this case, although a full description of the phenomenon requires a simulation

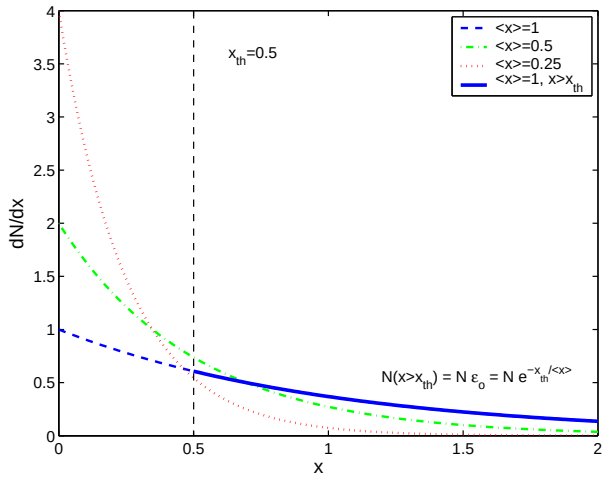

Figure 8.9: Example of exponential spectra normalized to one, for different values of the mean. Also shown the relation between the number of events above the threshold ('observed') to the total.

of the avalanche under photon illumination, that is not available at the moment.

4. The average total charge $\bar{q}$ is related with the average prompt charge $\bar{q}_p$:

$$\bar{q}_p \simeq b\bar{q} \tag{8.37}$$

and the constant b is independent from the voltage in the gap. Different descriptions of this relation can be found in [53], [54], where it is suggested that, in fact, b depends on V. It must be recalled that the prompt charge measured with the present setup refers to the charge integrated in a 200 ns window, while the pure prompt-electronic component would correspond only to the first few nanoseconds of signal induction. Therefore the prompt charge measured has a contribution coming from the induction of the ions.

The assumption is kept and its validity discussed at the end.

Now, a global model that describe the data can be proposed. The average prompt charge for each position is described by the expression:

$$\bar{q}_p(x) = \frac{ab(V\frac{T}{T_o} - V_{th})}{1 + ad/\varepsilon_o\phi_p(x)\rho(T)\frac{T}{T_o}} \tag{8.38}$$

which is nothing but eq. 8.20, 8.36 and 8.37 put together.

The efficiency of an exponential charge distribution for a detection threshold placed at q_{th} is given by:

$$\varepsilon(x) = \int_{q_{th}}^{\infty} \frac{dN}{dq_p} dq_p = e^{-\frac{q_{th}}{\bar{q}_p(x)}} \tag{8.39}$$

and, recalling 8.36, the observed rate is given by:

$$\phi(x) = \varepsilon(x)\Phi_p(x) = \varepsilon(x)/\varepsilon_o\phi_p(x) \tag{8.40}$$

The required functional dependences for the model are given by eq. 8.30 (observed primary rate ϕ_p), eq. 8.38 (average prompt charge $\bar{q}_p$) and eq. 8.40 (observed rate ϕ).

The free parameters are $\bar{p}$= $\{ab,\ V_{th},\ a/\varepsilon_o\rho(T)\}$, i.e., 2+6 (one for each temperature studied) = 8 parameters. They were obtained from a global fit to 45 curves, excluding those runs at $T > 55$°C (the dark counting rate becomes important) and $V^* > 3.2$ kV (the fraction of streamers becomes important). A χ^2 minimization of the following functional was performed:

$$\chi^2(q_{ik}, \phi_{ik}, \bar{p}) = \sum_k \sum_i [(\frac{q_{ik} - q(\bar{p})}{w_{q,\ ik}})^2 + (\frac{\phi_{ik} - \phi(\bar{p})}{w_{\phi,\ ik}})^2] \qquad (8.41)$$

where q_{ik} and ϕ_{ik} are, respectively, the prompt charge and observed rate for each position i and run k. $q(\bar{p})$ and $\phi(\bar{p})$ are the expectations of the model as a function of the set of parameters $\bar{p}$. The average charge q_{ik} is obtained from an exponential fit in each of the position slides within the first 600 ADC channels (fig. 8.4). The weights used were the pure Poissonian weights in the case of $w_{\phi,\ ik}$ (square root of the number of counts), and the uncertainty obtained from the exponential fit in the case of w_q. It was seen that to multiply w_q by 2 improves the description of the prompt charge data; due to the different nature of the errors this seems to be reasonable.

The fit to the model, together with the data, are shown in figs. 8.10 and 8.11. The overall agreement suggests an adequate interpretation of the underlying physical processes. A detailed evaluation of the results is given in the next section.

8.3.3 Interpretation of the results

Of the eight parameters of the fit $\bar{p}$=$\{ab,\ V_{th},\ a/\varepsilon_o\rho(T)\}$, 6 can be directly interpreted:

- The increase on the rate capability κ is related to the parameters $g(T) = a/\varepsilon_o\rho(T)$. In particular, κ can be referred to T_o=21 °C, thus providing $\kappa = \frac{T}{T_o}\frac{\rho(T_o)}{\rho(T)} = \frac{T}{T_o}\frac{g(T_o)}{g(T)}$ (eq. 8.22).
- The voltage at which Space-Charge starts, V_{th}, is obtained directly from the fit.

The other two parameters, $a' = ab$ and $g(T_o) = a/\varepsilon_o\rho(T_o)$, are not relevant for the purposes of this work and hardly comparable with known data. However, a rough estimation of a can be provided, by taking the value of $\rho(T_o)$ from fig. 8.1 and assuming an exponential behavior of the primary spectrum below threshold (for estimating ε_o), yielding $a = 1.144$ pC/kV, which is not unreasonable. Further comparisons on this issue require an improved setup.

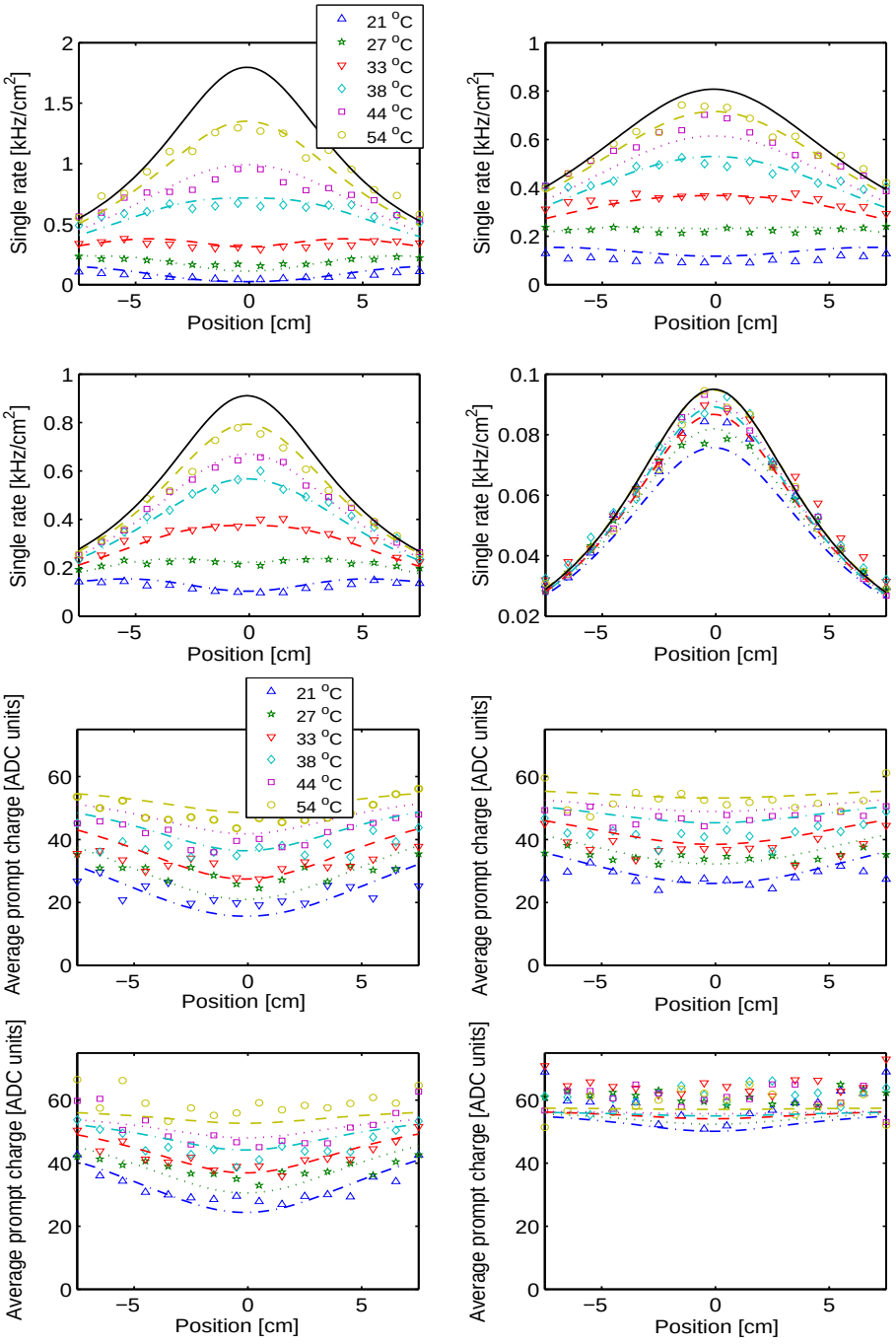

Figure 8.10: Comparison between model and data for different temperatures (21 °C ·-, 27 °C ··, 33 °C - -, 38 °C ·-, 44 °C ··, 54 °C - -). The study was done for different sources (1, 2, 4 and 3 clockwise from up-left corner) and the reduced voltage was kept constant at a value $V^* = 3.2$ kV/gap.

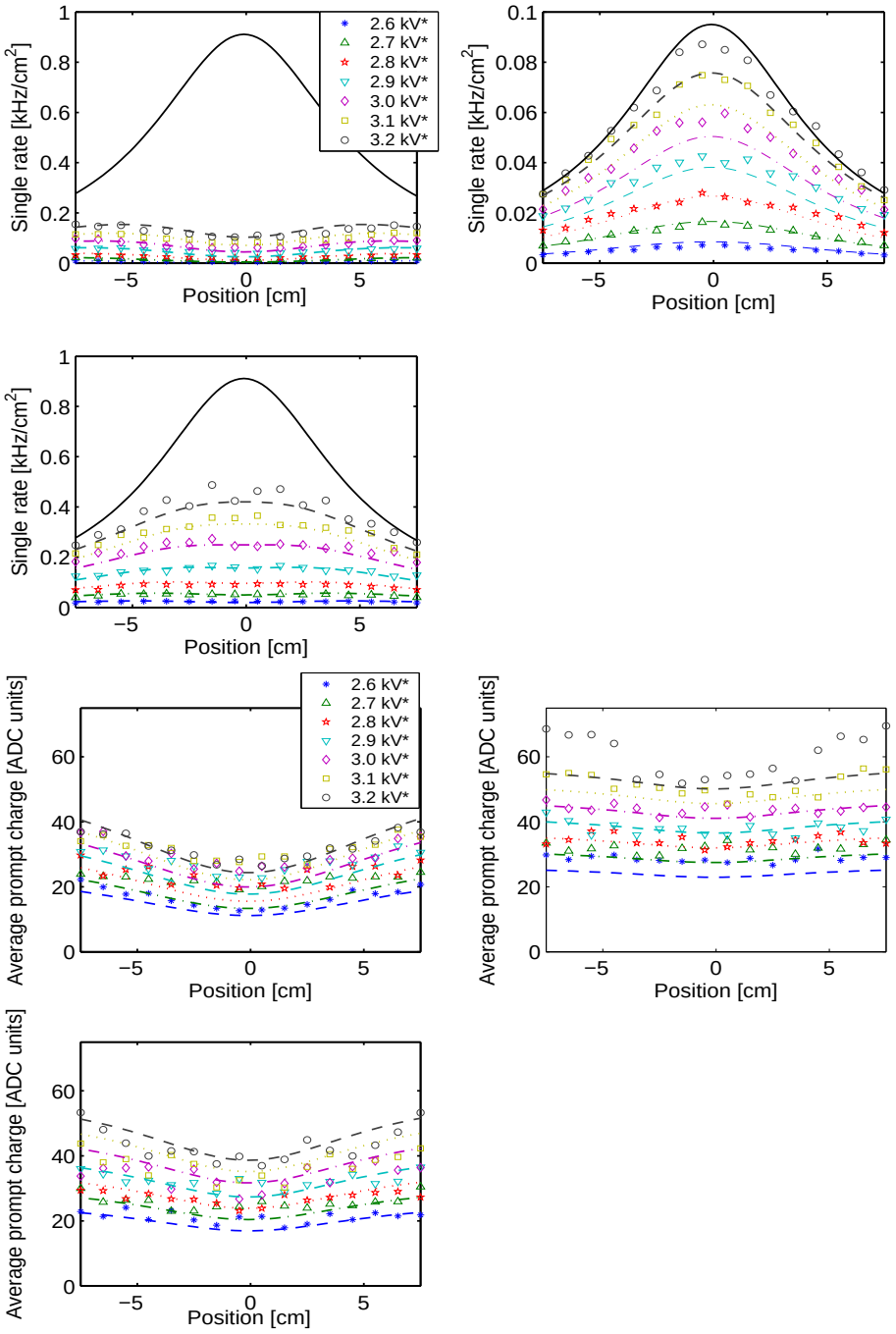

Figure 8.11: Comparison between model and data for different values of the reduced voltage V^*/gap (2.6 kV - -, 2.7 kV ·-, 2.8 kV ··, 2.9 kV - -, 3.0 kV ·-, 3.1 kV ··, 3.2 kV - -). The study was done for different sources (3, 4, 3) and temperatures (21, 21, 33) (clockwise from up-left corner).

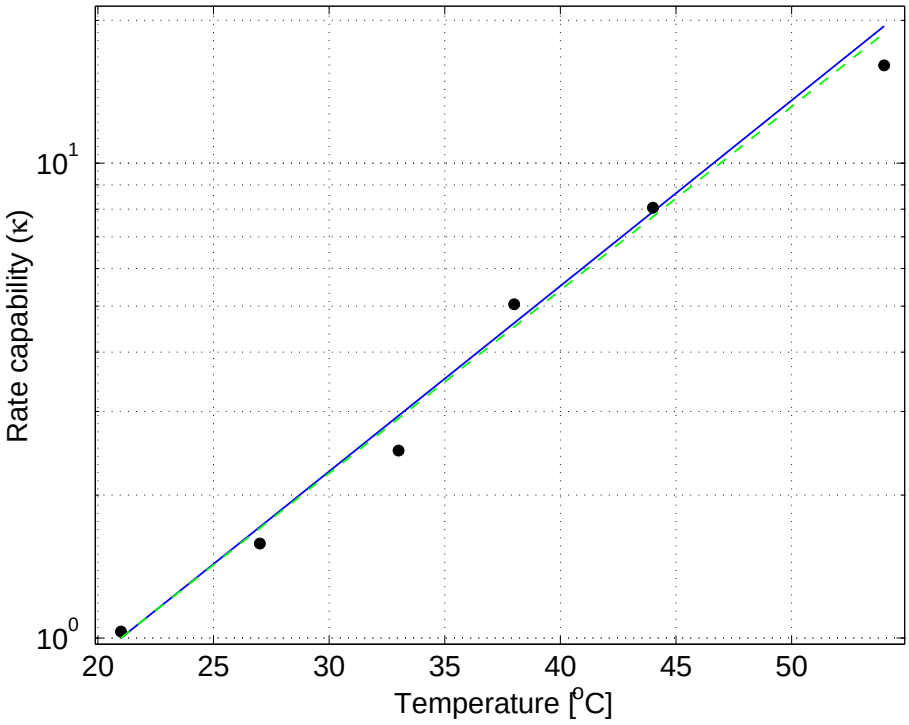

Figure 8.12: Comparison between the behavior of the rate capability from independent measurements of the resistivity (eq. 8.1) in dashed line, and the output of the model (dots). The continuous line is the best fit to the points.

The increase of rate capability relative to $T_o = 21°$C is shown in fig. 8.12 together with the expectations from laboratory measurements of the glass resistivity (fig. 8.1, [164]). From the fit, the coefficient ΔT that regulates the behavior of the resistivity (eq. 8.14) can be obtained. The result of the fit is $\Delta T_{fit} = 24.5 \pm 1.5$ to be compared with the value obtained in the laboratory $\Delta T_{lab} = 25.0 \pm 0.3$ (fig. 8.1). Therefore, it seems to be strongly supported by the data the fact that the increase of the rate capability is compatible with the increase of the glass conductivity, as expected from the DC model.

On the other hand, the value obtained for V_{th} is 2.15 kV/gap, that is in qualitative agreement with the measurements of [68] for the standard mixture.

For an easier interpretation of the model, it is better to group all the curves in two 'Universal curves' of efficiency and charge as a function of ϕ_p/κ (see section 8.1.1). By looking at fig. 8.13 it is possible to interpret the results:

- As expected from eq. 8.9, all the points for different temperatures nicely superimpose, confirming that the model proposed provides the 'increase on rate capability' κ. Complementary, fig. 8.12 confirms that, indeed, the rate capability is proportional to the glass conductivity.

- The fact that the curve is not reproducing exactly the behavior of data indicates:

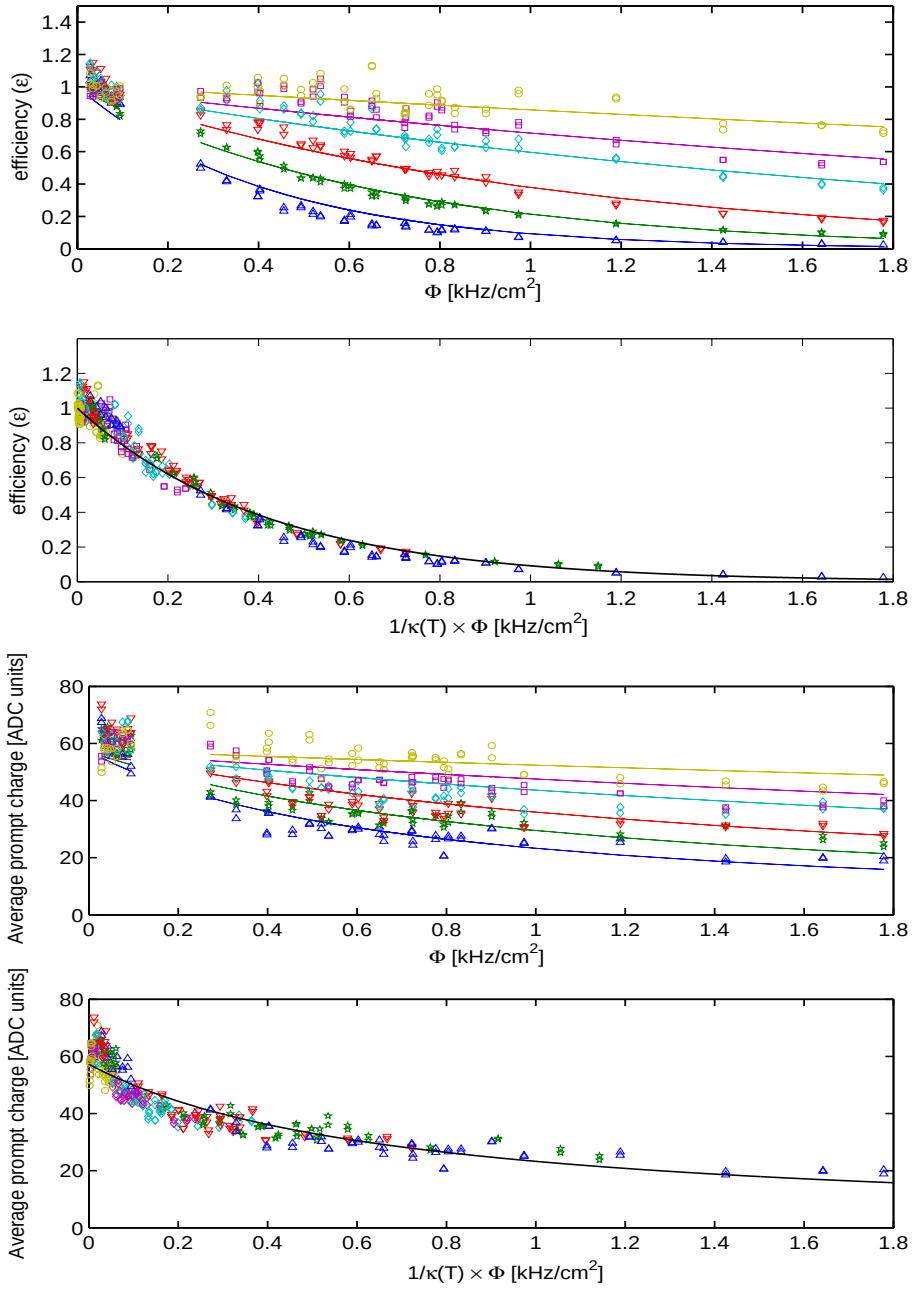

Figure 8.13: Figures for evaluating the goodness of the fit in a global view. It is shown the behavior of the efficiency and prompt charge at V^*=3.2 kV/gap as a function of rate for different temperatures (21, 27, 33, 38, 44, 54 °C from bottom to top). Also shown the behavior of the same magnitudes when all the curves are fused in a single one, after re-scaling the primary rate by $1/\kappa$.

- Deviations in the efficiency plot could indicate deviations from the exponential law of the charge spectrum (in particular a small effect is seen for the lower rates).
- Deviations in the charge plot could indicate that some of the hypothesis are wrong in the derivation of the functional dependence of the prompt charge. In particular they can be due to the fact that b (that relates the prompt and the total charge) is not exactly a constant but depends on V^*_{gap} and therefore on rate. A wrong description of the charge will also be related to a wrong description of the efficiency.

Despite the discrepancies between data and model, the fit is generally better than 10% and not worser than 30% for any point.

8.3.4 Dark rate

An anomalous increase of the dark counting rate has been observed at 63 °C, resulting in a deterioration of the tRPC performances. The effect is visible even when the source is illuminating the tRPC (fig. 8.14).

The observed dark counting rate is plotted in fig. 8.15 for source 3, showing an effect similar to the reported for trigger RPCs [165], i.e., a linear increase followed by an exponential increase. The difference is that here the transition is observed at 55 °C while in [165] it was seen at 30 °C. When looking at the fraction of streamers, an increase with the temperature is apparent. This is expected because the field in the gap is recovering, and a certain level of streamers was present in the absence of voltage drop in the plates. This explains the behavior up to 55 °C, where the fraction of streamers is similar to the value obtained for the source 4 at $V^*_{gap} \simeq 3.2$ kV/gap, being approximately 5% of the events. However, above 55 °C, the fraction of streamers doubles, suggesting that a different process starts in the gap.

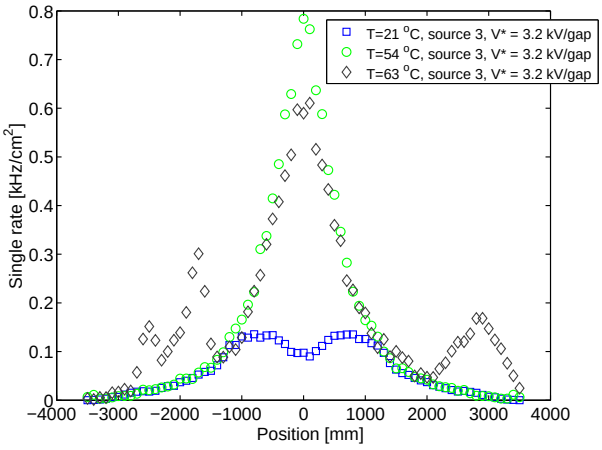

Figure 8.14: Position distribution of hits over the tRPC. There are two main effects above 54 °C: a) the rate at maximum decreases, indicating that some kind of saturation effect is present, likely related to the increase in the dark rate, b) the distribution close to the ends of the detector shows peaks that are not related to the source.

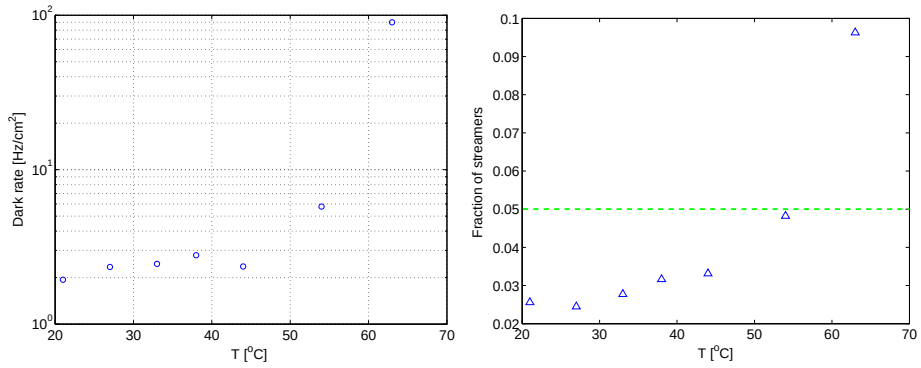

Figure 8.15: The left-most figure shows the dark counting rate at $V^* \simeq V^*_{gap} = 3.2$ kV/gap. Two separated regions are seen: one, up to 50 °C, where the variations are very small, and then a sudden increase up to 2 orders of magnitude. In the right, the fraction of streamers is shown as a function of T for source 3, at $V^* = 3.2$ kV/gap.

8.4 Time response

For measuring the tRPC time response as a function of temperature variations, one of the fast reference scintillators already described in section 6.2.3 has been used, yielding a time resolution of $\sigma_T = 110$ ps for 1 MeV γ photons (and Gaussian response). Both the Na^{22} and Co^{60} sources produce anti-parallel simultaneous photons and the time difference between them, being fixed, can be used for time resolution estimates. Therefore, as shown in fig. 8.3, for the purpose of timing measurements the source has been placed in between the tRPC and the reference scintillator.

A coincidence was defined by two signals arriving within a time window T_w=200 ns, coming from one end of the tRPC and one end of the scintillator. The time width of the distribution has been characterized by performing a Gaussian fit in an interval of $\pm$ 1.5σ around the center of the distribution, as described in [47].

8.4.1 Scintillator time response to photons

The reference scintillator used for timing provides a resolution of $\sigma_T = 35$ ps for ionizing particles. The smaller amount of light typically collected in the case of illumination with photons does not allow for a very good timing, yielding $\sigma_T = 110$ ps.

As argued in section 8.2.2, the tRPC time response under 1 MeV γ illumination is typically worst than in the case of ionizing particles. For example, a typical value of $\sigma_T \simeq 90$ ps has been already measured under similar conditions [161], as compared with $\sigma_T \simeq 50 - 80$ ps for similar detectors when illuminated with ionizing particles.

The setup used for determining the scintillator time resolution consisted in two identical scintillators placed perpendicularly and 20 cm apart. A Na^{22} source is placed in between, sticked to one of the detectors. The signals produced

are discriminated through a Philips 715 CFD[4].

For achieving the best resolution, it is necessary to apply a cut in events that produce 'enough light'. This condition is shown in fig. 8.16 and it can be translated roughly as a cut at the 60% of the Compton edge for photon annihilation. This cut mainly rejects the interactions close to any of the edges of the scintillator that are likely to produce small amounts of light and therefore larger time fluctuations. A region of ± 2.5 cm around the peak of the position distribution was also selected. The time spectra obtained after the cuts is shown in fig. 8.17, yielding a characteristic time resolution $\sigma_T = 110$ ps.

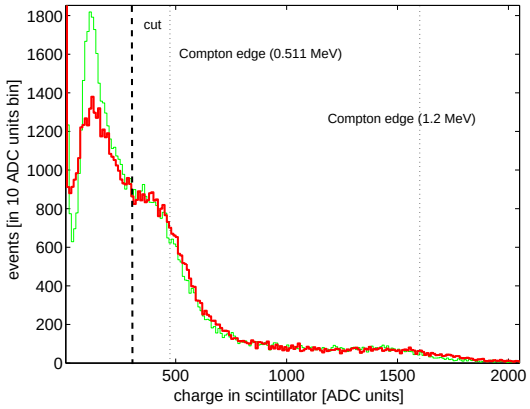

Figure 8.16: Charge distribution observed in the reference scintillators when illuminated with a Na^{22} source. A peak can be seen at low charges and also the Compton edge for photons coming from positron annihilation. The first peak has an unclear origin and the best timing requires to cut it. At high charges the contribution of the 1.2 MeV photon is also visible.

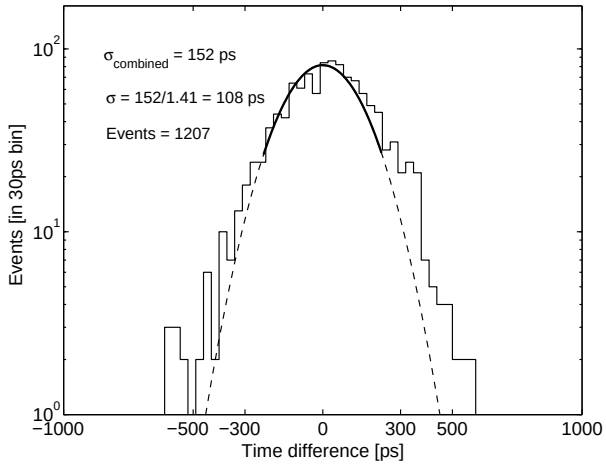

Figure 8.17: Time difference between the reference scintillators. After quality cuts in charge and position, the best timing is achieved, providing $\sigma_T = 110$ ps.

[4]Constant Fraction Discriminator.

8.4.2 Cuts and data analysis

After the external cuts are applied to the reference scintillators (previous section), the internal cuts and the more important correlations observed must be discussed:

1. A region of ± 1 cm was selected around the maximum of the tRPC position distribution. This eliminates the jitter due to the different path lengths, that can be estimated from fig. 8.18 to be less than:

$$\Delta t = t_{max} - t_{min} = 26 \text{ ps} \tag{8.42}$$

being essentially invisible when compared with the 110 ps of the reference scintillator.

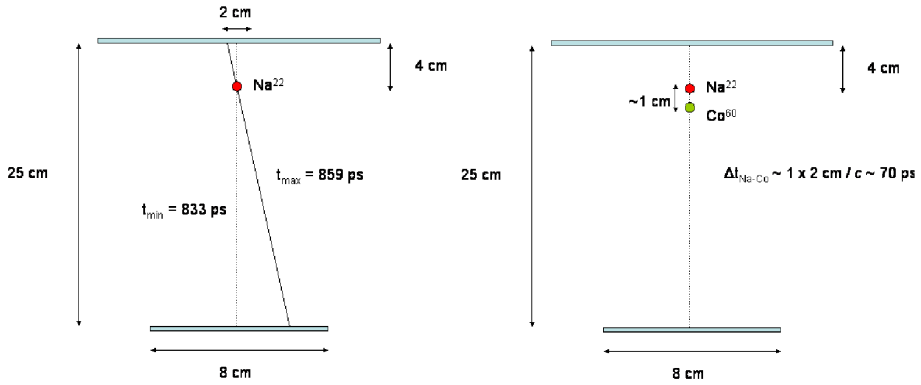

Figure 8.18: Two geometric effects are described: in the left, the maximum geometric jitter expected after the cut in tRPC position. In the right, the figure shows how the time distributions of sources containing Na^{22} and Co^{60} are displaced by 70 ps due to mechanical constraints, affecting the peak of the time distribution (t_o).

The cut also guarantees that the primary rate over the tRPC is reasonably constant in the region of study (see in fig. 8.10 the primary rate profile), allowing for a cleaner interpretation of the results.

2. In the case of sources 3 and 4, most of the events are below the Compton edge for annihilation, but coincidences with 1.2 MeV photons from Ne^{22} de-excitation may also take place (fig. 8.16). Due to the fast decay of Ne^{22} (3.7 ps, see [160]), and the typical delay times for positron annihilation (at the level of hundred ps), it is possible that the presence of this photon in the trigger introduces a certain time jitter. It is recalled that the presence of the 1.2 MeV photon was highly suppressed under trigger conditions due to its isotropic character. In order to evaluate the effect, its presence was enhanced on purpose by selecting large charge events in one of the scintillators, and it did not exert any effect over the time resolution. Therefore, no extra cut is performed for removing 1.2 MeV photons.

3. The geometry of the sources 1 and 2, that contain Co^{60}, is slightly different from 3 and 4. In sources 1 and 2, Co^{60} and Na^{22} are both present, and separated by $\Delta y = 1$ cm, i.e., $\Delta t = 2\Delta y/c = 70$ ps at the speed of light.

Moreover, in the case of source 2, it is displaced 2.5 cm from the tRPC as compared to source 1, resulting in an extra offset $\Delta t = (2.5 \times 2)/c = 170$ ps.

Aiming for a clean description, when looking for an interpretation of the tRPC timing properties under γ illumination, sources 1 and 2 will not be considered.

4. Times of flight out of a $\pm$ 1 ns interval, coming from random coincidences, are removed.

5. At least 1000 events must remain after cuts for guaranteeing a reasonable characterization of the time spectra. If the number of events fall below 1000, the run is rejected.

6. The slewing correction is performed as described in section 6.4.2, allowing for a typical improvement of 40-50 ps.

With these cuts performed it was observed that, for the same operating conditions, the variation in the time resolution between different runs was still at the level of 5-10 ps, that can be considered as the experimental accuracy of the timing measurements, within the current setup.

8.4.3 Time response measurements (σ)

An analytic expression for the tRPC time resolution has been already introduced in section 3.2.2:

$$\sigma_{_T} = \frac{K_\sigma}{S} \tag{8.43}$$

being K_σ=0.75 a reasonable value for MIPs in a single gap tRPC [67]. A similar functional dependence can be expected for the case of illumination with γ photons. Therefore, according to the *DC model* developed in previous sections, a decrease in the reduced field causes a reduction in S and therefore a worsening in the timing performances. The effect should visible in any of the V and T scans performed, whose data are shown in fig. 8.19. The time resolution observed is at the level of 90-100 ps, in agreement with previous observations of [161], however it shows a remarkable independence from the field in the gap, unlike the behavior for MIPs.

8.4.4 Time response measurements (t_o)

A deeper insight can be obtained from the study of the peaking time of the time distribution (t_o). It drifts from day to day, due to electronic walks, requiring to make inter-comparisons between different days, for the same operating conditions. Its functional dependence can be approximated by (section 3.2.2):

$$t_o = \frac{K_{_T}}{S} \tag{8.44}$$

In the particular case where the avalanche is initiated by a single electron, it can be straightforwardly derived that $K_{_T} = \ln(m_t)$ where m_t is the gain necessary to reach the threshold, which is assumed to be $m_t \sim 10^5$ (usual thresholds in timing RPCs).

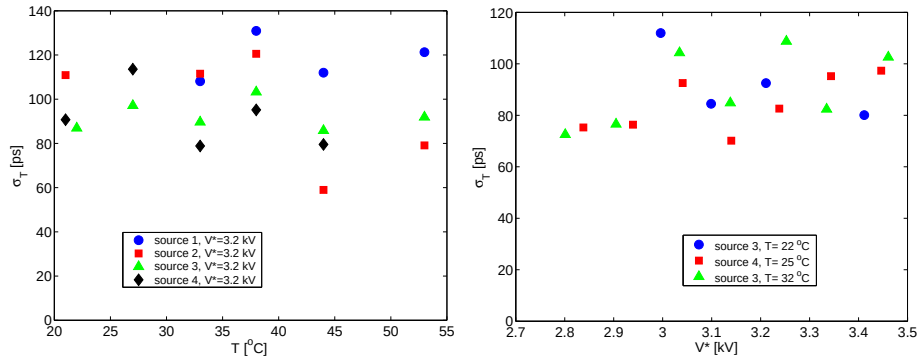

Figure 8.19: Figures showing the behavior of the time resolution as a function of voltage and temperature. The behavior is essentially flat at the level of 90 ps.

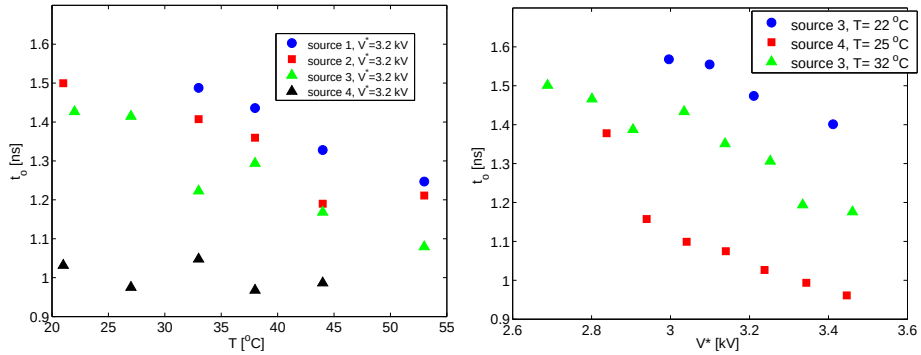

Figure 8.20: Figures showing the behavior of the peak time as a function of voltage and temperature. It behaves as expected, decreasing with the increase of V^* and T, indicating that the field in the gap is also increasing.

Being precise, t_o refers to the distribution of times from the avalanche formation until the threshold of the comparator is reached. However, the time measured contains a certain offset t_{OFF} that comes from the geometry, cables and electronics. Therefore, the measurements of t_o are shown in fig. 8.20, with a time offset t_{OFF} arbitrarily set to 1 ns for $V^*_{gap} = 3.2$ kV; the proper determination of the offset is postponed.

The behavior observed in fig. 8.20 is in qualitative agreement with expression 8.44: when the field in the gap increases, also S does, and t_o becomes smaller (the detector faster). However, no significative effect is seen over the time resolution (see fig. 8.21).

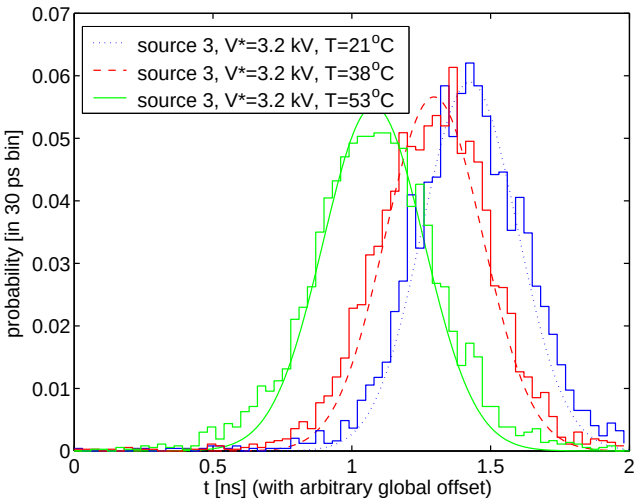

Figure 8.21: Time spectra for the source 3 at three different temperatures. The time scale has an arbitrary offset. The picture shows how the time distribution is shifted by almost half a nanosecond without showing *any significative effect in its shape*.

8.4.5 σ vs t_o

It is arguable that the analytic expression 8.43 must be applied by keeping the charge-time correlation that may be intrinsic of the detector [55]. Therefore the uncorrected time resolution is also studied in the plot σ_T vs t_o shown in fig. 8.22. Both time resolutions show a flat behavior as a function of t_o.

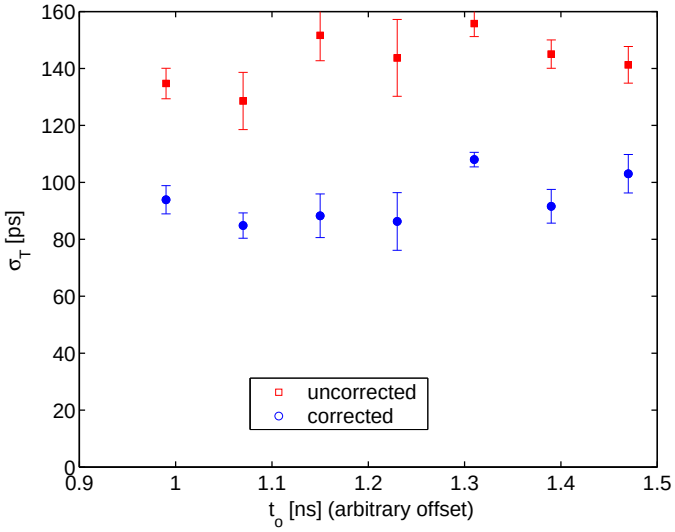

Figure 8.22: Plot showing the time resolution as a function of the peak time for all the runs analyzed. The plot is consistent with a flat behavior both for the corrected and uncorrected resolutions, in disagreement with the simple description proposed.

8.4.6 Description of the time response to γ rays

Looking at the behavior of t_o in fig. 8.20 and its functional dependence given by eq. 8.44, it is tempting to try a simple description:

1. Let's assume that t_o is described by eq. 8.45:

$$t_o = \frac{K_{_T}}{S(V_{gap})} \tag{8.45}$$

   where $K_{_T} = \ln(m_t/n'_o)$ Although n'_o is not known for a Compton electron with an energy of some hundreds of keV emitted under γ illumination, the assumption is not critical, as $K_{_T}$ depends only logarithmically on n'_o, being helpful to consider the simpler case ($n'_o = 1$).

2. The behavior of S as a function of the field in the gap was obtained for the gas mixture used as described in chapter 7:

$$S[\mathrm{ns}^{-1}] = (4.3 \pm 1.0)V_{gap}[\mathrm{kV}] - 5.3 \pm 2.7 \tag{8.46}$$

3. The DC model applies.

4. There is a linear relation between charge and reduced voltage.

5. The last two items allow for an estimate of $V^*_{gap}(\phi, V^*, T)$, whose parameterization is obtained from the fit performed in section 8.3.2.

6. The unknown overall offset $t_{_{OFF}}$ is left as the only free parameter.

7. Only measurements with source 3 and 4 (Na^{22} sources) are considered.

The results of the fit are shown in fig. 8.23, where the value of $t_{_{OFF}}$ has been obtained and already subtracted for all the data sets. The agreement is reasonable, despite the scattering of the points, seeming to be rather conclusive in indicating that the variations of t_o can be explained through the variations of S within the proposed model. Model and data also reproduces the fact that the ohmic drop on source 4 is very small, in agreement with the efficiency measurements of section 8.3.2.

At last, fig. 8.22 (σ vs t_o) was re-obtained, but taking only data from sources 3 and 4, and subtracting to t_o the offset determined from the fit. The results are shown in fig. 8.24.

By using eqs. 8.43 and 8.44, the functional relation between the resolution and the time at maximum can be derived:

$$\sigma_{_T} = \frac{K_\sigma}{K_T} t_o \tag{8.47}$$

predicting a linear dependence in fig. 8.24. The natural interpretation of the flat behavior of σ is that, in the case of photons, the width of the time distribution is dominated by a process different than avalanche formation and growth (possible explanations are discussed in the next section).

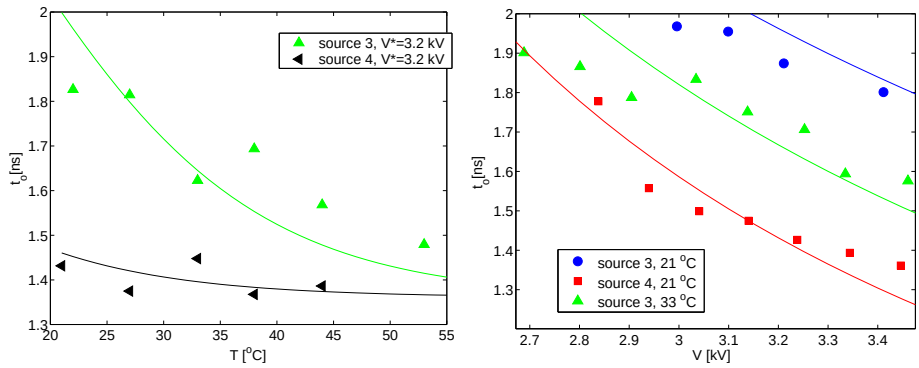

Figure 8.23: Comparison between model and data from sources 3 and 4. It shows a reasonable agreement, suggesting that the behavior of t_o is connected to the behavior of S.

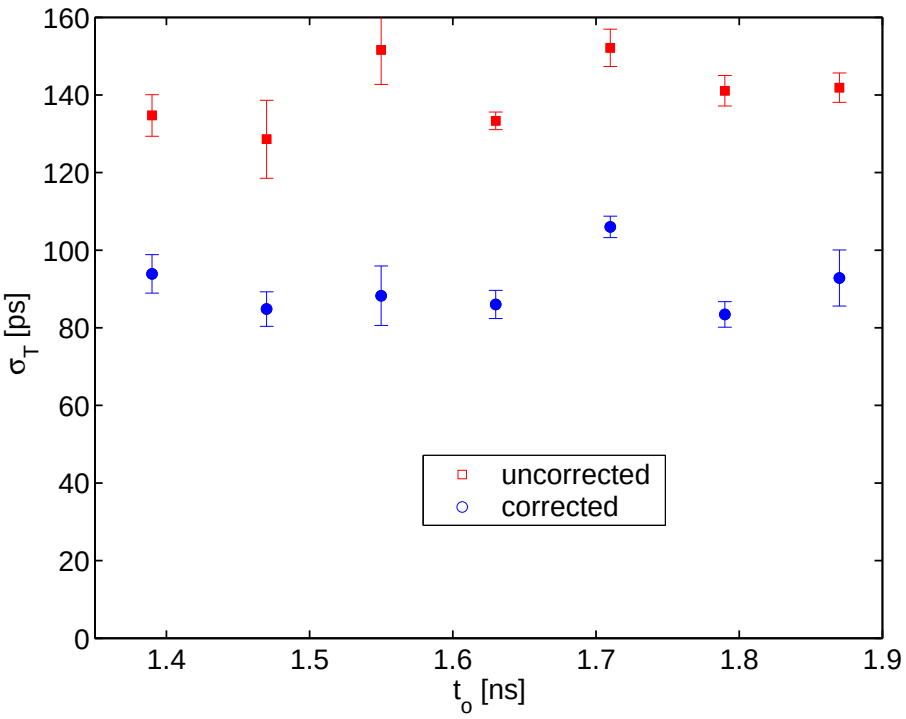

Figure 8.24: Plot showing the time resolution as a function of the peak time for all the runs corresponding to sources 3 and 4. The time offset t_{OFF} has been already subtracted. The behavior is consistent with a flat trend both for the corrected and uncorrected resolutions.

8.5 Conclusions

1. The increase of the operating temperature of a timing RPC in 25 °C is not high enough to modify significantly the properties of the gas, apart from the expected change in density that can be compensated by keeping constant the reduced voltage $V^* = VT/T_o$. This fact can be seen by examining the case of source 4, where $V^* \simeq V^*_{gap}$, and the observables ε, σ_T and t_o are not depending on the temperature.

2. On the other hand, the increase of the temperature causes an exponential increase of the glass conductivity, allowing for a faster recovery of the plates. The effect can be quantified by defining the relative rate capability $\kappa = \frac{\rho(T_o)}{\rho(T)}\frac{T_o}{T}$. For the glass used, an increase of the rate capability in a factor 10 over 25 degrees was demonstrated.

3. The behavior of q_p (average prompt charge) and ε (efficiency) as a function of the applied field V, primary rate ϕ_p and temperature T, can be described within the following hypotheses:

   (a) Both magnitudes depend on the average reduced voltage $\bar{V}^*_{gap}$ (DC model).

   (b) For strong Space-Charge effect, the relation between average charge and the reduced voltage in the gap is reasonably well described by a straight line.

   (c) The charge spectrum characteristic of illumination by 1 MeV γ photons is well described by an exponential.

4. The behavior of the peak-time t_o as a function of V, T and ϕ can be interpreted as the result of the variation of $S = \alpha^* v_e$ with the field in the gap. However, under the same conditions, no variation was observed in the time resolution both for the corrected and uncorrected time distributions. This suggests that the time resolution can not be ascribed to the avalanche process, as in the case of t_o, but is probably shadowed by another source of fluctuations. Natural sources of this extra jitter could be:

   (a) Positron annihilation delay: if the 'parasitic' 1.2 MeV photon coming from the almost instantaneous decay of Ne^{22} (3.7 ps) enters in the trigger, it will be sensitive to the variations in the positron annihilation delay (taken as reference), introducing a time jitter. Despite this photon is geometrically disfavored due to the isotropy of Ne^{22} emission, they can be selected from the scintillator charge distribution, showing the same time response as for annihilation photons.

   (b) Compton electron delay: the Compton electron produced in the electrode is moderately relativistic so that it can spend some time before leaving it, depending on its energy and point of emission. Preliminary Geant simulations indicate that the jitter coming from this effect is at the level of 10 ps [166].

   (c) In the case of illumination with photons over a 4-gap tRPC with metallic electrodes, the process of extraction of the electron shows an asymmetry. It means that the electron can be emitted either from a

metallic or a resistive cathode, depending on the gap. However, in accordance to what is said before, the jitter due to Compton emission seems to be negligible.

(d) Random coincidences: random coincidences in the time window will artificially make the time response broader. This effect should be more visible for the more intense sources, that is not the case.

(e) Geometric jitter: due to the projection of the solid angle over the detectors different track lengths are possible within the trigger acceptance. The cut used in the tRPC position (± 1 cm) reduces it to be less than 30 ps.

(f) The angular spread of the Compton electrons would provide an explanation for the larger time jitter observed (90-100 ps as compared with 50-80 ps for MIPs). However in that case the jitter should depend on the avalanche formation process and, therefore, it should be sensitive to changes in S.

As a result, it is very difficult to ascribe the invariance of the timing resolution observed for irradiation under 1 MeV γ illumination to any of these effects. The final explanation is rather puzzling and requires probably a full simulation.

Based on the strength of the DC model, the data analyzed in chapter 6 can be extrapolated to the expected behavior under 25 °C increase in temperature, as shown in fig. 8.25. The expected improvement has been recently proved, qualitatively, in [1].

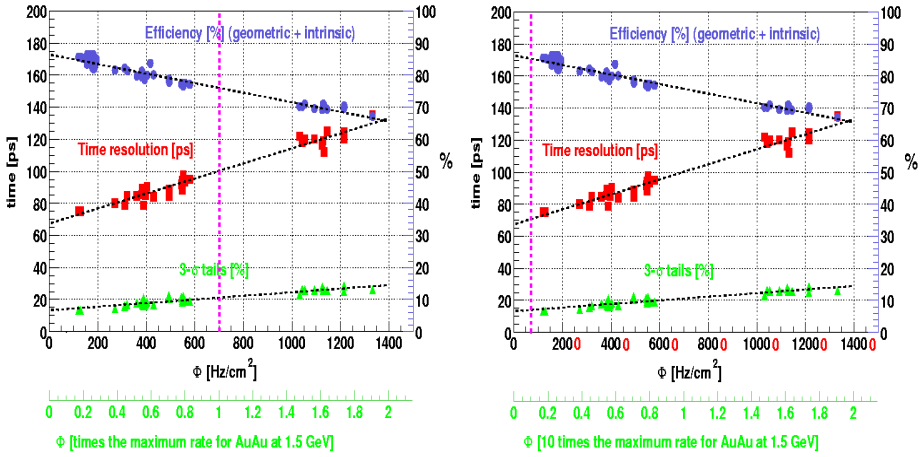

Figure 8.25: Left: figure showing the behavior of the tRPC cells tested in HADES as a function of the rate (see chapter 6). Right: expected improvement under 25 °C temperature increase, extrapolated from the results of this chapter under γ illumination. The vertical dashed line indicates the maximum rates foreseen in HADES.

As a summary: it has been shown that timing RPCs can be operated under modest variations of the temperature up to 25 degrees, without loss of the performances. Moreover, the heating of the glass allows for an increase in the rate capability of a factor 10. Under γ illumination, the observables t_o, ε, q_p, are well described by assuming that they depend on the average reduced voltage in the gap (DC model), with exception of the time resolution, that remains unaltered.

A worsening in the performances is observed above 25 °C increase, connected to an 'anomalous' exponential increase of dark counting rate and streamers with temperature. A similar effect has been also reported for trigger RPCs, despite there is no explanation for it available at the moment.

Chapter 9

Analytic description of rate effects

Aiming for a general description of the RPC time resolution in a dynamic situation, like the one taking place under high irradiation, it is necessary to account not only for the *average drop* of the electric field (*DC model*), but also for its *fluctuations*. The treatment proposed in the following sections was introduced in [61] and developed in [62]; it lays on the fact that the avalanche time t can be factored out as $t = \tau/S$ [55], [67]. On one hand, the non-dimensional time τ depends on primary and multiplication statistics, whereas S is the growth coefficient of the gas, that depends on the electric field. Hence it is expected that the fluctuations of the field in the gap affect the time response mainly through the variations of S.

9.1 An analytic model for the RPC time response

The model developed through [55] and [67] mainly by P. Fonte, A. Gobbi and A. Mangiarotti is summarized here. It aims to describe the RPC timing properties, based on a set of assumptions:

1. The number of effective primary clusters k created inside the gap follows a Poisson distribution with average n'_o:

$$P(k) = \frac{(n'_o)^k}{(e^{n'_o} - 1)k!} \tag{9.1}$$

   where n'_o is related to the detection efficiency:

$$n'_o = -\ln(1 - \varepsilon) \tag{9.2}$$

2. The avalanches are initiated, in first approximation, by a single electron, and the multiplication statistics follows the Furry law.

3. The current induced over the pick-up electrode by the movement of the electrons is:

$$i(t) = N i_e e^{St} \tag{9.3}$$

being i_e the current induced by a single electron and N the number of electrons estimated in previous items, where all the fluctuations belonging to the avalanche process are already included.

4. An exponential signal delivered through a linear electronic network does not experience any change on its growth coefficient (S for the present case) [151] but just on its amplitude. Therefore, the threshold voltage at the comparator is related to an equivalent threshold current at the amplifier input.

5. In the proposed derivation, it is implicitly assumed that the avalanche growth is not affected by Space-Charge below the level of the comparator. In this sense, for the timing properties, the signals are regarded as if they were produced under a proportional regime.

   An extensive discussion on this assumption can be found in [56], where it is shown how, even if Space-Charge is present already at the level of the comparator, the feedback mechanism characteristic of the multiplication process will preserve the time resolution unaltered, making the present description still valid. The conclusion from [56] is in agreement with the detailed simulations from [57].

By using these assumptions, it is possible to obtain the distribution of avalanche times, i.e., time that takes from the cluster formation up to when the threshold of the comparator is fired:

$$\rho_\tau(\tau) = \frac{n'_o}{e^{n'_o}-1}\frac{e^{(\tau_{th}-\tau)-\exp(\tau_{th}-\tau)}}{\sqrt{n'_o e^{(\tau_{th}-\tau)}}} I_1\left(2\sqrt{n'_o e^{(\tau_{th}-\tau)}}\right) \tag{9.4}$$

being $\tau = tS$ a non-dimensional time in units of $1/S$, I_1 the modified Bessel function and $\tau_{th} = \ln[m_t(1-\eta/\alpha)]$. The last is defined as a function of the threshold m_t and the multiplication and attachment coefficients, α and η, respectively.

The rms of the distribution of non-dimensional times τ given by eq. 9.4 was obtained in [67] as an analytic function of the effective number of clusters n'_o, denoted by $K(n'_o)$ within this work. Therefore, the final time resolution can be expressed as:

$$\mathrm{rms}_T = \frac{K(n'_o)}{S} \tag{9.5}$$

Since n'_o is given by the detector efficiency, it is possible to relate $K(n'_o)$, the intrinsic time resolution in units of $1/S$, to the efficiency of the detector, in a single 'universal' curve, that is shown in fig. 9.1.

9.1.1 Conditions for comparison with data

For an appropriate comparison of the model with data, the following points have to be stated:

1. The pdf[1] 9.4 is not Gaussian, having tails towards delayed times. The usual experimental procedure of fitting in an interval of $\pm 1.5\sigma$ around

[1] Probability Distribution Function.

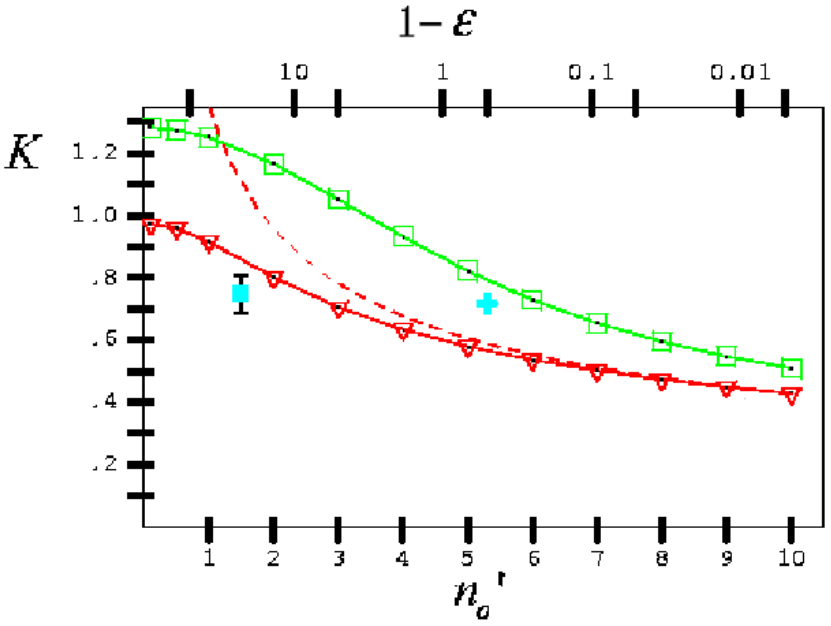

Figure 9.1: Universal curve showing $K(n'_o)$ (the intrinsic time resolution) as a function of the efficiency of the detector (equivalently, the number of effective primary clusters). The squares correspond to the rms of expression 9.4, K, whereas the triangles correspond to the Gaussian width from a fit in a $\pm 1.5\sigma$ interval, that must be used for comparison with data (K_σ). The points correspond to [55] (1-gap 0.3 mm RPC, square) and [47] (4-gap 0.3 mm RPC, cross). The figure has been taken from [61]. Also shown (dashed line) the approximate $1/\sqrt{n'_o}$ scaling.

the maximum of the time distribution must be performed, allowing for an estimate of $K_\sigma(n'_o)$, also shown in fig. 9.1. Note that, in this way, $K_\sigma(\neq K)$ is defined for an adequate description of the data.

2. The walk of the electronics for the lower charges is not included in the model and must be subtracted. However, the correlation for the intermediate charges is arguable to be intrinsic of the detector response [157].

   Avoiding the discussion on the nature of the q-t correlation, in the following it was preferred to cut the distribution at the lower charges, where the contribution of the electronics is more apparent, but without applying the slewing correction, for keeping the possible intrinsic correlation.

3. Eq. 9.4 stands for the intrinsic response of the detector. The effects of imperfect mechanics are not included.

9.2 Data analysis

9.2.1 Data set

The attention was focused on the data analyzed in chapter 6 for ionizing particles. Data collected with tRPC *II* (inner), made of aluminum-glass-aluminum in a symmetric configuration (see fig. 6.2) was chosen because several rate and voltage combinations were available.

A total of **35** different runs were selected, corresponding to a scan in rate from 100 Hz/cm^2 to 1300 Hz/cm^2 at 4 different voltages (3.1-3.4 kV/gap). The observables ε, t_o, σ_T and $\bar{q}_{prompt}$ (efficiency, time at maximum, resolution, average prompt charge in 200 ns) were studied. The efficiency was obtained after correction for the geometric losses estimated in chapter 6.

The statistics were large enough to allow for a division of each run in small sub-runs, providing an estimate of the uncertainty of the observables. If only one run is available for a certain set of operating conditions, this is the more reasonable way for estimating the error. The minimum sub-run considered statistically significative must contain at least 1000 events, otherwise it was rejected. The uncertainty of the observables under these conditions in a single run was determined to be around ± 3 ps for time measurements and $\pm 0.5\%$ for efficiency estimates, caused by the TDC/ADC binning.

The final value of a given observable was obtained from the average of all the runs/sub-runs with similar operating conditions. The 68% confidence levels were obtained from the standard deviation of the average value, after adding quadratically the effect of the TDC/ADC binning. It was assumed that all the errors have a Gaussian origin and a correction for small number of events was applied [167]:

$$\sigma\big|_{\bar{x}}(68\%\ \text{C.L.}) = \sigma\big|_{\bar{x}}\ t_p \tag{9.6}$$

Namely, the 68% confidence bounds for the average value $\bar{x}$, obtained over N measurements of the magnitude x, are given by the estimator of the uncertainty of $\bar{x}$ after multiplication by the correction factor t_p; the last depends on the number of measurements (degrees of freedom) that contribute [167], becoming 1 when $N \to \infty$.

After this analysis is performed, the initial set of data was reduced to **18** points with their corresponding uncertainties.

9.2.2 Cuts applied

External (Reference scintillators):

1. Time overflows in any channel of the reference scintillators are removed.
2. Particles with $\beta < 0.75$ are eliminated, being β determined as shown in chapter 6. In this way, particles with similar energy depositions are selected, close to the MIP dip (fig. 6.9).
3. Charges in the reference scintillators within $\pm 2\sigma$ around the value corresponding to the most probable energy deposition were selected. This avoids edge effects due to inclined tracks.
4. Position in the reference scintillators was selected within $\pm 2\sigma$ around the maximum. This cut reduces the presence of inclined tracks also.

Internal (tRPC):

1. Measured times corresponding to the TDC overflow as well as charges compatible with the ADC pedestal were cut. They contribute to the detector inefficiency, defined before the external cuts have been applied.

2. A cut of $\pm$ 1σ around the maximum of the tRPC position distribution was performed. This has a slight effect over the time response, reducing the fraction of inclined tracks.

3. Events with a registered charge lower than 200 fC were purged. This cut reduces the influence of the electronics in the time response (q-t correlation), leaving the intrinsic tRPC time response.

4. After a sudden high irradiation, it takes a certain time before the glass plate reaches a stationary situation, of the order of its relaxation time, indeed. Although this effect is of practical importance, it was skipped in order to allow for a clean comparison with the model, and will be discussed at the end. It was checked that it is enough to cut the first 2 s of each spill for guaranteeing that the plate is reasonably stationary. The mentioned effect is shown in fig. 9.2 for $\Phi = 1200$ Hz/cm^2 and a voltage $V = 3.2$ kV/gap, together with the behavior of the average charge. It must be said that $\bar{q}_{prompt}$ in the absence of rate effects was around 150 ADC units; therefore, the charging-up time is a phenomenon relatively fast for the acquisition system and only the latest stages of the process (from $q \sim 50$ to $q \sim 15$ ADC units) can be cleanly elucidated.

5. Cut in 'spill quality'. The stability within a spill was reasonable but still some runs show different spill profiles. However, no significant differences were appreciated on the observables obtained under illumination with different kind of spills (see fig. 6.13 for illustration). A marginal number of runs showed instabilities from one spill to the next; they are excluded from the analysis.

Spurious correlations

1. After all the cuts are performed, the possible walks of the FEE electronics were studied for the time distribution measured (fig. 9.3). In the following, $\Delta t_{scin-RPC}$ denotes the measured scintillator time minus the tRPC time (eq. 6.6), that was used to evaluate the timing performances. It is shown that, after a cut in the first 2 seconds in-spill, the effect of the charging-up of the plate is mostly eliminated, and the resulting cut distribution does not show any systematic effect, indicating that the presence of drifts of electronic origin is small within the same run.

9.3 DC description

9.3.1 Time at maximum (t_o) and efficiency (ε)

The main problem for evaluating the time resolution using the model described in eqs. 9.4 and 9.5 is to obtain the true voltage in the gap as a function of the

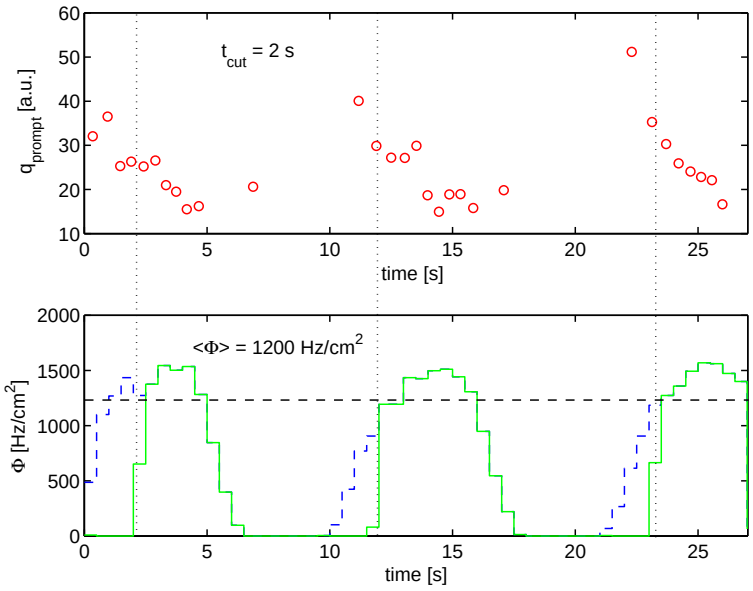

Figure 9.2: Average prompt charge (up) and rate (down) as a function of the time measured with an external clock, showing correlation with the arrival of the spill. A cut is set below the first 2 s, that roughly corresponds to the charging-up time of the resistive plates.

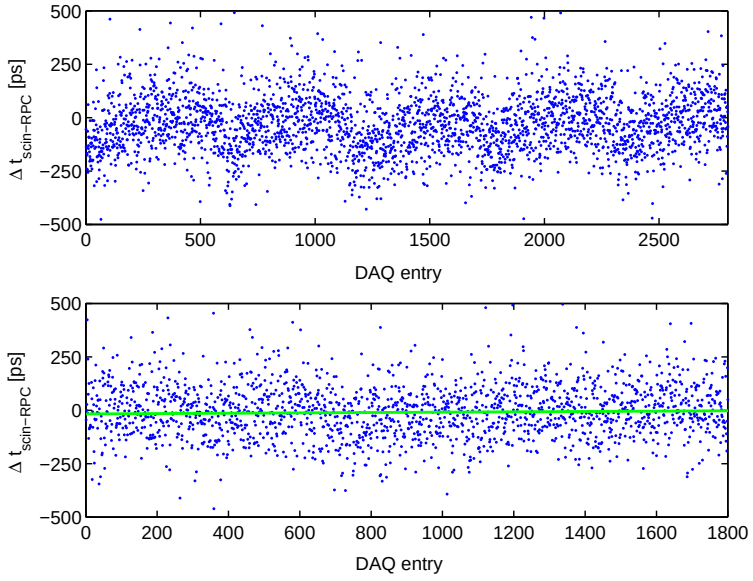

Figure 9.3: Evolution within the spill for a run taken at $V = 3.2$ kV and $\Phi = 580$ Hz/cm^2. The time measured with the tRPC is represented as a function of the DAQ entry. In the upper plot the spill structure can be seen, being characterized by a drift from fast-negative times (the glass plate is charge depleted) towards slower times (the plate is charged-up); after a few seconds this drift is stopped. In the lower plot it is shown the same situation after a cut in the first 2 seconds of each spill: no remanent correlation is present (the continuous line shows a linear fit to the points), indicating that no significative drift is present along the run.

rate. This can be accomplished by resorting to the DC model, that proved to be adequate for describing the behavior of ε, q_{prompt} and t_o (see chapter 8).

Following the steps of chapter 8, the field in the gap as a function of the rate ϕ was approximated by expression 8.21 as:

$$V_{gap} = V_{th} + \frac{(V - V_{th})}{1 + ad\phi\rho} \tag{9.7}$$

where the only free parameters are a and V_{th}. For testing the validity of the DC model, it was chosen the time t_o corresponding to the maximum of the time distribution and the efficiency ε. The behavior of t_o can be determined from expression 9.4 to be:

$$t_o = \frac{K_{_T}}{S(V_{gap})} \tag{9.8}$$

$$K_{_T} = \ln(m_t/n'_o) \tag{9.9}$$

being n'_o obtained from the measured efficiency. The derivation of eq. 9.8 is given in Appendix A.

On the other hand, the value of S as a function of V_{gap} has been measured in chapter 7 for the gas mixture used:

$$S(V_{gap})\ [\mathrm{ns}^{-1}] = (6.0 \pm 1.2)V_{gap}[\mathrm{kV}] - 7.2 \pm 3.1 \tag{9.10}$$

The efficiency as a function of V_{gap} has been also parameterized[2], assuming a Fermi-like function, that proved to be accurate for describing the efficiency close to the 'plateau' ([41], for instance):

$$\varepsilon(V_{gap}) = \frac{\varepsilon_o}{1 + e^{-\theta(V_{gap} - V_{ref})}} \tag{9.11}$$

$$n'_o(V_{gap}) = -\ln(1 - \varepsilon) \tag{9.12}$$

where $\varepsilon_o = 0.995$ is the plateau efficiency for a 4-gap tRPC extrapolated from [68], V_{ref} is the voltage at 'half-plateau' and θ the parameter that regulates the sharpness of the distribution.

Knowing the dependence of the variables ε and t_o with the field in the gap V_{gap} (eqs. 9.8 and 9.11), and the dependence of V_{gap} itself with the rate ϕ and voltage V (eq. 9.7), it is possible to perform a global fit to the data under different operating conditions, and to evaluate the DC model. The fitting procedure used is similar to the one described in chapter 8, namely, a weighted χ^2 minimization where the weights are given by the uncertainties of the points.

The results of the fit are represented in figure 9.4, indicating an overall good agreement. In particular, the obtained $\bar{q}(V)$ characteristic curve is described by the parameters a=2.9 pC/kV and V_{th}=2.1 kV, that are in qualitative agreement with the curves $\bar{q}$ vs V reported in [68], but for a different gas admixture. The behavior obtained for V_{gap} as a function of the primary rate Φ is shown in fig. 9.5.

[2]This is not required, however it provides a smooth behavior of efficiency and therefore of n'_o.

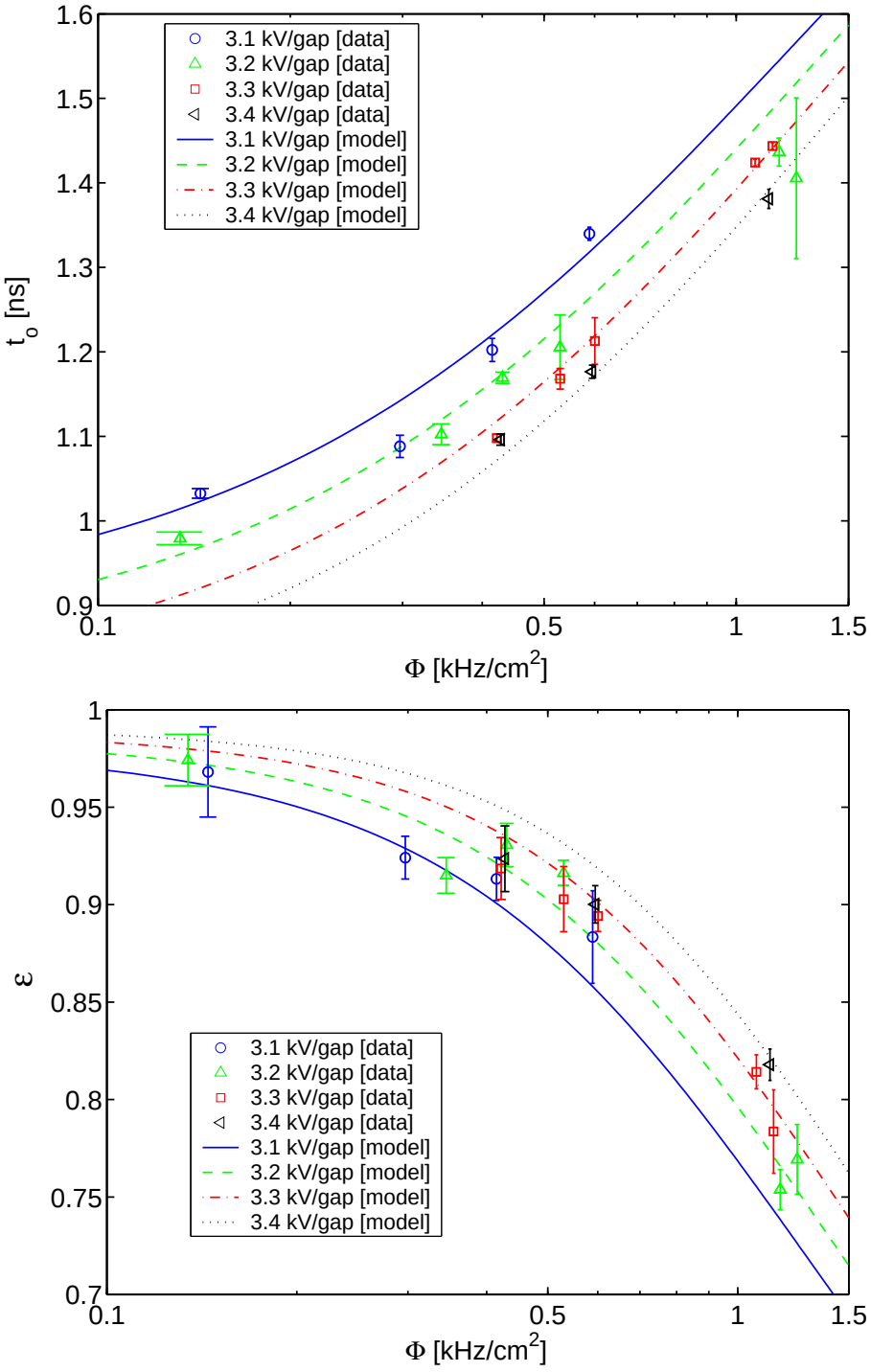

Figure 9.4: Results of the DC model applied to the description of t_o and ε for 4 different operating voltages (3.1 kV (circles), 3.2 kV (up-triangles), 3.3 kV (squares), 3.4 kV (left-triangles)). Uncertainty bars stand for 68% CL (Confidence Level) bounds.

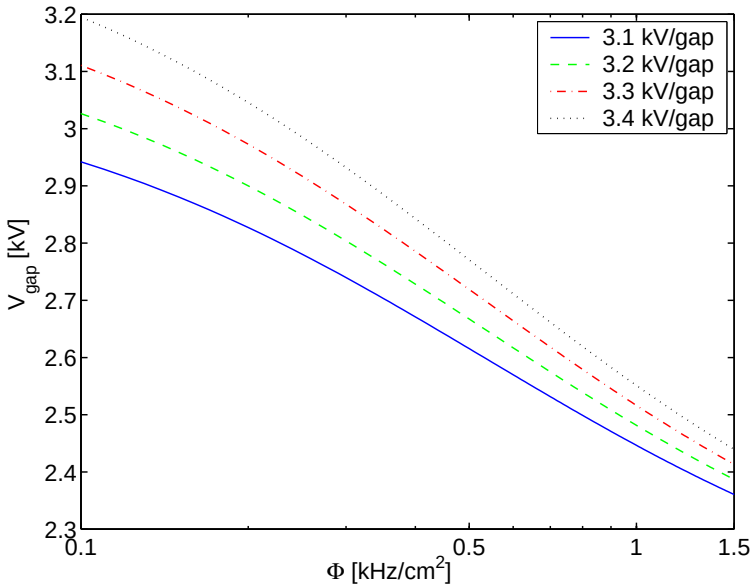

Figure 9.5: Behavior of the average voltage as a function of the rate is shown, obtained from the DC model.

9.3.2 Time resolution (σ_T)

Once the parameters of the DC model are determined, the analytic expression for the time resolution 9.5 (replacing K by K_σ) can be evaluated.

The time resolution is a delicate observable, more sensitive than t_o to in-spill effects, environmental fluctuations or small variations on timing tails. As a consequence, the uncertainty bars obtained are larger than in the case of t_o and ε. For providing a statistically significant set of data, some of the points were grouped and those where less than two runs had been used for determining the CL were neglected. This reduced set of data (7 points) provides reasonably small 68% CL bounds and is compared in fig. 9.6 with the expectation from the DC model.

It is remarkable that the lines in fig. 9.6, corresponding to the prediction of the DC model, are independent from any parameter (they were obtained from the fit to ε and t_o). The good description indicates that *at high rates the main effect on the time resolution comes from the ohmic drop in the resistive plates.* The points (open) without applying a cut in the first 2 s in-spill are also shown: this indicates that the ohmic drop is the dominant effect over an infinite time duration spill, but, due to the finite charging-up time of the plate, the situation is more complicated in general.

For better evaluating the consequences of the dominance of the ohmic drop and the effect of the charging-up time of the plate, it was developed a formalism that starts from the individual avalanche shots over the plate towards the final distribution of instantaneous fields on the gap, whose average value is given by the DC model. The following sections are dedicated to this study.

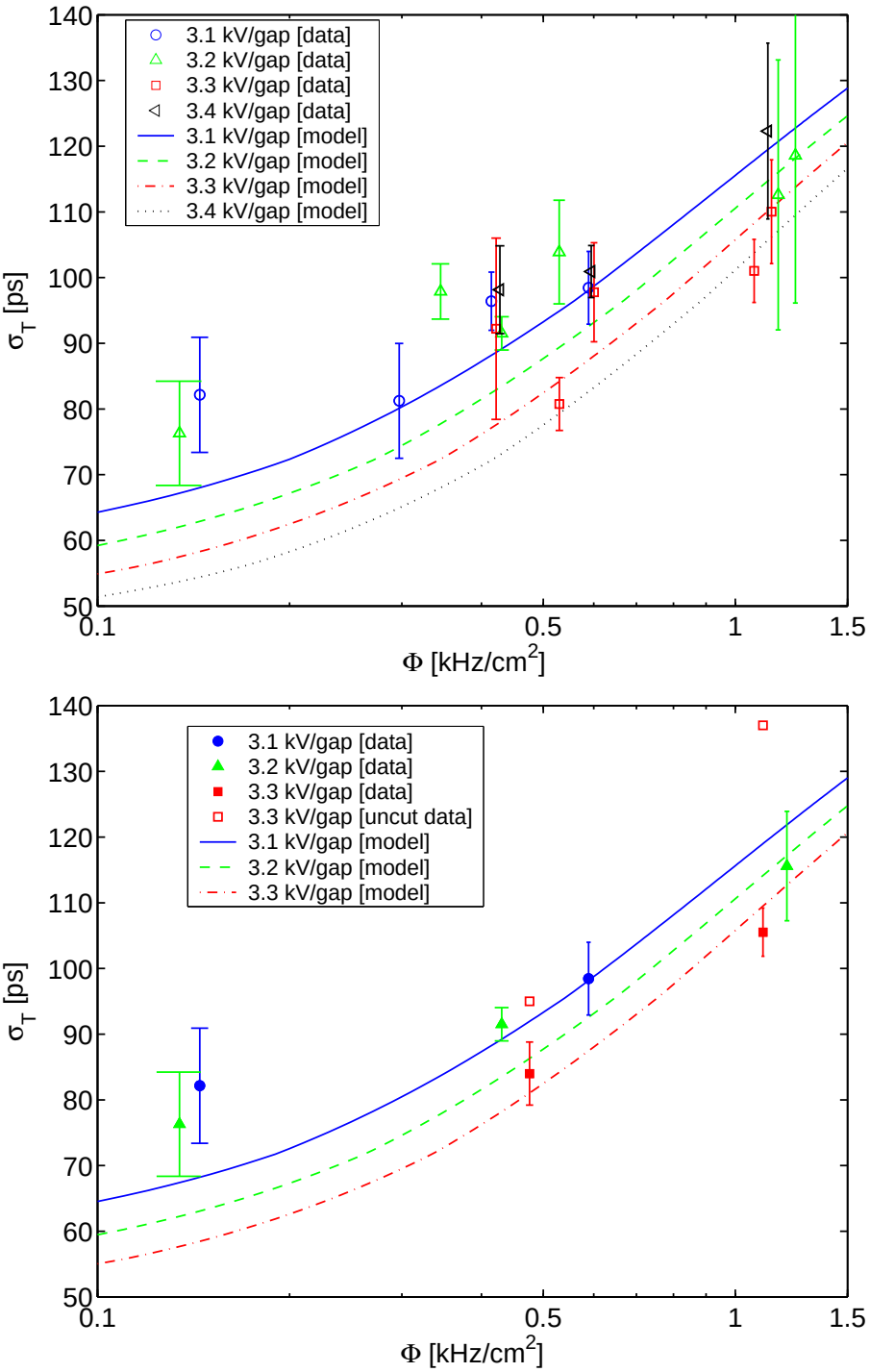

Figure 9.6: Up: time resolution K_σ/S obtained from the DC model, for the entire set of data. Points and model correspond to 3.1 kV (circles, full line), 3.2 kV (triangles, dashed line), 3.3 kV (squares, dash-dotted line), 3.4 kV (left triangles, dotted line). Uncertainty bars stand for 68% CL bounds. Down: set of data with improved statistical significance, as described in text. Also shown (open squares) the points at 3.3 kV without cutting the contribution coming from the charging-up time of the plate.

9.4 Fluctuations in the time response

9.4.1 Static non-uniformity of the electric field

It is said 'static' for referring to fluctuations that are *always* present, as it is the case for variations in the gap size due to, for example, spacers, mechanic stress, edges, rugosity of the plates or dust. This study is, in principle, of no big interest for our present purposes; however, the problem has a relatively easy treatment, that allows to introduce the formalism required for dealing with the fluctuations of the field in a dynamic situation.

In a parallel-plate geometry, the variations of the gap size are directly related to the fluctuations in the field:

$$\frac{\mathrm{rms}_E}{E} = \frac{\mathrm{rms}_g}{g} \tag{9.13}$$

being g the gap size. As the avalanche time is given by:

$$t = \frac{\tau}{S} \tag{9.14}$$

the extra time jitter coming from the fluctuations of the gap size can be derived from eq. 9.5, following the standard 'error propagation' formula:

$$\mathrm{rms}_T^2 = \left[\frac{K^2}{S^2} + \frac{\bar{\tau}^2}{S^2}\left(\frac{E}{\bar{\tau}}\frac{d\bar{\tau}}{dn'_o}\frac{dn'_o}{dE} - \frac{E}{S}\frac{dS}{dE}\right)^2\left(\frac{\mathrm{rms}_E}{E}\right)^2\right]_{E=\bar{E}_{gap}} \tag{9.15}$$

where $\bar{E}_{gap}$ is the average field across the gap, $\bar{\tau}$ the average intrinsic time and all the other magnitudes have been already defined. Eq. 9.15 applies if the fluctuations of the field are relatively small, but the exact derivation of the formula can be found in Appendix A. It can be seen that, for typical values of the parameters, the second term in the right hand side is very small as compared to the third, indicating that the relative variation of the intrinsic average time $\bar{\tau}$ with the field is much smaller than the relative variation of S[3]. Therefore:

$$\mathrm{rms}_T^2 = \left[\frac{K^2}{S^2} + \frac{\bar{\tau}^2}{S^2}\left(\frac{E}{S}\frac{dS}{dE}\right)^2\left(\frac{\mathrm{rms}_E}{E}\right)^2\right]_{E=\bar{E}_{gap}} \tag{9.16}$$

In the case where fluctuations have a mechanic origin, it is natural to consider that the average field $\bar{E}_{gap}$ in eq. 9.16 is given by the applied voltage ($\bar{E}_{gap} = V/d$). By recalling eq. 9.13, the formula can be evaluated for different configurations as a function of the fluctuations in the gap size, as shown in fig. 9.7.

It is remarkable that 4% inhomogeneities in the gap size corresponds to a worsening of 20% in the resolution of a 1-gap timing RPCs for the usual threshold $m_t = 10^5$ (15 fC). The result gives a *tight limit for the tolerances required on the surfaces that face the gap.*

A first attempt to generalize the result to the multi-gap case is devised. It must be noted that there is no formalism available that allows to study the

[3] A qualitative argument can be provided by realizing that $\bar{\tau}$ (the average time in units of $1/S$) is well described by expression 9.9, showing a logarithmic functional dependence, as compared with the linear dependence of S.

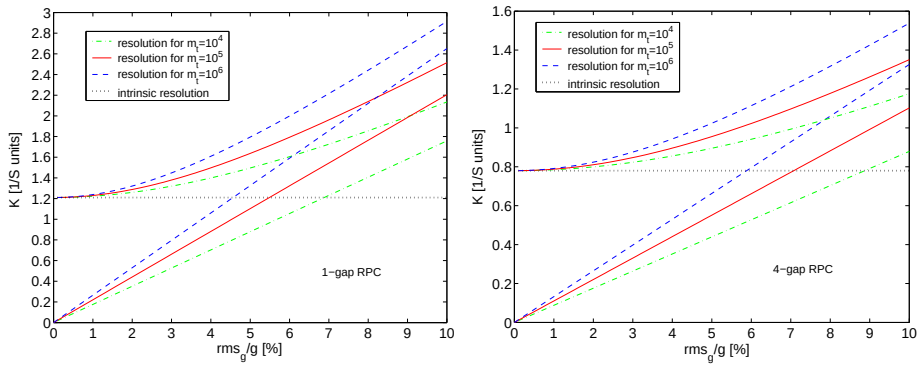

Figure 9.7: Pictures showing the expected worsening of the time resolution in units of $1/S$ for different values of the threshold $m_t = 10^6$ (dashed line), $m_t = 10^5$ (full), $m_t = 10^4$ (dot-dashed). The behavior for 1-gap (left) and 4-gap (right) tRPCs is compared. Also shown the intrinsic contribution (dotted) and the contribution owing to mechanics (straight lines).

fluctuations on each gap in an independent way; therefore the following approach is proposed: a) the N gaps contribute in a similar way to the time resolution, b) the fluctuations are independent gap to gap and c) reasonably Gaussian. Under these assumptions, the contribution of the fluctuations is expected to decrease with $\sqrt{N}$:

$$\mathrm{rms}^2_{T,N} = \left[\frac{K_N^2}{S^2} + \frac{1}{N} \frac{\bar{\tau}^2}{S^2} \left(\frac{E}{S} \frac{dS}{dE} \right)^2 \left(\frac{\mathrm{rms}_E}{E} \right)^2 \right]_{E=\bar{E}_{gap}} \tag{9.17}$$

and $\bar{\tau}$ stands again for the average time associated to the single gap. As K_N shows also a $1/\sqrt{N}$ scaling for large number of gaps, the *relative* contribution of the mechanics is, in a first approach, not depending on N. However, the absolute contribution of the mechanics is expected to be smaller for the multi-gap. The expectations of the proposed description are shown in fig. 9.7.

9.4.2 Dynamic non-uniformity of the field

This section is central for the description of rate effects. First of all, let us note that eq. 9.16 is general enough to cope with dynamic effects (rate effects). This is so because the characteristic time scales of the fluctuations of S (seconds) and τ (nanoseconds) are 9 orders of magnitude apart, so that their variations can be considered as decoupled[4]. Therefore, expression 9.16 still holds in a dynamic situation.

The development of an analytic model for dealing with the fluctuations under these conditions is the subject of the following chapter. The harder step to be accomplished consists in developing a general expression for $\mathrm{rms}_{V_{gap}}$, that will be ruled as natural, by the charge spectra of the avalanches and their time interval distribution.

[4] In the situation discussed S changes at the scale of the relaxation time of the glass.

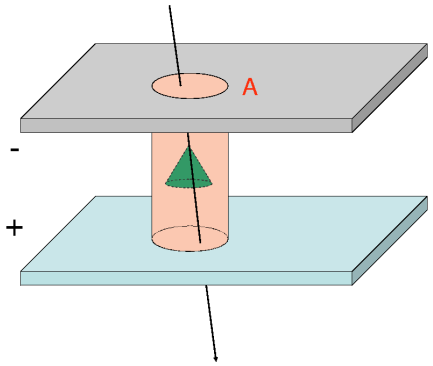

Figure 9.8: Picture showing the region considered for modeling the behavior of the tRPC.

Introduction to noise theory

The problem of the fluctuations in the field is studied by resorting to the well established theory of noise in electronic devices [168], [169]. In a certain sense, the charge released by the avalanche produced in the detector can be treated as if it were an instantaneous shot at the surface of the resistive plate. This is so, again, due to the fact that the diffusion through the plates, that is the process to be characterized, takes place at a time scale much larger than the avalanche formation. The main strength of the approach lays in the possibility of accounting for the fluctuations through related magnitudes, not requiring a detailed description of the charge spectra of the 'noise'. At first sight, the estimate of the fluctuations in the field requires to know the shape of the avalanche charge spectra: for each avalanche, there is a probability that the final charge takes any value from the charge distribution; depending on its value, the field in the gap will be affected in a different way and so the charge of the forthcoming avalanches. *It will be shown how to obtain* rms_V *as a function of* $\bar{q}$ *and* rms_q *together with the shot rate* ϕ*, without requiring to know the exact shape of the avalanche charge spectra.*

Electric model

The influenced region per avalanche is approximated by a cylinder of area A, with typical dimensions of the order of square mm following M. Abbrescia [60]. The selected cell A can be represented by the equivalent electronic circuit shown in 9.9, allowing for the adoption of techniques used in electric noise analysis. In order to compare with the data from chapter 6, the case where one of the electrodes is metallic needs to be considered.

Definitions

Some of the necessary theorems that can be found in [168], [169] will be briefly introduced here without proof, for the sake of consistency:

The *autocorrelation function* of a given random variable $x(t)$ is defined as:

$$a_x(t) = \lim_{T\to\infty} \frac{1}{2T} \int_{-T}^{T} x(t')x(t'+t)dt' \tag{9.18}$$

The associated *spectral density* is $S_x(\omega) = |X(\omega)|^2$, being $X(\omega)$ the Fourier Transform of the variable $x(t)$:

$$X(\omega) = \int_{-\infty}^{\infty} x(t)e^{-j\omega t}dt \tag{9.19}$$

$$x(t) = \frac{1}{2\pi} \int_{-\infty}^{\infty} X(\omega)e^{j\omega t}d\omega \tag{9.20}$$

The magnitude $S_x(\omega)$ is interesting because it is related to the mean squared magnitude X through *the Parseval's theorem*:

$$\overline{X^2} = \int_0^{\infty} S_x(\omega)d\omega \tag{9.21}$$

It is relevant for the proposed description to know the *Wiener-Khintchine theorem*, that relates the spectral density with the Fourier Transform of the autocorrelation function:

$$S_x(\omega) = 2\int_{-\infty}^{+\infty} a_x(t)e^{-j\omega t}dt \tag{9.22}$$

Shot-noise

As said, it is assumed that the charge released per avalanche causes an 'instantaneous' current at C_{gap} (see fig. 9.9):

$$I(t) = \sum_k q_k \ \delta(t - t_k) \tag{9.23}$$

consisting in shots of different charges q_k and arrival times t_k. The distribution of the number of shots per unit time is assumed to be Poissonian with an average rate ϕ. Working in the frequency domain:

$$I(\omega) = \sum_k q_k \ e^{-j\omega t_k} \tag{9.24}$$

This instantaneous current causes a drop in the voltage V(t) at C_{gap} that can be calculated by solving the equivalent circuit showed in fig. 9.9.

The AC response of the circuit is shown in fig. 9.10, and the voltage $V(\omega)$ is given by the Fourier transform of the shot current through the impedance $Z(\omega)$:

$$V(\omega) = I(\omega)Z(\omega) \tag{9.25}$$

$$Z(\omega) = \frac{R}{1 + j\omega CR} \tag{9.26}$$

$$Z(\omega) = \frac{R}{1 + j\omega\tau_g} \tag{9.27}$$

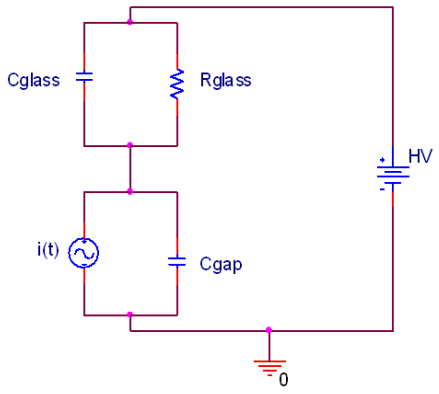

Figure 9.9: Equivalent electric circuit for the process of charge flowing through the glass plates in the case of metallic electrode.

where $C = C_{glass} + C_{gap}$. In the time domain:

$$V(t) = \sum_k \frac{q_k}{2\pi} \frac{R}{\tau_g} \int_{-\infty}^{\infty} \frac{1/\tau_g}{1/\tau_g^2 + \omega^2} e^{j\omega(t-t_k)} (1 - j\omega\tau_g) d\omega \tag{9.28}$$

$$V(t) = \sum_k \frac{q_k}{C} e^{-\frac{t-t_k}{\tau_g}} \Theta(t - t_k) \tag{9.29}$$

being Θ the step function. Each shot induces a drop q_k/C in the gap, going down to zero with the time constant τ_g of the circuit. A derivation of the last step can be found in Appendix A.

The exact expression for τ_g can be calculated in the configuration with one metallic and one glass electrode:

$$\tau_g = RC = \rho\epsilon_o \left(\epsilon_r + \frac{d}{g}\right) \tag{9.30}$$

being d and g the glass thickness per gap and the gap width, respectively. In the present configuration, recalling the behavior of the resistivity (fig. 8.1) at a $T = 25°\text{C}$ and preliminary estimates of $\epsilon_r(\omega = 0) \simeq 6$ from capacity measurements:

$$\tau_g \simeq 5 \ s \tag{9.31}$$

It must be said that there is experimental evidence that the electric properties of the glass plates may have a complicated behavior, specially regarding its relaxation time [170] and therefore the role of ϵ_r; the influence of the surface conductivity (see [38] for phenolic plates, for instance) must be also parameterized.

Along this work, the electric properties of the glass were obtained just from measurements of ρ and ϵ_r under DC conditions; there is still a (unknown) free parameter A that contains, among others, the effect of the transverse diffusion of the charge over the plates.

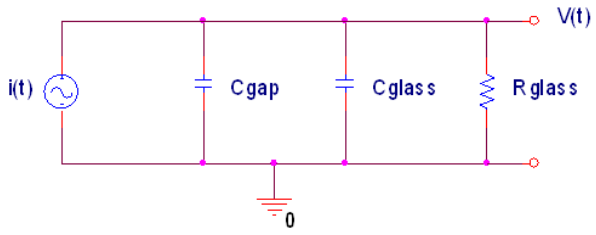

Figure 9.10: AC response of circuit 9.9. The instantaneous drop $V(t)$ is caused by the shot $I(t)$.

Uncorrelated shot-noise model

The case of charge shots that are not correlated in magnitude is treated first, since it can be dealt with analytically. The validity of the assumption is discussed at the end.

In the absence of event-by-event correlations, the autocorrelation function of $I(t)$ can be calculated following eq. 9.18 as:

$$a_{_I}(t) = \lim_{T\to\infty} \frac{1}{2T} \int_{-T}^{T} I(t')I(t'+t)dt' = A\phi\overline{q^2}\delta(t) \tag{9.32}$$

and the derivation is addressed in Appendix A. Note that ϕ is the rate in units of $[T^{-1}][L^{-2}]$ so that ϕA is the frequency of events in the cell. The spectral density $S_{_I}$ can be derived by using the Wiener-Khintchine theorem (eq. 9.22):

$$S_{_I}(\omega) = 2\int_{-\infty}^{+\infty} a_{_I}(t)e^{-j\omega t}dt = 2A\phi\overline{q^2} \tag{9.33}$$

which does not depend on the frequency (white noise), showing that no correlation is present. In order to obtain the fluctuation of the voltage, the current must be converted to voltage in the frequency domain through the complex impedance, $Z(\omega)$ (eq. 9.25). Using the Parseval's theorem (eq. 9.21):

$$S_{_V}(\omega) = S_{_I}(\omega)\left|Z(\omega)\right|^2 \tag{9.34}$$

$$\mathrm{rms}^2_{_{V_{gap}}} = \frac{1}{2\pi}\int_o^\infty S_{_I}(\omega)\left|Z(\omega)\right|^2 d\omega \tag{9.35}$$

$$= \frac{R^2}{\pi} A\phi\overline{q^2}\int_o^\infty \frac{d\omega}{1+\omega^2\tau_g^2} \tag{9.36}$$

$$= \frac{R^2}{2\tau_g} A\phi\overline{q^2} \tag{9.37}$$

As a function of fundamental quantities, the last expression can be rewritten as:

$$\mathrm{rms}^2_{_{V_{gap}}} = \frac{\rho^2 d^2}{2\tau_g}\frac{\phi}{A}\bar{q}^2\left(1+\frac{\mathrm{rms}_q^2}{\bar{q}^2}\right) \tag{9.38}$$

which is a form of the Campbel theorem [168] for uncorrelated shot-noise. Following the Campbel theorem, the effect of the charge spectra over $\mathrm{rms}_{_{V_{gap}}}$ is parameterized trough $\bar{q}$, rms_q and ϕ.

Eq. 9.38 can be expressed in a compact form as a function of the macroscopic variables ruling the shot-noise phenomenon:

$$\mathrm{rms}^2_{V_{gap}} = \frac{1}{2}\bar{V}_{drop}\bar{V}_{shot}\left(1 + \frac{\mathrm{rms}^2_q}{\bar{q}^2}\right) \tag{9.39}$$

being $\bar{V}_{drop} = R\phi A\bar{q}$ the average voltage drop in the glass over time, and $\bar{V}_{shot} = \bar{q}/C$ the average instantaneous drop created by a single shot.

It is a consequence of the correlation between the voltage in the gap and the avalanche charge (not included in the Campbel theorem) that, the larger the instantaneous drop produced by an avalanche, the smaller the size of the forthcoming shot. A possible way of introducing it consists in replacing $\bar{q}$ in eq. 9.38 by its approximate behavior:

$$\bar{q} = \frac{a(V - V_{th})}{1 + ad\phi\rho} \tag{9.40}$$

In this way, *the average effect of the correlation* is introduced and denoted by 'Campbel theorem with drop'. It does not represent an event-by-event correlation, that is discussed in next section, but an approximation more accurate than the simple 'Campbel theorem'.

MC for shot-noise

The expression for $\mathrm{rms}_{V_{gap}}$ obtained from eqs. 9.38 and 9.40 is an approximation to the real problem where event-by-event correlations are present. For evaluating the validity of the analytic description, a MC calculation of the shot-noise process including the correlations has been developed.

For simplicity, it is assumed in the following that *the shape of the charge spectra is not changing with the field in the gap.* The approximation is reasonable according to the measurements on the charge spectra for γ photons (chapter 8) but it was observed to be also a reasonable assumption in the case of ionizing particles, as long as streamers do not contribute to the charge spectra (see fig. 9.11). In the following, when comparing with data, $\mathrm{rms}_q/\bar{q}$=0.7 is assumed and the effect of the streamers at the lower rates was neglected; this leads to $\mathrm{rms}_q/\bar{q}$=1.4 when extrapolated to the relative fluctuations per gap.

The correlation was introduced by recalling the relation:

$$\bar{q} = a(V_{gap} - V_{th}) \tag{9.41}$$

with parameters a and V_{th} obtained from the fit performed in section 9.3. At last, the MC simulation is performed according to the following steps:

1. The time is sampled in $t_{_N}$ random intervals.
2. An initial charge q is selected from a distribution $\frac{dN}{dq}\big|_{\bar{q}}$ with a certain average $\bar{q}$.
3. The charge produces a drop $u_k = \frac{q_k}{C}$ of the voltage in the gap.
4. The voltage starts to recover in time towards its initial value following $u_k(t) = \frac{q_k}{C}e^{-t/\tau}$.

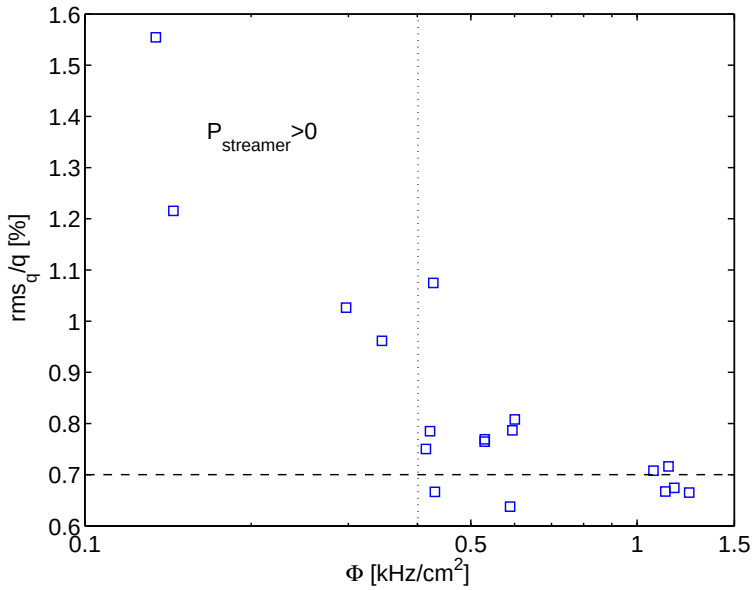

Figure 9.11: rms_q/q as a function of the primary rate ϕ, showing a flat behavior at around 0.7 in the absence of streamers.

5. At an instant t_i, taken from a random time distribution with average $(\phi A)^{-1}$, a new shot is produced. It finds a voltage given by $V(t_i) = V - \sum_k^{i-1} u_k(t_i)$, being i-k the number of previous shots. Therefore, the average charge of the distribution changes to $\bar{q}(t_i) = a(V(t_i) - V_{th})$.

6. The charge of the new shot is sampled from the new charge distribution $\frac{dN}{dq}|_{\bar{q}(t_i)}$.

7. The process is repeated from step 4.

The shot-noise process is reproduced in fig. 9.12. In this approach, the average voltage can be computed at the end, but also its instantaneous values at times t_i, and the distribution of voltages $V(t_i)$ can be therefore obtained. Fig. 9.13 shows the distribution of voltages in the gap for $A = 1$ mm^2, using as input a flat charge spectra and an applied voltage of V=3.2 kV/gap, for 10 different rates.

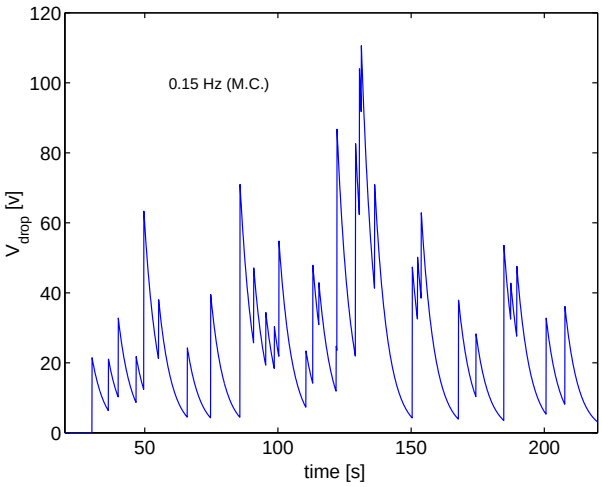

Figure 9.12: Graphical representation of the shot-noise process over the resistive plates. The average drop of the voltage was only 25 volts in this case.

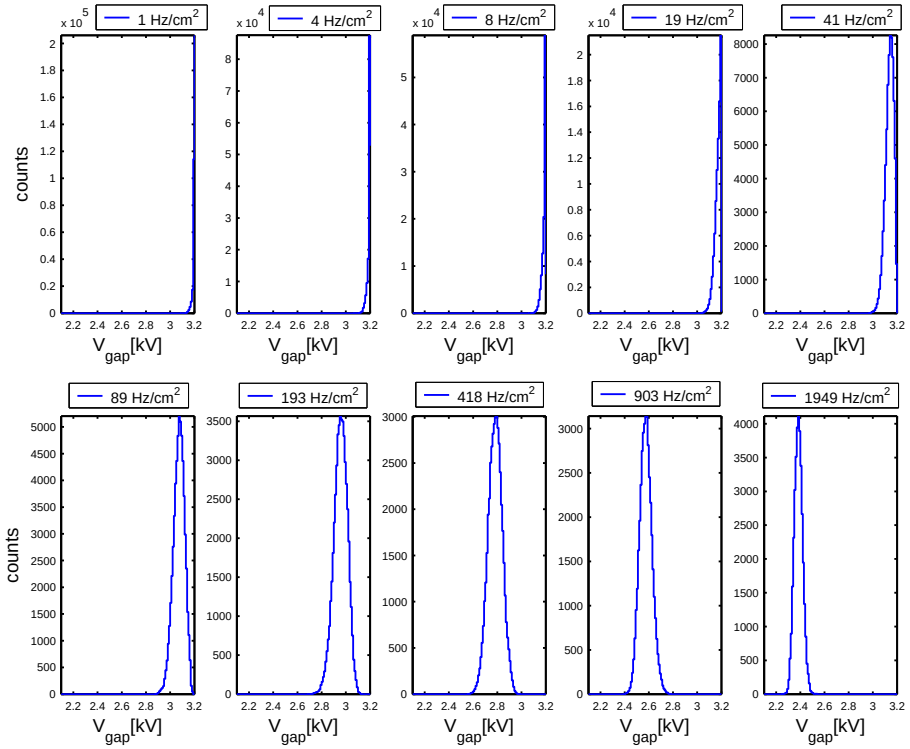

Figure 9.13: Histograms of the voltage in the gap $V(t_i)$ for an applied voltage V=3.2 kV and $A = 1$ mm^2. The distribution of charge shots used as input is flat.

The time to reach equilibrium, t_{eq}

The first observation that can be made with the MC is that it takes a finite time to reach the stationary situation, where the resistive plate is 'charged-up' (fig. 9.14). The concept has been first introduced in section 9.2.2 and it must be considered for a correct interpretation of data (see figs. 9.2 and 9.3). The time to reach equilibrium can be defined in a general context: assuming that there are infinite cells of area A per detector, the average voltage drop on the detector plates as a function of the time of illumination is given by:

$$\bar{V}_{drop}(t) = \lim_{N\to\infty} \frac{1}{N} \sum_{i=1}^{N} V_{cell,i}(t) \tag{9.42}$$

where V_{cell} is the voltage drop in a single cell as a function of time, obtained from the MC.

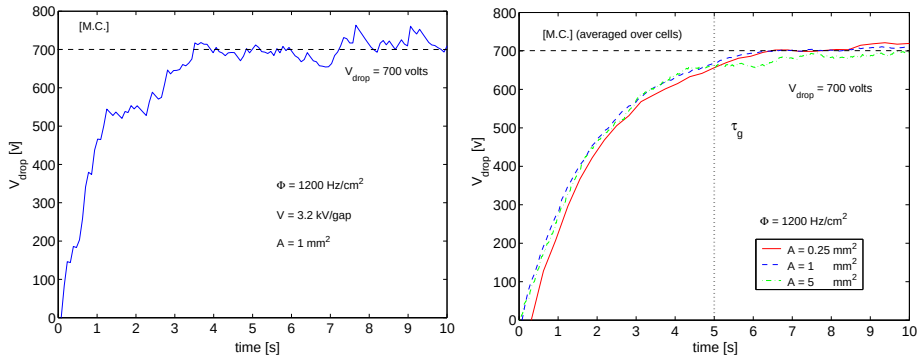

Figure 9.14: Charging-up time of the cell (left) at high rates. In the right the average behavior of the voltage drop as a function of time is shown (integrated over a large number of cell histories), for three different values of the area of influence of the avalanche. The curves are rather independent from that parameter and show a typical stabilization time of the order of the relaxation time of the tRPC.

$\bar{V}_{drop}(t)$ is represented in fig. 9.14 (right) for three values of the influenced area and Φ=1200 Hz/cm^2. The figure can be also interpreted as what one may see by monitoring the current driven by the tRPC as a function of time, as $\bar{V}_{drop}(t) = \bar{I}(t)R$. It is remarkable that the stabilization time does not depend on the influenced area. In particular it takes a value close to the relaxation time τ_g. The stabilization time t_{eq} can be defined from eq. 9.42 as the time it takes to reach a certain fraction f of the average drop corresponding to the stationary situation $\bar{V}_{drop}$:

$$\bar{V}_{drop}(t_{eq}) = \lim_{N\to\infty} \frac{1}{N} \sum_{i=1}^{N} V_{cell,i}(t_{eq}) = f\bar{V}_{drop} \tag{9.43}$$

In the limit of low rates (and low drop), only one shot per cell contributes to the infinite sum in 9.43, and it can be re-expressed in a simple way as:

$$\bar{V}_{drop}(t_{eq}) = A\Phi \int_0^{t_{eq}} \bar{V}_{shot,o} e^{-(t_{eq}-t')/\tau_g} dt' \tag{9.44}$$

being $\bar{V}_{shot,o}$ the average shot at zero rate. Therefore, the equilibration time in the low rate limit can be obtained as:

$$\bar{V}_{drop}(t_{eq}) = A\Phi\bar{V}_{shot,o}\tau_g[1 - e^{-t_{eq}/\tau_g}] = f\bar{V}_{drop} \tag{9.45}$$

$$\bar{V}_{drop}(t_{eq}) = A\Phi\bar{V}_{shot,o}\tau_g[1 - e^{-t_{eq}/\tau_g}] \simeq f\bar{V}_{shot,o}A\Phi\tau_g \tag{9.46}$$

$$[1 - e^{-t_{eq}/\tau_g}] = f \tag{9.47}$$

$$t_{eq} = -\ln(1-f)\tau_g \tag{9.48}$$

In the low rate limit, the charging-up time must be related to the relaxation time τ_g. Therefore, the following convention is adopted for the fraction of drop f at which t_{eq} is defined:

$$f = 1 - 1/e = 63\% \tag{9.49}$$

that provides $t_{eq} \simeq \tau_g$. The functional behavior of the stabilization time t_{eq} for high rates is derived in Appendix A under a set of simplifying assumptions. In average, t_{eq} has a flat behavior for intermediate rates following $t_{eq} \simeq \tau_g$ and starts to decrease when the drop of the field is high:

$$t_{eq} = \frac{\tau_g}{ad\rho\phi}\ln(1 + ad\rho\phi) \tag{9.50}$$

Expression 9.50 indicates that t_{eq} is highly independent from the influenced area. The intuitive explanation for this fact is that, the larger is the influenced area, the higher the number of events impinging over it, but the smaller the drop per shot (the capacity is higher). These two effects balance, leading to a smooth dependence of t_{eq} with A, as shown in fig. 9.15, where the values of the average time t_{eq} obtained from MC are represented.

The MC estimate of t_{eq} from eq. 9.43 is shown in fig. 9.15, together with the analytic expression 9.50. Remarkably, the trend has a similar behavior to that reported in [170], without requiring to assume any change in the electric properties of the glass with rate.

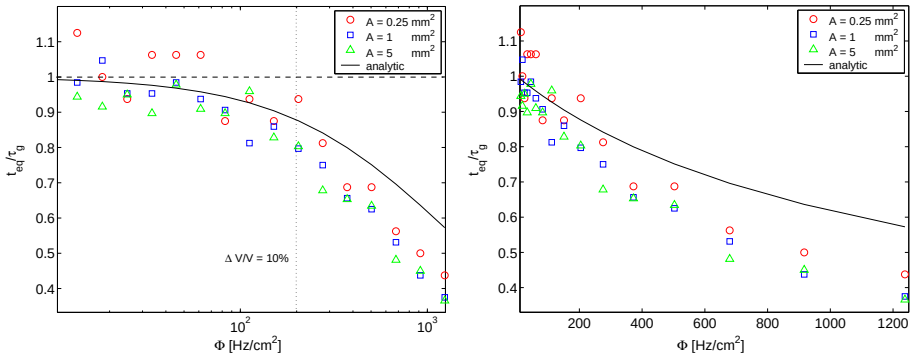

Figure 9.15: Stabilization time normalized to the relaxation time, represented as a function of rate for three values of the area of influence. Also the analytic approach given in eq. 9.50 is shown.

Therefore, it can be said with generality that, as long as the time duration of the spill is smaller than τ_g, the tRPC is not completely charged-up. This

effect leads to an over-estimation of the efficiency capabilities (as shown in [71], for instance) and has to be taken into account when comparing between sets of data that are measured at different spill lengths.

Once the curve $\bar{V}_{drop}(t)$ is obtained (fig. 9.14) from MC, the expected behavior of observables like $t_o(t)$ can be evaluated. Due to the small dependence of the influenced area on the charging-up process, the estimate of $t_o(t)$ is essentially parameter-free ($A = 1$ mm^2 has been taken, for instance). The comparison is shown in fig. 9.16 and the estimate of t_o in data was obtained as the average over time intervals containing 200 events. For an adequate description of data, a value of $\epsilon \simeq 2.5$ must be assumed, *resulting in a relaxation time twice smaller than the measured in DC (eq. 9.31)*. The description obtained in this way is rather reasonable, although an accurate determination of t_o as a function of the spill time requires much higher statistics than presently available. As in the case of the average charge (fig. 9.2), the small fraction of triggered events as compared to the total allows to observe the charging process only at its final stage.

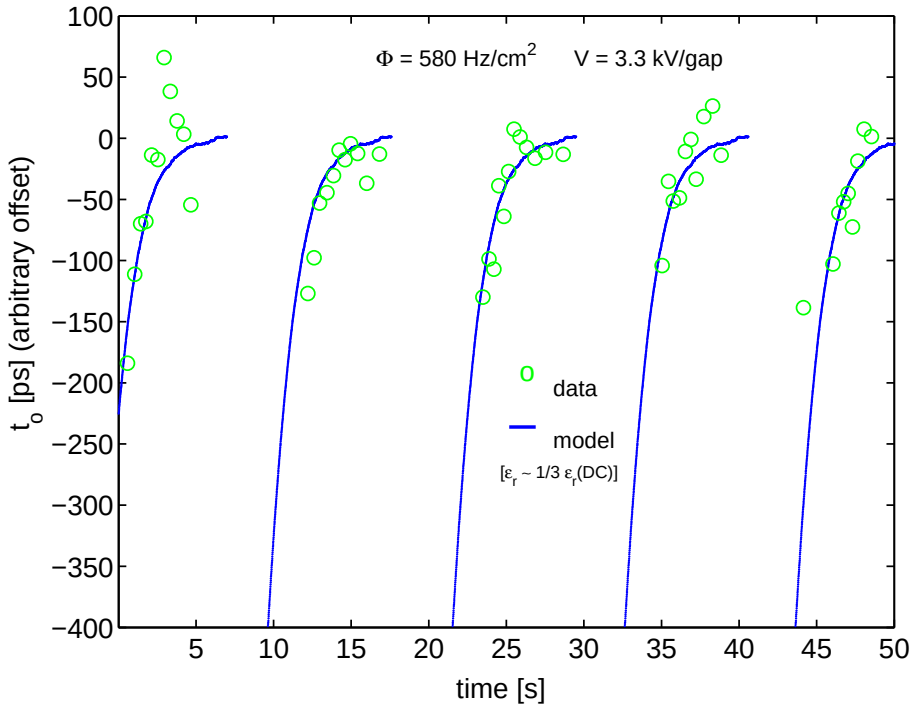

Figure 9.16: Example of the charging-up process observed from data (circles) and comparison with the shot-noise model developed.

After the good description obtained in fig. 9.16 for the charging-up process, it is tempting to extrapolate the RPC behavior to short spills (as CERN-PS, for example). For that, the average drop $\bar{V}_{drop}(t)$ at the end of the spill is represented in fig. 9.17, and compared with the stationary situation. The MC description points to a high over-estimation on efficiency and timing capabilities when testing at CERN-PS, coming from the fact that less than 1/3 of the drop

corresponding to the stationary situation is reached during the spill.

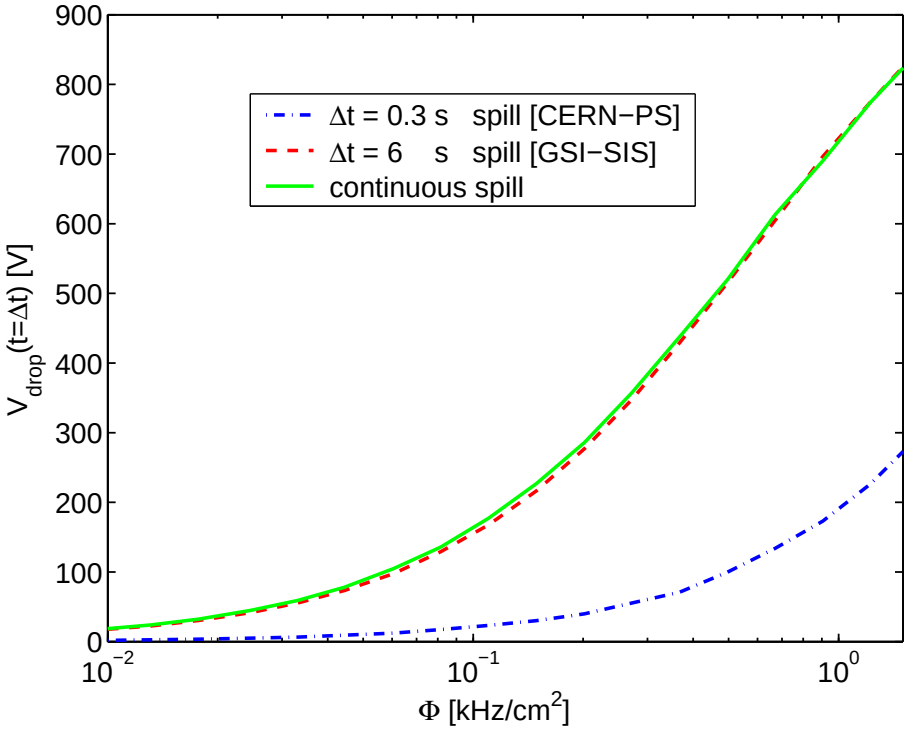

Figure 9.17: Extrapolation of the drop at the end of the spill $\bar{V}_{drop}(\Delta t)$ in the present prototype to the CERN-PS (dot-dashed) and comparison with the typical GSI-SIS conditions (dashed).

Comparison between the MC and analytic approaches

As it has been thoroughly discussed, for comparisons between model and data it is preferable that the stationary situation has been reached; therefore the first 2 seconds corresponding to the most of the charging-up time are cut.

It must be noted that the spectrum of voltages in the gap is highly Gaussian (see fig. 9.13 for instance). This behavior depends, in fact, on the value of A, and it is given by the condition:

$$(\Phi A)^{-1} \ll \tau_g \tag{9.51}$$

Therefore, if the frequency of events is very high as compared with the relaxation time, the central limit theorem causes the distribution of fields to become Gaussian. For the values discussed here, the Gaussian assumption is perfectly reasonable.

With the MC developed, the magnitude of interest, $\mathrm{rms}_{V_{gap}}$, has been calculated as a function of the primary rate, for three different charge spectra: $\frac{dN}{dq} \propto 1$, $\frac{dN}{dq} \propto 1/q$, $\frac{dN}{dq} \propto e^{-q/\bar{q}}$. In the three cases, the shape of the distributions has been chosen so that it yields the same values of $\bar{q}$ and $\mathrm{rms}_q/\bar{q}$. In

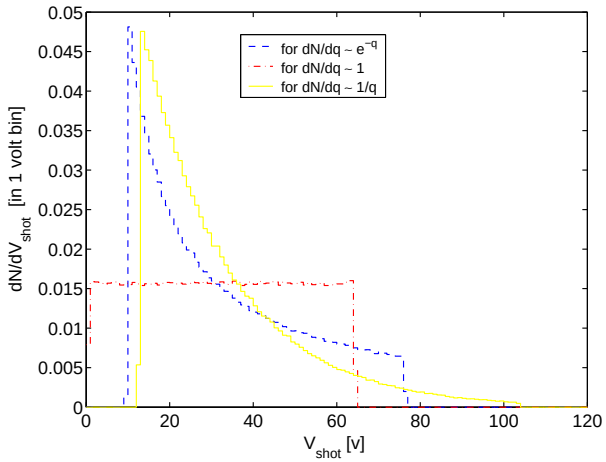

Figure 9.18: The distribution of charges (shots) used in the MC calculation. They are natural choices for testing the analytic description of shot-noise: $1/q$ is expected for an uniform distribution of the first cluster in the gap [51], e^{-q} is the Furry law, and 'flat' is a reasonable approximation if Space-Charge is important [53].

particular, their average corresponds to the value determined at V=3.2 kV/gap (recalling eq. 9.40) with $\mathrm{rms}_q/\bar{q} = 1/\sqrt{3} \simeq 0.6$, that is the value corresponding to a flat spectrum extending from zero.

The studied spectra of shots are plotted in fig. 9.18. The upper and lower limits of the distributions are defined to provide the same $\bar{q}$ and $\mathrm{rms}_q/\bar{q}$.

The results of the MC are represented, together with the Campbel theorems, in figure 9.19. The following conclusions can be drawn:

1. For low drops in the field, the Campbel theorem 9.38 reproduces the data, indicating that correlation is still not important.

2. The Campbel theorem is completely wrong if the drop of the field is high.

3. The 'Campbel theorem with drop' (9.38 and 9.40) over-estimates the true $\mathrm{rms}_{V_{gap}}$ by a factor 2 at the higher rates considered. Despite this, the behavior is reasonably similar to MC.

4. The results for the $\mathrm{rms}_{V_{gap}}$ are independent from the shape of the charge distribution as long as the rms_q and $\bar{q}$ are the same. This indicates that an extension of the Campbel theorem to the case where the events are correlated may be achievable.

Looking at fig. 9.19 and having in mind the functional behavior of the Campbel theorem (eq. 9.38), it is reasonable to think that $\mathrm{rms}_{V_{gap}}(\phi)$ depends only on the area A influenced per avalanche once the parameters rms_q and $\bar{q}$ of the charge distribution are fixed. Therefore, the relative contribution of the fluctuations can be studied for different sizes of the influenced region A, with the values rms_q and $\bar{q}$ fixed from data. This is done in fig. 9.20, where the behavior of $\frac{\mathrm{rms}_{V_{gap}}}{V_{drop}}$ is plotted as a function of ϕ. In fact, from eq. 9.39 it can

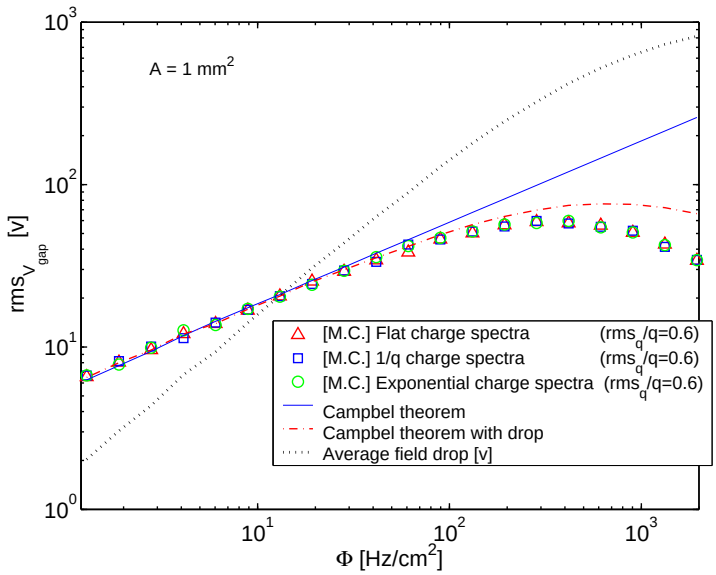

Figure 9.19: $\mathrm{rms}_{V_{gap}}$ vs the rate ϕ over orders of magnitude, showing the exact solution (points) including even-by-event correlations. Different shapes of the charge spectra are considered. Also shown the different versions of the Campbel theorem discussed in the text.

be seen that the ratio $\frac{\mathrm{rms}_{V_{gap}}}{\bar{V}_{drop}}$ is given by the law:

$$\frac{\mathrm{rms}_{V_{gap}}}{\bar{V}_{drop}} = \sqrt{\frac{\bar{V}_{shot}}{2\bar{V}_{drop}}\left(1+\frac{\mathrm{rms}_q^2}{\bar{q}^2}\right)} = \sqrt{\frac{\left(1+\frac{\mathrm{rms}_q^2}{\bar{q}^2}\right)}{2A\phi\tau_g}} \tag{9.52}$$

It indicates that the relative contribution of the fluctuations is decreasing with the larger area A and the higher rate ϕ as long as the shape (related to the factor $\left[1+\frac{\mathrm{rms}_q^2}{\bar{q}^2}\right]$) is roughly constant.

Fig. 9.20 shows the approximate $1/\sqrt{A\phi\tau_g}$ scaling, deviating at high rates in agreement with fig. 9.19. The monotonic decrease with the rate and influenced area is expected, as $A\phi\tau_g$ is just the average number of shots contributing per affected region, being smaller the fluctuations as that number increases.

9.5 Constraints from the model

Combining the DC model (eq. 9.7) and the estimate of the magnitude of the fluctuations ($\mathrm{rms}_{V_{gap}}$) from the MC, it is possible to evaluate the time resolution under rate effects from eq. 9.17 in this, more general, scenario. Although it has been shown that the behavior of the time resolution as a function of rate can be explained by a simple DC model (fig. 9.6) there are two reasons for pursuing a comparison that includes the fluctuations:

1. Current available data do not allow to clearly state an effect at the level of 10-20%, that may be originated by the fluctuations of the field.

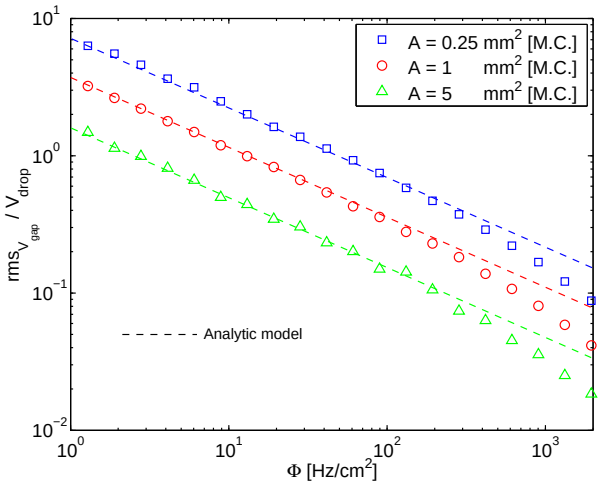

Figure 9.20: Relative contributions of the fluctuations with respect to the average ohmic drop in the glass as a function of the rate for three different areas of the avalanche. The approximate $1/\sqrt{A\phi}$ scaling described in text is also shown.

2. Instead, it is possible to set upper bounds to the parameters that govern those fluctuations.

The starting point is the generalized version of eq. 9.17, including dynamic (rate) and static (mechanics) effects. For simplicity, the average time $\bar{\tau}/S$ per gap is approximated by the peaking time t_o (see Appendix A), and written, in the following as:

$$\mathrm{rms}_T^2 = \left[\frac{K_N^2}{S^2} + \frac{t_o^2}{N} \left(\frac{E}{S}\frac{dS}{dE} \right)^2 \left(\frac{\mathrm{rms}_E^2}{E^2}\Big|_{static} + \frac{\mathrm{rms}_E^2}{E^2}\Big|_{dynamic} \right) \right]_{E=\bar{E}_{gap}} \tag{9.53}$$

As the field is dropping with the rate, it is natural to expect that the contribution of the mechanics becomes smaller at high rates. Knowing the dependence of the field in the gap with rate from eq. 9.7, it is straightforward to derive that:

$$\mathrm{rms}_{E_{gap}}\big|_{static} = \frac{\mathrm{rms}_E\big|_{static}}{1 + ad\phi\rho} \tag{9.54}$$

It is also interesting to evaluate the quantity $\frac{\mathrm{rms}_{E_{gap}}}{\bar{E}_{drop}}$:

$$\frac{\mathrm{rms}_{E_{gap}}}{\bar{E}_{drop}}\bigg|_{static} = \frac{\mathrm{rms}_g}{g}\frac{V}{(V - V_{th})ad\rho\phi} \sim \frac{1}{\phi} \tag{9.55}$$

where g is the gap width. This must be compared with the approximate scaling $1/\sqrt{\phi}$ for the dynamic contribution (eq. 9.52). Therefore, it is expected that *at high rates, the fluctuations due to rate effects dominate over those due to mechanics.*

As said, in the situations considered, it is reasonable to assume that the dynamic fluctuations are Gaussian at high rates. For comparison with data is

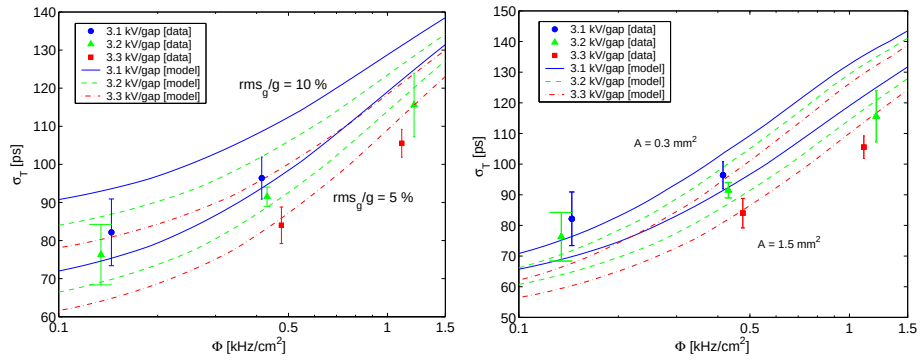

Figure 9.21: Results of the comparison with data for the two different sources of fluctuations by assuming static (left) and dynamic (right) origin. Different values of the parameters are shown.

therefore preferable to use K_σ (intrinsic Gaussian width in $\pm 1.5\sigma$) instead of K (true rms) in eq. 9.53.

The results of the evaluation of eq. 9.53 are presented in fig. 9.21 for two different values of the parameters rms_g/g and A, that govern the fluctuations of 'static' and 'dynamic' origin respectively.

It is shown how values of $\mathrm{rms}_g/g = 5\%$ and $A = 1.5$ mm^2 still allow for a reasonable description of data, while $\mathrm{rms}_g/g = 10\%$ and $A = 0.3$ mm^2 are in complete disagreement. Therefore, a conservative limit can be set from data to the parameters, yielding $\mathrm{rms}_g/g < 10\%$ and $A > 0.3$ mm^2. Clearly, it is easy to distinguish between both origins for the fluctuations by studying the behavior at very low rates (ϕ <100 Hz/cm^2), but no data was acquired in that regime.

9.6 Conclusions

An analytic framework has been developed based on electric noise techniques, that allows to study the time response of RPCs under high irradiation in an easy way. This framework, together with the DC model introduced already in chapter 8, has been used to describe experimental data.

The following can be considered as the central conclusions of the present work:

1. The time resolution as a function of rate and voltage is reasonably well described by a simple DC model once a stationary situation is reached. It indicates that the behavior under rate effects is ruled by the average ohmic drop in the resistive plates. If confirmed in forthcoming works, it would open the possibility of RPC operation at high rates by just increasing the applied voltage. The required over-voltage is far from being modest: for the present prototype it can be inferred that around 2.5 kV/gap increase would be necessary at the rates $\Phi = 1200$ Hz/cm^2 for having the same average voltage in the gap than at zero rate.

2. The data can be used to set limits on the contributions of the fluctuations of the field. In particular, scenarios with an avalanche area of influence

$A < 0.3$ mm^2 can be excluded.

In fact, present estimates of this magnitude based on electrostatic considerations [63] and cluster size measurements [148] point to values at the scale of mm^2.

3. A general limit to the degree of gap uniformity required for operating timing RPCs has been set: an uniformity better than a 4% is required for an effect smaller than 20% on the time resolution.

4. The contribution of the dynamic fluctuations has been accounted by a MC that follows each charge shot individually. The analytic model proposed (denoted as 'Campbel theorem with drop') shows an accuracy below a factor 2 for the higher rates considered, but possesses scaling properties similar to the MC.

5. It has been pointed out that a time close to the relaxation time τ_g is required in order that the RPC arrives to a stationary situation. If the duration of the spill is smaller, the glass is not fully charged-up and the net result could be an over-estimation of the rate capabilities, specially regarding efficiency measurements, an effect that has been already reported in literature [71]. This stabilization time produced, conversely, a worsening in the timing performances in the present situation. However, it will result also in an over-estimation if $t_{spill} \ll \tau_g$.

6. Remarkably, the predicted stabilization time is in reasonable agreement with the one estimated from resistivity and permittivity measurements in lab under DC conditions. However, the best description is obtained assuming a value for ϵ_r that is 2.4 times smaller than the measured one, providing $\tau_g = 2.5$ s.

7. The contribution of the fluctuations respect to the average drop of the field scales as $1/\sqrt{A\phi\tau_g}$. This is natural, since the average number of shots contributing per cell is $\bar{N} = A\phi\tau_g$. The larger the number of shots per influenced region, the smaller the fluctuations of the field around its mean value.

8. From the previous point it can be concluded, in general, that the larger the area affected per shot, the smaller the fluctuations and the better the behavior. This could be counter-intuitive, but certainly the larger area implies also a lower drop of the field per charge shot and, therefore, for the same average ohmic drop the fluctuations will be smaller. Anyhow, for the case of timing RPCs the effect of the fluctuations seems to have a minor role in the performance at high rates.

9. The available data allows for an estimate of a lower bound on A, but better data is required including improved statistics, absolute efficiency measurements and current monitoring; regarding the model used, an improved study of the multi-gap is still lacking.

Chapter 10

Conclusions and outlook

As each of the chapters of this thesis has its own set of *conclusions*, only the more relevant features will be mentioned here.

The main contribution of the present work is to develop a robust concept of a timing RPC wall for the HADES experiment at GSI, based on the electric isolation of the cells. The design predicts detection efficiencies for leptons close to 90% with highly unbiased first level trigger performances, even in the worst scenario expected in HADES under current SIS18. By construction, multi-hit capabilities were expected and later confirmed on a realistic prototype, due to the very low levels of cross-talk.

For providing sufficient rate capability, the practical possibility of a moderate warming of the detector has been explored, allowing for an increase of one order of magnitude in the rate capability each 25 °C, by using still standard float glass.

The ultimate possibilities of improvements on RPC rate capability were explored by following an analytic model that includes explicitly the effect of the fluctuations of the field in the gap over the time resolution. The formalism allows to isolate the main variables ruling the fluctuations.

The process of charging-up of the resistive plates has been described in an easy way and compared with data, providing a simple explanation for the overestimation observed on rate capabilities for short spills. This charging-up process takes place, in a natural way, at the scale of the relaxation time of the glass.

Appendix A

A compilation of useful results

A.1 Derivation of the time at maximum t_o

The time at maximum can be extracted from the intrinsic time response 9.4 by derivation:

$$\rho_{_\tau}(\tau) = \frac{n'_o}{e^{n'_o}-1}\frac{e^{(\tau_{th}-\tau)-\exp(\tau_{th}-\tau)}}{\sqrt{n'_o e^{(\tau_{th}-\tau)}}} I_1\left(2\sqrt{n'_o e^{(\tau_{th}-\tau)}}\right) \tag{A.1}$$

Let's consider the non-dimensional units $\tau = St$ and therefore the time at maximum can be denoted by τ_o. For simplicity, let's define $x = 2\sqrt{n'_o e^{(\tau_{th}-\tau)}}$, then:

$$\frac{d\rho_{_\tau}}{d\tau} = \rho_{_\tau}[e^{(\tau_{th}-\tau)}-1] + \rho_{_\tau}\frac{I_2(x)}{I_1(x)}\frac{dx}{d\tau} = 0 \tag{A.2}$$

Using that $\frac{dx}{d\tau} = -\frac{1}{2}x$, and $\rho_{_\tau}$ never vanishes, it can be obtained:

$$[e^{(\tau_{th}-\tau)}-1]I_1(x) + -\frac{1}{2x}I_2(x) = 0 \tag{A.3}$$

Relation 31.46 in [171] allows to rewrite eq. A.3 as:

$$\frac{I_1(x)}{x}e^{(\tau_{th}-\tau)} - \frac{1}{2}I_o(x) = 0 \tag{A.4}$$

that can be exactly solved in two limits:

In the limit $x \to 0$ ($n'_o \to 0$), substituting I_1 and I_0 by the first term of their Taylor expansions:

$$\frac{1}{2}e^{(\tau_{th}-\tau)} - \frac{1}{2} = 0 \tag{A.5}$$

and then $\tau_o = \tau_{th} = \ln m_t$.

In the limit $x \to \infty$ ($n'_o \to \infty$) then $I_1 \sim I_o$:

$$\frac{I_o(x)}{x}e^{(\tau_{th}-\tau)} - \frac{1}{2}I_o(x) = 0 \tag{A.6}$$

$$\frac{1}{x}e^{(\tau_{th}-\tau)} = \frac{1}{2} \tag{A.7}$$

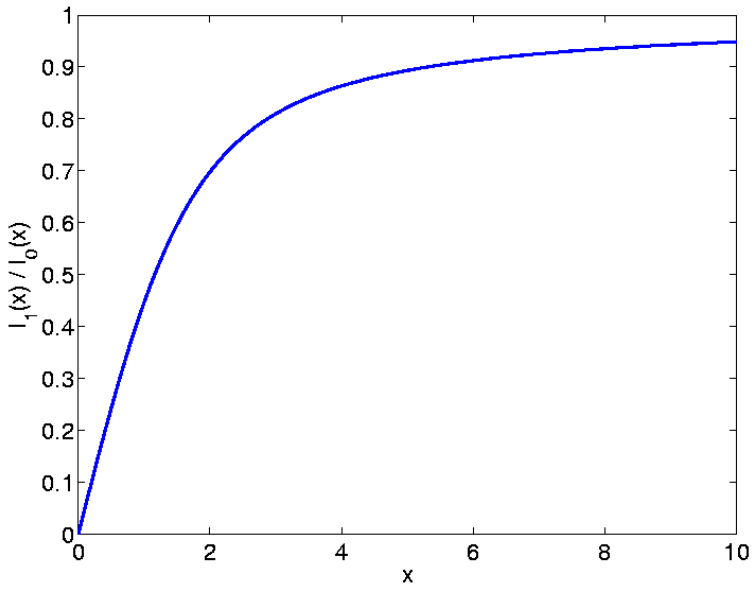

Figure A.1: Behavior of the ratio $\frac{I_1(x)}{I_0(x)}$ as a function of x.

whose solution is $\tau_o = \ln m_t - \ln n'_o$, that is used in text. The accuracy of the expression depends on the condition $I_1 \sim I_o$. For evaluating the effect, it is plotted the ratio I_1/I_o as a function of the independent variable x in fig. A.1.

It is shown that the accuracy of the approximation is above an 80% if $x \sim 2n'_o > 3$. This corresponds to $n'_o > 1.5$, i.e., $\varepsilon \gtrsim 80\%$.

A.2 Influence of the dead region

According to [67], if the dead region is very large, the assumption that the effective number of clusters follows a Poisson distribution is not true anymore, and an extra correction must be added to the time response. Following [67], the correction for a dead region smaller than 70% is still around 10% on the time resolution $K(n'_o)$. Taking the value of $\lambda^{-1} = 9$ clusters/mm from [66] and the minimum efficiency observed in the present data $\varepsilon = 75\%$, the dead region x_t can be estimated to be, in the worst case:

$$\frac{x_t}{g} = \frac{n'_o}{n_o} = \frac{-\ln(1-0.75)}{0.3\lambda^{-1}} \simeq 85\% \tag{A.8}$$

There is no available analytic expression of the time response for including the effects of the dead region, but the observables $K(n'_o)$ (intrinsic time resolution) and $\bar{\tau}(n'_o)$ (intrinsic average time) can be evaluated with the series given in [67]. Here these magnitudes are used to estimate the effect over the observables of interest $\tau_o(n'_o)$ (intrinsic time at maximum) and $K_\sigma(n'_o)$ (intrinsic Gaussian width).

Fig. A.2 shows the comparison. In the case of the average time, no significant effect is seen beyond 10%, while the parameterization of the time at maximum

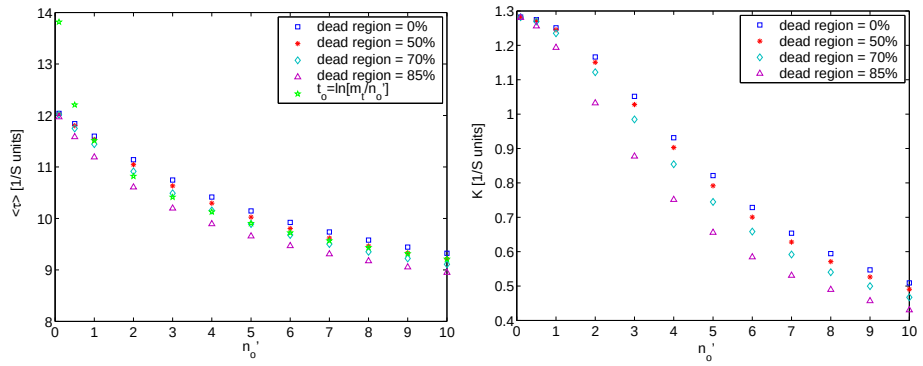

Figure A.2: Intrinsic average time (left) and time resolution (right) as a function of the effective number of clusters. Also shown the approximation followed in text for the time at maximum, namely $t_o \simeq \ln(m_t/n'_o)$.

followed in this work $t_o \simeq \ln(m_t/n'_o)$, is also perfectly consistent within the same error. The discrepancy for $n'_o \to \infty$ is expected as $\ln(m_t/n'_o)$ diverges, but this extreme situation was never reached under the present experimental conditions.

In the case of the time resolution $K(n'_o)$, the effect of a dead region around an 85% is more significative. However, if only the field in the gap is modified, a larger dead region also implies a smaller number of effective clusters, in particular in our case $\varepsilon \sim 75\%$ implies that $x_t/g \sim 85\%$ but also $n'_o \sim 1.4$, and for this value of n'_o the effect is kept at a low level.

A.3 Formal derivation of the effect of fluctuations

Eq. 9.15 is derived here in a completely general way[1]. Let's start by assuming that the avalanche time is given by:

$$t = \frac{\tau}{S} \tag{A.9}$$

The independent random variables are τ, affected by the avalanche fluctuations, and E affected by static (mechanics) or dynamic (rate) sources of jitter. Even if E is changing dynamically it varies at a time scale much larger than the time scales of the avalanche formation, so that these variations can be considered as decoupled. Therefore, the probability distributions for this 2 random variables can be factored out. Calling F to the 2-D pdf of the random variables E and τ:

$$F(\tau, E) = \rho_\tau(\tau) \times \rho_E(E) \tag{A.10}$$

The rms_T is given by:

$$\mathrm{rms}_T^2 = \int\int \rho_E \rho_\tau \left[\frac{\tau}{S}\right]^2 d\tau dE - \left[\int\int \rho_E \rho_\tau \frac{\tau}{S} d\tau dE\right]^2 \tag{A.11}$$

$$\mathrm{rms}_T^2 = \int \rho_E \overline{\left[\frac{\tau}{S}\right]^2} dE - \left[\int \rho_E \frac{\bar{\tau}}{S} dE\right]^2 \tag{A.12}$$

[1] That equation aims at including the fluctuations of the field over the time response.

$\bar{\tau}$ and S are expanded in Taylor series around the average value of the field E_o. Calling Δ_E to $E - E_o$ it is obtained, up to second order in the expansion:

$$\frac{1}{S} = \frac{1}{S_o} - \frac{1}{S_o^2}\frac{dS}{dE}\bigg|_{E_o}\Delta_E + \left(\frac{1}{S_o^3}\frac{dS}{dE}\bigg|_{E_o}^2 - \frac{1}{2S_o^2}\frac{d^2S}{dE^2}\bigg|_{E_o}\right)\Delta_E^2 \quad \text{(A.13)}$$

$$\frac{1}{S^2} = \frac{1}{S_o^2} - \frac{2}{S_o^3}\frac{dS}{dE}\bigg|_{E_o}\Delta_E + \left(\frac{3}{S_o^4}\frac{dS}{dE}\bigg|_{E_o}^2 - \frac{1}{S_o^3}\frac{d^2S}{dE^2}\bigg|_{E_o}\right)\Delta_E^2 \quad \text{(A.14)}$$

$$\bar{\tau} = \bar{\tau}_o + \frac{d\bar{\tau}}{dE}\bigg|_{E_o}\Delta_E + \frac{d^2\bar{\tau}}{dE^2}\bigg|_{E_o}\Delta_E^2 \quad \text{(A.15)}$$

$$\overline{\tau^2} = \overline{\tau_o^2} + 2\bar{\tau}_o\frac{d\bar{\tau}}{dE}\bigg|_{E_o}\Delta_E + \left(\frac{d\bar{\tau}}{dE}\bigg|_{E_o}^2 + \bar{\tau}_o\frac{d^2\bar{\tau}}{dE^2}\bigg|_{E_o}\right)\Delta_E^2 \quad \text{(A.16)}$$

The last expression is obtained under the assumption that $\frac{dK}{dE} \simeq 0$[2] being $K = \text{rms}_\tau$. The expansions allow to calculate $\frac{\bar{\tau}}{S}$ and $\frac{\overline{\tau^2}}{S^2}$ that can be substituted into eq. A.12 and the integral performed. The linear terms in Δ_E goes to zero after the integration. Doing some algebra, the following expression can be obtained:

$$\begin{aligned}\text{rms}_T^2 = \quad & \left[\frac{K^2}{S^2} + \left(\frac{\bar{\tau}}{S^2}\frac{dS}{dE} - \frac{1}{S}\frac{d\bar{\tau}}{dE}\right)^2 \text{rms}_E^2\right]_{E=E_o} + \\ & \left[\frac{3\ \text{rms}_E^2 K^2}{S^4}\left(\frac{dS}{dE}\right)^2\right]_{E=E_o} - \\ & \left[\frac{\text{rms}_E^2 K^2}{S^3}\frac{d^2S}{dE^2}\right]_{E=E_o}\end{aligned} \quad \text{(A.17)}$$

The following facts can be appreciated:

1. The first row is the result expected from the standard error propagation, that essentially keeps the first order in the derivatives and fluctuations (rms), and is the result already discussed in chapter 9.

2. The second row is still first order in derivatives but second in the fluctuations, so it goes to zero as long as they are not very large.

3. The third row includes the second order derivatives, a term that is very small in general, due to the linear behavior of $S(E)$ for the fields of interest.

[2] In an exact way, it is necessary to assume that all the derivatives of K respect to the applied field E are small. The assumption that the intrinsic width K is very slightly dependent on the field E is reasonable, as this dependence is related to the dependence of n'_o or, equivalently, to the efficiency. Therefore, as long as the efficiency is not changing enormously the approximation mentioned is valid.

A.4 Derivation of the instantaneous ohmic drop $V(t)$

Let's take the expression of the Fourier transform of $V(\omega)$ as the starting point. This expression has been derived in section 9.4.2:

$$V(t) = \sum_k \frac{q_k}{2\pi}\frac{R}{\tau_g}\int_{-\infty}^{\infty}\frac{1/\tau_g}{1/\tau_g^2+\omega^2}e^{j\omega(t-t_k)}(1-j\omega\tau_g)d\omega \tag{A.18}$$

It remains to solve the proposed integral. For that it is necessary to use the Fourier Transform of an exponential function:

$$e^{-a|x|} = \frac{1}{2\pi}\int_{-\infty}^{+\infty}\frac{2a}{p^2+a^2}e^{ipx}dp \tag{A.19}$$

Therefore, the first part of the integral is immediate:

$$V(t) = \sum_k \frac{q_k R}{\tau_g}\left[\frac{1}{2}e^{-\frac{|t-t_k|}{\tau_g}} - \frac{1}{2\pi}\int_{-\infty}^{\infty}\frac{1/\tau_g}{1/\tau_g^2+\omega^2}e^{j\omega(t-t_k)}j\omega\tau_g d\omega\right] \tag{A.20}$$

that can be rewritten as:

$$V(t) = \sum_k \frac{q_k R}{\tau_g}\left[\frac{1}{2}e^{-\frac{|t-t_k|}{\tau_g}} - \frac{\tau_g}{2\pi}\frac{d}{dt}\int_{-\infty}^{\infty}\frac{1/\tau_g}{1/\tau_g^2+\omega^2}e^{j\omega(t-t_k)}d\omega\right] \tag{A.21}$$

The Fourier transform is again immediate:

$$V(t) = \sum_k \frac{q_k R}{\tau_g}\left[\frac{1}{2}e^{-\frac{|t-t_k|}{\tau_g}} - \frac{\tau_g}{2}\frac{d}{dt}e^{-\frac{|t-t_k|}{\tau_g}}\right] \tag{A.22}$$

$$V(t) = \sum_k \frac{q_k R}{\tau_g}\left[\frac{1}{2}e^{-\frac{|t-t_k|}{\tau_g}} + \frac{1}{2}e^{-\frac{|t-t_k|}{\tau_g}}\right] \tag{A.23}$$

$$V(t) = \sum_k \frac{q_k}{C}e^{-\frac{|t-t_k|}{\tau_g}} \tag{A.24}$$

that is the result used in section 9.4.2.

A.5 Derivation of the autocorrelation function for white noise

Let's assume a shot-noise current of the form:

$$I(t) = \sum_k q_k\ \delta(t-t_k) \tag{A.25}$$

and the magnitude of the shots q_k is not constant in general. The autocorrelation function is given by:

$$a_{_I}(t) = \lim_{T\to\infty}\frac{1}{T}\int_{T/2}^{T/2}\sum_K\sum_{K'} q_{_K}q_{_{K'}}\delta(t'-t_{_K})\delta(t'-t_{_{K'}}+t)dt' \quad (A.26)$$

$$= \lim_{T\to\infty}\frac{1}{T}\sum_K\sum_{K'} q_{_K}q_{_{K'}}\delta(t_{_K}-t_{_{K'}}+t) \quad (A.27)$$

$$= \lim_{T\to\infty}\frac{1}{T}\left[\sum_K q_{_K}^2\delta(t)+\sum_K\sum_{K'\neq K} q_{_K}q_{_{K'}}\delta(t_{_K}-t_{_{K'}}+t)\right] \quad (A.28)$$

The second term, when the Fourier transform is calculated, leads to a sum of random phases with zero result in the limit of many pulses (i.e. $T\to\infty$). Therefore, the only relevant term is the first one, leading to:

$$a_{_I}(t) = A\phi\overline{q^2}\delta(t) \quad (A.29)$$

being $r = A\phi$ the frequency of events, A the influenced area per avalanche and ϕ the primary rate.

A.6 Derivation of the stabilization time t_{eq}

A simple description of the RPC charging-up process is devised here. Let's assume a train of k shots arriving at different times. Each shot takes an average value from the instantaneous value of the field $V_o - V(t)$ (applied field minus drop of the field):

$$V_{shot}(t) = \frac{a}{C}(V_o - V(t) - V_{th}) \quad (A.30)$$

The number of shots k necessary to reach a certain value of the average drop $\bar{V}_{drop}$ can be calculated. For this, it is taken into account that, the larger the value of V, the smaller the next shot:

$$V_{shot,o} = \frac{a}{C}(V_o - V_{th}) \quad (A.31)$$

$$V_{shot,1} = \frac{a}{C}(V_o - V_{shot,o} - V_{th}) = V_{shot,o}\left[1-\frac{a}{C}\right] \quad (A.32)$$

$$V_{shot,n} = V_{shot,o}\left[1-\frac{a}{C}\right]^n \quad (A.33)$$

where the exponential decay of the equivalent RC circuit has been neglected for the sake of simplicity. The condition required is:

$$\bar{V}_{drop} = \sum_{i=0}^{k} V_{shot,o}\left[1-\frac{a}{C}\right]^i = V_{shot,o}\frac{1-(1-\frac{a}{C})^k}{a/C} \quad (A.34)$$

that can be rewritten as:

$$k = \frac{\ln(1-\frac{\bar{V}_{drop}}{V_{shot,o}}\frac{a}{C})}{\ln(1-\frac{a}{C})} \quad (A.35)$$

The number of shots k necessary to reach $\bar{V}_{drop}$ is nothing else than:

$$k = \phi A t_{eq} \tag{A.36}$$

therefore:

$$t_{eq} = \frac{1}{\phi A} \frac{\ln(1 - \frac{\bar{V}_{drop}}{V_{shot,o}} \frac{a}{C})}{\ln(1 - \frac{a}{C})} \tag{A.37}$$

For the values used here it is reasonable to assume that $\frac{a}{C}$ is small so that:

$$t_{eq} = \frac{C}{aA\phi} \ln[(1 - \frac{\bar{V}_{drop}}{V_{shot,o}} \frac{a}{C})^{-1}] \tag{A.38}$$

At last, the expression for $\bar{V}_{drop}$ from eq. 9.7 is used:

$$\bar{V}_{drop} = V_o - V_{th} + \frac{(V_o - V_{th})}{1 + \frac{aA\phi}{C}\tau_g} \tag{A.39}$$

arriving to:

$$t_{eq} = \frac{C}{aA\phi} \ln(1 + \frac{aA\phi}{C}\tau_g) \tag{A.40}$$

$$t_{eq} = \frac{\tau_g}{ad\rho\phi} \ln(1 + ad\rho\phi) \tag{A.41}$$

being $\tau_g = RC$.

The condition for applicability of eq. A.40 is that the average drop induced per shot is below the average drop. This condition is equivalent to ask for $k > 1$ (more than one shot). It can be written as:

$$V_{shot,o} < \bar{V}_{drop} \tag{A.42}$$

$$\frac{a}{C}(V_o - V_{th}) < (V_o - V_{th}) \left[1 - \frac{1}{1 + aA\phi R}\right] \tag{A.43}$$

$$\frac{a}{C} < \frac{aA\phi R}{1 + aA\phi R} \tag{A.44}$$

and finally:

$$\frac{1}{A\phi} < \tau_g(1 - \frac{a}{C}) \tag{A.45}$$

as said, a/C is significantly lower than one for the values considered here. Therefore, it is enough to consider, in a first approach, that:

$$\frac{1}{A\phi} < \tau_g \tag{A.46}$$

Appendix B

The weighting field

Here, a direct way for evaluating the weighting field in some usual RPC configurations is proposed. For illustration, let's take a stack of materials with permittivities $\epsilon_1, \epsilon_2, \epsilon_3$, as shown in fig. B.1. The starting point is the relation:

$$i(t) = \vec{E}_w \cdot \vec{v}_e(t) n_e e \tag{B.1}$$

For calculating the value of E_w in the simple geometry given in fig. B.1 it is required to put 1 volt across the electrodes A and B and to evaluate the field. But formula B.1 can be also written as:

$$i(t) = \frac{E_w}{\Delta V_w} v_e(t) n_e e \tag{B.2}$$

being ΔV_w a generic voltage drop applied between A and B electrodes (see also [66]). Under these conditions the field on material i is given by:

$$E_i = \frac{\Delta V_i}{d_i} \tag{B.3}$$

and the weighting field:

$$\frac{E_i}{\Delta V_w} = \frac{1}{d_i}\frac{\Delta V_i}{\Delta V_w} = \frac{1}{d_i}\frac{Q_w}{C_i}\frac{C}{Q_w} = \frac{1}{d_i}\frac{C}{C_i} \tag{B.4}$$

The charge Q_w is the same because the 3 materials behave as capacitors in series. In that way, the weighting field can be related to the ratio between the total capacity C and the capacity of the material C_i.

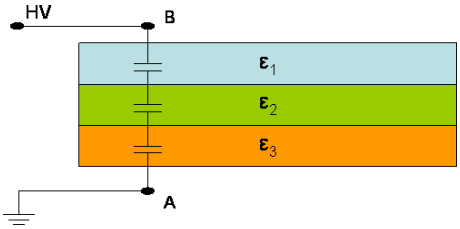

Figure B.1: Example of an RPC-like configuration with 3 layers of different permittivities.

Using eq. B.4 and integrating eq. B.2 in time, the relation between the charge released and the charge induced during the drift through material i can be extracted:

$$q_{induced} = \frac{C}{C_i} q \tag{B.5}$$

as is used in text. For the particular case of material 2, the evaluation of the weighting field gives:

$$C_i = \frac{\epsilon_i A}{d_i} \tag{B.6}$$

$$E_{w2} = \frac{1}{d_2} \frac{C}{C_2} \tag{B.7}$$

$$E_{w2} = \frac{\epsilon_1 \epsilon_3}{\epsilon_1 \epsilon_2 d_3 + \epsilon_1 \epsilon_3 d_2 + \epsilon_2 \epsilon_3 d_1} \tag{B.8}$$

Exactly as derived in [64]. Eq. B.7 can be extended to an arbitrary number of layers with permittivities $\epsilon_1 \ldots \epsilon_n$.

Appendix C

Resumo

C.1 Introducción

O desenvolvimento das cámaras de placas paralelas resistivas (RPCs) no ano 1981 [33] abriu a posibilidade de operar detectores gaseosos de xeometrías paralelas a campos eléctricos tan altos como 100 kV/cm [45]. A principal vantaxe con respecto á tecnoloxía de placas paralelas convencionais (PPC) é que calqueira proceso que precise do fornecemento dunha grande cantidade de carga, como por exemplo descargas continuadas ou faíscas, non poderá ter lugar dentro dunha RPC, na que a taxa de fornecemento de carga (ou corrente), está limitada pola resistividade das placas. Ó mesmo tempo, a elevada resistividade dos materiais frecuentemente utilizados ($\rho \sim 10^9 - 10^{12}$ Ωcm) non afecta á inducción de sinal nin á física das avalanchas producidas, fenómenos respecto ós cales a RPC é equivalente a unha PPC. Unha característica habitualmente atribuída ás RPCs é a presencia de 'UV-quenchers' ou atenuadores de fotóns ultravioleta, os cales poderían levar á delocalización transversal da avalancha de modo similar a como acontece nun detector Geiger. Mentres que a delocalización transversal é un efecto aceptado, a relación dos fotóns UV de pequeno percurso cos chamados 'streamers'[1] catódicos [28] precisa, nembargantes, de ser verificada experimentalmente. En xeral, o uso de mesturas baseadas en moléculas complexas, como é de praxe común en RPCs, poderá ser particularmente favorable en vistas á reducción destes efectos.

Pouco a pouco estase establecendo que, o feito da multiplicación ter lugar inmediatamente despois da primeira ionización, representa unha diferencia esencial da xeometría paralela en comparación coa xeometría cilíndrica empregada a cotío en detectores proporcionais. É por isto que se acostuma decir que as fluctuacións na resposta temporal do detector veñen determinadas únicamente polas fluctuacións no proceso de formación e multiplicación de carga (avalancha) [55].

A observación, no ano 2000, da extrema importancia da boa definición da distancia de separación entre electrodos, permitiu mellorar as resolucións temporais ata o nivel dos 50 ps, resultando as RPCs competitivas cos centelladores mais rápidos do momento e tendo ademais a grande vantaxe de proporcionar un

[1] Grandes avalanchas que transportan cargas 10-100 veces maiores que unha avalancha normal e que unen os electrodos a través dun filamento luminoso.

precio por canle moito menor, sendo asimesmo máis robustas frente a campos magnéticos elevados.

Hai numerosos traballos que mostran que a operación de RPCs, en calquera das súas configuracións máis usuais, ten lugar baixo un grande efecto Espacio-Carga [56] debido a interacción entre as pares ión-electrón liberados e o propio campo da avalancha. Existe un argumento clásico debido a Raether que predí unha forte relación entre o Espacio-Carga e a aparición de 'streamers' [29]. No caso das RPCs tal vínculo parece ser máis feble, sendo posible atinxir valores elevados do campo para os que o efecto de Espacio-Carga e importante mais non hai a penas 'streamers'. Este efecto é particularmente beneficioso, pois a presencia destes últimos resulta nun empeoramento da capacidade de taxa da RPC, limitando por tanto a máxima tensión atinxible en moitas aplicacións. Unha explicación adecuada da orixe dos streamers non existe aínda.

Como acontecera no caso das RPCs standard con resolucións temporais ao nivel de 1 ns, desenvolvidas nos anos 80, a introducción das RPCs de tempo de voo ou 'timing RPCs' no ano 2000, acadando resolucións abaixo dos 100 ps, ten aberto a posibilidade de aplicación en diversos experimentos de física de partículas a enerxías altas e intermedias [89].

O traballo recollido nesta tese representa unha pequena parte dun grande proxecto que pretende cubrir a rexión interna (baixos ángulos) do espectrómetro HADES[2] no centro GSI en Darmstadt, Alemaña. O tal muro RPC representa unha mellora do espectrómetro actual, que permitirá estudar colisións de ións pesados ata Au+Au a enerxías cinéticas por volta de 1 GeV/A, aumentando o noso coñecemento das propiedades da materia hadrónica a densidades máis de dúas veces superiores ás presentes na materia nuclear ordinaria.

O proxecto dun muro de RPCs para HADES tense baseado en recentes desenvolvimentos de conceptos e aplicacións similares, pero incorporando aqueles detalles que fan de HADES un entorno singular. Os requerimentos máis esixentes inclúen unha alta capacidade multi-traza para taxas cercanas a 1 kHz/cm^2, xunto cunha resolución temporal homoxénea á volta de 100 ps cunha presencia moderada de caudas. HADES foi concebido para sondar materia nuclear densa a través de pares de di-leptóns procedentes do decaemento de mesóns vectoriais lixeiros. A pequena probabilidade de dito proceso (10^{-5}-10^{-4}) require dunha elevada eficiencia de detección e aceptancia xeométrica, para propocionar unha estatística razoabel.

En vistas ao recente interese por acadar taxas cada vez máis elevadas, unha parte da tese esta adicada ao desenvolvimento dunha tecnoloxía que permite extender a taxa de contaxe nunha orde de magnitude, sempre empregando vidro normal de ventana. Nesa dirección, proponse neste traballo unha descrición teórica dos efectos de taxa neste tipo de detectores, que vai alén dunha simple descrición DC, e permite introducir explícitamente na resposta temporal o efecto das fluctuacións do campo eléctrico orixinadas polo carga depositada no vidro.

O chamado proxecto ESTRELA ('Electrically Shielded Timing RPCs Ensemble for Low Angles', traducido: sistema de RPCs te tempo de voo isoladas eléctricamente para baixos ángulos) evolúe con rapidez, e unha parte deste traballo ten sido inevitabelmente superada, mesmo se o espíritu inicial continúa vixente.

[2]High Acceptance Di-Electron Spectrometer: espectrómetro de alta aceptancia para di-electróns.

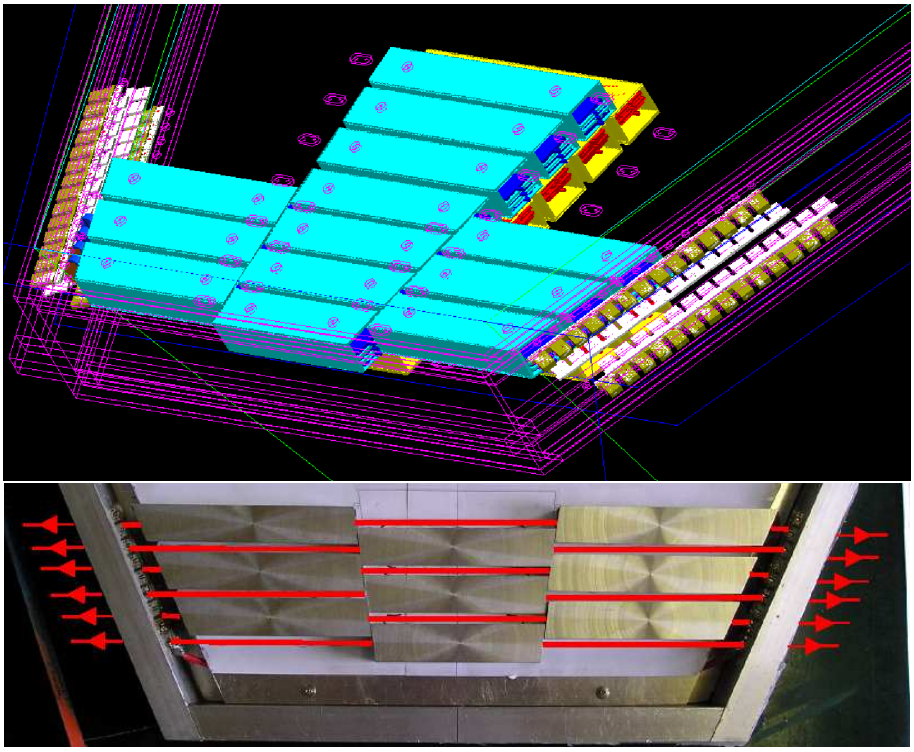

Figure C.1: Detalle do muro ESTRELA a baixos ángulos polares, deseño 3D (arriba) e disposición das celdas na caixa de gas (abaixo). As liñas vermellas representan o camiño dos cabos que recollen a sinal.

A presente tese tamén pretende proporcionar unha visión xeral do cambiante campo das RPCs desde o punto de vista do autor, o cal poderá ser utilizado como referencia, pero non considerado máis alá dunha simple descrición da situación actual, a espera de novos avances e desenrolos que están xa a vir.

C.2 Deseño

O muro de RPCs ESTRELA foi optimizado para proporcionar unha probabilidade total de detección da orde do 90% para leptóns procedentes do blanco, tendo ao mesmo tempo unha grande aceptancia xeométrica. A principal característica do muro é o isolamento eléctrico das celdas, o cal pretende proporcionar boas prestacións no caso de existir trazas simultáneas en celdas próximas (entorno multi-traza). A proposta natural para proporcionar a blindaxe necesaria consiste en colocar as celdas no interior de perfís rectangulares, segundo se mostra na figura C.1. Debido ao espazo morto creado polos perfís, foi proposta unha xeometría en dous pisos (na figura C.1 móstrase un detalle do muro na zona de baixo ángulo) e o solape é fixado de maneira que todas as trazas de interese procedentes do blanco atravesan polo menos 4 ocos de gas, garantindo eficiencias intrínsecas preto do 99% [68].

Resulta útil definir a eficiencia do detector para leptóns, $\mathcal{D}$, en base a tres

magnitudes independentes:

1. A *eficiencia intrínseca* ε. É unha propiedade do propio detector, sendo preto do 99% para RPCs de 4 ocos [88], a taxas baixas.

2. A *aceptancia xeométrica* $\mathcal{A}$. Unha vez o solape é escollido adecuadamente, as zonas ineficientes permanecen por debaixo dun 2% para incidencia perpendicular.

3. A *probabilidade de detección ideal para leptóns* $\mathcal{L}$. Fica fixada polo deseño. Refírese á probabilidade de que o sinal inducido polo leptón sexa recollido pola electrónica, tendo en conta a probabilidade de ocupación da celda por outras trazas dentro do mesmo evento. Para esta estimativa considerouse a situación máis desfavorable esperada en HADES, isto é, colisións de Au+Au a 1.5 GeV/A. O resultado estimado é $D > 95\%$ para momentos do electrón maiores que 100 MeV.

A probabilidade de detecctión esperada para pares e^+/e^- ven dada polo producto destes 3 factores independentes, resultando para o deseño proposto:

$$\mathcal{D} = \mathcal{L} \times \mathcal{A} \times \varepsilon > 88.5\% \tag{C.1}$$

C.3 Verificación do concepto

Na primavera do ano 2003 foi probado na caverna de HADES baixo un feixe de Carbono a 1 GeV/A un novo concepto de muro tRPC baseado en celdas eléctricamente isoladas [96], [97]. A finalidade do teste foi avaliar o concepto desde o punto de vista mecánico xunto coa posibilidade de operar tRPCs nun entorno multi-traza con partículas de diferentes velocidades e especies e, por tanto, diferentes probabilidades de perda de enerxía dentro do detector. As dimensións das tres celdas estudadas foron de 2×60 cm^2, inspiradas no deseño definitivo, e móstranse na figura C.2.

Ademáis de verificar a posibilidade de operación do detector con normalidade para tensións da orde de 3 kV/gap, a demostración definitiva das capacidades 'multi-traza' consistiu en estimar a resposta temporal para aqueles casos nos que existía unha traza simultáneamente en algunha das celdas veciñas. O resultado deste estudio móstrase na figura C.3. O que é mellor, foi verificado que o 'cross-talk'[3] entre celdas veciñas estaba abaixo dun 1%, aumentando coa carga do sinal.

Non puido ser feita unha medida absoluta da eficiencia do detector, debido á presencia de trazas inclinados entre os seleccionados para o estudo, pero puido determinarse que era superior ao 95% cara o centro do detector.

[3] Inducción de orixe electromagnético que ten lugar entre conductores que están próximos cando se aplica un campo eléctrico sobre un de eles.

Figure C.2: Vista dianteira do prototipo coas tres celdas no seu interior. A celda máis cara á esquerda foi substituída por outra de electrodos de vidro. Na fotografía de embaixo móstrase unha das celdas RPC antes de ser introducida na blindaxe.

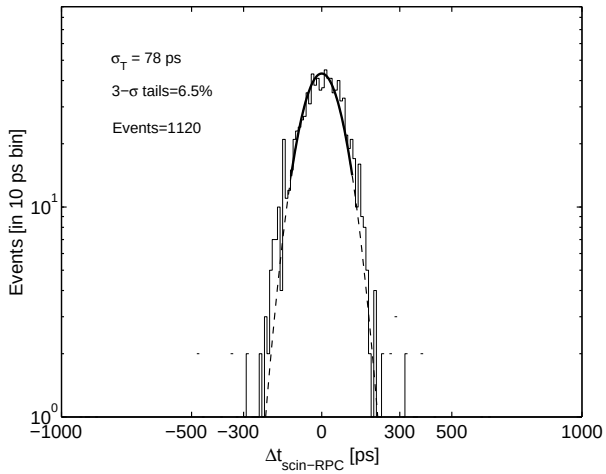

Figure C.3: Distribución temporal baixo condicións multi-traza (a celda veciña tamén rexistrou unha traza dentro dese mesmo evento). A distribución observada é esencialmente a mesma que no caso de única-traza, suxerindo que o deseño proporciona capacidades multi-traza moi robustas.

C.4 RPCs mornas

Para aumentar a capacidade de taxa de RPCs feitas con vidro de ventana normal, proponse o aquecemento do detector. O uso de RPCs de tempo de voo mornas [59] (*Warm Timing RPCs*) orixina variacións típicas da resistivididade nunha orde de magnitude por cada 25° o que, dentro do modelo DC que se acostuma usar para a descrición de efectos dinámicos en RPCs [59], permite esperar melloras dunha orde de magnitude tamén nas taxas atinxibles polo detector. Este resultado ten sido confirmado recentemente [1].

Sempre dentro do modelo DC, foi posible describir as medidas feitas baixo iluminación con fontes γ intensas, a diferentes temperaturas. O modelo permite obter de maneira simple que a eficiencia ε e a carga rápida media $\bar{q}_{prompt}$ dependen da cantidade Φ/κ sendo $\kappa = \frac{\rho(T_o)d_o}{\rho(T)d}$ (ρ a resistividade do vidro, d o espesor do vidro) a capacidade de taxa referida a $T = T_o$. Desta maneira é posible relacionar a capacidade de taxa coa resistividade medida directamente en laboratorio sobre o vidro.

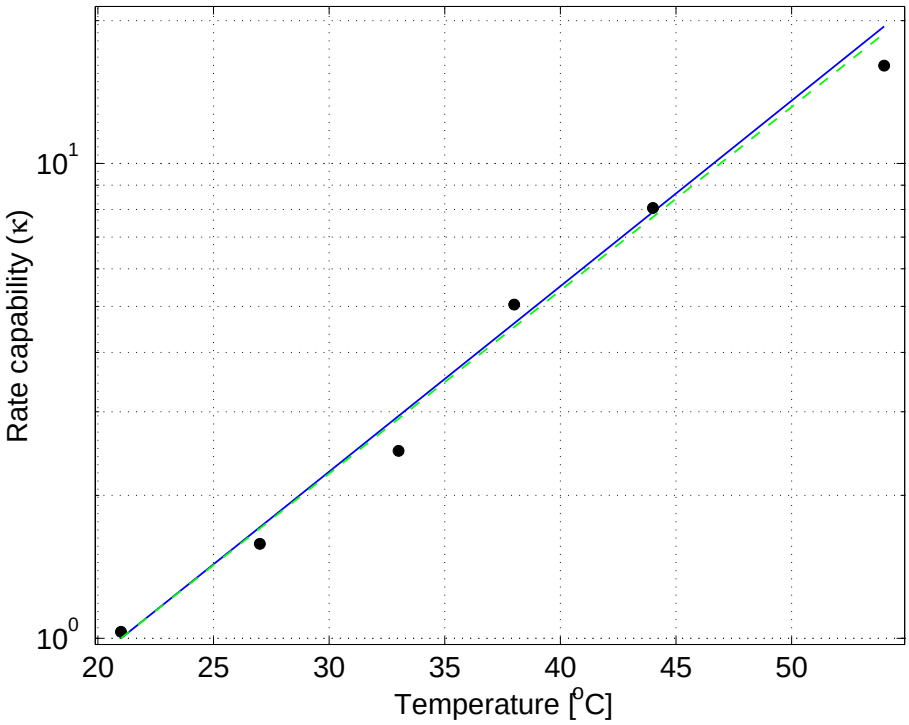

Figure C.4: Comparativa entre o comportamento da taxa de contaxe estimada a través de medidas da resistividade (en trazo discontinuo), xunto co resultado do modelo (puntos). A linha continua mostra o melhor axuste aos puntos, indicando un bo acordo.

Os resultados da descrición do modelo móstranse na figura C.5 e o valor da capacidade de taxa así obtida permite inferir un valor para a resistividade do vidro moi semellante ao medido no laboratorio (figura C.4).

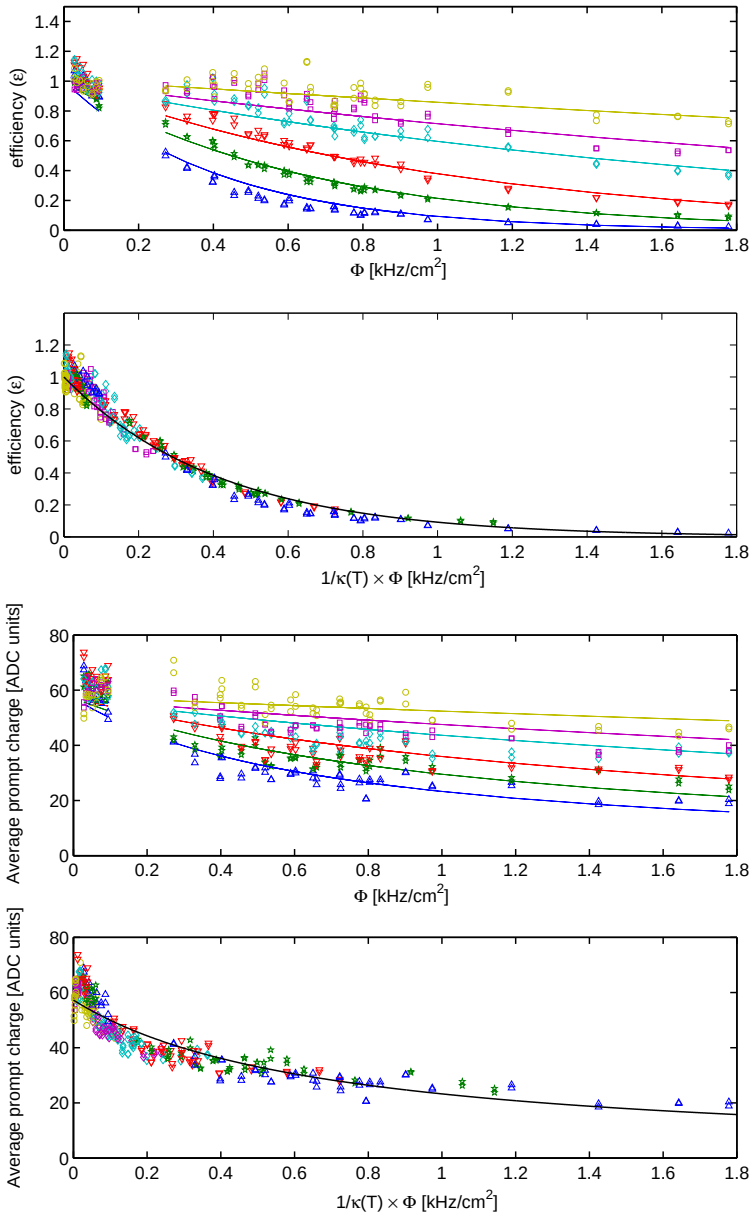

Figure C.5: Figuras representando o axuste ao modelo DC. Móstrase o comportamento da eficiencia e carga rápida a VT/T_o=3.2 kV/gap como función da taxa na RPC para diferentes temperaturas (21, 27, 33, 38, 44, 54 °C de abaixo a arriba). Tamén se mostra o comportamento das mesmas cantidades cando todas as curvas se funden nunha soa tras re-escalar a taxa primaria por $1/\kappa$.

C.5 Un tratamento analítico das fluctuacións

Neste traballo ten sido proposta unha extensión analítica do modelo DC que permite introducir na resposta temporal da RPC o efecto das fluctuacións do campo eléctrico debido ao proceso de conducción no vidro [61], [62]. É mostrado que a importancia das fluctuacións depende críticamente da cantidade $A\tau_g$, sendo A a rexión afectada por avalancha e τ_g o tempo de relaxación da RPC. O resultado analítico obtido para as fluctuacións do campo aproxima a correlación entre sucesivas avalanchas de forma promediada, o cal causa diferencias da orde dun factor 2 con respecto ao cálculo M.C. que describe o mesmo proceso. Nembargantes, ambas descricións presentan comportamentos similares en función do número promedio de avalanchas na zona afectada do vidro ($\bar{N} = A\tau_g\Phi$), na forma:

$$\frac{\mathrm{rms}_V}{\bar{V}_{drop}} = \sqrt{\frac{\left(1 + \frac{\mathrm{rms}_q^2}{\bar{q}^2}\right)}{2\bar{N}}} \tag{C.2}$$

sendo $\frac{\mathrm{rms}_V}{\bar{V}_{drop}}$ a razón das fluctuacións na tensión no gas respecto ao valor promedio da caída de tensión no gas. A descrición proposta foi comparada cos datos de [96], [97] na figura C.6, dentro do modelo DC, mostrando un bo acordo.

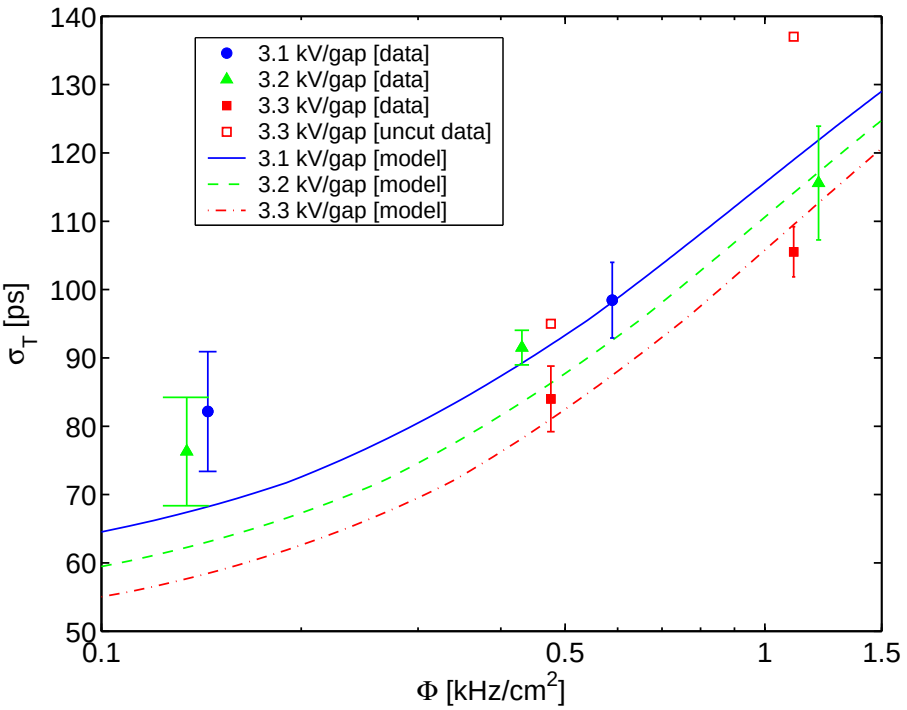

Figure C.6: Resolución temporal obtida a partir do modelo DC para todo o conxunto de datos. Os puntos e o modelo corresponden a 3.1 kV (círculos, liña continua), 3.2 kV (triángulos, liña a trazos), 3.3 kV (cadrados, liña a puntos e trazos). As barras de erro refírense aos intervalos de confianza do 68%. Tamén se mostran (cadros baleiros) os puntos a 3.3 kV antes de cortar a contribución debida ao tempo de carga do vidro.

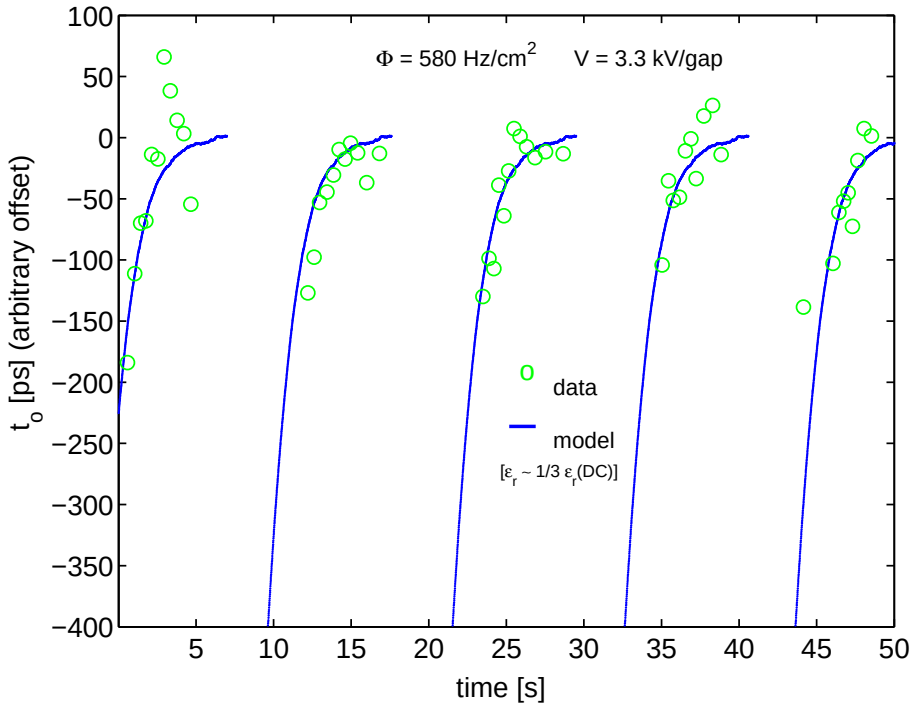

Figure C.7: Efecto do proceso de carga do vidro observado sobre o tempo medio medido (círculos), comparado cos resultados segundo o modelo desenvolvido.

Por tanto, dentro da situación experimental actual, o efecto das fluctuacións do campo parece ser pequeno sobre unha tRPC que opera a altas taxas. Este feito pódese utilizar para constrinxir o valor da área de influencia A, resultando que valores menores que $A \lesssim 0.3$ mm^2 están en desacordo cos datos.

O M.C. desenvolvido tamén permite describir o efecto de amontoamento da carga das avalanchas na superficie do vidro, ata que se acada unha situación estacionaria, describindo ben a evolución da resposta da RPC en función do tempo de iluminación, segundo se mostra na fig. C.7. Desta maneira pódense interpretar de maneira simple as sobre-estimacións da eficiencia de RPCs anteriormente publicadas para feixes moi curtos temporalmente e taxas altas [71].

C.6 Conclusións

As principais aportacións deste traballo enmárcanse dentro do campo das RPCs de tempo de voo, unha tecnoloxía emerxida no CERN hai apenas 6 anos. Máis en concreto, ten sido probada a súa aplicabilidade ao experimento HADES no GSI, Alemaña, mostrando boas prestacións nun entorno multi-traza característico de colisións nucleares a enerxías intermedias por volta de 1 GeV/A. Preséntase tamén un deseño realista para tal entorno, proporcionando probabilidades de detección próximas ao 90% para as partículas de interese (electróns e positróns).

O proxecto para a construcción dun muro de RPCs de tempo de voo para HADES, denominado ESTRELA (Electrically Shielded Timing RPCs Ensemble for Low Angles), está xa nun estado avanzado e espérase que sexa completado nos próximos anos.

Neste traballo móstrase tamén cómo a capacidade de taxa se pode incrementar enormemente (unha orde de magnitude) e de maneira práctica a través dun moderado aquecemento da RPC (unha tecnoloxía que ten sido denominada *RPCs mornas para tempo de voo*).

As posibilidades últimas de mellora da capacidade de contaxe das RPCs foron exploradas a través dun modelo analítico que inclúe de maneira explícita o efecto das fluctuacións da tensión no gas sobre a resolución temporal. O proceso de carga do vidro foi descrito tamén de maneira simple e comparado cos datos, mostrando que acontece, de maneira natural, na escala temporal do tempo de relaxación da RPC, τ_g.

Appendix D

Frases célebres

"Facer unha RPC é como facer unha tortilla." **(O catedrático)**.

"Facer unha tese non é como facer unha tortilla." **(O bolseiro)**.

"Chega un momento na vida no que hai que facerse un modelito." **(O catedrático)**.

"Facer unha boa tese require plantexarse abandonala polo menos nun par de ocasións." **(O bolseiro)**.

"Last night I had a dream..." **(O supervisor)**.

"Non me creo iso." **(O supervisor)**.

"Pois... agranda as barras de erro!" **(O día antes de enviar o artículo)**.

"Nunca lle fagas caso ó teu supervisor." **(O supervisor)**.

"Eu creo que é necesario descansar polo menos 8 horas diarias..." **(O bolseiro)**.

"Ok, prepárao para o luns." **(O venres pola tarde)**.

"Non, hoxe tampouco podo quedar." **(O bolseiro)**.

"Ah, pero ti tamén traballas nisto?" **(Ó compañeiro de grupo)**.

"Por qué non organizamos reunións semanais e contamos o que facemos...?" **(Ese vello soño)**.

"Bos dias!, como madrugamos hoxe eh?." **(A noite antes do *dead line*)**.

"Algún doutor na sala quere formular preguntas?" **(A derradeira pregunta da tese)**.

"Hai que aumentar a sinerxia." **(O catedrático)**.

*"rm -rf *"* (**A crise**).

"Que fermoso!. Que é?." (**O supervisor**).

"Os datos nunca están mal. O que pode fallar é a teoría. (**O bo físico experimental**)

"Este é o modelo. Se fan ben o experimento deben ser capaces de reproducilo." (**O bo físico teórico**)

"Eu traballo na casa." (**O catedrático**).

"Ola!, traballando no fin de semana?." (**De bolseiro a bolseiro, o fin de semana.**).

"Os xaponeses traballan mentras durmen e os españois durmen mentras traballan." (**O choque de civilizacións**).

"Sí, sí." (**O insconciente**).

"Non te preocupes pola tese porque ninguén as lé." (**O pragmático**).

"Segmentation violation, core dumped." (**O compilador**).

"Moi boa idea, por qué non o fas ti?" (**A dúbida**).

"O problema é que o código está mal documentado." (***O problema***).

"A física é así." (**A causa última de calqueira frustración**).

Bibliography

[1] P. Fonte et al., PoS(HEP2005)376.

[2] U. Fano, "Penetration of protons, alpha particles and mesons", Ann. Rev. Nucl. Sci. 13(1963)1.

[3] S. Eidelman et al., Phys. Lett. B 592(2004)1.

[4] "Stopping Powers and Ranges for Protons and alpha Particles", ICRU report 49.

[5] Aguilar-Benitez M. et al., Phys. Lett. B 24(1988).

[6] J. D. Jackson, "Classical electrodynamics", 3^{rd} edition, John Wiley & Sons, New York 1998.

[7] Enrico Fermi, Phys. Rev. 57(1940)485.

[8] P. Budini, L. Taffara, Nuovo Cimento, IV/1(1956)22.

[9] B. Rossi, "High Energy Particles", Prentice-Hall, Inc., Englewood Cliffs, NJ, 1952.

[10] F. Sauli, "Principles of operation of multiwire proportional and drift chambers", CERN 77-09.

[11] E. J. Kobetich and R. Katz, Phys. Rev. 170(1968)391.

[12] Glenn F. Knoll, "Radiation Detection and Measurement", John Wiley and Sons, Inc., 1999.

[13] P. Rice-Evans, "Spark, Streamer, Proportional and Drift Chambers", Richelieu Press, 1974, London.

[14] Townsend J. S., "The theory of ionization of gases by collision", Constable & Co, Londres 1910.

[15] S. Biagi, http://consult.cern.ch/writeup/magboltz/.

[16] S. Biagi, CERN.

[17] http://consult.cern.ch/writeup/heed/main.html.

[18] W. Riegler, C. Lippmann, Nucl. Instr. and Meth. A 518(2004)86-90.

[19] P. Fonte, PhD. Thesis, Lisbon 1992.

[20] V. Palladino, B. Sadoulet, Nucl. Instr. Meth. A 128(1975)323.

[21] G. Shultz, J. Gresser, Nucl. Instr. Meth. A 151(1978)413.

[22] A. J. Davies, C. J. Evans, "The theory of ionization growth in gases under pulsed static fields", CERN 73-10.

[23] J. M. Meek, J. D. Craggs, "Electrical breakdown in gases", Clarendon Press, Oxford, 1953.

[24] C. Lippmann, PhD. Thesis, Frankfurt (2003).

[25] W. H. Furry, Phys. Rev. 15(1937)569.

[26] R. D. Evans, "The Atomic Nucleus", Krieger, New York, 1982.

[27] E. D. Lozanskii, Sov. Phys. Usp. 18(1975)83.

[28] P. Fonte, IEEE Trans. Nucl. Sci. 43(1996)2135.

[29] H. Raether, "Electron avalanches and breakdown in gases", Butterworths, London, 1964.

[30] V. A. Davidenko, B. A. Dolgoshein, V. K. Semenov, S. V. Somov, Nucl. Instr. Meth. 75(1969)325.

[31] J. Keuffel, Phys. Rev. 73(1948)531.

[32] V. V. Parkhomchuck, Yu. N. Pestov, N. V. Petrovykh, Nucl. Instr. and Meth. A 93(1971)269.

[33] R. Santonico and R. Cardarelli, Nucl. Instr. and Meth. A 187(1981)377.

[34] R. Cardarelli, R. Santonico, A. Di Biagio and A. Lucci, Nucl. Instr. and Meth. A 263(1988)20.

[35] Jian Gui Wang, Nucl. Instr. and Meth. A. 508(2003)133.

[36] D. Piccolo et al, Nucl. Instr. and Meth. A 477(2002)435.

[37] C. Bacci et al, Nucl. Instr. and Meth. A 456(2000)121.

[38] I. Crotty, J. Lamas Valverde, G. Laurenti, M. C. S. Williams, A. Zichichi, Nucl. Instr. and Meth. A 337(1994)370.

[39] I. Duerdoth, S. Clowes, J. Freestone, F.K. Loebinger, J. Lomas, S. Snow, R. Thompson, Nucl. Instr. Meth. A 348(1994)303.

[40] R. Cardarelli, A. Di Ciaccio and R. Santonico, Nucl. Instr. and Meth. A 333(1993)399.

[41] M. Alviggi, V. Canale, M. Caprio, G. Carlino, R. de Asmundis, M. Della Pietra, D. della Volpe, P. Iengo, S. Patricelli, G. Sekhniaidze, Nucl. Instr. Meth. A 518(2004)79.

[42] M. Abbrescia, R. Trentadue et al., Nucl. Instr. Meth. A 533(2004)102.

[43] E. Cerron Zeballos, I. Crotty, D. Hatzifotiadou, J. Lamas Valverde, S. Neupane, M.C.S. Williams, A. Zichichi, Nucl. Instr. and Meth. A 374(1996)132.

[44] P. Fonte, IEEE Trans. Nucl. Sci. 49,3(2002)881.

[45] P. Fonte, A. Smirnitski, M.C.S. Williams, Nucl. Instr. and Meth. A 443(2000)201.

[46] P. Fonte, R. Ferreira Marques, J. Pinhão, N. Carolino, A. Policarpo, Nucl. Instr. Meth. A 449(2000)295.

[47] A. Blanco, R. Ferreira-Marques, Ch. Finck, P. Fonte, A. Gobbi, A. Policarpo, M. Rozas, Nucl. Instr. Meth. A 485(2002)328.

[48] P. Camarri, R. Cardarelli, A. Di Ciaccio and R. Santonico, Nucl. Instr. and Meth. A 414(1998)317.

[49] A. V. Akindinov, E. Scapparone et al., Nucl. Instr. Meth. A 533(2004)93.

[50] C. Gustavino, M. D'Incecco, E. Tatanami, G. C. Trinchero, Nucl. Instr. Meth. A 457(2001), 558.

[51] M. Abbrescia et al., Nucl. Instr. Meth. A 431(1999)413.

[52] M. Abbrescia et al., Nucl. Phys. B (Proc. Suppl.) 78(1999)459.

[53] P. Fonte, Nucl. Instr. and Meth. A 456(2000)6.

[54] G. Aielli, P. Camarri, R. Cardarelli, A. Di Ciaccio, B. Liberti, A. Paoloni, R. Santonico, Nucl. Instr. Meth. A 508(2003)6.

[55] A. Blanco, P. Fonte, L. Lopes, A. Mangiarotti, R. Ferreira-Marques, A. Policarpo, Nucl. Instr. and Meth. A 513(2003)8.

[56] A. Mangiarotti, C. C. Bueno, P. Fonte, A. Gobbi, D. González-Díaz, L. Lopes, Nucl. Phys. B (Proc. Suppl.) 158(2006)118.

[57] Christian Lippmann, Werner Riegler, Nucl. Instr. and Meth. A 517(2004)54.

[58] G. Carboni, G. Collazuol, S. De Capua, D. Domenici, G. Ganis, R. Messi, G. Passaleva, E. Santovetti, M. Veltri, Nucl. Instr. and Meth. A 498(2003)135.

[59] D. González-Díaz, D. Belver, A. Blanco, R. Ferreira Marques, P. Fonte, J. A. Garzon, L. Lopes, A. Mangiarotti, J. Marin, Nucl. Instr. and Meth. A 555(2005)72.

[60] M. Abbrescia, Nucl. Instr. and Meth. A 533(2004)7.

[61] A. Blanco, N. Carolino, C.M.B.A. Correia, R. Ferreira-Marques, P. Fonte, A. Gobbi, D. González-Díaz, M.I.Lopes, L.Lopes, M.P. Macedo, A. Mangiarotti, V. Peskov, A. Policarpo, Nucl. Instr. and Meth. A 535(2004)272.

[62] D. Gonzalez-Díaz, P. Fonte, J. A. Garzón, A. Mangiarotti, Nucl. Phys. B (Proc. Suppl.) 158(2006)111. .

[63] C. Lippmann, W. Riegler, A. Kalweit, Nucl. Phys. B (Proc. Suppl.) 158(2006)127.

[64] Werner Riegler, Nucl. Instr. Meth. A, 491(2002)258.

[65] W. Riegler, D. Burgarth, Nucl. Instr. Meth. A 481(2002)130.

[66] W. Riegler, C. Lippmann, R. Veenhof, Nucl. Instr. and Meth. 500(2003)144.

[67] A. Mangiarotti, P. Fonte, A. Gobbi, Nucl. Instr. and Meth. A 533(2004)16.

[68] P. Fonte, V. Peskov, Nucl. Instr. and Meth. A 477(2002)17.

[69] P. Fonte, L. Lopes, private comunication.

[70] S. Ramo, Proc. of the IRE 27(1939)584.

[71] P. Colrain, E. Polycarpo et al., Nucl. Instr. and Meth. A 456(2000)62.

[72] J. Va'vra, Nucl. Instr. Meth. A 515(2003)354.

[73] C. Gustavino, A. Candela, M. De Deo, M. D'Incecco, N. Redaelli, A. Tonazzo, G.C. Trinchero, Nucl. Instr. Meth. A 533(2004)116.

[74] J. Zarzycki, "Glasses and the vitreous state", Cambridge University Press, 1991.

[75] Yu. N. Pestov, Nucl. Instr. Meth. A 494(2002)447.

[76] G. Carboni, G. Collazuol, S. de Capua, D. Domenici, R. Messi, G. Passaleva, E. Santovetti, M. Veltri, Nucl. Instr. Meth. A 533(2004)107.

[77] H. R. Band, Nucl. Phys. B (Proc. Suppl.) 158(2006)139.

[78] V. Golovatyuk, F. Grancagnolo, R. Perrino, Nucl. Instr. Meth. A 508(2003)29.

[79] F. Anulli, C. Lu et al, Nucl. Instr. Meth. A 508(2003)128.

[80] S. Park, S.J. Hong et al., Nucl. Instr. Meth. A 533(2004)37.

[81] G. Aielli, P. Camarri, R. Cardarelli, A. Di Ciaccio, A. Di Simone, B. Liberti, L. Palummo, R. Santonico, Nucl. Phys. B (Proc. Suppl.) 158(2006)143.

[82] R. Santonico, Nucl. Phys. B (Proc. Suppl.)158(2006)5.

[83] L. Lopes, R. Ferreira-Marques, P. Fonte, A. P. Piedade, A. Policarpo, Nucl. Instr. Meth. A 533(2004)121.

[84] T. Kubo, H. Sakaue, Y. Teramoto, E. Nakano, T. Takahashi, Nucl. Instr. Meth. A 508(2003)50.

[85] F. Anghinolfi, P. Jarron, A. N. Martemiyanov, E. Usenko, H. Wenninger, M.C.S. Williams, A. Zichichi, Nucl. Instr. Meth. 533(2004)183.

[86] A. Schüttauf, Nucl. Instr. Meth. A 533(2004)65.

[87] D. Belver, J. A. Garzón, A. Gil, D. González-Díaz, W. Koenig, S. Lange, J. Marín, N. Montes, P. Skott, M. Traxler, M. Zapata, Nucl. Phys. B (Proc. Suppl.) 158(2006)47.

[88] M. Bogomilov, D. Dedovich, R. Dumps, F. Dydak, V. Gapienko, A. Semak, Y. Sviridov, E. Usenko, J. Wotschack, V. Zaets, Nucl. Instr. Meth. A 508(2003)152.

[89] G. Barr, D. Dedovich, A. De Min, A. De Santo, F. Dydak, V. Koreshev, L. Linssen, C. Pattison, S. Robbins, J. Wotschack, Nucl. Instr. Meth. A 533(2004)214.

[90] A. N. Akindinov, D. Hatzifotiadou et al., 533(2004)74.

[91] B. Bonner, H. Chen, G. Eppley, F. Geurts, J. Lamas-Valverde, Ch. Li, W. J. Llope, T. Nussbaum, E. Platner, J. Roberts, Nucl. Instr. Meth. A 508(2003)181.

[92] F. Geurts et al., Nucl. Instr. and Meth. A 533(2004)60.

[93] J. Wu et al., Nucl. Instr. and Meth. A 538(2005)243.

[94] M. Petrovici et al., Nucl. Instr. Meth. A 508(2003)75.

[95] "HADES, Proposal for a High-Acceptance Di-Electron Spectrometer", GSI 1994.

[96] H. Alvarez-Pol, R. Alves, A. Blanco, N. Carolino, J. Eschke, R. Ferreira-Marques, P. Fonte, J. A. Garzón, D. González-Díaz, A. Pereira, J. Pietraszko, J. Pinhão, A. Policarpo, J. Stroth, Nucl. Instr. and Meth. A 533(2004)79.

[97] H. Alvarez-Pol, R. Alves, A. Blanco, N. Carolino, J. Eschke, R. Ferreira-Marques, P. Fonte, J. A. Garzón, D. González-Díaz, A. Pereira, J. Pietraszko, J. Pinhão, A. Policarpo, J. Stroth, Nucl. Instr.and Meth. A 535(2004)277.

[98] CBM Technical Status Report, GSI, January 2005.

[99] M. J. Price, Nucl. Instr. Meth. A 478(2002)46.

[100] W. A. Zajc, Nucl. Instr. Meth. A 453(2000)25.

[101] Ch. Finck, P. Fonte, A. Gobbi, Nucl. Instr. Meth. A 508(2003)63.

[102] H. Stöker and W. Greiner, Phys. Rev. E, 137(1986)277.

[103] H. Stöker and W. Greiner and W. Scheid, Z. Phys. A, 286(1978)121.

[104] J. Aichelin and C. M. Ko, Phys. Rev. Lett., 55(1985)2661.

[105] E. Grosse, Prog. Part. Nucl. Phys., 30(1993)89.

[106] J. Aichelin, Phys. Rev. E, 202(1991)233.

[107] C. Sturm et al., Phys. Rev. Lett., 86(2001)39.

[108] J. H. Lattimer and M. Prakash, Astrophys. Jour., 550(2001)426.

[109] J. Shaffner-Bielich and I. N. Mishustin and J. Bondorf, Nucl. Phys. A, 625(1998)12.

[110] G. E. Brown and M. Rho, Phys. Rev. Lett., 66, 21(1991)2720.

[111] T. Hatsuda and S. H. Lee, Phys. Rev. C, 46(1992)R34.

[112] F. Klingl, N. Kaiser and W. Weise, Nucl. Phys. 624(1997)527.

[113] W. Weise, Prog. Theor. Phys. Suppl., 149(2003)1.

[114] G. Agakichiev et CERES collaboration, Phys. Rev. Lett., 75(1995)1272.

[115] G. Agakichiev et CERES collaboration, Eur. Phys. J. C, 4(1998)231.

[116] D. Adamova et CERES collaboration, Phys. Rev. Lett., 91(2003)042301.

[117] G. Agakichiev et CERES collaboration, Eur. Phys. J. C, 41(2005)475.

[118] R. Rapp and J. Wambach, Adv. Nucl. Phys., 6(1999)415.

[119] R. Shahoyan et NA60 collaboration, Eur. Phys. J. C, 43(2005)209.

[120] G. Usai et NA60 collaboration, Eur. Phys. J. C, 43(2005)415.

[121] S. Damjanovič et NA60 collaboration, nucl-ex/0510044, 2005.

[122] R. J. Porter et al., Phys. Rev. Lett. 79(1997)1229.

[123] W. K. Wilson et al., Phys. Rev. C 57-4(1998)1865.

[124] E. L. Bratkovskaya et al., Nucl. Phys. A 634(1998)168.

[125] K. Shekhter, C. Fuchs, Amand Faessler, M. Krivoruchenko, B. Martemyanov, Phys. Rev. C, 68(2003)014904.

[126] HADES, http://www-hades.gsi.de.

[127] P. Salabura et HADES collaboration, Progr. Part. Nucl. Phys. 53(2004)49.

[128] http://www.gsi.de.

[129] C. Garabatos et al., Nucl. Instr. and Meth. 98(1972)577.

[130] M. Boehmer, R. Gernhauser et al., Nucl. Instr. and Meth. 471(2001)25.

[131] C. Muntz, J. Markert et al., Nucl. Instr. and Meth. A 535(2004)242.

[132] C. Agodi et al., IEEE Trans. Nucl. Sci. 45, 3(1998)665.

[133] A. Balanda, J. Pietraszko et al., Nucl. Instr. and Meth. A 531(2004)445.

[134] A. Toia, I. Frohlich, W. Kuhn, J. Lehnert, E. Lins, M. Petri, J. Ritman, M. Traxler, Nucl. Instr. and Meth. A 502(2003)270.

[135] T. Eberl et HADES collaboration, Nucl. Phys A 752(2005)433.

[136] HADES collaboration, nucl-ex/0608031, submitted to PRL.

[137] http://wwwasdoc.web.cern.ch/wwwasdoc/geant_html3/geantall.html.

[138] http://www-hades.gsi.de, under sim/analysis.

[139] P. Salabura et al., HADES internal report.

[140] W. Koenig, former HADES technical coordinator, private communication.

[141] Discussions at XIII HADES collaboration meeting, Nicolosi, 3-12-2003.

[142] http://www.th.physik.uni-frankfurt.de/~urqmd/.

[143] P. Cabanelas Eiras, Diploma Thesis, Santiago de Compostela, 2005.

[144] M. Sánchez García, PhD Thesis, Santiago de Compostela, 2003.

[145] LIP-Coimbra, USC-Santiago de Compostela, "An RPC TOF WALL for the HADES spectrometer", March 2002, HADES internal report.

[146] http://www.blecha.at.

[147] A. Akindinov et al., IEEE Trans. Nucl. Sci. 48, 5(2001)2135.

[148] A. Schüttauf, Nucl. Phys. B (Proc. Suppl.) 158(2006)52.

[149] Internal ESTRELA-Santiago pages, http://www.usc.es/~genp/estrela.html.

[150] A. Kugler, J.A. Garzon, M. Golubeva, D. Gonzalez-Diaz, F. Guber, R. Holzmann, J. Novotny, P. Tlusty, proc. of Bormio conference, 2006.

[151] A. Blanco, N. Carolino, P. Fonte, A. Gobbi, IEEE Trans. Nucl. Sci. 48(2001) 1249.

[152] Model SK1201EQ5, http://www.imvo-roure.com.

[153] V. Ammosov et al., Nucl. Phys. B (Proc. Suppl.) 158(2006)56.

[154] P. Fonte, private comumication.

[155] http://www.femlab.com.

[156] A. Mangiarotti and A. Gobbi, Nucl. Instr. and Meth. A 482(2002)192.

[157] A. Gobbi, A. Mangiarotti, Nucl. Instr. and Meth. A 508(2003)23.

[158] G. Aielli, P. Camarri, R. Cardarelli, A. Di Ciaccio, L. Di Stante, B. Liberti, A. Paoloni, R. Santonico, Nucl. Instr. and Meth. A 456(2000)82.

[159] D. Belver, talk given at IV CBM collaboration meeting, GSI, Darmstadt, 2005.

[160] C. M. Lederer and V. S. Shirley, "Table of Isotopes", John Wiley & Sons, New York, 1978.

[161] L. Lopes, R. Ferreira Marques, P. Fonte, A. Pereira, V. Peskov, A. Policarpo, Nucl. Instr. and Meth. A 533(2004)69.

[162] P. Fonte, L. Lopes, private comumication.

[163] T. Soulfanidis, McGraw-Hill, New York, 1983.

[164] L. Lopes.

[165] G. Aielli, P. Camarri, R. Cardarelli, A. Di Ciaccio, L. Di Stante, B. Liberti, A. Paoloni, E. Pastori, R. Santonico, Nucl. Instr. and Meth. A 508(2003)44.

[166] M. Couceiro, private comunication.

[167] International Organization for Standarization, "Guide to the expression of uncertainty in measurement", Switzerland, 1995.

[168] P. W. Nicholson, "Nuclear Electronics", John Wiley & Sons, 1974.

[169] A. Van der Ziel, "Noise in measurements", John Wiley & Sons, 1976.

[170] M. M. Fraga et al., Nucl. Instr. and Meth. A 419(1998)485.

[171] M. Spiegel, L. Abellanas Rapun, "Fórmula y tablas de Matemática Aplicada", McGraw-Hill, 2000.